AD-A157 215   AIR FORCE ACADEMY AERONAUTICS DIGEST(U) AIR FORCE   1/3
ACADEMY CO J E DEJONGH ET AL. APR 85 USAFA-TR-85-2

UNCLASSIFIED   F/G 20/4   NL

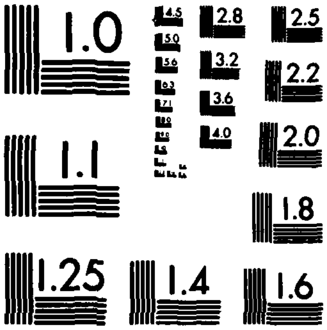

MICROCOPY RESOLUTION TEST CHART
NATIONAL BUREAU OF STANDARDS-1963-A

2

USAFA-TR-85-2

AIR FORCE ACADEMY
Aeronautics Digest

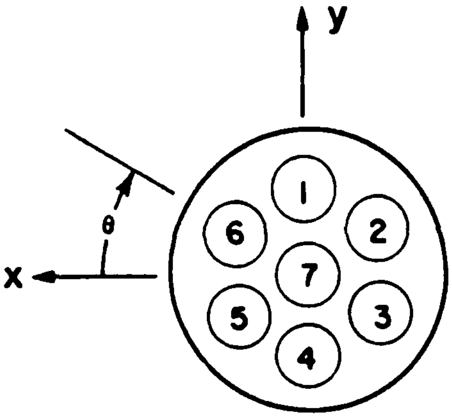

FRONT VIEW

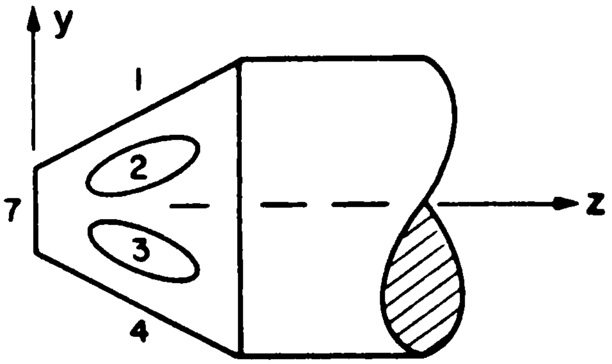

SIDE VIEW

APRIL 1985
FINAL REPORT

APPROVED FOR PUBLIC RELEASE: DISTRIBUTION UNLIMITED

Department of Aeronautics
Dean of the Faculty
United States Air Force Academy
Colorado 80840-5831

85 7 30 002

COVER:

The cover shows the geometry of a seven-hole pressure probe. This device was developed at the USAF Academy over the last seven years. During this time, the Department of Aeronautics has published several TN's and many *Digest* articles on the theory behind, and the application of, both the seven-hole probe and its precurser, the five-hole probe. The feature article in this issue of the *Digest* is "The Seven-Hole Pressure Probe," by Lawrence Reed, Jack Mattingly, and Frederick Jonas. This article documents, in one place, the latest and best information on the design, construction, calibration, and measurement capabilities of the seven-hole probe. In addition, the authors present several research applications of the probe.

Editorial Review by Capt. Michael Hale, Department of English
USAF Academy, Colorado Springs, Colorado 80840.

This *Digest* has been cleared for open publication and/or public release by the appropriate Office of Information in accordance with AFR 190-1 and DODD 5230.9. There is no objection to unlimited distribution of the *Digest* to the public at large, or by DTIC to the National Technical Information Service.

This *Digest* has been reviewed and is approved for publication.

Thomas E McCann

THOMAS E. McCANN, Lt. Col., USAF
Director of Research and
Computer Based Education

UNCLASSIFIED
SECURITY CLASSIFICATION OF THIS PAGE

AD A157 215

REPORT DOCUMENTATION PAGE

1a. REPORT SECURITY CLASSIFICATION UNCLASSIFIED	1b. RESTRICTIVE MARKINGS
2a. SECURITY CLASSIFICATION AUTHORITY	3. DISTRIBUTION/AVAILABILITY OF REPORT Approved for public release. Distribution unlimited.
2b. DECLASSIFICATION/DOWNGRADING SCHEDULE	
4. PERFORMING ORGANIZATION REPORT NUMBER(S) USAFA-TR-85-2	5. MONITORING ORGANIZATION REPORT NUMBER(S)
6a. NAME OF PERFORMING ORGANIZATION Department of Aeronautics 6b. OFFICE SYMBOL *(If applicable)*	7a. NAME OF MONITORING ORGANIZATION
6c. ADDRESS *(City, State and ZIP Code)* U.S. Air Force Academy Colorado Springs, CO 80840 - 5831	7b. ADDRESS *(City, State and ZIP Code)*
8a. NAME OF FUNDING/SPONSORING ORGANIZATION 8b. OFFICE SYMBOL *(If applicable)*	9. PROCUREMENT INSTRUMENT IDENTIFICATION NUMBER
8c. ADDRESS *(City, State and ZIP Code)*	10. SOURCE OF FUNDING NOS. PROGRAM ELEMENT NO. / PROJECT NO. / TASK NO. / WORK UNIT NO.

11. TITLE *(Include Security Classification)*
Air Force Academy Aeronautics Digest

12. PERSONAL AUTHOR(S)
Editors: DeJongh, J., Heiser, W., Hale, M.

13a. TYPE OF REPORT	13b. TIME COVERED	14. DATE OF REPORT *(Yr., Mo., Day)*	15. PAGE COUNT
Final Report	FROM _____ TO _____	April 1985	

16. SUPPLEMENTARY NOTATION

17. COSATI CODES

FIELD	GROUP	SUB. GR.

18. SUBJECT TERMS *(Continue on reverse if necessary and identify by block number)*
Seven-hole probe, dynamic stall, flight mechanics, flight control system design, computer controlled aircraft, data reduction, Fourier transform, T-38 aerodynamic drag, ventral fin.

19. ABSTRACT *(Continue on reverse if necessary and identify by block number)*

This Digest covers unclassified research in aeronautics performed by individuals assigned to or associated with the United States Air Force Academy. This report includes technical papers in the specific areas of aerodynamics, instrumentation, and flight mechanics.

20. DISTRIBUTION/AVAILABILITY OF ABSTRACT UNCLASSIFIED/UNLIMITED ☒ SAME AS RPT. ☐ DTIC USERS ☐	21. ABSTRACT SECURITY CLASSIFICATION UNCLASSIFIED

22a. NAME OF RESPONSIBLE INDIVIDUAL	22b. TELEPHONE NUMBER *(Include Area Code)*	22c. OFFICE SYMBOL
Major Jay E. DeJongh	303-472-4010	DFAN

DD FORM 1473, 83 APR EDITION OF 1 JAN 73 IS OBSOLETE.

UNCLASSIFIED
SECURITY CLASSIFICATION OF THIS PAGE

PREFACE

This report is the thirteenth issue of the Air Force Academy Aeronautics Digest.* Our policy is to print articles which represent recent scholarly work by students and faculty of the Department of Aeronautics, members of other departments of the Academy and the Frank J. Seiler Research Laboratory, researchers directly or indirectly involved with USAFA-sponsored projects, and authors in fields of interest to the USAFA.

In addition to complete papers, the Digest includes, when appropriate, abstracts of lengthier reports and articles published in other formats. The editors will consider for publication contributions in the general field of Aeronautics, including:

- Aeronautical Engineering
  - Aerodynamics
  - Flight Mechanics
  - Propulsion
  - Structures
  - Instrumentation
- Fluid Dynamics
- Thermodynamics and Heat Tranfer
- Biomechanics
- Engineering Education
- Aeronautical History

Papers on other topics will be considerd on an individual basis. Contributions should be sent to:

Editor, Aeronautics Digest
HQ USAFA/DFAN
US Air Force Academy
Colorado Springs, CO 80840-5831

The Aeronautics Digest is edited at present by Maj. Jay E. DeJongh, PhD; William H. Heiser, PhD; and Capt. Michael Hale, who provided the final editorial review. Our thanks also to Contract Technical Services, Inc. for illustration services and to Associate Editor, Kathleen Brandt Maddox of Contract Technical Services Inc.

---

*Previous issues of the Digest can be ordered from the Defense Technical Information Center (DTIC), Cameron Station, Alexandria, VA 22324.

CONTENTS

SECTION I.

Instrumentation

THE SEVEN-HOLE PRESSURE PROBE

Lawrence Reed*, Jack D. Mattingly**, and Frederick Jonas**

Abstract

This paper documents recent and past developments with respect to the seven-hole pressure probe. Included are discussions on probe design, construction, calibration, and measurement capabilities. The effects on probe measurements in shear flows, as well as methods of correction, are also included. Finally, research applications in the measurement of unknown flowfields are presented. As shown, the seven-hole pressure probe is a valuable and highly accurate device for quantitatively documenting unknown flowfields.

I. Introduction

The purpose of this paper is to document recent and past developments with respect to the seven-hole pressure probe developed at the United States Air Force Academy in conjunction with the NASA Ames Research Center. As with all pressure probes, the seven-hole probe can be used to map unknown internal or external flowfields, giving valuable information to the aerodynamicist. The advantage of the seven-hole probe over other flowfield measuring devices is its widely expanded measurement range and flexibility. To document this effort, Section II presents brief background material about the probe's design and use. Section III includes an overview of probe calibration in uniform flows, both compressible and incompressible. In Section IV, recent results of investigations into probe measurement capablities in shear flow environments are presented. Measurement capabilities as well as

---

*2nd Lt., USAF, Graduate Student, Univ. of Washington

**Major, USAF, Associate Professor, Dept. of Aeronautics

measurement sources of error are discussed in Section V. Finally, recent research efforts on the application of seven-hole probe measurements in unknown flows are presented in Section VI.

II. Background

Numerous techniques are available to measure unknown flow fields. While methods such as tufts, streamers, and vanes are primarily used for flow visualization, they are insufficient for quantitative information. Detailed data on flow size, direction, and pressure usually require direct obtrusive flow measurement.

One of the oldest known quantitative techniques may be found in the pressure probe. Although other techniques, such as hot wire anemometers and laser doppler anemometers, have been developed, pressure probes are desirable from a *flight* vehicle standpoint because of their simplicity and ruggedness (Ref. 1). Coupled with relatively low cost, pressure probes are an excellent measurement device for research, development, and industrial applications.

One of the classic problems in obtrusive flow measurement is the disturbance caused by a probe to the flowfield it is measuring. For certain applications, such as aircraft pitot-static tubes, this disturbance or perturbation is relatively unimportant. These probes may be large, for the relative perturbation of the probe to that of the aircraft is negligible; further, installation of the probes is accounted for in the airspeed measurement. To determine the effect of flow disturbances for other applications requires varying levels of knowledge about the flowfield being measured as well as probe geometry and installation. The accuracy and measurement ranges of such probes also depend on the size, geometry, number of holes, and installation. The seven-hole probe was developed at the United States Air Force Academy to increase the measurement range of an non-nulling pressure probe while minimizing probe size.

A. Nulling Versus Stationary Probes

The increased measurement range of a multi-hole probe revolves on its ability to sense more pressures at the face of the probe. Two procedures, nulling and stationary, may be used to acquire the pressure data. A nulling probe is rotated in one or two planes until opposing peripheral ports measure equal pressures. The corresponding angle of rotation determines the flow angle. For the non-nulling approach, the probe is held stationary as pressures in opposing peripheral ports are recorded. The pressure differences are then transformed to flow angles through previously known calibration relationships. Although the nulling procedure allows analysis of high angle flow, it is mechanically complex, time consuming, and hence, may not be cost effective. On the other hand, stationary probes with up to five holes are incapable of accurate measurements at high local flow angles (greater than 30 degrees) because of flow separation around the probe tip. Explained in detail in a later section, the seven hole probe is the only non-nulling probe that can determine flow angles up to 70 degrees relative to its axis. When combined with a computerized data acquisition system, the probe may record nearly two data points per second. This rate is significantly faster than current nulling devices, which require considerable time for the balancing of probe tip pressures before each measurement can be taken (Ref. 2).

B. Analytical Model of Pressure Probe

Pressure probes used for measurement of flow direction and magnitude normally consist of an aerodynamic body with a symmetrical arrangement of sensing holes (Figure 1). Some typical geometries for pressure probes are reviewed in References 3 through 17 and pressure probes are treated in more general terms in References 18 and 19.

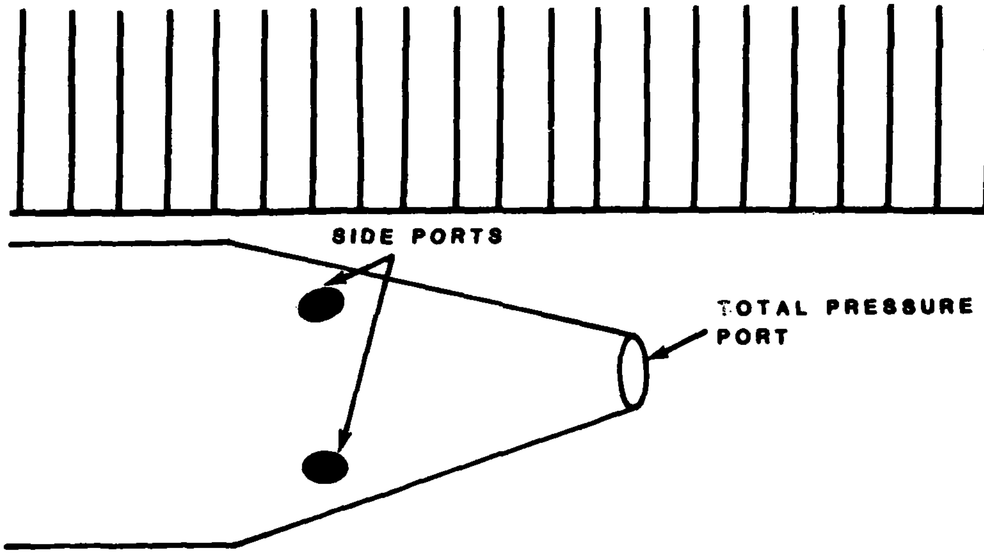

Figure 1. TYPICAL FLOW-DIRECTION PROBE (EACH UNIT ON SCALE REPRESENTS 0.5mm)

Since the pressure probes of interest are to be used without rotation, the sensitivity to flow angularity is extremely important. A general analytical model was developed by Huffman using slender body theory (Ref. 20), which permits synthesizing a sensor geometry for a special application and analysis of probe behavior.

While numerically solving the three-dimensional potential flow equations for the flow around an aerodynamic probe may be more accurate than slender body theory under some conditions (Ref. 21 and 22), it does not lend itself to synthesis of probe shapes. The slender body approach to the analysis of the probe provides a basis for formulating analytic calibration relations and provides considerable insight into the physical process.

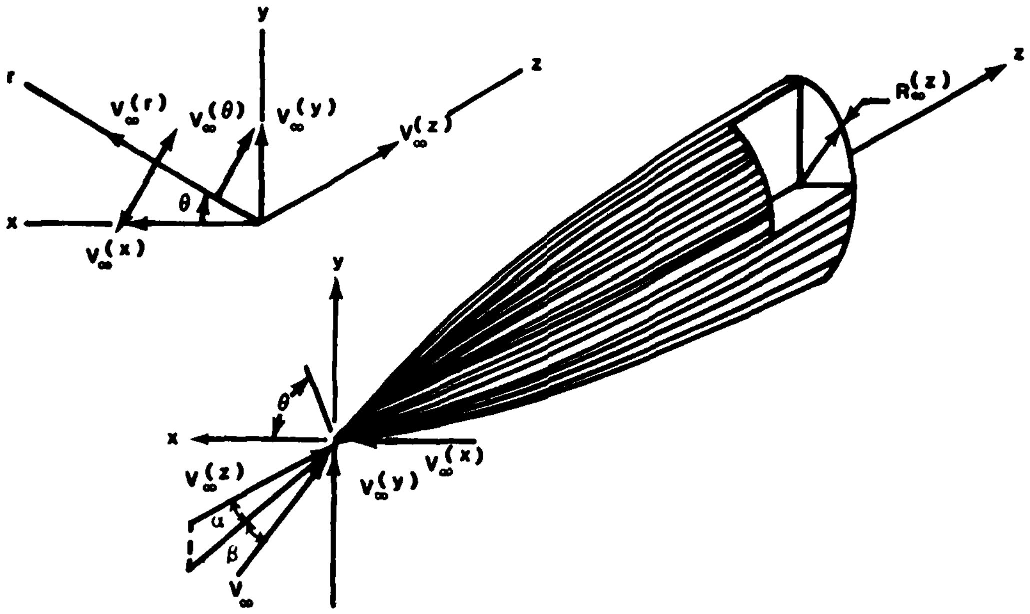

Figure 2. SLENDER BODY OF REVOLUTION IN A CROSS-FLOW (REF.18)

Huffman modeled the probe as a yawed body of revolution as shown in Figure 2. For a slender body, the equation of motion is linear and Huffman wrote the velocity potential as the sum of the axial flow and the cross flow components (this follows a method specified by Liepmann and Roshkow, Ref. 23). Solution of the equation of motion yielded the following velocity field in cylindrical coordinates:

$$\frac{v_r}{V_\infty} = R'\frac{R}{r}(\cos\alpha\ \cos\beta) + \left(1-\frac{R^2}{r^2}\right)(\sin\beta\ \cos\Theta + \sin\alpha\ \cos\beta\ \sin\Theta)$$

$$\frac{v_\theta}{V_\infty} = \left(1 + \frac{R^2}{r^2}\right)(\sin\alpha\ \cos\beta\ \cos\theta - \sin\beta\ \sin\theta) \qquad (1)$$

$$\frac{v_z}{V_\infty} = \left(1+\frac{f}{2}\right)(\cos\alpha\ \cos\beta\ ) + 2R'\frac{R}{r}(\sin\beta\ \cos\Theta + \sin\alpha\ \cos\beta\ \sin\Theta)$$

where f denotes the body-geometry function given by

$$\begin{aligned} f = & -\frac{1}{2}(R^2)'\left(\frac{1}{\sqrt{z^2+\delta^2 r^2}} - \frac{1}{\sqrt{(\ell-z)^2+\delta^2 r^2}}\right) \\ & +\frac{1}{2}(R^2)''\left[\frac{\ell-z}{\sqrt{(\ell-z)^2+\delta^2 r^2}} + \frac{z}{\sqrt{z^2+\delta^2 r^2}} + \ell n\left(\frac{-z+\quad z^2+\delta^2 r^2}{\sqrt{\ell-z+\quad(\ell-z^2+\delta^2 r^2)}}\right)\right] \qquad (2) \\ & -\frac{1}{4}(R^2)'''\left(\frac{z^2}{\sqrt{z^2+\delta^2 r^2}} - \frac{(\ell-z)^2}{\sqrt{(\ell-z)^2+\delta^2 r^2}} + 2\sqrt{(\ell-z)^2+\delta^2 r^2} - 2\sqrt{z^2+\delta^2 r^2}\right) + \ldots \end{aligned}$$

The superscript prime (') denotes the derivative with respect to the variable z, and $\delta^2 = 1 - M_\infty^2$.

The pressure coefficient is defined as

$$C_p = \frac{P-P_\infty}{\frac{1}{2}\rho V_\infty^2} = 1 - \frac{V^2}{V_\infty^2} \qquad (3)$$

And when evaluated on the body the following expression results:

$$\begin{aligned} C_p = & -[f+f^2/4+(R')^2]\cos^2\alpha\ \cos^2\beta + \sin^2\beta\ [1-4\sin^2\Theta - 4(R')^2\cos^2\Theta] \qquad (4) \\ & +\sin^2\alpha\ \cos^2\beta\ [1-4\cos^2\Theta - 4(R')^2\sin^2\Theta] + 2\sin\alpha\ \sin2\beta\ \sin2\Theta\ [1-(R')^2] \\ & -2R'(1+f/2)\ [\cos\alpha\ \sin2\beta\ \cos\Theta + \sin2\alpha\ \cos^2\beta\ \sin\Theta] \end{aligned}$$

where f is to be evaluated on the body surface, i.e. r=R. Equation 4 represents the major result of Huffman's analysis and can be used to determine probe angular and static pressure sensitivity for arbitrary geometries.

The pressure difference between ports on opposite sides of the probe is used to determine the flow angularity. Since the side ports of the probe are at the same z and r locations, the pressure difference is proportional to the difference of C_p values at different θ locations and

$$\begin{aligned} C_{p_i}-C_{p_j} &= 4\sin^2\beta\ [\sin^2\theta_j-\sin^2\theta_i+(R')^2(\cos^2\theta_j-\cos^2\theta_i)] \\ &\quad +4\sin^2\alpha\ \cos^2\beta\ [\cos^2\theta_j-\cos^2\theta\ +(R')^2(\sin^2\theta_j-\sin^2\theta_i)] \\ &\quad +2\sin\alpha\ \sin 2\beta\ [1-(R')^2]\ [\sin 2\theta_i-\sin 2\theta_j] \\ &\quad -2R'(1+f/2)[\cos\alpha\ \sin 2\beta\ (\cos\theta_i-\cos\theta_j)+\sin 2\alpha\ \cos^2\beta(\sin\theta_i-\sin\theta_j)] \end{aligned} \tag{5}$$

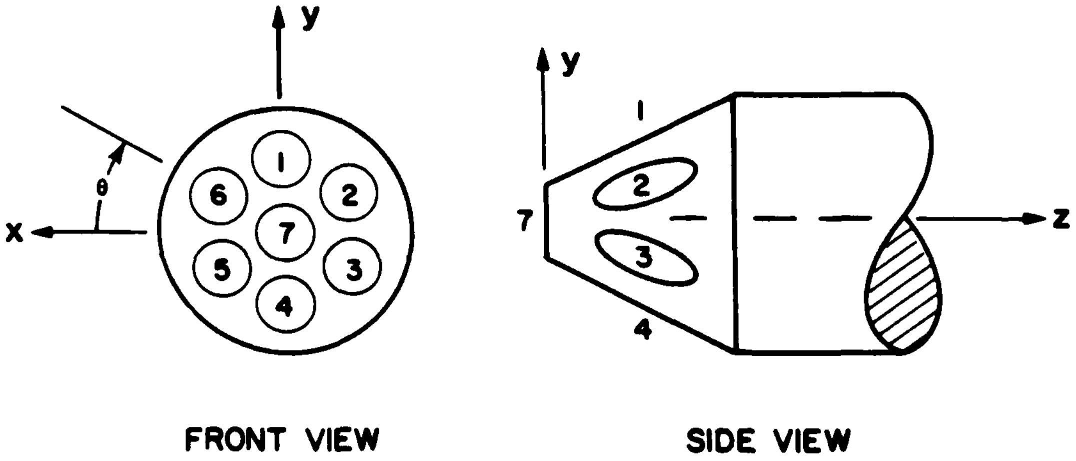

Figure 3. SEVEN-HOLE PROBE

For the seven-hole probe shown in Figure 3, the six holes on the side face are located at $\Theta_1=90°$, $\Theta_2=150°$, $\Theta_3=210°$, $\Theta_4=270°$, $\Theta_5=330°$, and $\Theta_6=30°$. The resulting three pressure coefficient differences for opposite side holes are

$$\Delta C_1 = C_{p_4} - C_{p_1} = 4R'(1+f/2)\ \sin 2\alpha\ \cos^2\beta$$

$$\Delta C_2 = C_{p_3} - C_{p_6} = 2R'(1+f/2)[\ 3\ \cos\alpha\ \sin 2\beta + \sin 2\alpha\ \cos^2\beta] \qquad (6)$$

$$\Delta C_3 = C_{p_2} - C_{p_5} = 2R'(1+f/2)[\ 3\ \cos\alpha\ \sin 2\beta - \sin 2\alpha\ \cos^2\beta]$$

These three pressure coefficients can be combined into a coefficient that is mainly dependent on the flow angle α and another coefficient that is mainly dependent on the flow angle β as follows:

$$\Delta C_\alpha = \frac{2\Delta C_1 + \Delta C_2 - \Delta C_3}{3} = 4R'(1+f/2)\ \sin 2\alpha\ \cos^2\beta$$

$$\Delta C_\beta = \frac{\Delta C_2 + \Delta C_3}{\sqrt{3}} = 4R'(1+f/2)\ \cos\alpha\ \sin 2\beta \qquad (7)$$

The sensitivity to changes in flow angle is defined as $\frac{\partial \Delta C_\alpha}{\partial_\alpha}$ or $\frac{\partial \Delta C_\beta}{\partial_\beta}$. These can be written as

$$\frac{\partial \Delta C_\alpha}{\partial_\alpha} = 8R'(1+f/2)\ \cos 2\alpha\ \cos^2\beta \qquad (8)$$

$$\frac{\partial \Delta C_\beta}{\partial_\beta} = 8R'(1+f/2)\ \cos\alpha\ \cos 2\beta \qquad (9)$$

Note that the sensitivity to flow direction in one plane depends to some extent on the flow angle in the other direction. Also, the sensitivity is proportional to the slope of the probe's surface, R'. Equation 8 is plotted in Figure 4 for f=0. It is quite apparent from the figure that the probe angularity sensitivity -- regardless of shape -- depends on α and β. Approximately a 10% reduction in sensitivity occurs for α and β values of 10°. Note that $\partial\Delta C\alpha/^2\alpha$ is the same for both positive and negative values of α and β.

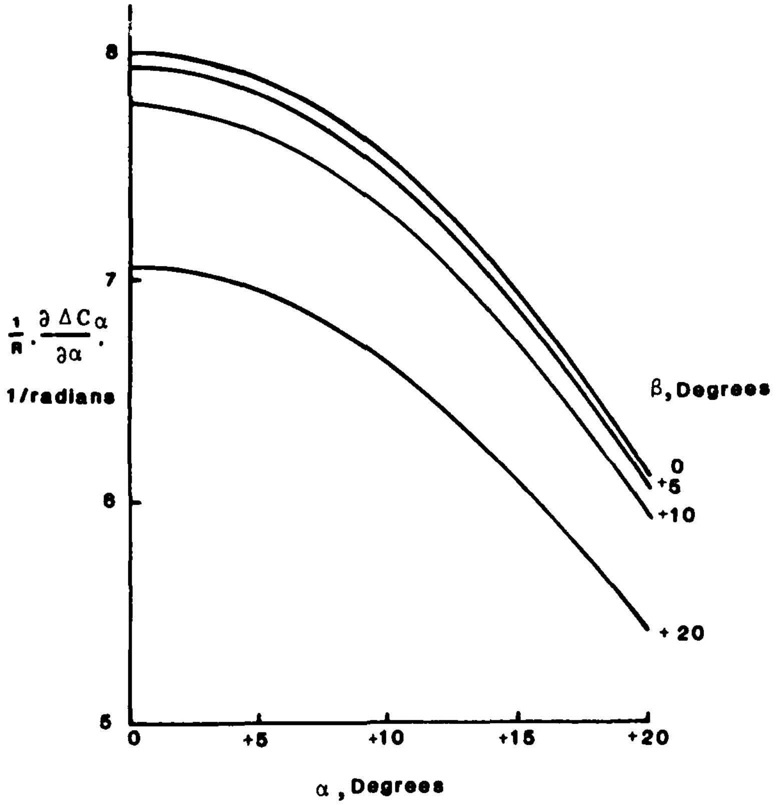

Figure 4. PROBE ANGULAR SENSITIVITY AS A FUNCTION OF α AND β (REF.18)

The average pressure coefficient can be used to determine the flowfield static pressure, P_∞. C_p is evaluated at a number of theta values and the results summed and divided by the number of theta values. For the seven-hole probe of Figure 3, this process yields

$$\left\langle C_p \right\rangle = [1-f-f^2/4+(R')^2]\cos^2\alpha\cos^2\beta-[1+2(R')^2] \tag{10}$$

Huffman developed an expression for a quasi total pressure from his analysis by integrating the pressure from the body surface, resolving this force into an axial component, and dividing by the cross sectional area. His relationship is

$$\left\langle C_p \right\rangle_z = -\frac{\cos^2\alpha\cos^2\beta}{R_\ell^2}\int_0^\ell (R^2)'[f+f^2/4+(R')]dz-\sin^2\beta-\sin^2\alpha\cos^2\beta \tag{11}$$

where ℓ denotes the integration length.

For a conical shaped body, R' is constant and Equation 11 reduces to

$$\left\langle C_p \right\rangle_z = [1-f-f^2/4-(R')^2]\cos^2\alpha\cos^2\beta-1 \tag{12}$$

A probe pressure coefficient that is proportional to the dynamic pressure can be obtained by subtracting Equation 10 from Equation 12 yielding a dynamic pressure coefficient.

$$\left\langle C_p \right\rangle_z - \left\langle C_p \right\rangle = 2(R')^2[1-\cos^2\alpha\ \cos^2\beta] \tag{13}$$

Some insight into probe calibration can be obtained by studying the plot of α and β versus $\Delta C\alpha$ and $\Delta C\beta$ in Figure 5, the plot of $\langle C_p \rangle$ versus α and β in Figure 6, the plot of $\langle C_p \rangle z$ versus α and β in Figure 7, and the plot of $\left[\langle C_p \rangle z - \langle C_p \rangle\right]$ versus α and β in Figure 8. Figures 1 through 8 were calculated for $R' = .268$ and $f = 0$. Note the near linear relation between each angle and its respective pressure coefficient as shown in Figure 5. Also, the nearly circular contours of constant $\langle C_p \rangle$, $\langle C_p \rangle z$, and $\left[\langle C_p \rangle z - \langle C_p \rangle\right]$ as shown in Figures 6,7, and 8, respectively. Probe manufacturing imperfection and angular misalignment of the pressure ports will cause these curves to become somewhat distorted.

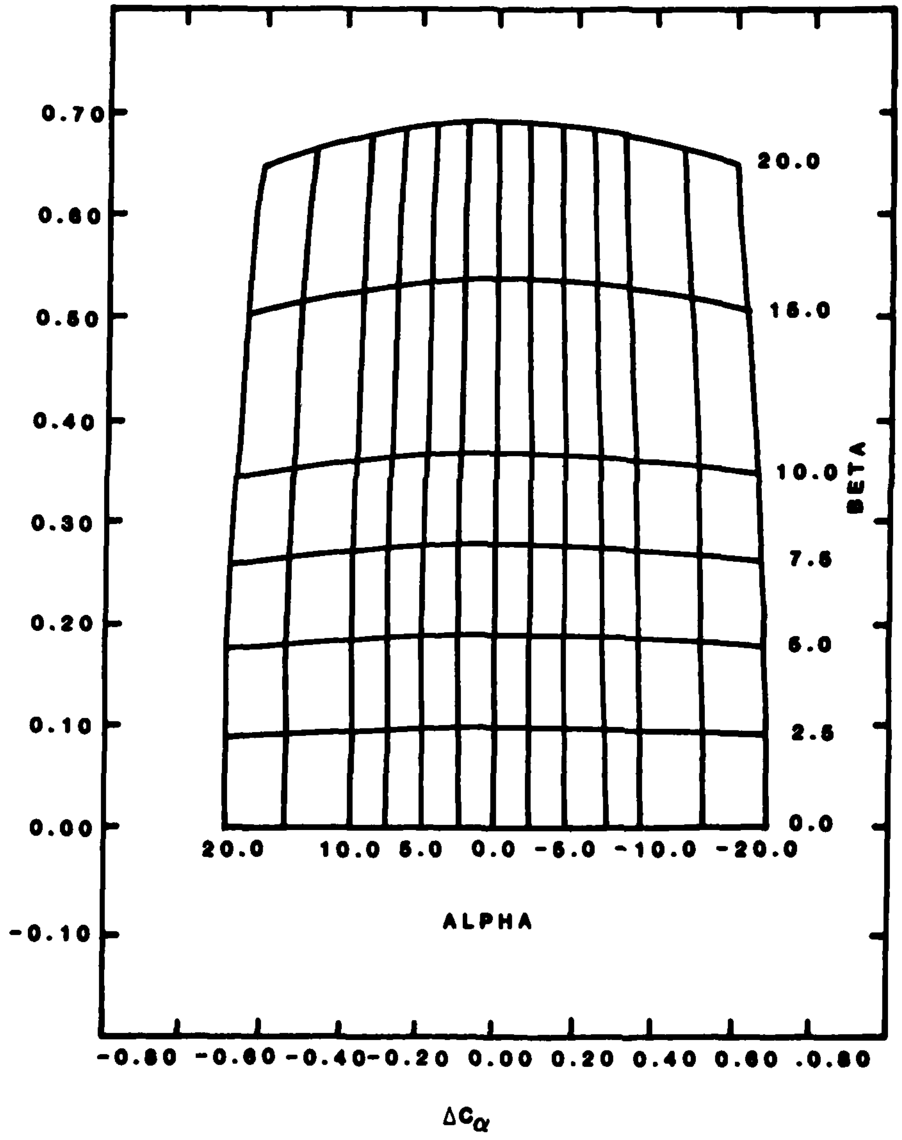

Figure 5. ΔC_α VERSUS ΔC_β FOR A TYPICAL FLOW DIRECTION PROBE (REF. 18)

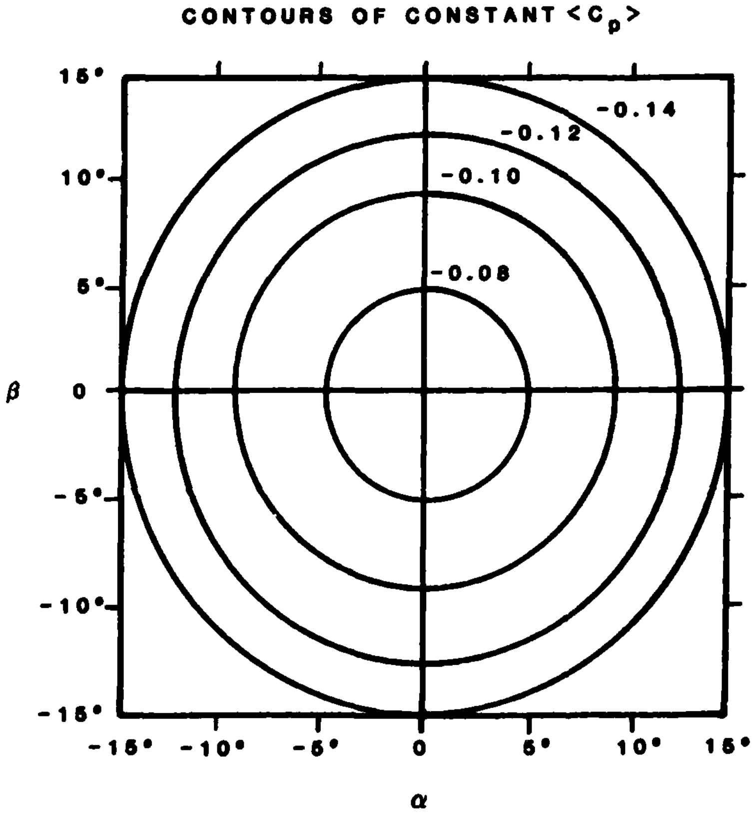

Figure 6. CONTOURS OF CONSTANT$<C_p>$

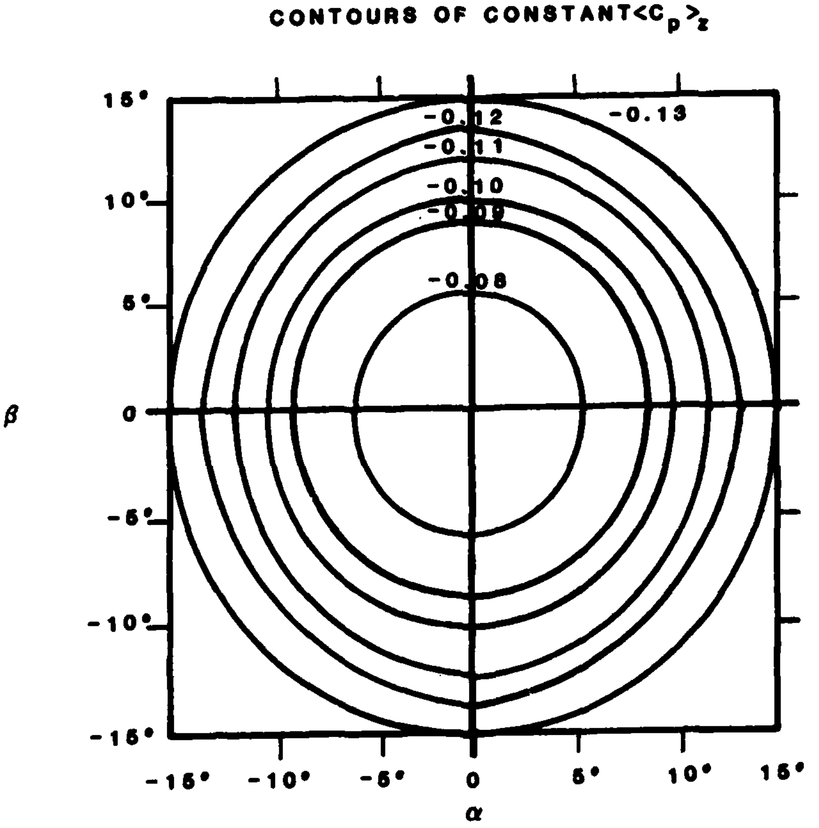

Figure 7. CONTOURS OF CONSTANT$<C_p>_z$

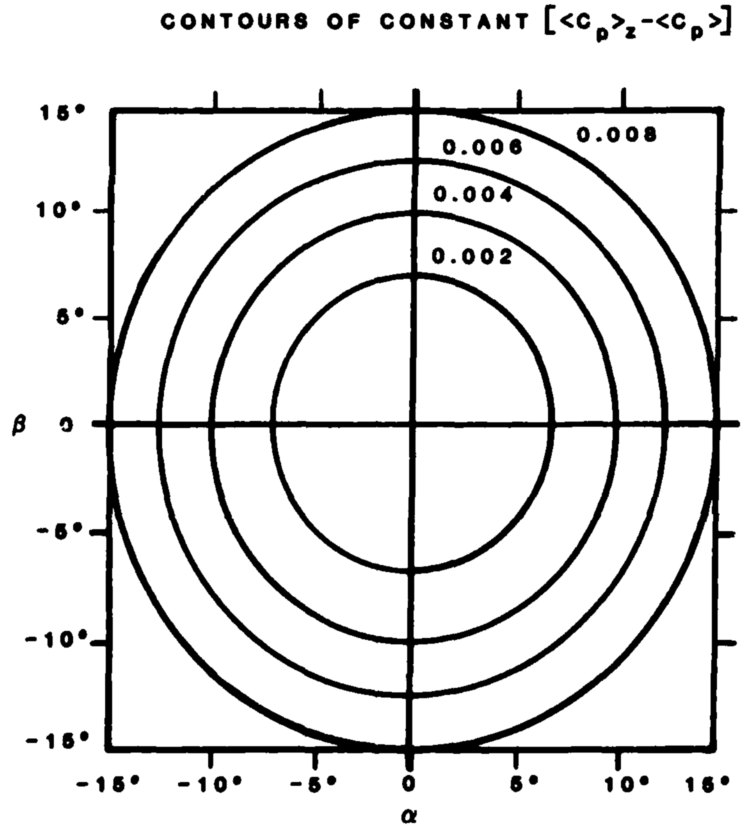

Figure 8. CONTOURS OF CONSTANT $\langle C_p \rangle_z - \langle C_p \rangle$

C. Seven-Hole Probe Design

The seven-hole probe is characterized by six periphery ports surrounding one central port (Fig. 9). The probe is constructed by packing seven properly sized stainless steel tubes into a stainless steel casing. For the current probe used at the Air Force Academy, the inner seven tubes have an outside diameter of .028 inches with a .0005-inch wall thickness. Once assembled in the order shown below, the tubes are soldered together and machined to the desired half angle (usually 25 or 30 degrees) at the tip (Ref. 2). It should be noted that the manufacture of seven-hole probes (versus four/five hole probes) is much simpler due to this packing arrangement.

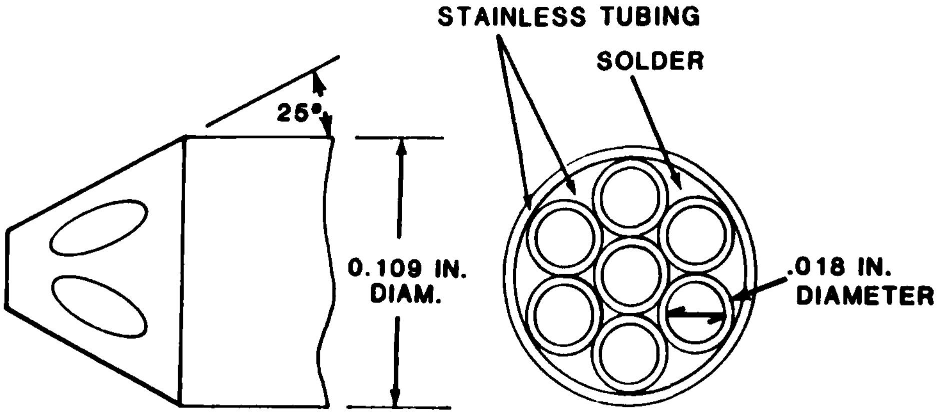

Figure 9. PROBE GEOMETRY

III. Seven-Hole Probe Calibration Theory

Because of their small size and individual construction, all probes have inherent manufacturing defects that require the unique calibration of each probe. Gallington (Ref. 24) developed the calibration theory required for incompressible, uniform flows. His power series method produces explicit polynominal expressions for the desired aerodynamic properties and is easily programmed. The following section presents a synopsis of Gallington's scheme for incompressible, uniform flow calibration as presented by Gallington (Ref. 20) and by Gerner and Mauer (Ref. 2).

A. Low Versus High Flow Angles, Incompressible Flow

In this calibration technique for incompressible, uniform flow, the probe face is divided into two sectors. The inner flow sector deals with low flow angles in which the angle between the probe's axis and the freestream velocity vector is less than 30 degrees. The other or outer sector deals with high flow angles of over 30 degrees. Thirty degrees is the dividing point because flow typically begins to detach over the top surface of the probe tip around this local flow angle. The hole numbering system used for both sectors and the remainder of the report is as follows:

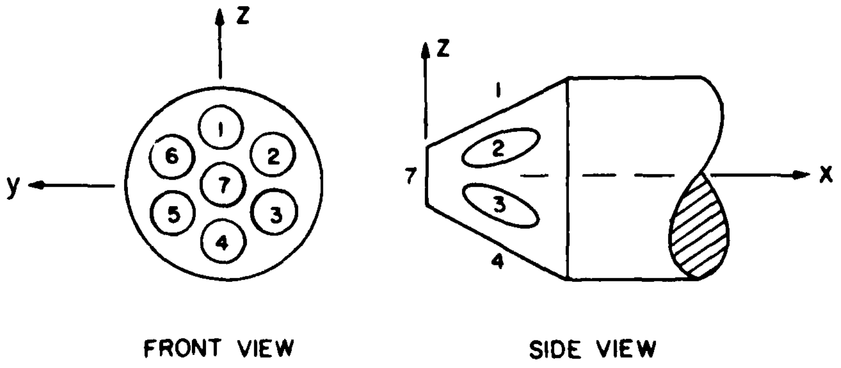

Figure 10. PORT NUMBERING CONVENTION AND PRINCIPAL AXES

The x-axis is defined to be positive in the unperturbed freestream flow direction. The origin is a point at the tip of the cone formed by the probe (Fig. 10).

B. Probe Axis System for Low Flow Angles

The axis system for low flow angles is the tangential alpha-beta system depicted below (Fig. 11). The angle of attack, alpha (α_T), is measured directly as the projection on the x-plane. To preserve symmetry, the angle of sideslip (β_T) is measured directly as the projection on the y-plane.

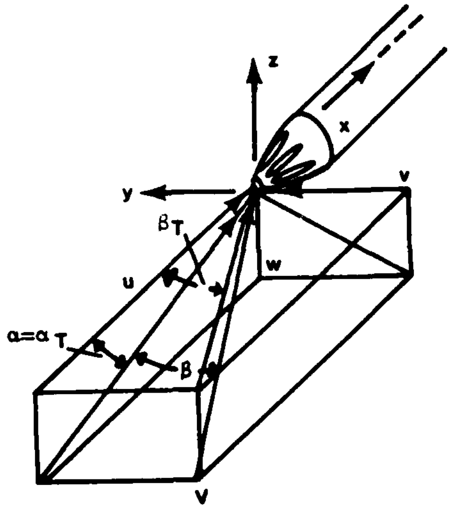

CONVENTIONAL	TANGENT
$u = V \cos\alpha\cos\beta$ $v = V \sin\beta$ $w = V \sin\alpha\cos\beta$	$\alpha_T = \arctan \frac{w}{u}$ $\beta_T = \arctan \frac{v}{u}$

Figure 11. LOW ANGLE REFERENCE SYSTEM

C. Pressure Coefficients for Low Flow Angles

The flow angle is determined as a function of dimensionless pressure coefficients. Three pairs of opposing peripheral ports measure the differences in pressure from one side of the probe to the other and form the following three relationships:

$$C_{\alpha_1} = \frac{P_4 - P_1}{P_7 - \overline{P}_{1-6}}, \quad C_{\alpha_2} = \frac{P_3 - P_6}{P_7 - \overline{P}_{1-6}}, \quad C_{\alpha_3} = \frac{P_2 - P_5}{P_7 - \overline{P}_{1-6}} \qquad (14)$$

As the numerator measures changes in flow angularity, the denominator nondimensionalizes the expression with the apparent dynamic pressure. The center port pressure, P_7, approximates the local total pressure while the average of the circumferential port pressures $\bar{P}_{1-6}$ approximates the local static pressure. To transform these pressure coefficients to the tangential reference system, Gallington (Ref. 24) formulates the following relationships:

$$C_\alpha = \frac{1}{3}(2C_{\alpha_1} + C_{\alpha_2} - C_{\alpha_3}) \quad , \quad C_\beta = \frac{1}{\sqrt{3}}(C_{\alpha_2} + C_{\alpha_3}) \qquad (15)$$

It is important to realize that C_α and C_β are not independent of each other; that is, C_α is a function of all six peripheral ports while C_β is a function of all but ports 1 and 4.

Besides the two angular pressure coefficients, two other low angle pressure coefficients, C_o and C_q, are defined in Gallington's work (Ref. 24):

$$C_o = \frac{P_7 - P_{oL}}{P_7 - \bar{P}_{1-6}} \qquad C_q = \frac{P_7 - \bar{P}_{1-6}}{P_{oL} - P_{\infty L}} \qquad (16)$$

C_o is the apparent total pressure coefficient with respect to each hole and is a means to convert actual pressures measured by the probe to accurate values of local total pressure. The numerator measures the difference between the approximate total pressure measured by the center port P_7 And the actual local total pressure P_{oL}. As with the previous coefficients, the denominator nondimensionalizes the expression with the apparent local dynamic pressure.

The velocity pressure coefficient, C_q, serves a similar conversion function as C_o except that it relates the probe pressures to the actual dynamic pressure. The numerator in this coefficient represents the probe's approximation of the local dynamic pressure while the denominator represents the actual dynamic pressure of the freestream test conditions.

D. Probe Axis System for High Flow Angles

The real advantage of using the non-nulling seven-hole probe over other multi-hole probes appears in the ability to measure high-angle flows. At high angles of attack (greater than 30 degrees), the flow detaches over the upper surface of the probe, and pressure ports in the separated wake are insensitive to small changes in flow angularity (Fig. 12).

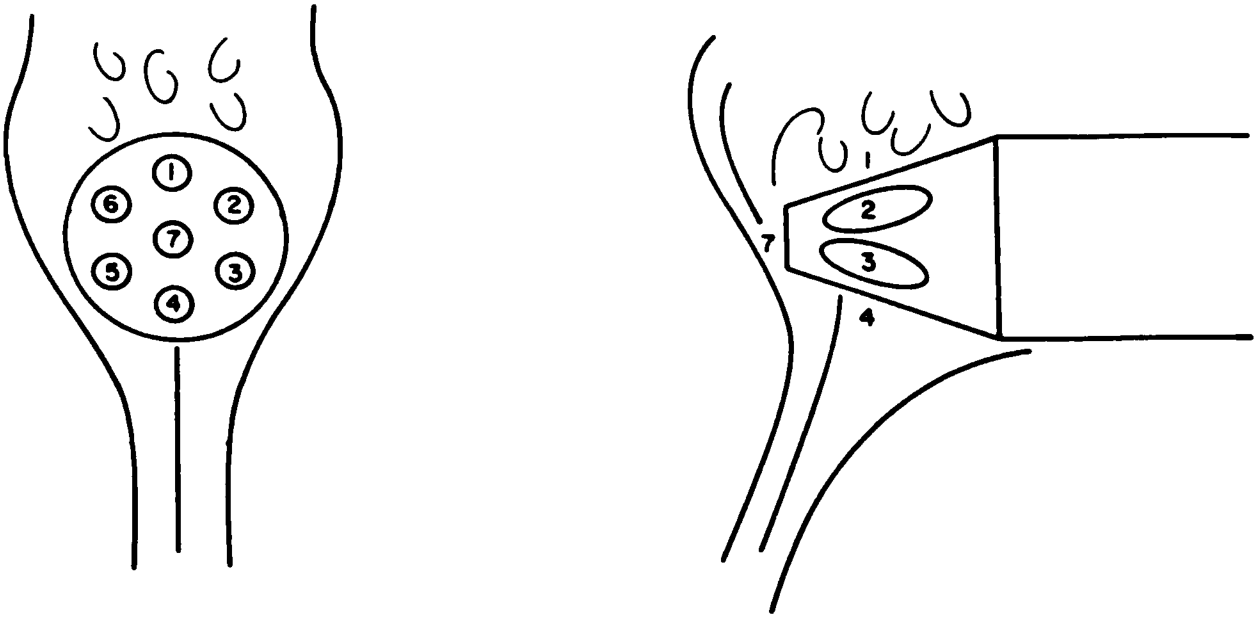

Figure 12. FLOW PATTERN OVER SEVEN-HOLE PROBE AT HIGH ANGLE OF ATTACK

Consequently, high angle measurements must only be made from ports in the attached flow. Five-hole and other pressure probes have been ineffective in this regime due to this flow separation and lack of sensing ports in the attached flow region. The seven-hole probe avoids this problem because at least three ports remain in the attached flow region, allowing sufficient data to be recorded to document the flow angle.

According to Gallington, the tangential reference system is inappropriate at high flow angles because of indeterminate angles and singularities (Ref. 24). Instead, the polar reference system is used (Fig. 13) where θ represents the pitch angle and ϕ represents the roll angle.

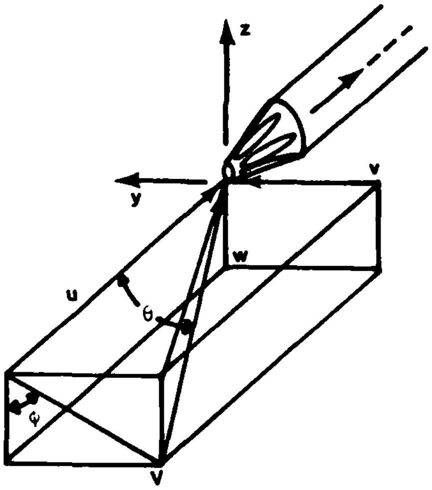

POLAR	TANGENT
$u = V\cos\theta$	$\alpha_T = \arctan \frac{w}{u}$
$v = V\sin\theta\sin\phi$	$\beta_T = \arctan \frac{v}{u}$
$w = V\sin\theta\cos\phi$	

Figure 13. HIGH ANGLE REFERENCE SYSTEM

More specifically, θ denotes the angle that the velocity vector forms with respect to the probe's x-axis, and ϕ signifies the azimuthal orientation of the velocity vector in the y-z plane. We should note that a positive ϕ is measured counterclockwise from the negative z axis when the probe is viewed from the front.

Based on Gallington's original work with the seven-hole probe at high angles of attack, Gerner and Mauer accomplished the following analysis (Ref. 2). Kuethe and Chow's Foundations of Aerodynamics: Bases of Aerodynamic Design, explains that the separation points of a cylinder in turbulent flow are over 100 degrees from the frontal stagnation point. Flow around a conical body such as a probe tip was likely to remain attached longer, and the u-velocity component was prone to extend the separation points downstream even further. Therefore, for the high angle flow shown in Figure 14, ports 3, 4, and 7 lie in attached flow, and port 1 lies in separated flow. The flow over ports 2 and 6 is unpredictable, and their readings are discarded (Ref. 2).

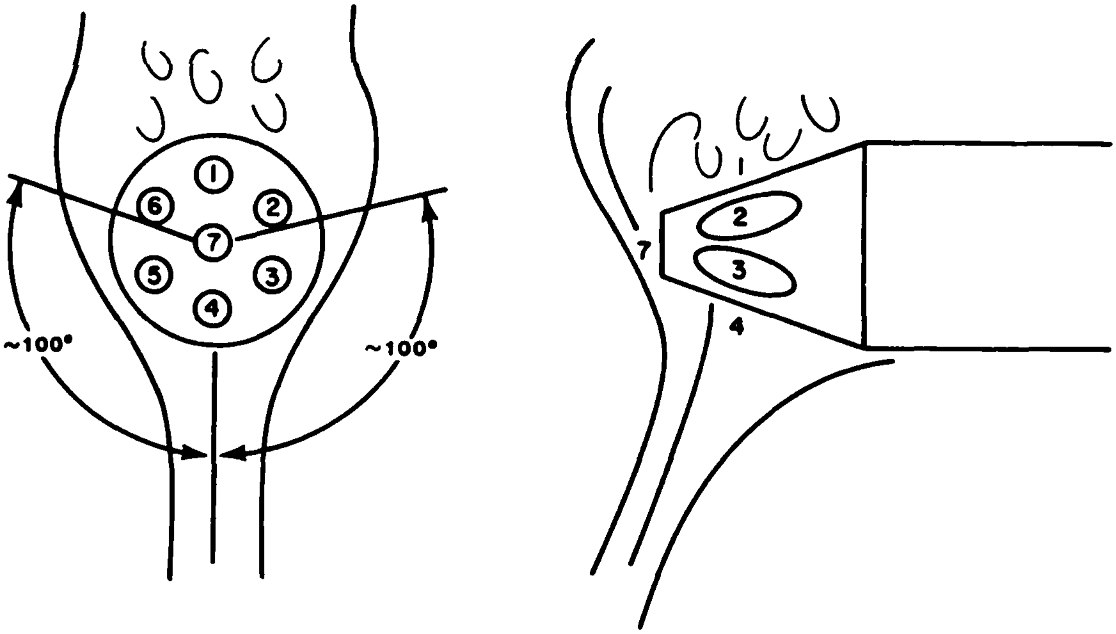

Figure 14. FLOW OVER PROBE AT HIGH ANGLE OF ATTACK

E. Pressure Coefficients for High Flow Angles

As with low flow angles, high flow angularity is measured by dimensionless pressure coefficients that are functions of port pressure differences. Unlike low flow angles, however, the center port pressure is now the most dependent port on local flow angle. Consequently, a pitch angular pressure coefficient should measure the difference between the center port and a new stagnation port. In the example below, the pressure at P_4 approximates the local total pressure.

$$C_{\theta_4} = \frac{P_4 - P_7}{P_4 - \frac{P_3 + P_5}{2}} \qquad (17)$$

The expression is again nondimensionalized by the apparent dynamic pressure. The average of P_3 and P_5 approximates the static pressure and is relatively independent to changes in roll.

Although the average is independent of ϕ, the difference is sensitive to roll angle. As the probe's azimuthal orientation changes, the windward pressure rises and the leeward pressure falls. The result is a roll angular pressure coefficient (example for port 4 is Equation 8) that is also nondimensionalized by the apparent dynamic pressure.

$$C_{\phi_4} = \frac{P_3 - P_5}{P_4 - \frac{P_3 + P_5}{2}} \qquad (18)$$

The high flow-angle C_o and C_q coefficients are translated from their low flow angle counterparts using the same rationale found in the development of C_θ and C_ϕ. The low-angle C_o and C_q coefficients are changed to account for the different ports that represent total and static pressures in the high-angle regime. The equations for C_θ, C_ϕ, C_o, and C_q are as follows:

$$\begin{aligned}
C_{\Theta_1} &= \frac{P_1 - P_7}{P_1 - \dfrac{P_2 + P_6}{2}} , &\qquad C_{\phi_1} &= \frac{P_6 - P_2}{P_1 - \dfrac{P_6 + P_2}{2}} \\[2ex]
C_{\Theta_2} &= \frac{P_2 - P_7}{P_2 - \dfrac{P_1 + P_3}{2}} , &\qquad C_{\phi_2} &= \frac{P_1 - P_3}{P_2 - \dfrac{P_1 + P_3}{2}} \\[2ex]
C_{\Theta_3} &= \frac{P_3 - P_7}{P_3 \quad \dfrac{P_2 + P_4}{2}} , &\qquad C_{\phi_3} &= \frac{P_2 - P_4}{P_3 - \dfrac{P_2 + P_4}{2}} \\[2ex]
C_{\Theta_4} &= \frac{P_4 - P_7}{P_4 = \dfrac{P_3 + P_5}{2}} , &\qquad C_{\phi_4} &= \frac{P_3 - P_5}{P_4 - \dfrac{P_3 + P_5}{2}} \\[2ex]
C_{\Theta_5} &= \frac{P_5 - P_7}{P_5 - \dfrac{P_4 + P_6}{2}} , &\qquad C_{\phi_5} &= \frac{P_4 - P_6}{P_5 - \dfrac{P_4 + P_6}{2}} \\[2ex]
C_{\Theta_6} &= \frac{P_6 - P_7}{P_6 - \dfrac{P_5 + P_1}{2}} , &\qquad C_{\phi_6} &= \frac{P_5 - P_1}{P_6 - \dfrac{P_5 + P_1}{2}}
\end{aligned} \tag{19}$$

$$
\begin{aligned}
C_{o_1} &= \frac{P_1 - P_{oL}}{P_1 - \frac{P_2 + P_6}{2}} \;, & C_{q_1} &= \frac{P_1 - \frac{P_2 + P_6}{2}}{P_{oL} - P_{\infty L}} \\
C_{o_2} &= \frac{P_2 - P_{oL}}{P_2 - \frac{P_3 + P_1}{2}} \;, & C_{q_2} &= \frac{P_2 - \frac{P_3 + P_1}{2}}{P_{oL} - P_{\infty L}} \\
C_{o_3} &= \frac{P_3 - P_{oL}}{P_3 - \frac{P_4 + P_2}{2}} \;, & C_{q_3} &= \frac{P_3 - \frac{P_4 + P_2}{2}}{P_{oL} - P_{\infty L}} \\
C_{o_4} &= \frac{P_4 - P_{oL}}{P_4 - \frac{P_5 + P_3}{2}} \;, & C_{q_4} &= \frac{P_4 - \frac{P_5 + P_3}{2}}{P_{oL} \quad P_{\infty L}} \\
C_{o_5} &= \frac{P_5 - P_{oL}}{P_5 - \frac{P_6 + P_4}{2}} \;, & C_{q_5} &= \frac{P_5 - \frac{P_6 + P_4}{2}}{P_{oL} - P_{\infty L}} \\
C_{o_6} &= \frac{P_6 - P_{oL}}{P_6 - \frac{P_1 + P_5}{2}} \;, & C_{q_6} &= \frac{P_6 - \frac{P_1 + P_5}{2}}{P_{oL} - P_{\infty L}}
\end{aligned}
\qquad (20)
$$

F. Division of Angular Space

The most obvious difference between low and high pressure coefficients is that six high coefficients are needed for the high angles. This fact leads to the question of what factors determine when a certain set of coefficients should be employed. Gallington proposes the "division of angular space" shown in Figure 15 (Ref. 24).

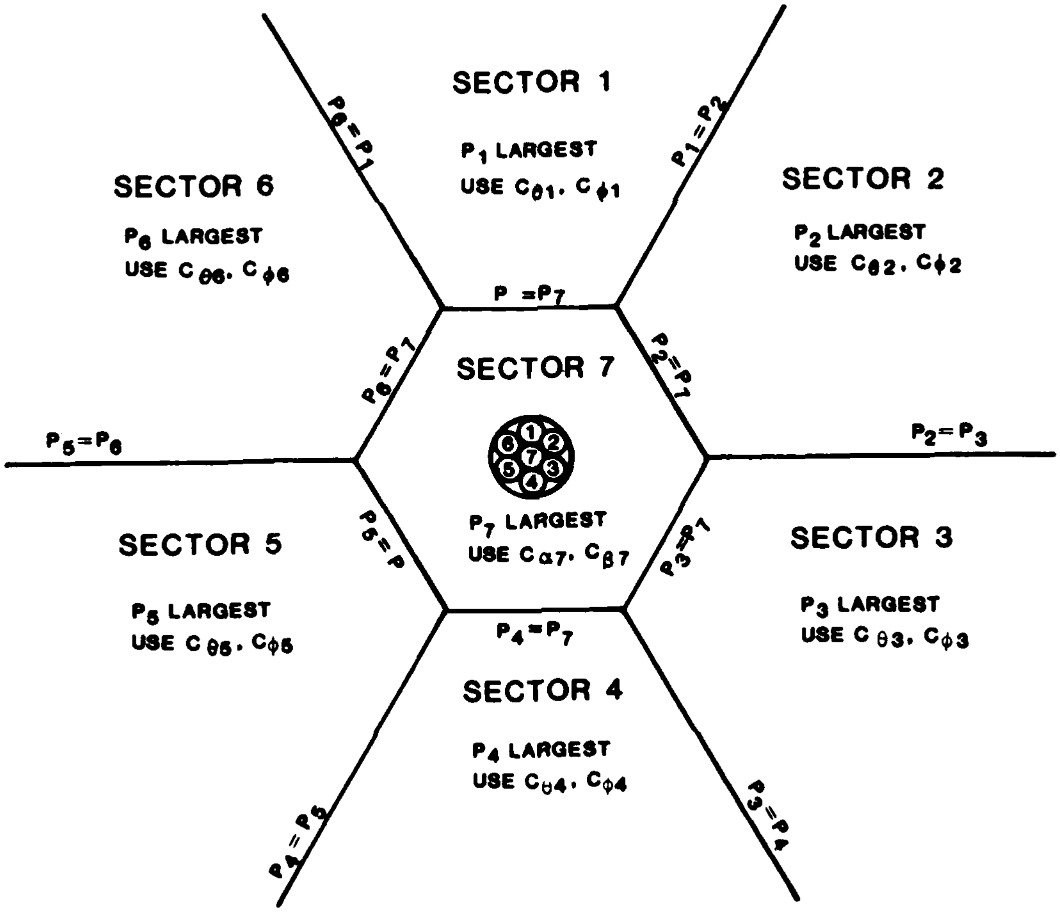

Figure 15. DIVISION OF ANGULAR SPACE

This method separates probe measurements into seven sectors -- a central low angle sector and six circumferential high angle sectors. Data points are placed in a given sector based on the highest port pressure measured on the probe.

G. Polynomial Power Series Expansion

Once the pressure coefficients are calculated, they must be converted to α_T, β_T, C_o, or C_q for low angle flows and θ, ϕ, C_o, or C_q for high angle flows. This conversion is accomplished by solving the following fourth order power series:

$$\begin{array}{lll}
 & & \underline{\text{Order of Terms}} \\
A_i = K_1^A + & & \text{0th} \\
\quad K_2^A C_{\alpha i} + K_3^A C_{\beta i} + & & \text{1st} \\
\quad K_4^A C_{\alpha i}^2 + K_5^A C_{\alpha i} C_{\beta i} + K_6^A C_{\beta i}^2 + & & \text{2nd} \qquad (21) \\
\quad K_7^A C_{\alpha i}^3 + K_8^A C_{\alpha i}^2 C_{\beta i} + K_9^A C_{\alpha i} C_{\beta i}^2 + K_{10}^A C_{\beta i}^3 + & & \text{3rd} \\
\quad K_{11}^A C_{\alpha i}^4 + K_{12}^A C_{\alpha i}^3 C_{\beta i} + K_{13}^A C_{\alpha i}^2 C_{\beta i}^2 + K_{14}^A C_{\alpha i} C_{\beta i}^3 + K_{15}^A C_{\beta i}^4 & & \text{4th}
\end{array}$$

"A" signifies the desired output quantity with the subscript denoting the ith such quantity. "K" denotes the presently unknown calibration coefficients. The calibration process entails finding these calibration coefficients with the A's as known conditions and the C's as measured pressure coefficients at these known conditions.

H. Determination of Calibration Coefficients

Rewriting in matrix notation for n terms, the power series becomes

$$\begin{bmatrix} A_1 \\ A_2 \\ A_3 \\ \cdot \\ \cdot \\ \cdot \\ A_n \end{bmatrix} = \begin{bmatrix} 1 & C_{\alpha_1} & C_{\beta_1} & C_{\alpha_1}^2 & C_{\alpha_1} & C_{\beta_1} & C_{\beta_1}^2 & \cdots\cdots & C_{\beta_1}^4 \\ 1 & C_{\alpha_2} & C_{\beta_2} & C_{\alpha_2}^2 & C_{\alpha_2} & C_{\beta_2} & C_{\beta_2}^2 & \cdots\cdots & C_{\beta_2}^4 \\ 1 & C_{\alpha_3} & C_{\beta_3} & C_{\alpha_3}^2 & C_{\alpha_3} & C_{\beta_3} & C_{\beta_3}^2 & \cdots\cdots & C_{\beta_3}^4 \\ \cdot & \cdot & \cdot & \cdot & \cdot & \cdot & \cdot & & \cdot \\ \cdot & \cdot & \cdot & \cdot & \cdot & \cdot & \cdot & & \cdot \\ \cdot & \cdot & \cdot & \cdot & \cdot & \cdot & \cdot & & \cdot \\ 1 & C_{\alpha_n} & C_{\beta_n} & C_{\alpha_n}^2 & C_{\alpha_n} & C_{\beta_n} & C_{\beta_n}^2 & \cdots\cdots & C_{\beta_n}^4 \end{bmatrix} \begin{bmatrix} K_1^A \\ K_2^A \\ K_3^A \\ \cdot \\ \cdot \\ \cdot \\ K_{15}^A \end{bmatrix} \tag{22}$$

or simply

$$[A] = [C]\ [K] \tag{23}$$

Solving for $[K]$ by the least squares curve fit outlined by Netter and Wasserman in Gallington (Ref. 24), the following is obtained:

$$[K] = [C^T C]^{-1} [C]^T [A] \tag{24}$$

With known calibration coefficients, the probe can be used to determine output quantities (α_T, β_T, C_o, C_q, or θ, ϕ, C_o, C_q) explicitly for an unknown flowfield. It is important to remember that to this point the flowfield has been uniform and incompressible. Temperature or velocity gradients have not been accounted for. Finally, while the local total and dynamic pressures are not found explicitly from the power series, they are easily determined by substituting C_o and C_q into Equation 16 (low angles) or Equation 20 (high angles).

I. Extension to Compressible Flows

Gerner and Mauer (Ref. 2) expanded the technique to subsonic compressible flows with the introduction of a nondimensional pressure coefficient representative of compressibility effects. This coefficient, C_M, had to become insignificant at very low Mach numbers; thus, any terms bearing C_M in the power series expansion would have to approach zero as Mach approached zero. This would leave essentially an incompressible power series with the regular two angular pressure coefficients as previously described. Because pressure probes are unable to determine Mach number in the hypersonic range, C_M had to approach a finite limit at very high Mach numbers. Consequently, large changes of Mach numbers in this region would have negligible effect on the compressibility coefficient.

Gerner and Mauer (Ref. 2) found that these requirements were satisfied by the apparent dynamic-to-total-pressure ratio (low angles).

$$C_M = \frac{P_7 - \overline{P}_{1-6}}{P_7} \tag{25}$$

Similarly, for high angle flow, the compressibility coefficient in each sector is:

$$C_{M_1} = \frac{P_1 - \frac{P_6 + P_2}{2}}{P_1} \qquad C_{M_4} = \frac{P_4 - \frac{P_3 + P_2}{2}}{P_4}$$

$$C_{M_2} = \frac{P_2 - \frac{P_1 + P_3}{2}}{P_2} \qquad C_{M_5} = \frac{P_5 - \frac{P_4 + P_6}{2}}{P_5} \tag{26}$$

$$C_{M_3} = \frac{P_3 - \frac{P_2 + P_4}{2}}{P_3} \qquad C_{M_6} = \frac{P_6 - \frac{P_5 + P_1}{2}}{P_6}$$

One of the primary problems of extending the seven-hole probe's capabilities into compressible flow lies in the mathematics. First, by adding a third coefficient to the fourth order power series, the number of terms and hence calibration coefficients jumps from 15 to 35. Gerner and Mauer say that approximately 80 data points in two variables (C_{α} and C_{β}) for each of the seven sectors are needed for a complete incompressible calibration. That fact results in 560 data points, and the addition of a Mach number compressibility coefficient makes the data set unwieldy (Ref. 2). These two factors create complex and time consuming matrix operations. Additionally, the amount of run time needed to operate the wind tunnel for all of the calibration data points is prohibitive as well as costly.

Gerner and Mauer suggest a two-part solution to make the addition of C_M feasible. By reducing the fourth order power series to a third order, the number of calibration coefficients is reduced to 20. Gerner and Mauer also decrease the number of data points required for calibration by employing a 6x6 Latin Square technique (Ref. 2) for purposes of obtaining calibration data. The Latin Square is a numerical method that ensures a homogeneous, random sample of a three-dimensional parameter space.

Seven hole probe work incorporating these two changes results in the following conclusions for compressible flow. The third order polynominal expansion accurately represents the parameter space up to but not beyond 70 degrees of pitch. Next, based on reasonably close correlations between the standard deviations of compressible calibrations and incompressible calibration, Latin Squares produce a sample which accurately represents a very large three-dimensional parameter space.

With these changes, the seven-hole probe may now be used in an unknown, uniform compressible flow. Since the seven-hole probe has never been subjected to supersonic applications, no shocks will lie ahead of the probe, and the isentropic flow relationship is employed to find Mach number (Ref. 2).

$$M_\infty^2 = \frac{2}{\gamma - 1} \left(\left[1 - \frac{P_o - P_\infty}{P_o}\right]^{(1-\gamma)/\gamma} - 1\right) \tag{27}$$

Knowing C_o, C_q, and the seven port pressures, the local Mach number may be determined explicitly from the dynamic to total pressure ratio. This ratio for the inner sector is represented in Equation 28 below (Ref. 2).

$$\frac{P_{oL} - P_{\infty L}}{P_{oL}} = \left[Cq \left(\frac{P_7}{P_7 - \overline{P_{1-6}}} - C_o\right)\right]^{-1} \tag{28}$$

Similar equations for the outer sectors may be derived, using the appropriate port pressures for approximate total and dynamic pressures.

IV. Seven-Hole Probe in Shear Flow

Under the present calibration scheme, the existence of a velocity gradient in the flow will cause the probe to measure an erroneous uniform flow at fictitious flow angle. For example, a flow having the properties $M = .3$, $\alpha = 0°$, $\beta = 0°$, with a velocity gradient (Fig. 16) might cause the probe to "think that it sees a flow with a certain angularity, say $\beta = 10°$ (see Fig. 17).

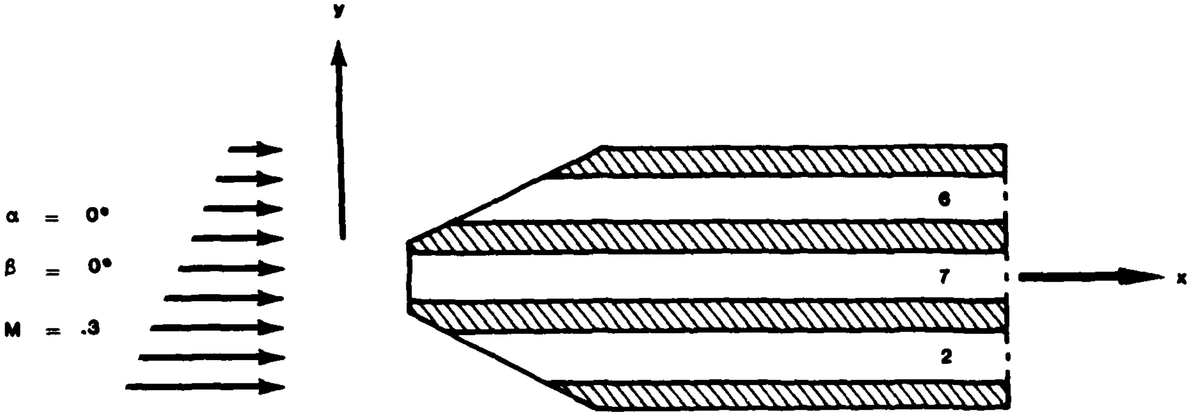

Figure 16. ACTUAL FLOW CONDITION

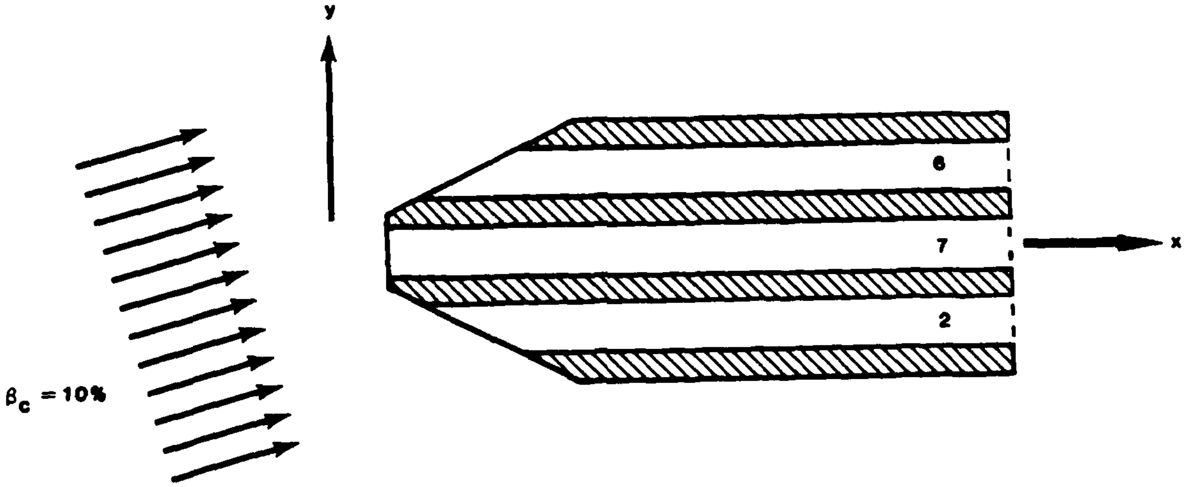

Figure 17. APPARENT FLOW CONDITION

Although the probe has seven pressure ports, each with a different pressure coefficient, all seven values compute a single point property in the flow. The use of these point properities in a uniform flow calibration produces an apparent flow condition that does not truly represent the actual flow. However, by comparing adjacent points in a flowfield, a velocity gradient can be determined. Then using the "backstepping" technique developed in the following sections, the apparent measured values can be corrected to the actual flow values.

A. Slender Body Theory

The slender body theory developed by Huffman is utilized in this section to model flow around the probe (Ref. 20). With this model, the probe's port pressure coefficients can be estimated as a function of flow angularity. Using Huffman's method of viewing the probe as a small perturbation to an otherwise uniform stream, the pressure coefficients are determined by analytic means. Further, the model determines the variation of pressure coefficients with flow direction. Not included are viscous or flow separation effects as the theory is based on potential flow.

The body-geometry function, f, is a parameter used to define the geometric characteristics of a slender body and is given in Equation 2. Huffman incorporates the body shape function into calculations for the pressure coefficient as given in Equation 4. *A simplified form of* Equation 4 was used in this analysis as given below.

$$\begin{aligned} C_{p_{i_c}} &= \cos^2\alpha\cos^2\beta[-f-(R')^2] + \sin^2\beta[1-4\sin^2\theta] \\ &+ \sin^2\alpha\cos^2\beta[1-4\cos^2\theta] + \cos\alpha\sin 2\beta[-2R'\cos\theta] \\ &+ \sin 2\alpha\cos^2\beta[-2R'\sin\theta] + \sin 2\alpha\cos\beta[4\sin\theta\cos\theta] \end{aligned} \tag{29}$$

where R' is dR/dX with R as the radius of the probe, and (θ) is the angle measured from the y-axis to the pressure port in question. The subscript "c" signifies that the approximation is valid for uniform incompressible flow.

The function that Huffman develops for the pressure coefficient at port 7 simplifies to Equation 30.

$$C_{p_{7_c}} = \cos^2\alpha \cos^2\beta - \sin^2\beta - \sin^2\alpha \cos^2\beta \tag{30}$$

One must realize that slender body theory is only an approximate model of flow around the seven-hole probe. The reason for its use stems from the conditions that the body radius is much less than the body length (slender body), and that it is easily applied to compressible flows. The only problem with this approach is that it assumes that the rate of change of body radius with respect ot body length must be small. The seven-hole probe does not completely conform to this assumption for two reasons. First, the probe has a blunt tip with a slope discontinuity, while slender body theory assumes an aerodynamically smooth body coming to a point. Because the tip is blunt, flow disturbances originate at that tip. Second, due to the orientation of the peripheral hole surfaces, separation occurs on the back holes at moderate angles of attack. Slender body theory assumes non-separated flow over the body for all flow angles. Even with these discrepancies, slender body theory is effective in predicting basic trends for coefficient of pressure data as shown in Figure 18. As a quick, computational technique, it generates reasonable pressure coefficient approximations for the following shear flow analysis. It can also be used to show that in a uniform flow with no flow angularity the probe tip disturbances (to within 1% of the freestream) are confined to within five body radii regardless of probe fineness ratio or Mach number ($M \leq 0.6$).

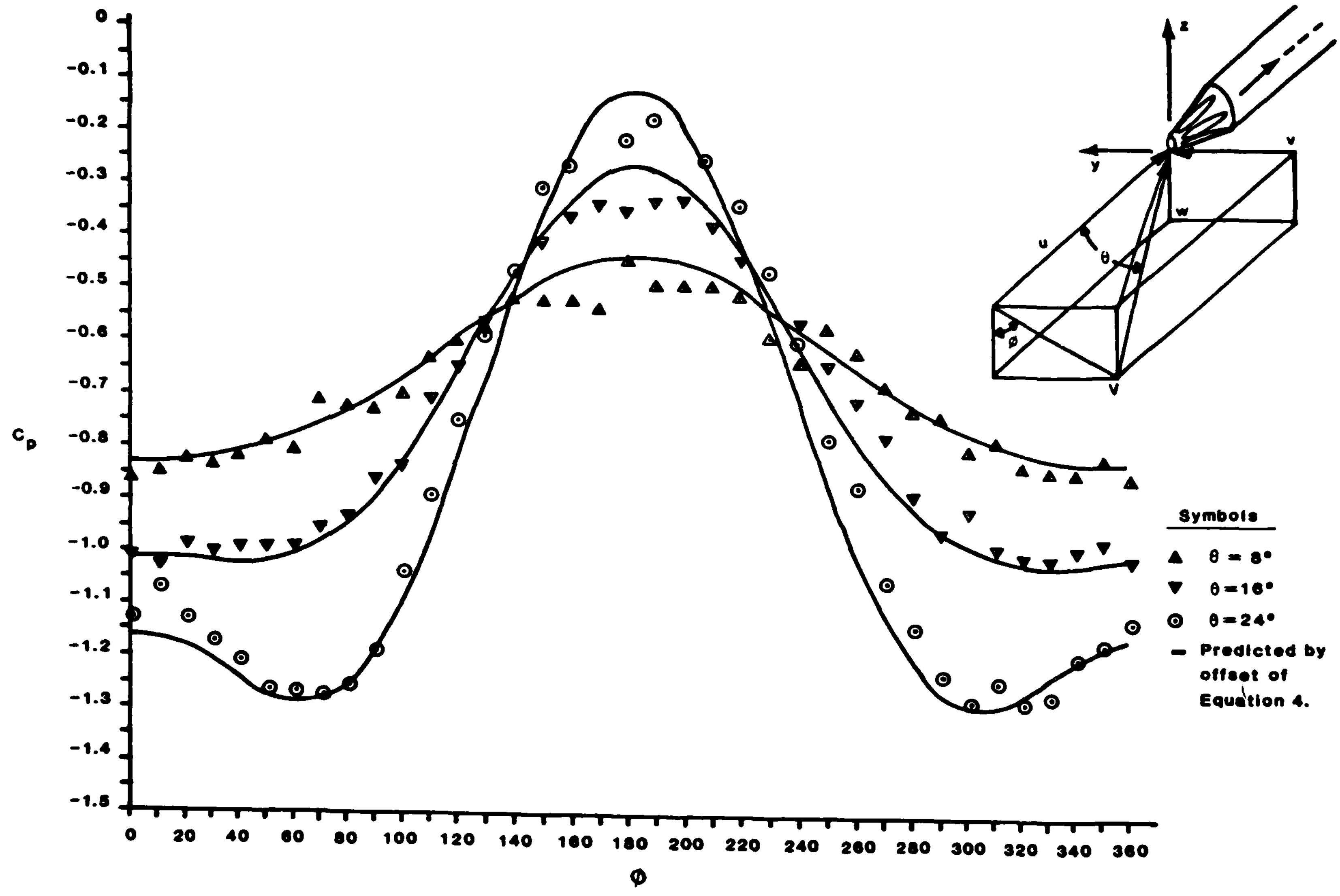

Figure 18 . PREDICTED AND MEASURED C_p FOR HOLE #1

B. The Shear Gradient

In order to work with a two-dimensional shear gradient, an alpha-beta plane is defined normal to the direction of the actual velocity and through the center point of port number 7 (Fig. 19a). The velocity at port 7 is used as a reference velocity; hence, $V_{7_c} = V_7$ for all gradient analysis.

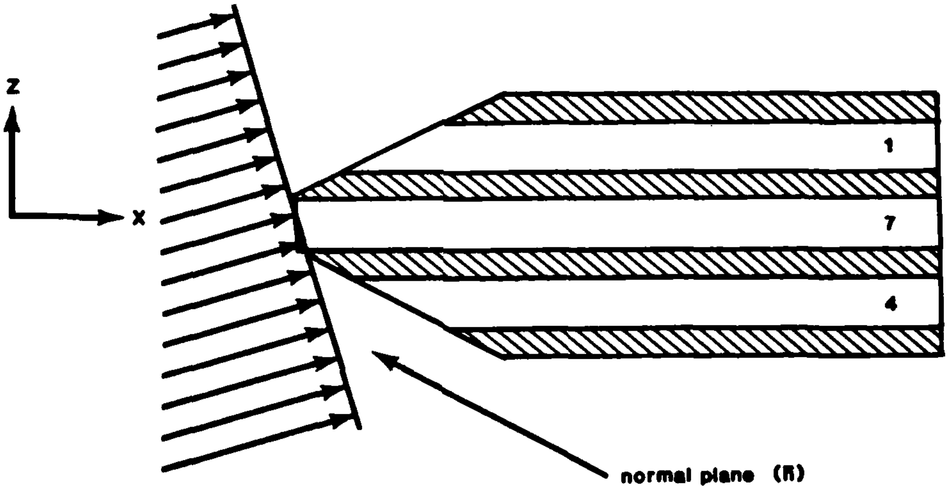

Figure 19a. SEVEN-HOLE PROBE IN A SHEAR GRADIENT

The shear gradient is defined on this normal plane. The gradient distance is measured from port 7 to the intersection of another velocity vector parallel to the one through port 7 and the normal plane (point x,y,z).

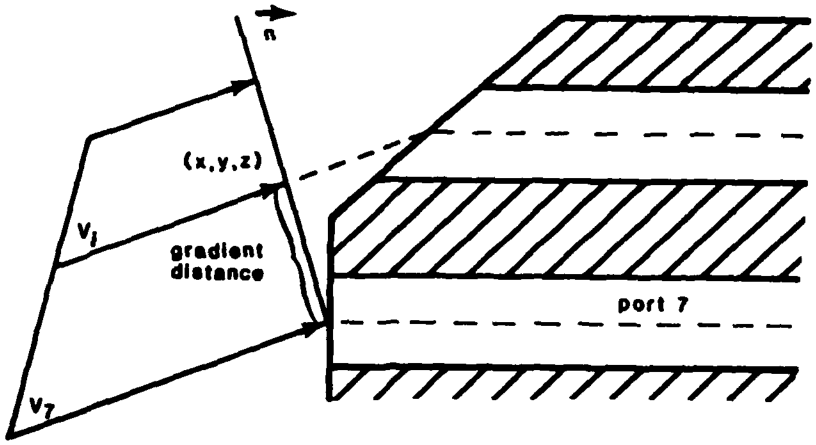

Figure 19b. CLOSE-UP OF NORMAL PLANE

By determining this gradient distance, the following general equation can be used to define the gradient's effect on the velocity.

$$V = V_7 + \frac{dV}{dy}\,y + \frac{dV}{dz}\,z \qquad (31)$$

where y and z are the components of the gradient distance and dV/dz and dV/dy are indicators of the magnitude of the alpha and beta shear gradients respectively. To put this equation in a more usable form, the gradients are non-dimensionalized:

$$V = V_7\ (1+ \frac{s}{V_7}\,\frac{dV}{dy}\,\frac{y}{s} + \frac{s}{V_7}\,\frac{dV}{dz}\,\frac{z}{s}\ ) \qquad (32)$$

where s is the distance between the centers of opposite ports. With this new equation, the terms $\frac{s}{V_7}\,\frac{dV}{dy}$ and $\frac{s}{V_7}\,\frac{dV}{dz}$ can be assigned a magnitude of relative gradient.

C. Gradient Effects on Port Pressure Coefficients

For a uniform calibration the pressure at the peripheral holes may be found by the following expression.

$$C_{p_i} = C_{p_{i_c}} \left(1 + \frac{s}{V_7}\frac{dV}{dy}\left(\frac{y}{s}\right) + \frac{s}{V_7}\frac{dV}{dz}\left(\frac{z}{s}\right)\right)^2 \tag{33}$$

Since $C_{p_{i_c}}$ is a uniform coefficient based on the geometry of the slender body theory, V_i is the only term that accounts for gradient effects. Consequently, V_i in shear flow differs for each peripheral hole. If the velocity term is kept constant at V_7 and the gradient effects are accounted for by the coefficients of pressure, the following expression results:

$$P_i = P_\infty + C_{p_{i_c}} (\tfrac{1}{2}\rho V_i^2) \tag{34}$$

Solving Equation 33 and 34 for C_{p_i}, it is evident that pressure is proportional to the square of velocity in incompressible flow.

$$P_i = P_\infty + C_{p_i} (\tfrac{1}{2}\rho V_7^2) \tag{35}$$

Since the velocity varies proportionally to the gradient correction factor (1+gradient effects) in Equation 32, the pressure coefficient varies in a shear gradient by the following relation:

$$C_{p_i} = C_{p_{i_c}} \left(\frac{V_i}{V_7}\right)^2 \tag{36}$$

D. Determination of Point (x, y, z)

To solve the previous equation, y and z must be found through the determination of point (x,y,z). The vector analysis behind the location of point (x,y,z) is explained in detail in Johnson and Reed (Ref. 25). The results are as follows:

$$
\begin{aligned}
x &= x_i + (x_7 - x_i)\cos\alpha\cos\beta - \cos\alpha\cos\beta\,[y_i\sin\beta + z_i\sin\alpha\cos\beta] \\
y &= y_i + (x - x_i)\tan\beta/\cos\alpha \\
z &= z_i + (x - x_i)\tan\alpha
\end{aligned}
\tag{37}
$$

Port (i)	x_i	y_i	z_i
1	$s/2\tan\varepsilon$	$(s/2)\cos\Theta_1$	$(s/2)\sin\Theta_1$
2	$s/2\tan\varepsilon$	$(s/2)\cos\Theta_2$	$(s/2)\sin\Theta_2$
3	$s/2\tan\varepsilon$	$(s/2)\cos\Theta_3$	$(s/2)\sin\Theta_3$
4	$s/2\tan\varepsilon$	$(s/2)\cos\Theta_4$	$(s/2)\sin\Theta_4$
5	$s/2\tan\varepsilon$	$(s/2)\cos\Theta_5$	$(s/2)\sin\Theta_5$
6	$s/2\tan\varepsilon$	$(s/2)\cos\Theta_6$	$(s/2)\sin\Theta_6$
7	$d/2\tan\varepsilon$	0	0

Since x_i, y_i, z_i, and x_7 are known values, the knowledge of alpha and beta will locate the point (x,y,z).

E. Shear Flow Measurement Corrections

At this point, the mathematical relationships necessary to compare the effects of velocity gradients are available. Equation 15 provides the ability to calculate C_α, C_{α_C}. and C_β, and C_{β_C} realizing that

$$C_{\alpha_1} = \frac{P_4 - P_1}{P_7 - \overline{P}_{1-6}} = \frac{C_{p_4} - C_{p_1}}{C_{p_7} - C_{p_{1-6}}} \qquad C_{\alpha_3} = \frac{P_3 - P_5}{P_7 - P_{1-6}} = \frac{C_{p_3} - C_{p_5}}{C_{p_7} - C_{p_{1-6}}}$$

$$C_{\alpha_2} = \frac{P_3 - P_6}{P_7 - \overline{P}_{1-6}} = \frac{C_{p_3} - C_{p_6}}{C_{p_7} - C_{p_{1-6}}}$$

By comparing the actual to the apparent angular pressure coefficients, the actual angles can be incremented until the apparent and actual coefficients are equal. This procedure indicates the flow angle errors inherent in the measurement of velocity gradients.

In order to determine the effects of different shear gradients at varying alphas and betas, Johnson and Reed (Ref. 25) calculated the apparent flow angles resulting from a span of actual flow angles and shear gradients. The calcuations show the errors between the apparent angles and actual input values. Consequently, the actual flow angles can be determined by backstepping from the apparent angles. Although these calculations only allow manual corrections to apparent measurements, the theory of this section can be used to generate a family of data points. These points may then be input into a computer surface fitting scheme for highly accurate, near real-time correction to the apparent data.

V. Seven-Hole Probe Measurement Capabilities

Three key elements of the seven-hole probe's measurement effectiveness in unknown flows are discussed further in order to provide an understanding of the basics behind its actual and potential capabilities. These three elements to be discussed are the probe's calibration, construction, and measurement error sources.

A. Calibration

Every pressure probe must be uniquely calibrated due to manufacturing imperfections. The specifics of the seven-hole probe's calibration scheme has been outlined in great detail in the previous sections. As in similar schemes for other multi-hole probes, seven-hole probe calibration allows for the relative flow angles, total pressure, and static pressure to be determined explicitly. With computer processing, these calculations are performed in near real time.

As discussed earlier, problems with the present calibration arise when attempting to make measurements in shear flow. This is because the present calibration and associated calibration coefficients are determined in a uniform flow. Jonas recorded measurement discrepancies in his attempts to use the seven-hole probe to map unknown flowfields with suspected shear (Ref. 26). Specifically, he compared seven-hole and total pressure probe measurements in a vortex wake created by the wing leading-edge extensions of a Northrop VATOL model.

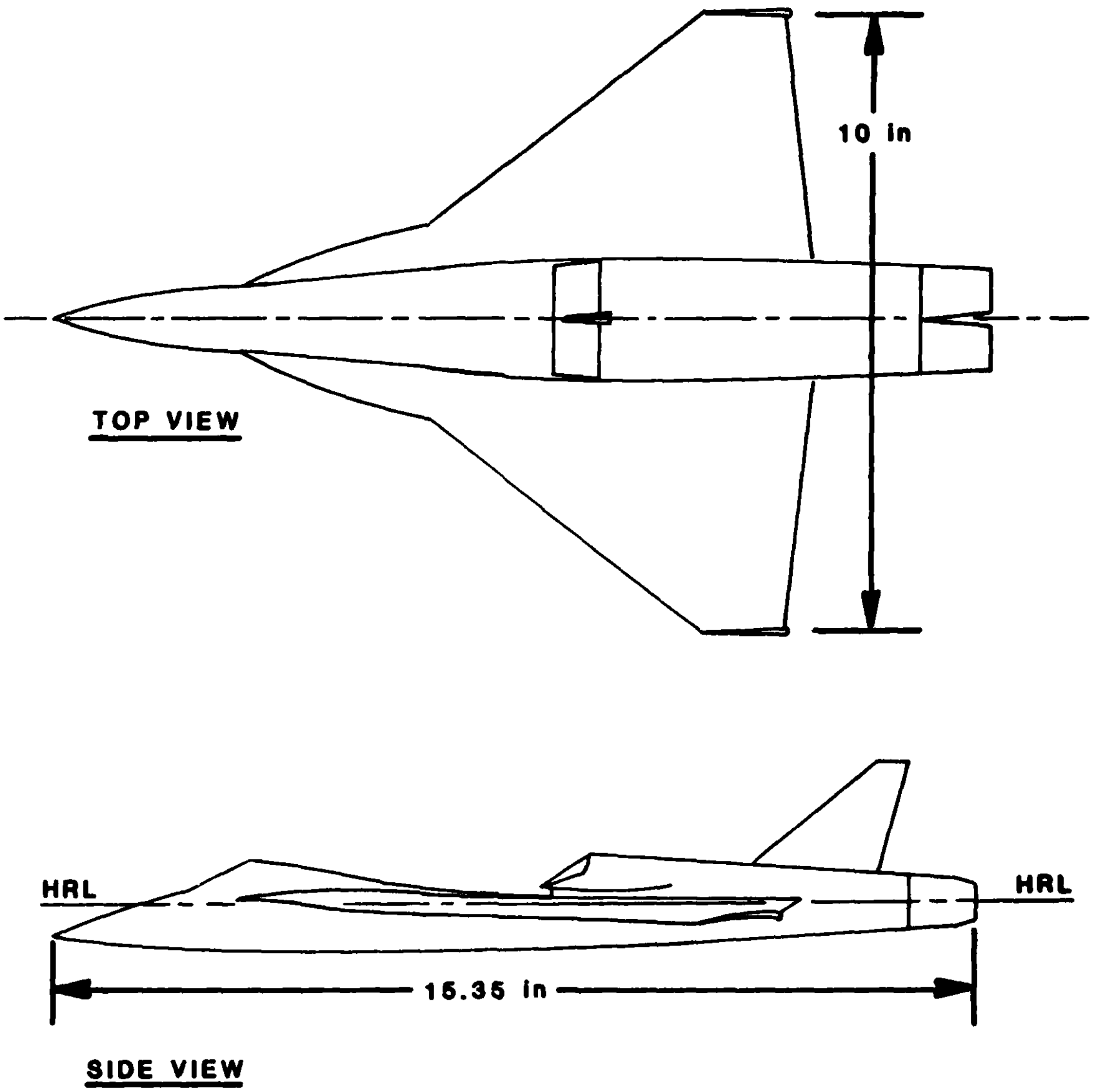

1/40th Scale Northrop VATOL Model

Figure 20. NORTHROP TOP-MOUNTED INLET VATOL CONCEPT

In a vortical flow, local total pressure should decrease through the wake because of viscous effects. This requires the coefficient $C_{TOTAL}\ (\frac{P_{oL} - P_o}{P_o - P_\infty})$ to be a negative value. The results of Jonas' pressure measurement comparison are shown in Table 1 below (Ref. 26).

	Seven-Hole Pressure Probe	Total Pressure Probe Aligned with Freestream	Aligned with Local Flow
Number of Readings (50 Data Samples Per Reading)	1	10	69
Average Value C_{TOTAL}	+0.197	-0.046	-0.013
Standard Deviation, σ	+0.003	+0.0237	+0.023
Maximum Value C_{TOTAL}	--	-0.003	+0.040
Minimum Value C_{TOTAL}	--	-0.067	-0.055
Percentage of Positive C_{TOTAL} Readings	--	0%	26%

Table 1

Jonas completed the following discussion based on the results of Table 1 (Ref.26). As can be seen from the data, the total pressure probe measurements do not agree with seven-hole probe pressure measurements. For the total pressure probe aligned with the freestream flow, no measurements existed where C_{TOTAL} was positive. However, these values may not be an accurate measure of local total pressure because flow angularity may have caused separation at the probe tip. For the total pressure probe aligned with the local flow, 26 percent of the measurements resulted in a local total pressure greater than that of the freestream value. These measurements, however, are lower than those obtained using the seven-hole probe. One must realize that the total pressure probe was bent at an angle based on measurements made using the seven-hole pressure probe. Since the seven-hole measurements were made in a region of high shear flow, the local flow angularity reading may also be erroneous. Consequently, the flow around the tip of the total pressure probe supposedly aligned with the local flow might also be separated, again leading to false pressure readings. The average value for C_{TOTAL} of the bent total pressure probe, however, remains negative. This evidence seems to confirm our theoretical expectations of viscous effects.

Although the contradictive probe readings seem to indicate incorrect probe measurements in the high shear regime, the possibility of positive C_{TOTAL} regions may not be totally excluded. A vortex flow is very complex and not completely understood. Comparisons in a low shear flow environment (airfoil wake) of seven-hole probe measurements and hot-wire anemometer measurements are, however, very favorable and no discrepancies or positive C_{TOTAL} measurements exist (Ref. 26). This seems to indicate that the problem of positive C_{TOTAL}'s are only associated with high shear flows, and are either due to the probe (manufacture, calibration, etc.) or actually represent a local flow phenomena not clearly understood. Whatever the case, care must be taken when making measurements in high shear flow environments.

B. Construction

A pressure probe should be as small as possible to keep the flow it is measuring undisturbed; however, this is accompanied by several construction disadvantages. For example, smaller probes require delicate, precise machining techniques. As size decreases, burrs and other manufacturing imperfections cause greater probe tip construction errors, and the port tubes are more likely to leak.

Although the five-hole probe may seem easier to construct than the seven-hole, the exact opposite is true. The construction of the seven-hole probe is greatly simplified since the port tubes are arranged in the only geometric fitting possible. Gallington and Hollenbaugh (Ref. 27) explain three difficulties that this geometric arrangement overcomes, difficulties which still exist in the five-hole probe.

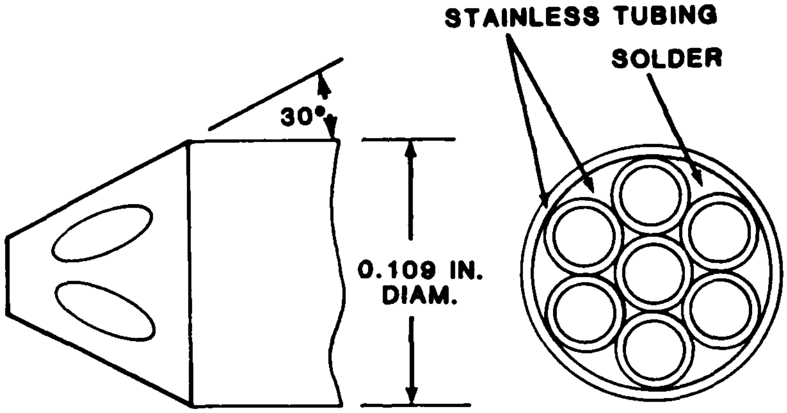

Figure 21. SEVEN-HOLE PROBE CONSTRUCTION

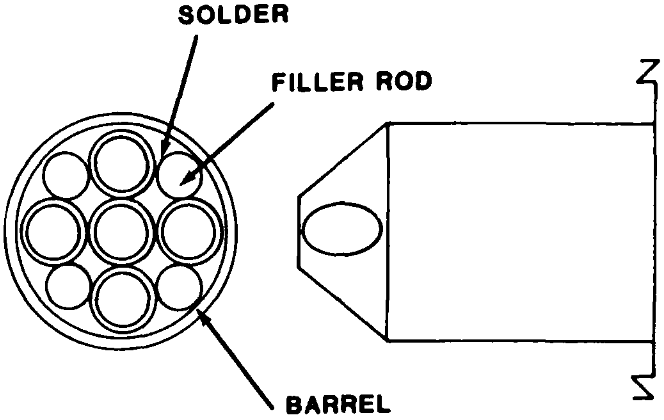

Figure 22. CONVENIENT PROBE DESIGN

First, it is difficult to hold five-hole tubing parallel with the center tube and in perfect azimuthal position for soldering. Second, a high-powered magnifier is required to assure equal chamfer on the four side tubes. Finally, there is no guarantee that the four solder fillets shown below will be equal or even nearly equal.

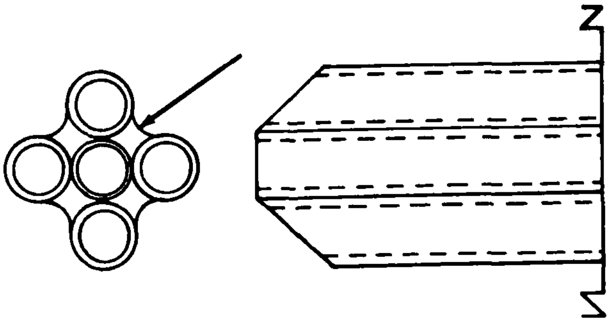

Figure 23. FIVE-HOLE PROBE ASSEMBLED FROM TUBES

As a quick note, a simpler geometric arrangement for five tubes is shown below. This order, however, lacks the required center tube.

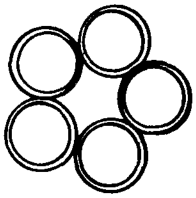

Figure 24. FIVE TUBES IN THE SMALLEST CIRCUMSCRIBED CIRCLE

Over the years, multi-hole probe construction has uncovered certain features that increase the accuracy of pressure measurement. Total pressure measurement can be largely desensitized to alpha and beta by flaring the stagnation port at an angle of 30 to 60 degrees. Yet, the probe's overall sensitivity to flow angularity can be increased by decreasing the tip half-angle (ε). The drawback to a small half-angle is that the flow will separate from the leeward surface when α_T exceeds ε (Ref. 1).

C. Measurement Error Sources

Once smaller probes are built, they are more sensitive to measurement errors caused by flow debris and damage. These two effects can be minimized prior to use by reverse airflow through clogged ports, by dust covers over port entrances, and by simple, careful handling of smaller probes.

Huffman identifies three other error sources that adversely affect a probe's measurement of pressure, orientation, and velocity (Ref. 1). These sources include the time lag between sensed and actual pressure, the pressure transducer resolution and frequency response, and the resolution of the analog-to-digital conversion. The pressure transducer resolution and analog-to-digital resolution are both beyond the scope of this report; however, the other error sources are discussed in the following paragraphs (Ref. 1).

As flowfield conditions change, the probe surface pressures change nearly instantaneously. These pressure changes are transmitted to the pressure transducers by a finite amount of air through a connection tube. Huffman discusses the fact that the pressure lag caused by this finite travel time is related to the speed of pressure propagation and the pressure drop due to the viscous effects of the tubing (Ref. 1). Three physical characteristics directly affect this time lag:

1. Tubing diameter
2. Tubing length
3. Transducer cavity

Decreasing the tubing diameter and increasing the tubing length both increase the viscous effects on the air and increase the pressure time lag. For a larger transducer cavity, more time is required for the pressure pulse to propagate from the tubing exit to the transducer face.

Schlapkohl and Buzzell (Ref. 28) define frequency response as

> the inverse of the maximum dwell time necessary for the probe system to react to the maximum pressure difference expected where the pressure sensed by the pressure transducer reaches 99 percent of the actual (surface) pressure.

The frequency response of the transducer, the computational time required to convert the measured pressure to the desired output, the pressure differential between the probe tip and the transducer face, and the fluid density all affect the probe's overall frequency response (Ref. 28).

Probe frequency response rates are generally of a few Hertz. Because modern transducers and microprocessors require only milliseconds to operate, their operation is essentially instantaneous, and little can be accomplished in these areas to decrease the overall frequency response. The final two factors are associated with the fluid dynamic properties of the flow. The difference between the fluid pressure at a port entrance and the pressure at the transducer face acts as a driving potential, and a greater differential increases the frequency response (Ref. 28). Since a higher density increases the collision rate between molecules, and therefore, increases the propagation rate of a pressure pulse, greater density is synonymous with greater frequency response. In considering the effect of density, one must remember the assumption of a constant static pressure across the face of the probe. Remembering $P=\rho RT$, one should realize that the density of the flow is dependent upon pressure.

VI. Applications: Measurements of Unknown Flows

Research efforts with the seven-hole probe center on two objectives: 1) to establish the capabilities and limitations of the seven-hole probe and 2) to map unknown flowfields. The following section explains how these two objectives are accomplished in the analysis of a simple vortex flow.

A. Vortex Flows

To create the vortex flow, a finite wing section of a NACA 0008 airfoil was placed in the two by three foot subsonic wind tunnel at the United States Air Force Academy (Figure 25). The tests were run with the wing at an angle of attack of 8 degrees and a uniform flow velocity of 150 ft/sec.

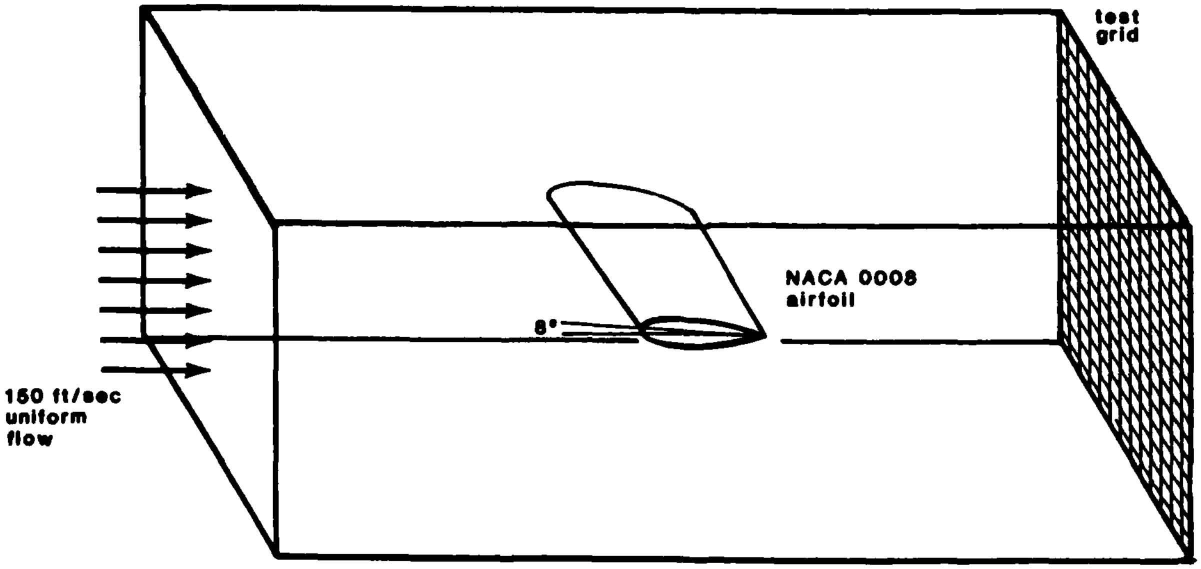

Figure 25. WING VORTEX TEST

Computer graphing techniques were used to map out the flow velocities and direction for all the points in a series of parallel two-dimensional planes, all of which were perpendicular to the uniform flow.

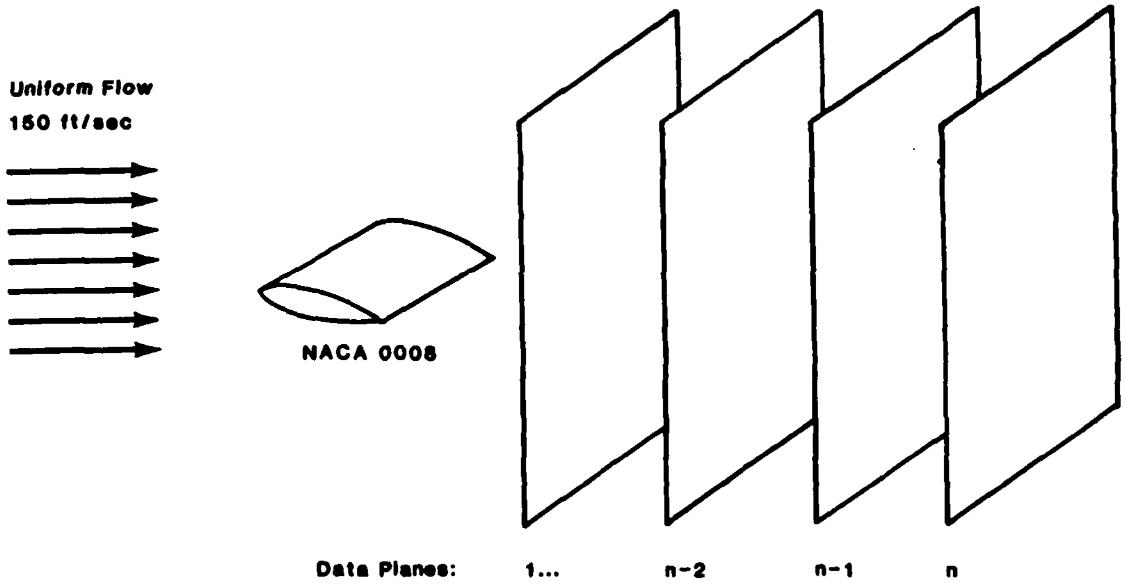

Figure 26. WING VORTEX DATA PLANES

The two-dimensional planes or test grids, started twelve inches aft of the wing's trailing edge and moved forward (toward the wing) by two inch increments for every data set. From these test runs, capabilities and limitations of the seven-hole probe under mild gradient conditions are examined and a wingtip vortex is mapped.

B. Crossflow Velocities

The first step in vortex analysis is to examine the crossflow velocities in each plane. Cross flow velocity plots, which are scaled by a factor of two are shown in Figures 26a to 27h (Ref. 29). With past errors in gradient regime, one would expect errors in seven-hole readings. Suspect data of this nature (Ref. 29) are identified by inconsistencies in the crossflow plots, such as an inordinately large or small arrow (Fig. 28) or an arrow in the wrong direction. However, the actual crossflow plots do not confirm these expectations. The velocities are well-behaved, and no inconsistancies are seen near the vortex core where high shear exists.

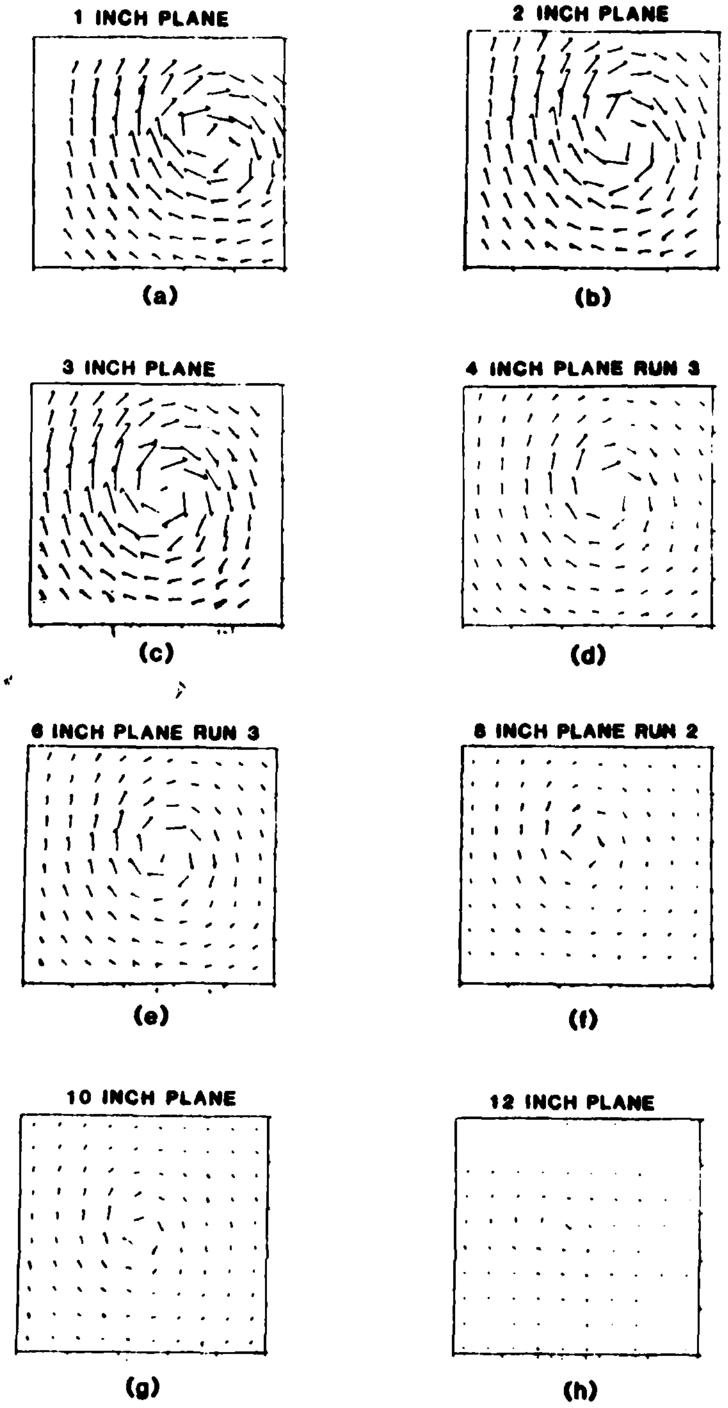

Figure 27. CROSSFLOW VELOCITIES OF WING TIP CORE VORTEX

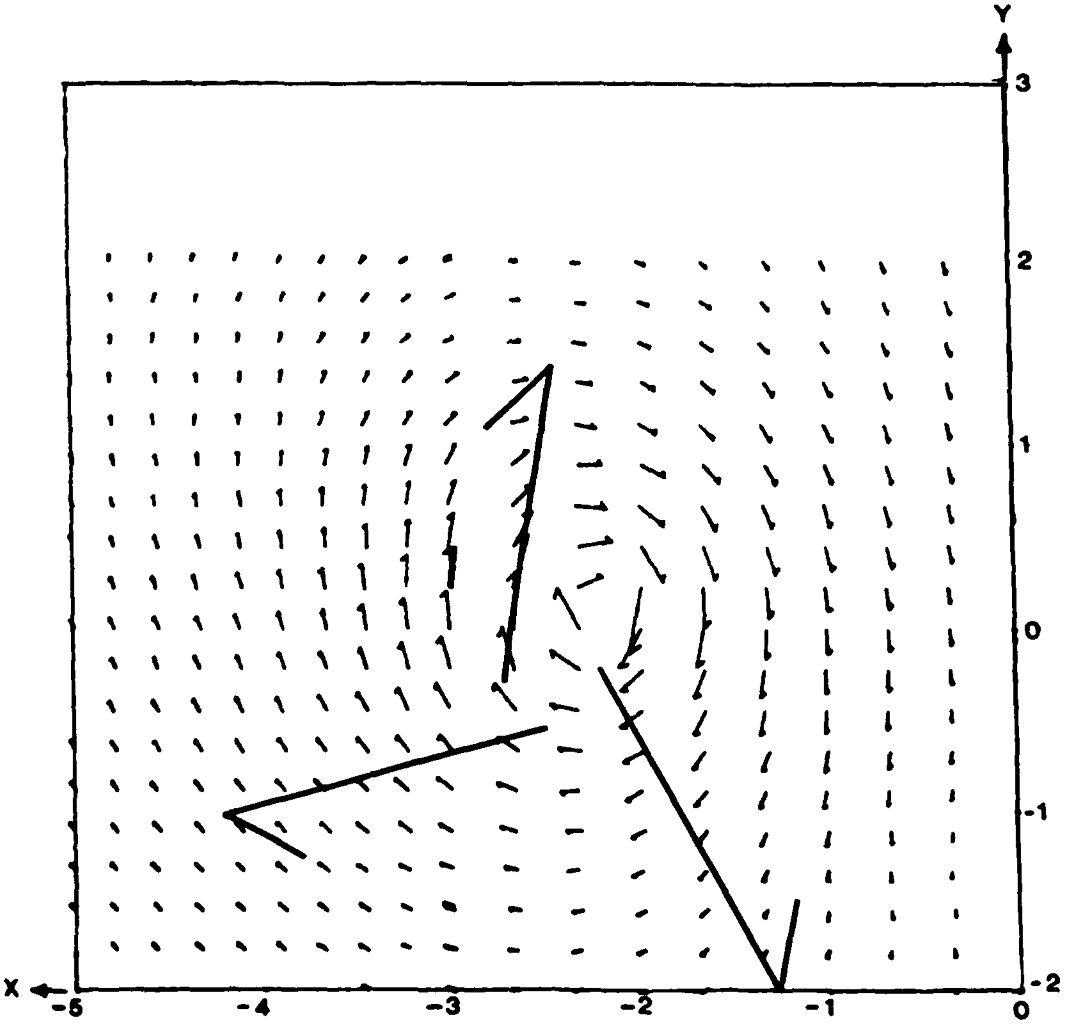

Figure 28. CROSSFLOW DATA ERRORS

The complete set of velocity data may be shown on a velocity magnitude centerline plot for ease of analysis (Figure 29).

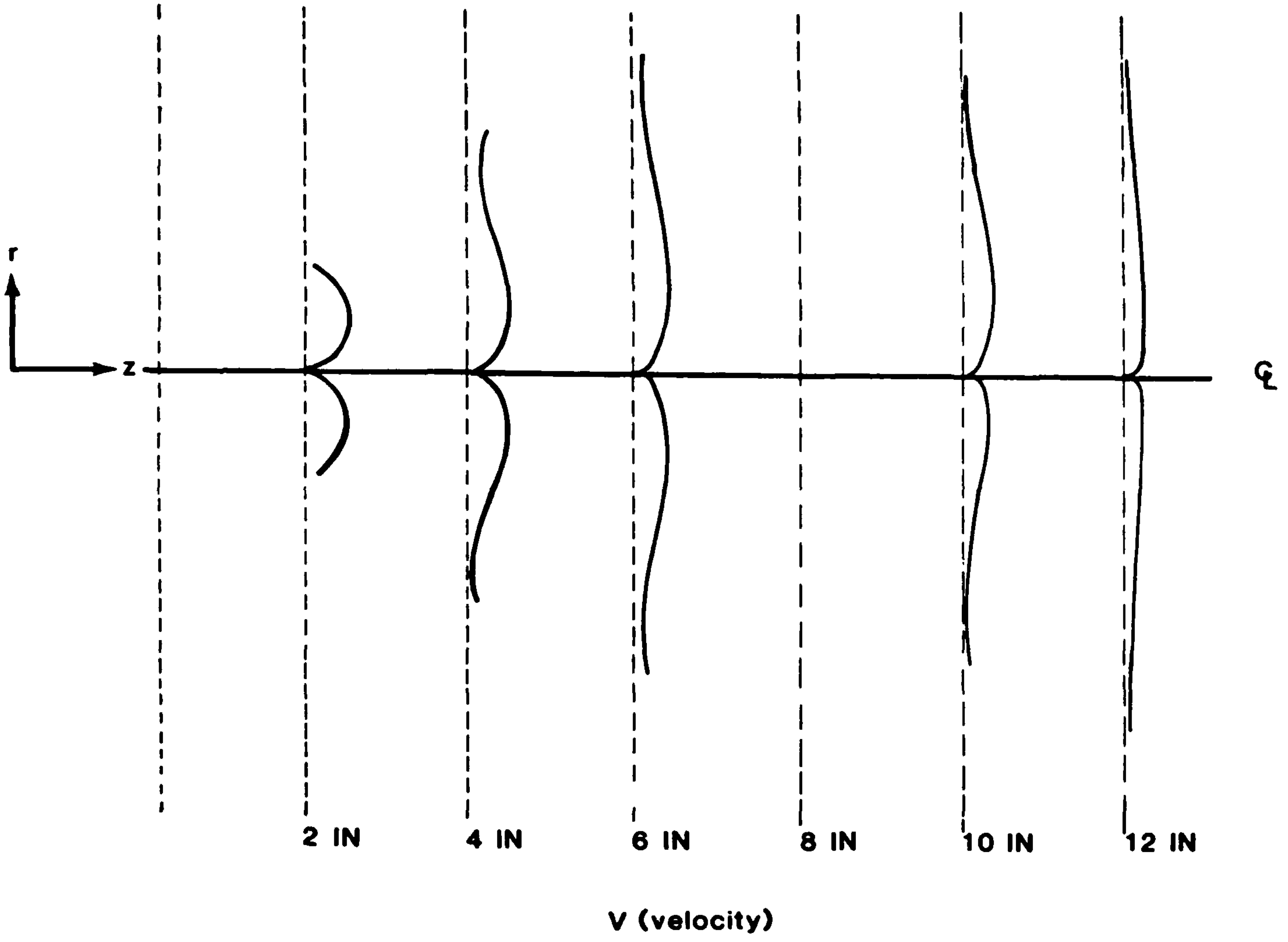

Figure 29. MAGNITUDE OF CROSSFLOW VELOCITY

This new representation of the velocity data shows how the vortex expands and decays as it moves downstream. Represented by the velocity magnitude, the vortex strength decreases as the vortex expands. The vortex velocity gradient also decreases since the vortex is diffusing. Discontinuities do occur, however, at the eigth-inch plane. As seen in Figure 29, the velocity magnitudes are smaller than those for the six-inch plane. This data must be incorrect, for the vortex cannot be weaker at eight inches downstream than it is at ten inches. Because of the suspect data, the eight-inch plane is removed from future analysis.

In order to find a point at which the velocity gradient in the flow is great enough to induce noticeable error, additional measurements were taken at planes one-quarter and one-half inch behind the trailing edge. Again, the seven-hole probe exceeds expectations by revealing no such noticeable error. The crossflow plots for the two additional planes are shown in Figures 30a and 30b and are scaled by a factor of ten.

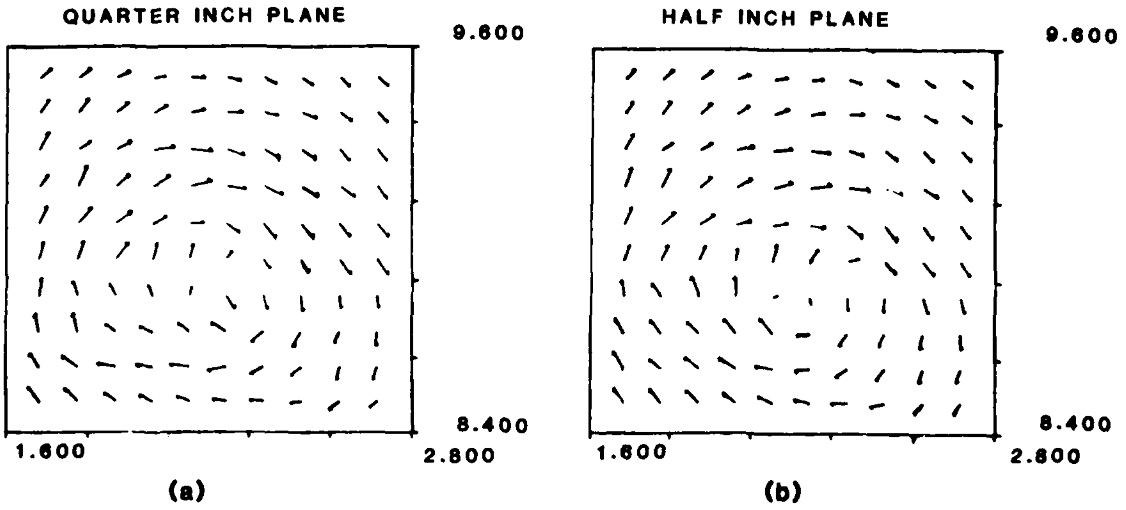

(a) (b)

Figure 30. CROSSFLOW VELOCITY OF WING TIP VORTEX

C. Definition of Flow Field Pressure Coefficients

Because pressure measurements are affected by slight shifts in wind tunnel velocity and temperature, pressure coefficients are used when the local and total tunnel pressures are compared and non-dimensionalized by the tunnel dynamic pressure. These three coefficients are defined below:

$$\begin{aligned} C_{STATIC} &= \frac{P_{\omega L} - P_{\infty}}{P_{o} - P_{\infty}} \\ C_{TOTAL} &= \frac{P_{oL} - P_{o}}{P_{o} - P_{\infty}} \\ C_{DYN} = C_{TOTAL} - C_{STATIC} &= \frac{P_{oL} - P_{\infty L}}{P_{o} - P_{\infty}} - 1 \end{aligned} \tag{39}$$

Probe measurement errors may be found by determining the correct values for these three pressure coefficients, either theoretically or experimentally with another device, and comparing these values with actual seven-hole probe data. Vortex pressure coefficient trends may be found through analysis of a two-dimensional vortex.

D. C_{TOTAL}

For an ideal two-dimensional vortex, angular velocity increases inversely as the distance to the vortex center decreases (Figure 31). Real vortices, however, are subject to viscous effects. Outside of point A, the flow is essentially inviscid. Inside that point, viscous forces reduce angular velocity until it reaches zero at the vortex center.

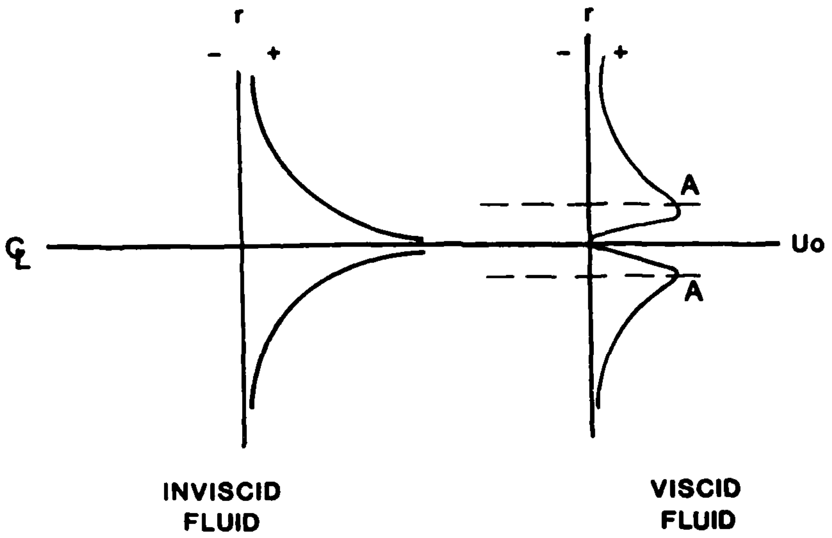

Figure 31. ANGULAR VELOCITY OF VORTEX

These two flow regions directly affect C_{TOTAL} values. Because total pressure is constant in incompressible, inviscid flow, C_{TOTAL} is zero in the inviscid region. On the other hand, the viscous forces found within the vortex core decrease the flow's fluid-mechanical energy. P_0 decreases causing C_{TOTAL} to become negative. Figure 32 diagrams C_{TOTAL}'s expected behavior.

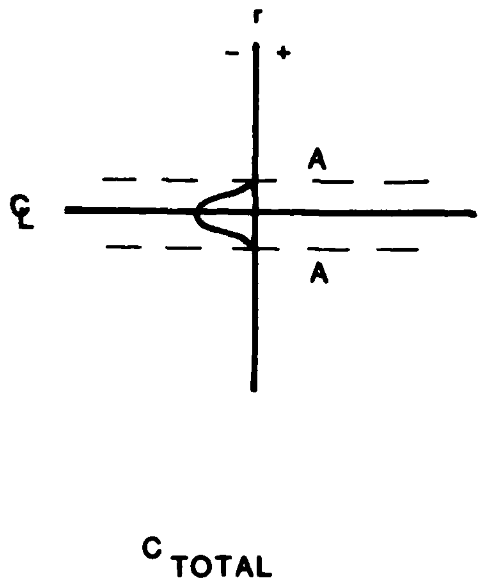

Figure 32. VORTEX C_{TOTAL}

The expected shape was derived by Jonas (Ref. 26) from theoretical considerations of a 2-D vortex decaying with time (Equation 40).

$$\frac{\partial P_{o_L}}{\partial r} = \frac{\rho}{r}\left(\frac{\Gamma_1}{2\pi}\right)^2 \frac{1}{2\nu t}\, e^{-r^2/4\nu t}\left(1-e^{-r^2/4\nu t}\right) \tag{40}$$

As discussed, the bucket-shaped phenomenon is present in the experimental vortex data shown in Figure 33.

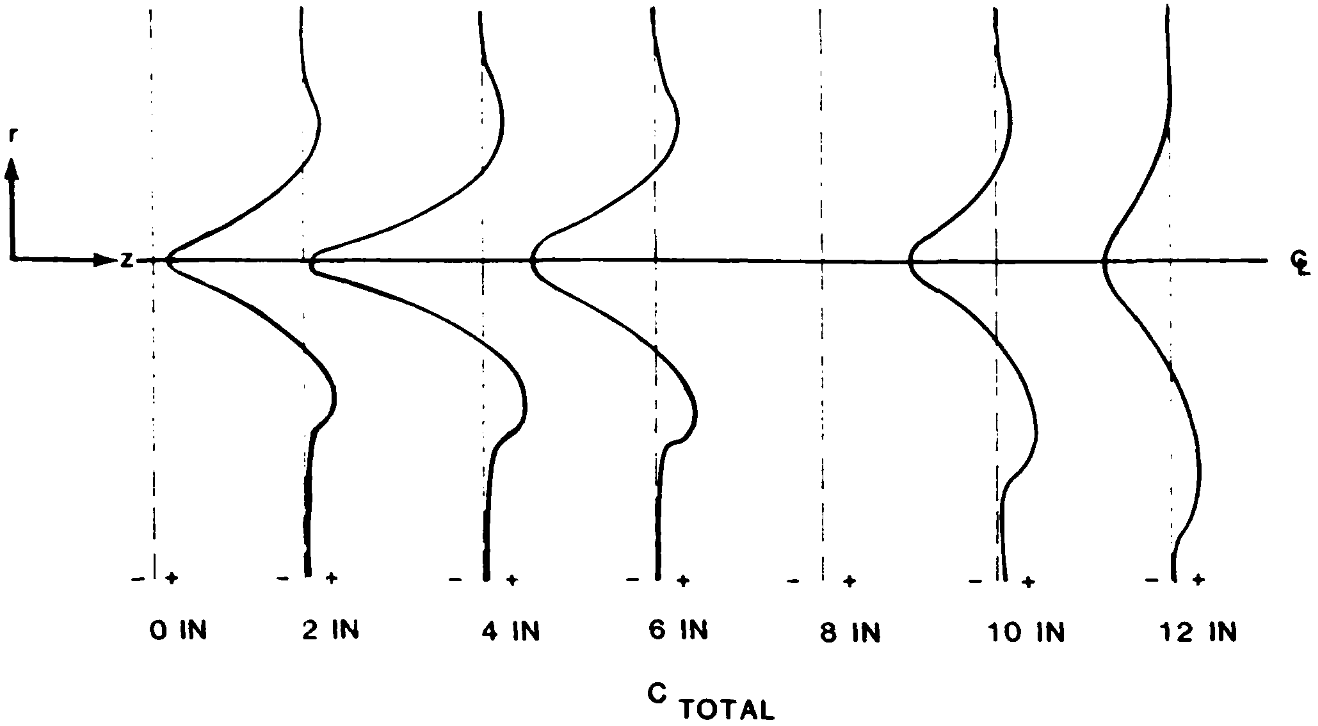

Figure 33. C_{TOTAL} OF WING VORTEX

As the flow progresses downstream, lower velocity gradients produce smaller viscous forces, smaller deficits of fluid-mechanical energy, and small bucket-shaped area plots. The two areas of positive C_{TOTAL} in each of the centerline plots is unexpected. The fact that the magnitude of the positive C_{TOTAL} values is always greater on the outboard side of the wing than on the inboard side is inexplicable. The sets of contour plots and axonometric plots (Appendix A) show that C_{TOTAL} is positive only on the two sides or the vortex parallel to the wing. The vortex data behaved normally above and below the wing. In duplicating Jonas's previous positive C_{TOTAL} results the vortex data seem to indicate a limitation in the seven-hole probe's measurement capabilities. It is still possible, however, that the positive C_{TOTAL} values may be the result of a transfer mechanism that is not yet understood.

E. C_{STATIC}

Like C_{TOTAL}, the presence or absence of viscosity affects the values of C_{STATIC}. At freestream conditions, C_{STATIC} equals zero. Progressing inward from the freestream conditions to point A, the angular velocity increases, static pressure drops, and C_{STATIC} decreases from zero to a negative value. To determine what happens in the viscous region, the following mathematical analysis is required.

$$\frac{dp}{dr} = \frac{\rho u_\theta^2}{r}$$

For a free vortex $u_\theta = \frac{c}{r}$ so, $\frac{dp}{dr} = \frac{\rho c^2}{r^3}$

For solid body rotation $u_\theta = \omega r$ so, $\frac{dp}{dr} = \rho w^2 r$

Integrating for p results in the following:

$$P = C_1 - \frac{\rho C^2}{2r^2} \qquad (41a)$$

$$P = C_2 + \frac{\rho w^2 r^2}{2} \qquad (41b)$$

Equations 41a and 41b, when superimposed, reveal a bucket-shape like that of C_{TOTAL}. The entire C_{STATIC} curve is shown in Figure 34.

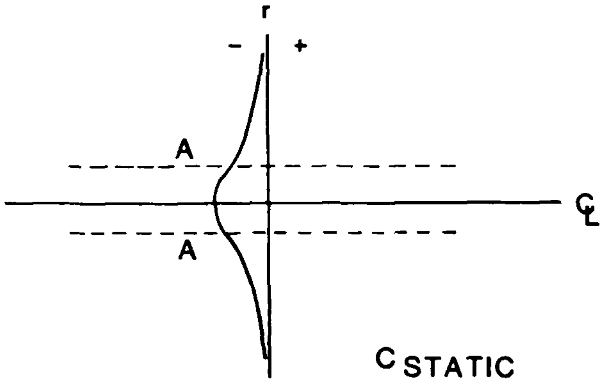

Figure 34. VORTEX C_{STATIC}

F. $C_{DYNAMIC}$

$C_{DYNAMIC}$ is simply the subtraction of C_{STATIC} from C_{TOTAL} as shown in Equation 39. Again, at the freestream, $C_{DYNAMIC}$ is ideally zero. $C_{DYNAMIC}$ equals the absolute value of C_{STATIC} from the freestream conditions inward to point A since C_{TOTAL} is zero. At the center of the vortex, local velocity and therefore local dynamic pressure are zero causing $C_{DYNAMIC}$ to equal -1. From point A to the center, $C_{DYNAMIC}$ changes as in Figure 35.

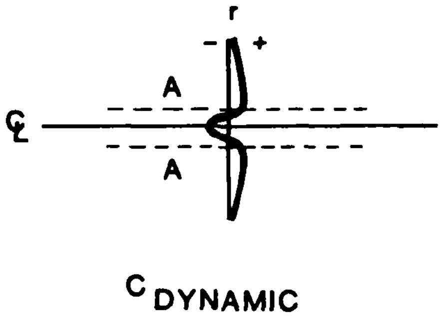

Figure 35. VORTEX $C_{DYNAMIC}$

Experimental data support the theoretical analysis of C_{DYN}. This seems somewhat surprising in lieu of the questionable positive C_{TOTAL} values. The important factor missing from the coefficient plots are the relative magnitudes. Because C_{TOTAL} values are very close to zero, the contribution of C_{TOTAL} is not very significant in the calculation of $C_{DYNAMIC}$.

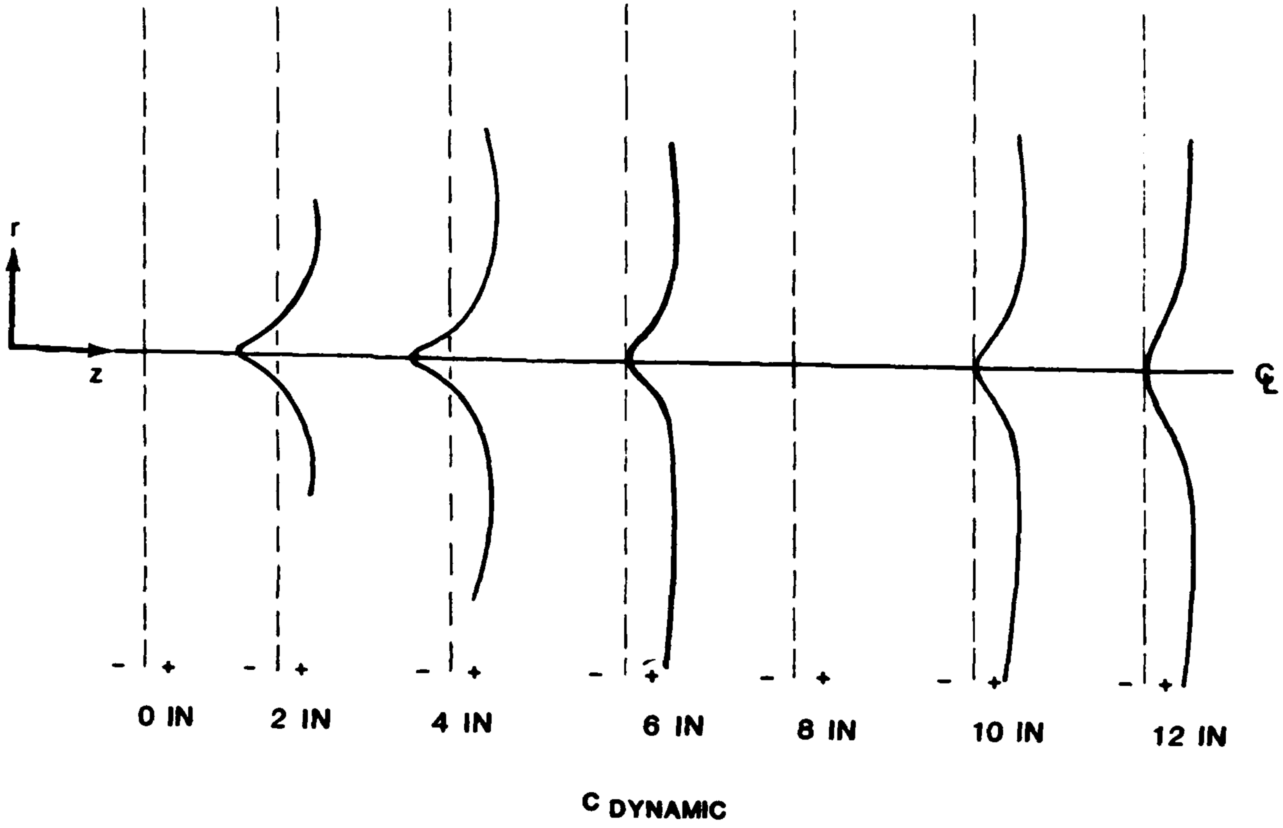

Figure 36. $C_{DYNAMIC}$ OF WING VORTEX

G. Research Applications

Today's flow mapping efforts are much more complex than the vortex example. Besides Jonas' VATOL flowfield measurements, seven-hole probe work at the Air Force Academy has examined canard wakes, lifting surface wakes of canard/swept wing aircraft, and flowfield characteristics of square cross-sectional missle bodies. Probe calibration and measurement of unknown flowfields have also been conducted at the NASA Ames Research Center in the 2x2 foot and 14 foot transonic wind tunnels (Ref. 30). Measurements of wing and canard jet-flap effects as well as the effects of prop fan installations have been made with multiple and single probe installations. Yet, these more complex research efforts are founded on the basic analysis and data presentation explained in the vortex example.

Griffin (Ref. 31) used cross velocity and pressure contours in his study of canard/forward swept wing aircraft. Figures 37 and 38 show the two types of data plots in the same spatial relationship that their data points have to the model.

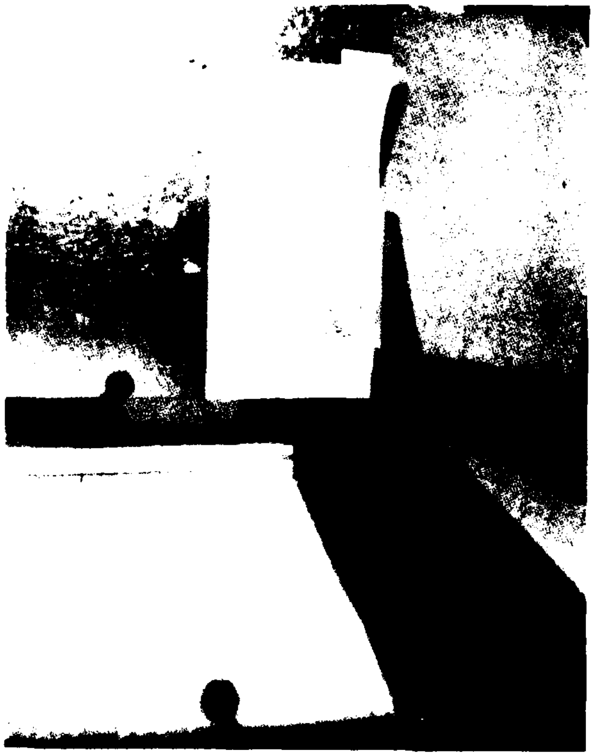

Figure 37. TYPICAL VELOCITY DATA PLANE LOCATION RELATIVE TO MODEL

Figure 38. TYPICAL PRESSURE DATA PLANE LOCATION RELATIVE TO MODEL

Jonas (Ref. 26) superimposed these two types of plots in his investigation of C_{TOTAL} (see Figure 39).

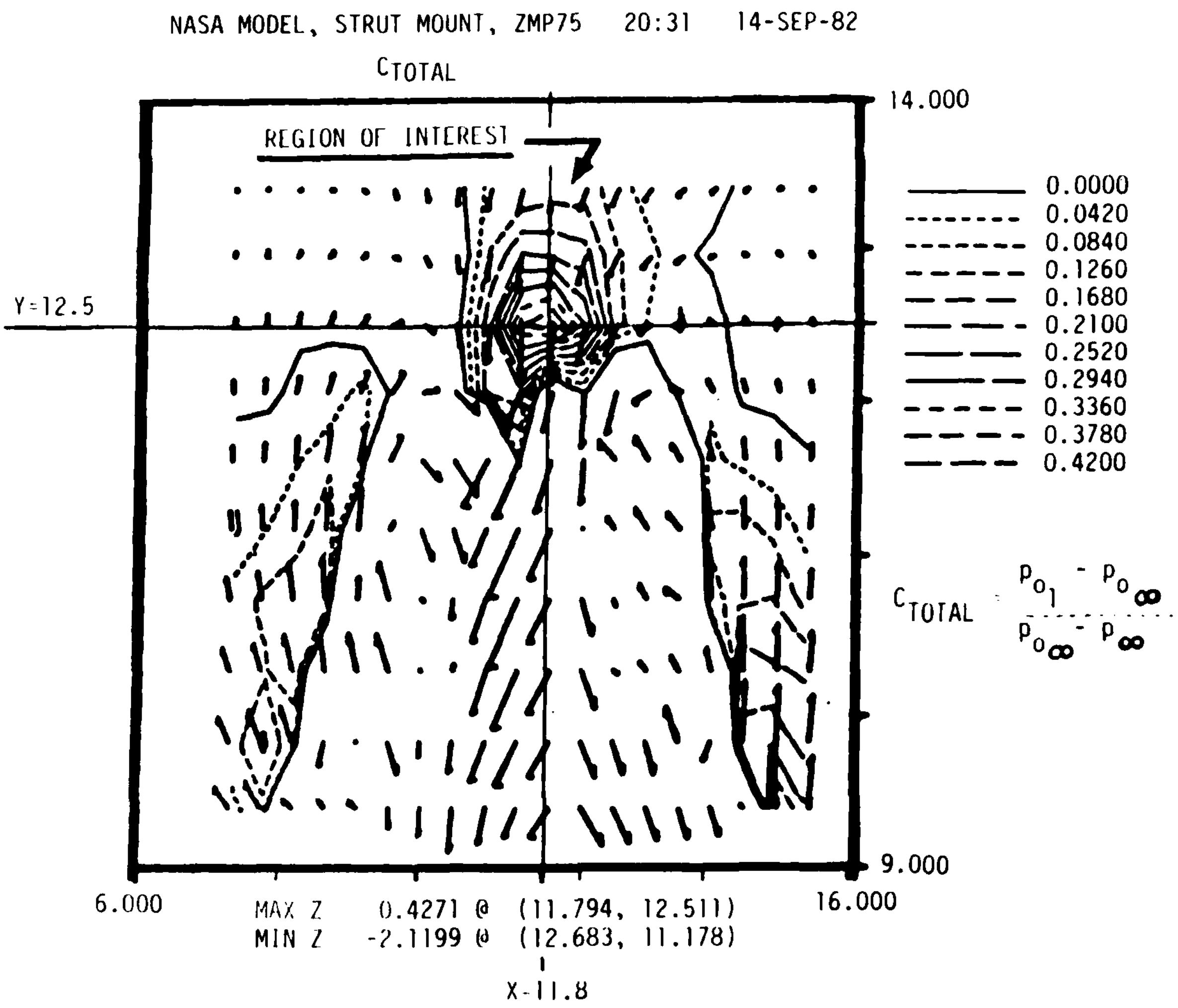

Figure 39. REGIONS OF POSITIVE C_{TOTAL}, DATA PLANE ZMP75

Jonas also used a series of axonometric projections to analyze the growth (diffusion) and decay (dissipation) of vortices. Evidence of mixing is found in the relative flattening of the C_{TOTAL} values (negative C_{TOTAL} being up or out of the plane of projection).

NASA MODEL, STRUT MOUNT, ZP6 15 27 16 SEP 82
CTOTAL

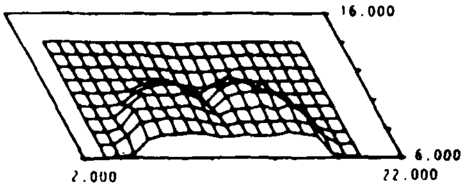

NASA MODEL, STRUT MOUNT, ZO
CTOTAL

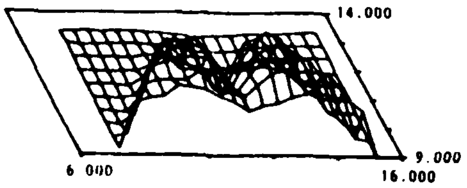

NASA MODEL, STRUT MOUNT, ZP2 14 46 16 SEP 82
CTOTAL

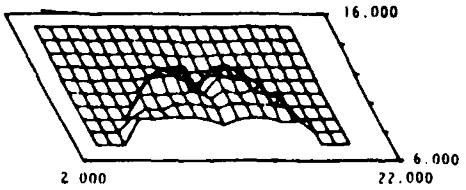

NASA MODEL, STRUT MOUNT, ZMP25
CTOTAL

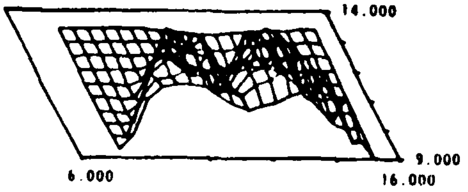

NASA MODEL, STRUT MOUNT, ZP1 12.15 16-SEP-82
CTOTAL

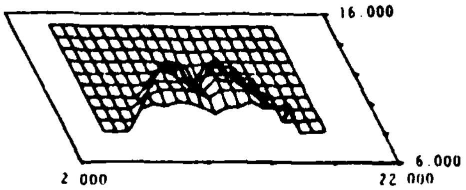

NASA MODEL, STRUT MOUNT, ZMP5 19:53 14-SEP-82
CTOTAL

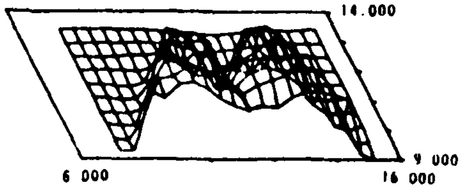

Figure40. AXONNMETRIC PROJECTIONS, C_{TOTAL}, DATA PLANES ZP6 TO ZMP5

Gerner and Durston at NASA Ames took Jonas' data and produced a series of 12 color contour photographs that span the development through decay of the VATOL vortices. The study was limited to the examination of local total pressure or C_{TOTAL}. The color contours allow more detail in data representations by making pressure differences easier to see. Regions of positive C_{TOTAL} are clearly distinguished from other points in the flowfield. As seen in the other data schemes, the color contours reveal that the VATOL is in a slight sideslip. This causes the right vortex to burst prior to the left vortex.

VII. Conclusions

As shown, the seven-hole pressure probe remains a valuable measurement tool for the documentation of unknown flowfields. The device has a greater measurement range and flexibility than other similar obtrusive flow measuring devices. The seven-hole probes themselves are easily constructed and calibrated for use in subsonic compressible flows. Measurements in adverse shear flows can be corrected to give actual flow conditions based on the methodology developed in this paper. Finally, as shown in the application section, the probe is not only a valuable research device but educational as well in demonstrating fundamental flow properties.

VIII. Acknowledgements

The authors would like to acknowledge Lt. Col. Roger Gallington, who developed the methodology for the seven-hole pressure probe. The authors would also like to thank Mr. Don Durston of the NASA Ames Research Center and the faculty and cadets of the USAF Academy who aided in the completion of this effort.

Symbols

A_i	the ith value of a particular data point either known or determined from calibration equations
C_{DYN}	local dynamic pressure coefficient
C_{ApM}	coefficient representative of compressibility effects
C_o	apparent total pressure coefficient
C_p	coefficient of pressure
C_q	apparent dynamic pressure coefficient
C_{STATIC}	local static pressure coefficient
C_{TOTAL}	local total pressure coefficient
C_α	angle of attack pressure coefficient
C_β	angle of sideslip pressure coefficient
C_ϕ	roll angle pressure coefficient
C_θ	pitch angle pressure coefficient
f	body geometry function
K_i	calibration coefficients
l	length
M	Mach number
P	Pressure
q	dynamic pressure
(r,θ,z)	cylindrical coordinates
R	radius
s	distance between centers of opposing holes
u	local velocity, perturbation velocity component
V	velocity
(x,y,z)	Cartesian coordinates
α	angle of attack
β	angle of sideslip

δ	$\sqrt{1-M_{\infty}^{2}}$
ϵ	probe tip half angle
ζ	ratio of specific heats
ϕ	roll angle
ρ	density
θ	pitch angle
subscripts	
c	uniform incompressible flow
(i,j)	local property or condition
o	total or stagnation condition
∞	freestream conditions

References

1. Huffman, G.J.D., Theory, Performance and Design of Flow Direction and Mach Number Probes, AFATL TR-81-44, Air Force Armament Laboratory, Eglin AFB, Florida, April 1981.

2. Gerner, A.A. and C.L. Mauer, "Calibration of Seven-Hole Probes Suitable for High Angles in Subsonic Compressible Flows, Aeronautics Digest, USAFA-TR-81-4, USAF Academy, Co., May 1981.

3. Schultz, W.M. et. al., Several Combination Probes for Surveying Static and Total Pressure and Flow Direction, NACA TN 2830, 1952.

4.Kettle, D.J., "Design and Calibration at Low Speeds of a Static Tube and Pitot-Static Tube with Semi-Ellipsoidal Nose Shapes," J. Ray. Aero. Soc., Vol. 58, p. 835, 1954.

5. Smetena, F.O. and J.W.M. Stuart, A Study of Angle-of-Attacks Angle-of-Sideslip Pitot-Static-Probes, WADC TR 5723A, AD 118209, 1957.

6. Bryer, O.W. et. al., "Pressure Probes Selected for Three-Dimensional Flow Measurement," Rep. Mem. Aero Res. Coun. London, No. 3037, 1958.

7. Morrison, D.F. et. al., "Hole Size Effect on Hemisphere Pressure Distribution." J. Roy. Aero Soc., Vol 71, 1967.

8. Wright, M.A., "The Evaluation of A Simplified Form of Presentation for Spherical and Hemispherical Pitometer Calibration Data," J. Sci.Instr. (J. Phys. E). Vol. 3, p.456, 1970.

9. Schaub, V.W. et. al., An Investigation of the Three-Dimensional Flow Characteristics of a Non-Nulling Five-Tube Probe, Nat. Res. Council of Canada, Aero Rpt. LR-393, NRC No. 7964, 1964.

10. Dudzinski, J.T. and L.N. Krause, Flow Direction Measurement with Fixed-Position Probes, NASA TMX-1904, 1969.

11. Beecham, L.J. and S.J. Collins, Static and Dynamic Response of a Design of a Differential Pressure Yawmeter at Supersonic Speeds, Roy. Aero Est. Report No. GW 19, 1954.

12. Hutton, P.G., Static Response of a Hemispherical-Headed Yawmeter at High Subsonic and Transonic Speeds, Roy. Aero Est. Tech. Note N. Aero 7525, CP No. 401, 1957.

13. Nowack, C.F.R., "Improved Calibration Method for a Five-Hole Spherical Pitot Probe," J. Sci. Inst. (J. Phys. E.), Vol. 3, p.21,1970.

14. Dau, K., et. al., "The Probes for the Measurement of the Complete Velocity Vector in Subsonic Flow," Aero. J., Vol. 72, p. 1066, 1968.

15. Spaid, F.W., et. al., "Minature Probe for Transonic Flow Direction Merasurement," AIAA J., Vol. 13, p. 253, 1975.

16. Glawe, G.F., et. al., A Small Combination Sensing Probe for Measurement of Temperature, Pressure and Flow Direction, NASA TN-D-4816, 1968.

17. Treaster, A.L. and A.M. Yocum, The Calibration and Application of Five-Hole Probes, Penn. State Univ. Applied Research Laboratory Report TM 78-W, 1978.

18. Bryer, D.W. and D.W. Pankhurst, Pressure Probe Methods for Determining Wind Speed and Flow Direction, Published by Her Majesty's Stationery Office, London, England, 1971.

19. Wuest, W., Measurement of Flow Speed and Flow Direction by Aerodynamic Probes and Vanes, Paper Presented at the 30th Flight Mechanics Panel Meeting in Montreal, Canada, 1967.

20. Huffman, G. David, "Flow Field Characteristics of Flow Direction and Mach Number Probes Using Slender Body Theory," Aeronautics Digest, USAFA-TR-79 1, USAF Academy, CO, Feb. 1979.

21. Hess, J.L. and A.M.O. Smith, "Calculation of Potential Flow about Arbitrary Bodies," Progress in Aeronautical Sciences, Vol. 8, Pergammon Press, p. 81, 1966.

22. Smith, A.M.O. and A.B. Bauer, "Static-Pressure Probes that are Theoretically Insensitive to Pitch, Yaw and Mach Number," J. Fl. Mech., Vol 44 p. 513, 1970.

23. Liepmann, H.W. and A. Roshko, Elements of Gas Dynamics, John Wiley and Sons, New York, 1958.

24. Gallington R.W. "Measurement of Very Large Flow Angles with Non-Nulling Seven-Hole Probes," Aeronautics Digest, USAFA-TR-80-17, USAF Academy, Co., October 1980.

25. Reed, L.S. and G.H. Johnson, Seven-Hole Probe in Shear Flow, AIAA Paper 85-0076 (to be published)

26. Jonas, F.M., External Flowfield Measurements on a Top-Mounted Inlet VATOL Configuration at High Angles of Attack, USAFA-TN-83-10, 25 March 1983.

27. Gallington, R. W. and C. F. Hollenbaugh, "A Fast Method for Accurate Manufacture of Small Five-Hole Probes," Aeronautics Digest, USAFA-TR-79-7, USAF Academy, Co., July 1979.

28. Schlapkohl, S.R. and W.A. Buzzell, "Determination of the Frequency Response Characteristics of a Redesigned Seven-Hole Pressure Probe," Aeronautics Digest, USAFA-TR-82-3, USAF Academy, Co., June 1982.

29. Dodson, Heckler, Herup, Pearson, The Determination and Evaluation of Errors in the Seven-Hole Probe, Student Paper, USAF Academy, 1984.

30. Everett, K.N., A.A. Gerner, and D.A. Durston, "Seven-Hole Cone Probes for High Angle Flow Measurement: Theory and Calibration," AIAA Journal, Vol. 21, No. 7.

31. Griffin, K.E. "Experimental Documentation of the Lifting Surface Wakes of a Canard and Forward-Swept Wing Configuration," Aeronautics Digest, USAFA-TR-82-3, USAF Academy, Co., June 1982.

32. Gerner, A.A. and C.L. Mauer, Non-Nulling Seven-Hole Probes for High Angle Flow Measurements, Student Paper, USAF Academy, 1980.

33. Gerner, A.A. and C.L. Mauer, Student Speech (text), USAF Academy.

34. Sand, D.E., The Seven-Hole Probe in a Velocity Gradient, *Student* Paper, USAF Academy, 1983.

35. Anderson, Bednark, Gerity, A Report on Validation of an Analytical Model for the Pressure Coefficients of a Seven-Hole Probe, Student Paper, USAF Academy, 1980.

APPENDIX A

Wing Tip Vortex C_{TOTAL} Plots

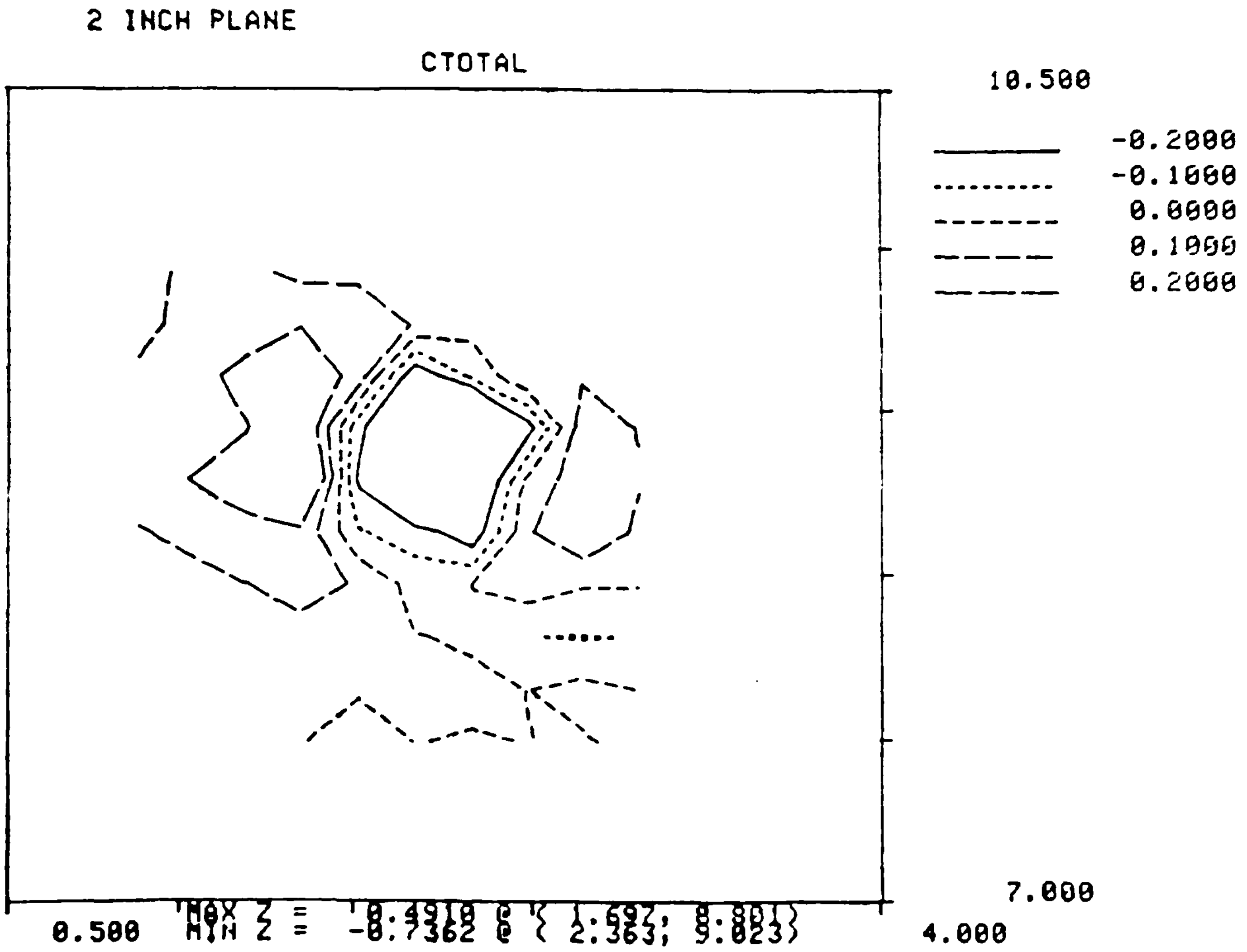
2 INCH PLANE
CTOTAL
10.500
-0.2000
-0.1000
0.0000
0.1000
0.2000
7.000
0.500
4.000
MAX Z = 0.4910 @ (1.692, 8.801)
MIN Z = -0.7362 @ (2.363, 9.023)

Figure A-1

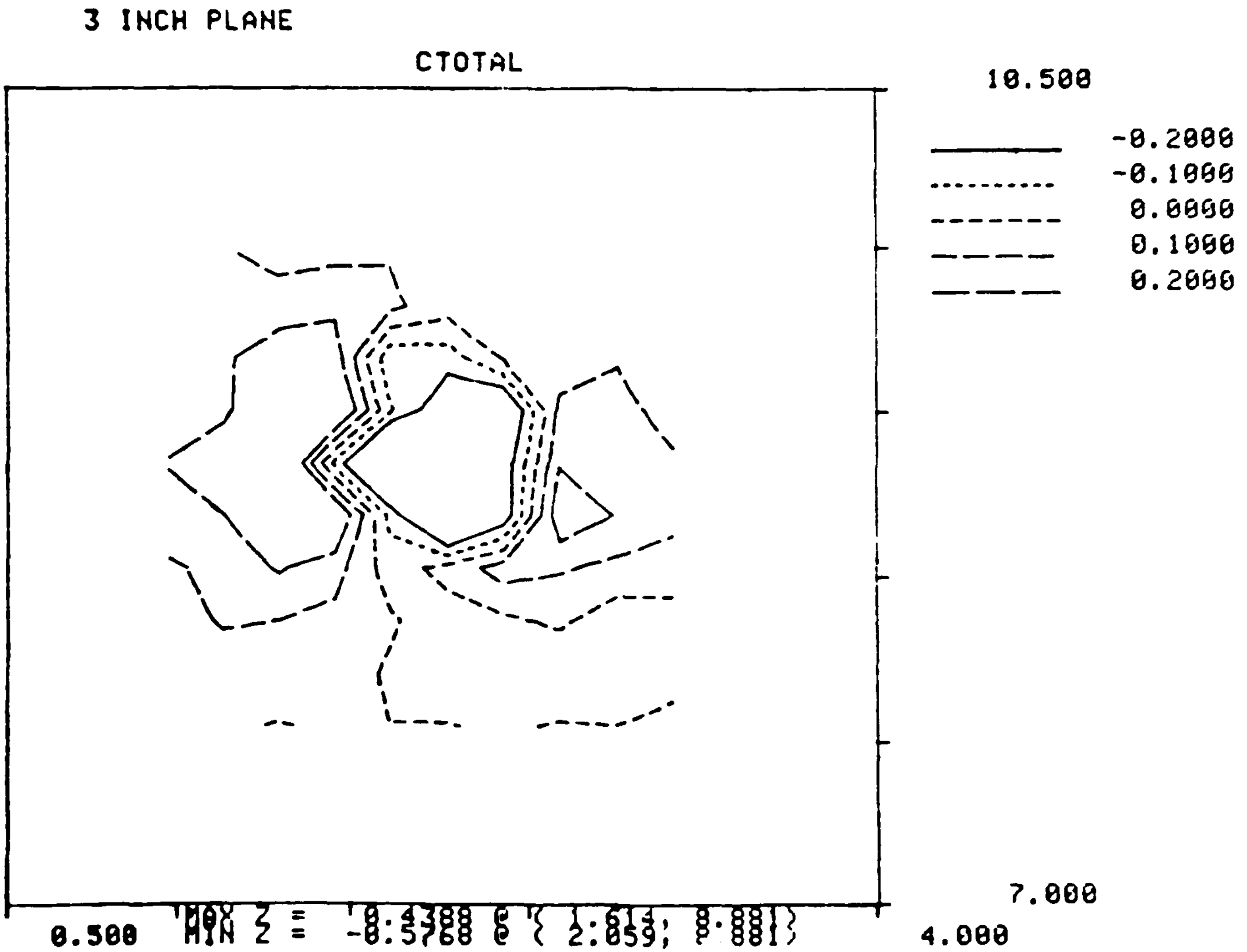
3 INCH PLANE
CTOTAL
10.500
7.000
0.500
4.000
-0.2000
-0.1000
0.0000
0.1000
0.2000
MAX Z = 0.4388 @ (1.614, 8.881)
MIN Z = -0.5768 @ (2.059, 8.881)

Figure A-2

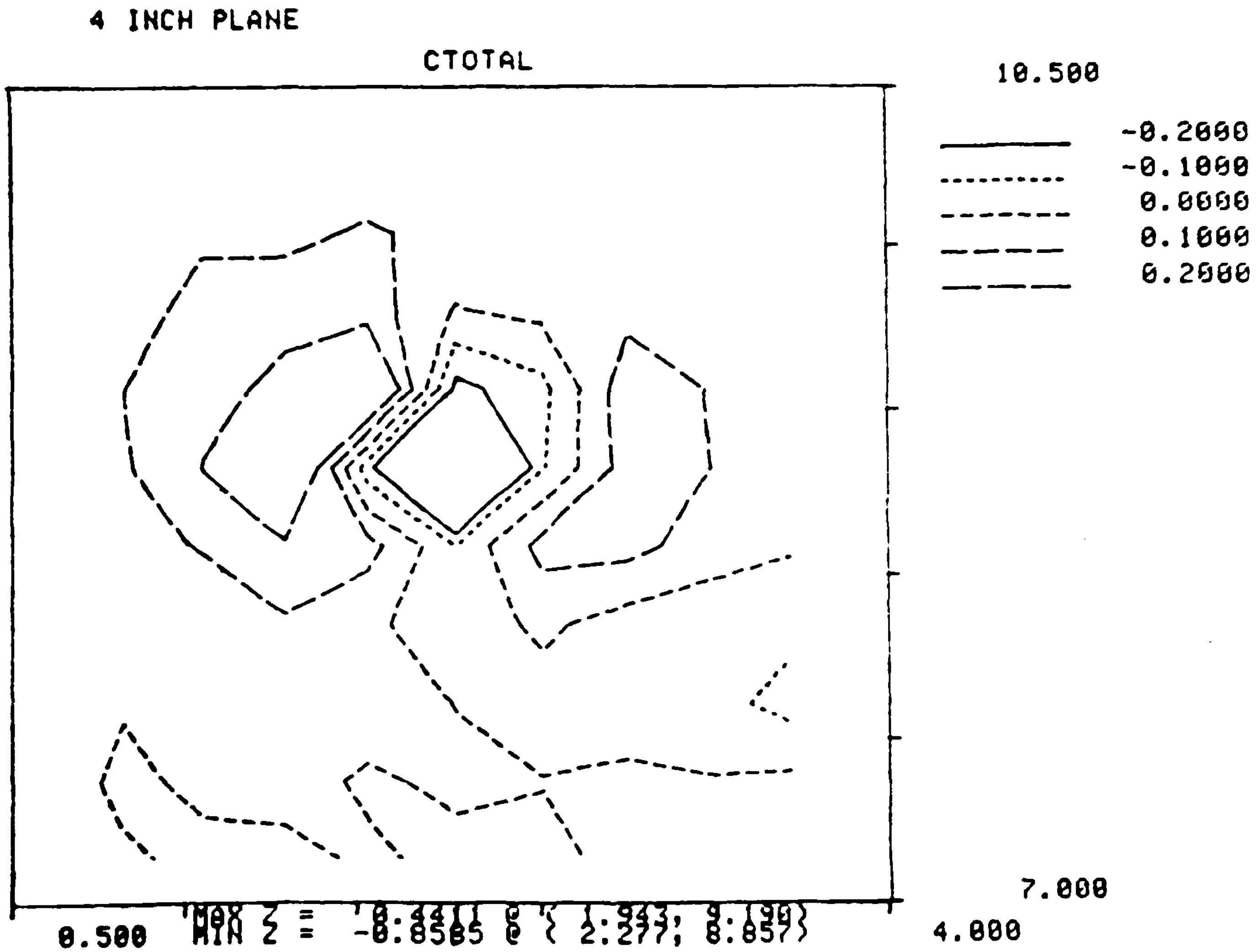
4 INCH PLANE
CTOTAL
10.500
-0.2000
-0.1000
0.0000
0.1000
0.2000
7.000
0.500
4.000
MAX Z = 0.4411 @ (1.943, 9.190)
MIN Z = -0.8585 @ (2.277, 8.857)

Figure A-3

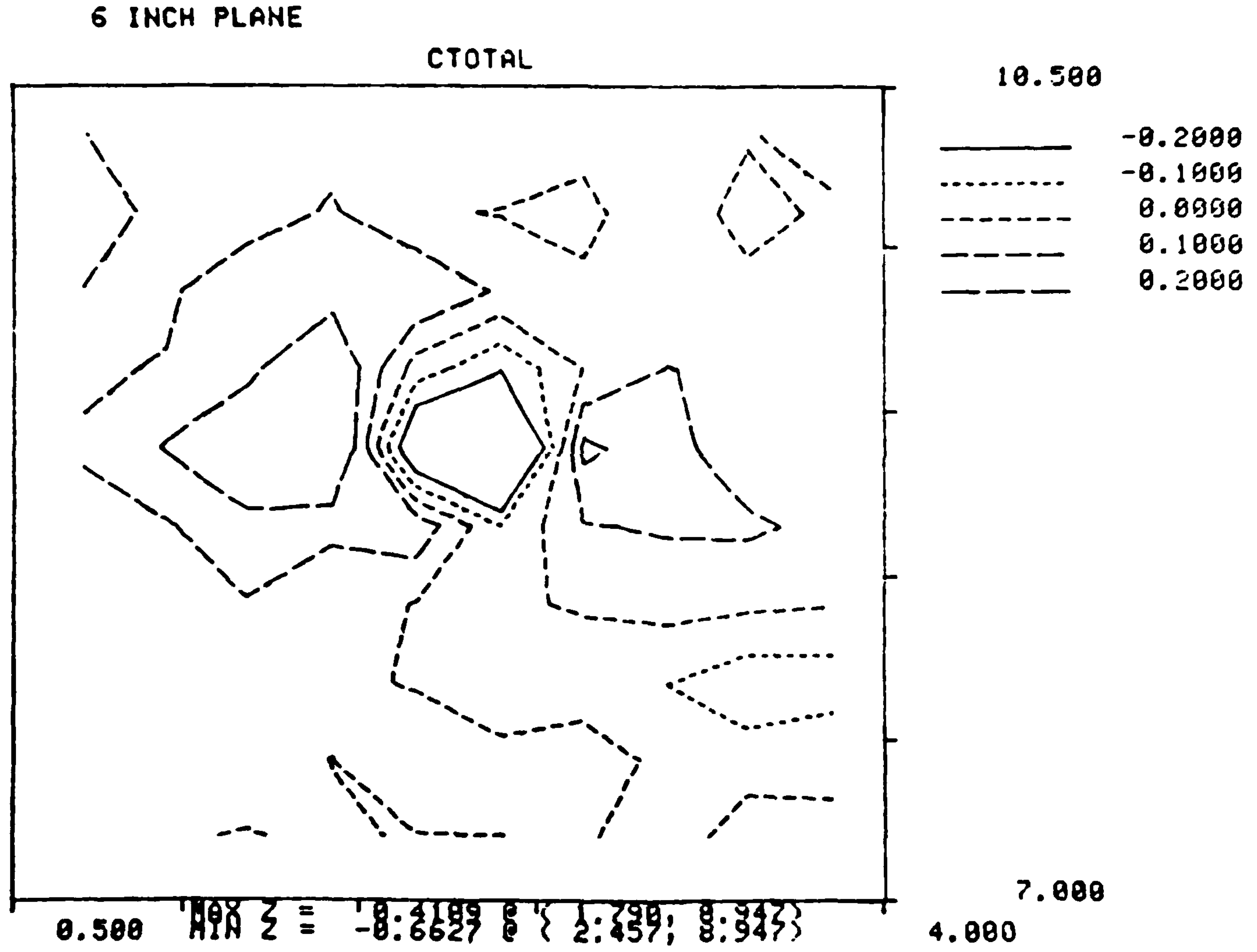
6 INCH PLANE
CTOTAL
10.500
7.000
0.500
4.000
-0.2000
-0.1000
0.0000
0.1000
0.2000
MAX Z = 0.4189 @ (1.790, 8.947)
MIN Z = -0.6627 @ (2.457, 8.947)

Figure A-4

1 INCH PLANE

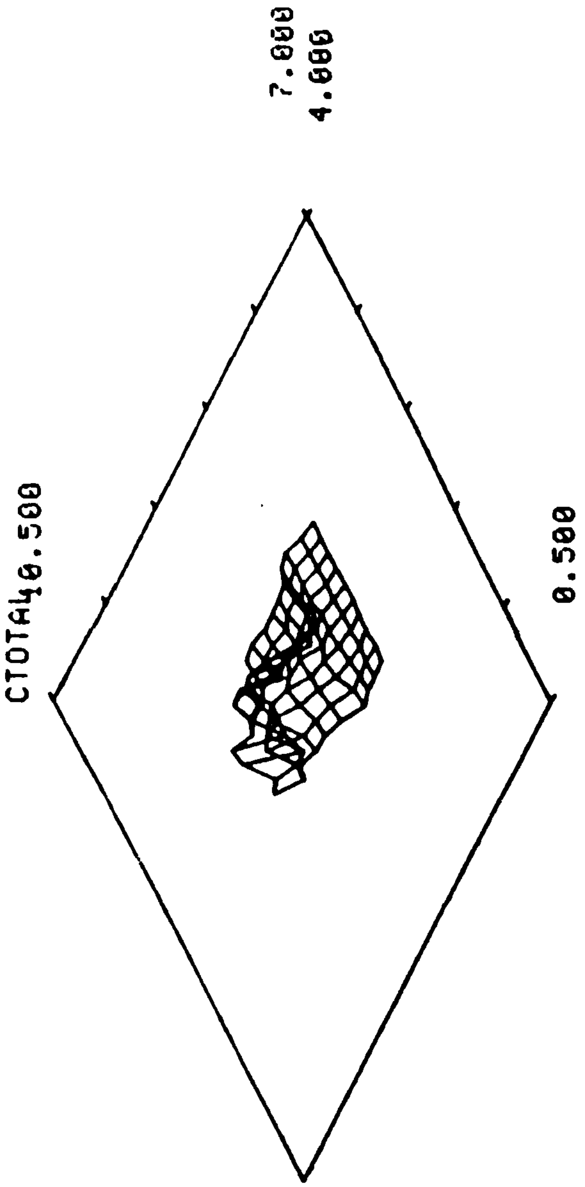

Figure A-5

2 INCH PLANE

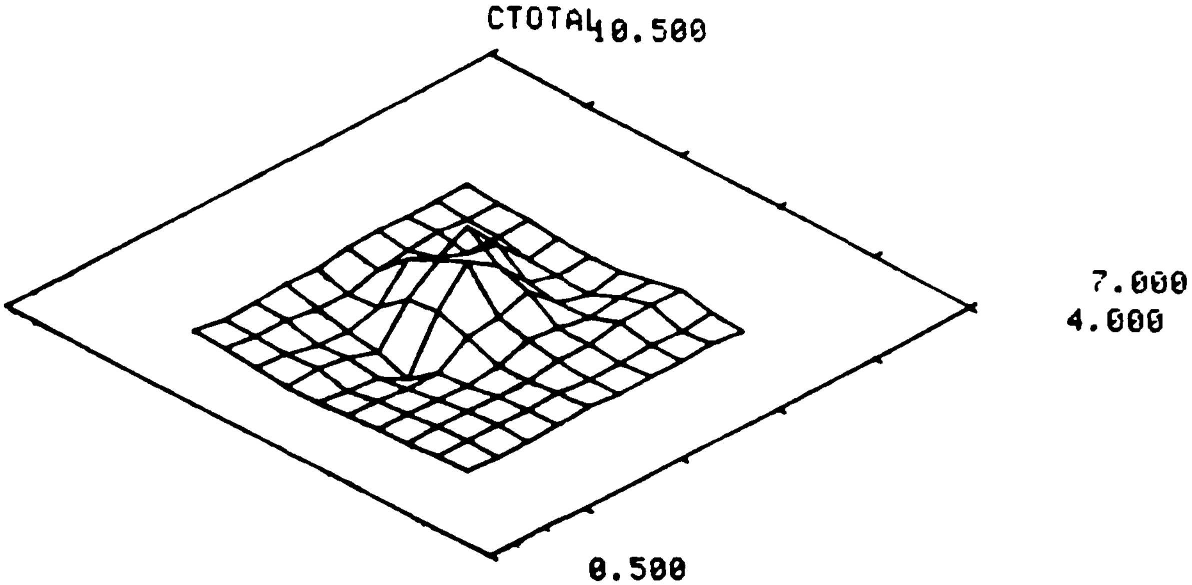

Figure A-6

3 INCH PLANE

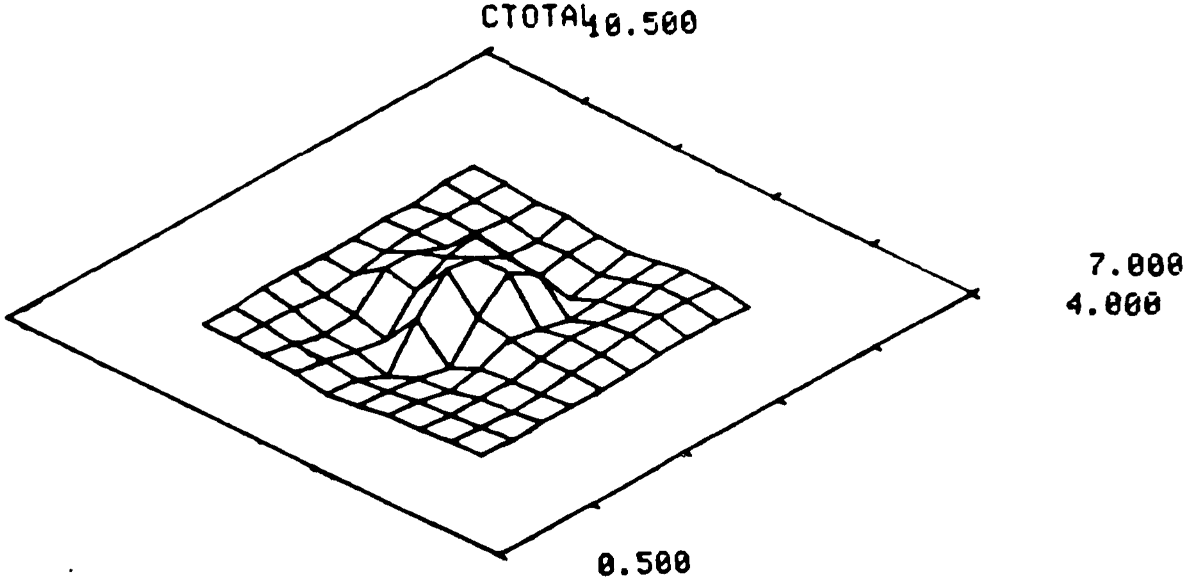

Figure A-7

4 INCH PLANE

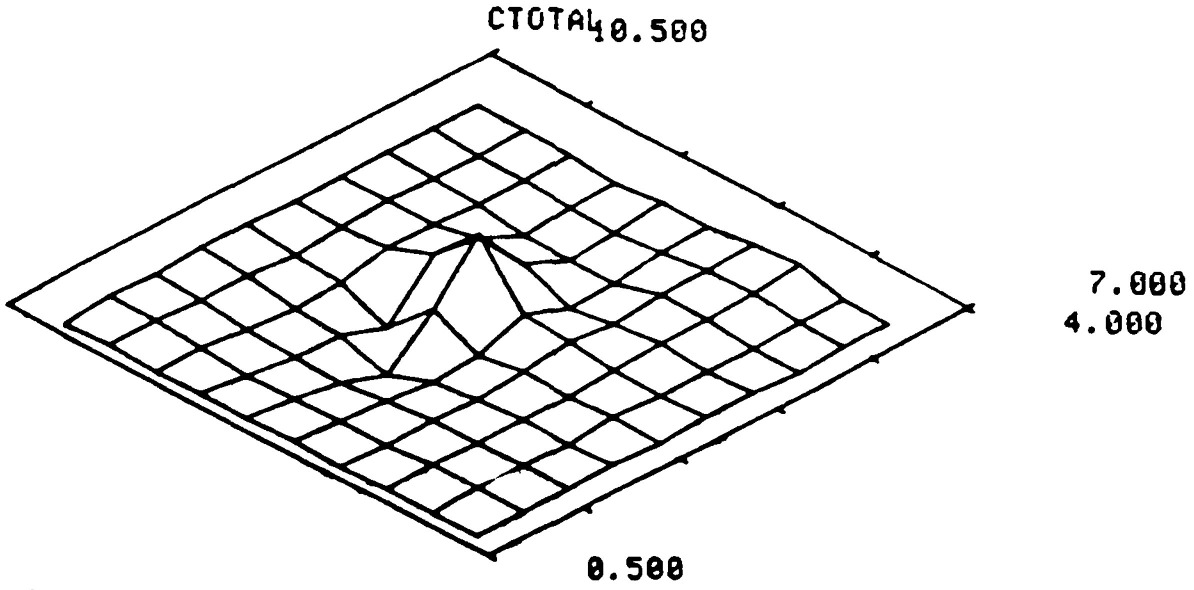

Figure A-8

SECTION II.

Aerodynamics

WIND TUNNEL STUDY ON THE DRAG REDUCING EFFECTS OF AN AFT-MOUNTED VENTRAL FIN ON A T-38 MODEL

Gregory W. Bice*

Editor's Note

This article is the result of the author's Aero 499 Independent Study Project. It will also be presented at the 1985 American Institute of Aeronautics and Astronautics Region V Student Paper Competition.

Abstract

The effects of an aft-mounted ventral fin on a 1/18.4 scale T-38 model's subsonic drag characteristics were investigated in the 2'x3' Subsonic Wind Tunnel at the USAF Academy. Wind tunnel tests were performed on the baseline model using boundary layer trips and with a ventral fin and clipped vertical tail as configuration variables. Data were taken to determine the effects of the configuration changes on the aerodynamic coefficients and stability derivatives. Data were obtained by varying angle of attack and sideslip angle of the model in separate test runs at 100 fps. A six component internal balance was used to measure force and moment data. Test results showed that a consistent reduction in drag coefficient of up to 5% resulted from the addition of the ventral fin to the baseline model at low angles of attack. The drag coefficient increased up to 17% over the baseline model with the ventral fin when the vertical tail was clipped. Results of oil flow tests showed no significant vortex or turbulent wake patterns for any configuration tested. The exact nature of the cause-effect relationship by which ventral fin reduced the subsonic drag coefficient remains unknown.

I. Objective

The purpose of this study was to measure the reduction in drag due to the addition of an aft-mounted ventral fin on a 1/18.4 scale T-38 model. In addition, lateral/directional static stability derivatives were compared for model configurations with a normal vertical tail and with a clipped vertical tail. Finally, the cause-effect relationship of the ventral fin's drag reducing properties was analyzed and documented.

---

*Cadet, United States Air Force Academy

II. Theory

Aerodynamic drag can be divided into three major categories: parasite, induced, and wave drag. Since our wind tunnel tests were conducted at subsonic speeds, wave drag is not present. Induced drag, or drag-due-to lift, is primarily dependent on the wing aspect ratio and wing-body combination. Since all test runs were conducted at identical alpha sweeps with no changes to the wing, the induced drag can be considered a constant for all alpha testing. This leaves only parasite drag to consider.

At angles of attack below stall, drag data for many configurations, such as the T-38, can be expected to fit the classic drag curve equation,

$$C_D = C_{D_o} + KC_L^{\ 2} \qquad (1)$$

where $KC_L^{\ 2}$ is the induced drag coefficient and C_{D_o} is the parasite drag coefficient (Ref. 1). Parasite drag is further divided into interference drag and profile drag. Both are functions of the airplane's shape, surface area, and configuration. Profile drag is composed of drag due to skin friction and flow separation. Since the skin friction coefficient, C_{D_f}, is a function of Reynolds number, it can be assumed that C_{D_f} remains essentially constant because all tests were conducted at almost the same velocity and temperature (Ref. 1). One purpose of modifying this aircraft by adding the ventral fin is to try and reduce the drag due to flow separation in the tail area of the T-38. Looking at a figure of the T-38, a slight upward slope or boattail can be seen at the tail. The ventral fin is to be added in this location. By adding this ventral fin, it is hoped that the airflow will somehow be changed, causing a decrease in separation or form drag.

As the flow moves aft on the surface of the plane, it will lose kinetic energy in the boundary layer due to skin friction. This decrease in kinetic energy in the form of reduced velocity, combined with the adverse pressure gradient, causes the flow to work "uphill" in the tail area. Consequently, the boundary layer may separate somewhere along the plane, causing a separated flow region and, hence, separation drag.

Besides using the ventral fin as a variable, boundary layer trips were also used. Many models have such smooth surfaces that the boundary layer flow remains laminar and never transitions to turbulent. The main reason it remains laminar, however, is due to the Reynold's numbers obtained in the wind tunnel which are typically one to two orders of magnitude lower than those of the actual plane in flight. The purpose of these trips, which are seen in Figure 3 as the thin strips of white tape, is to transition the boundary layer flow from laminar to turbulent at the same position that it would occur on the actual plane, simulating more of a "real" situation. Tripping the boundary layer to turbulent flow, more typical of actual flight, should result in higher skin friction drag but lower separation drag.

In adding the ventral fin to the T-38, elements other than drag had to be addressed, such as the static stability of the aircraft. Stability considerations are very important because they affect the flight control system and the pilot's ability to fly the plane. In the area of longitudinal stability, the fin should not affect the plane, at least theoretically, because it does not contribute to any longitudinal pitching moments about the center of gravity. However, in the area of lateral-directional stability, the fin will have an effect. Since it is mounted aft of the plane's center of gravity, the fin should have a stabilizing effect ($C_{n_\beta}>0$) on weathercock stability, meaning a positive sideslip will cause a positive yawing moment. The fin should also cause a decrease ($C_{l_\beta}<0$) in the lateral or roll stability of the plane. This implies a positive sideslip will cause a positive rolling moment which is destabilizing according to the conventions of aerodynamics (Ref. 2).

III. Apparatus and Procedure

This study was conducted in the 2'x3' Subsonic Wind Tunnel at the U.S. Air Force Academy. The tunnel, shown in Figure 1, consists of a 200 HP synchronous motor with a Gyrol fluid drive unit, a four-bladed compressor, flow conditioning regions such as the stilling chamber, a converging nozzle, a test section, and finally a diffuser. Velocities between 50 fps and 400 fps can be reached in the clean test section along with dynamic pressure ranging from 1.8 psf to 130 psf. During this study, a velocity of 100 fps was used which resulted in a test Reynolds number of about 0.2×10^6. This airspeed does not appear to be representative of T-38 flight speeds. However, at subsonic Mach numbers, which is the flight regime most used by the T-38, aerodynamic force coefficients stay relatively constant, making airspeed irrelevant. The velocity was limited due to model support system dynamics because serious vibrations resulted at higher airspeeds.

The T-38 model was supported by a sting and model support system shown in Figure 2. Variations in the angle of attack were achieved using a pitch sector, strut and boom assembly, and an electric motor. Sideslip angle tests were accomplished by rolling the model and balance 90° and by varying the sideslip angle while holding a constant zero degree angle of attack.

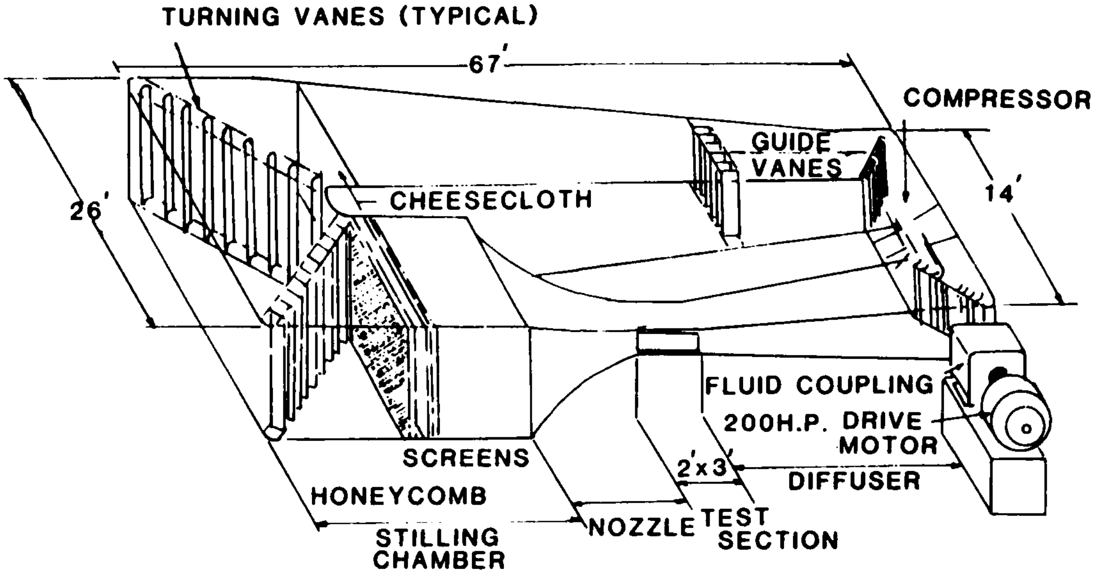

Figure 1. General Schematic of fh the 2' x 3' Subsonic Wind Tunnel at USAFA.

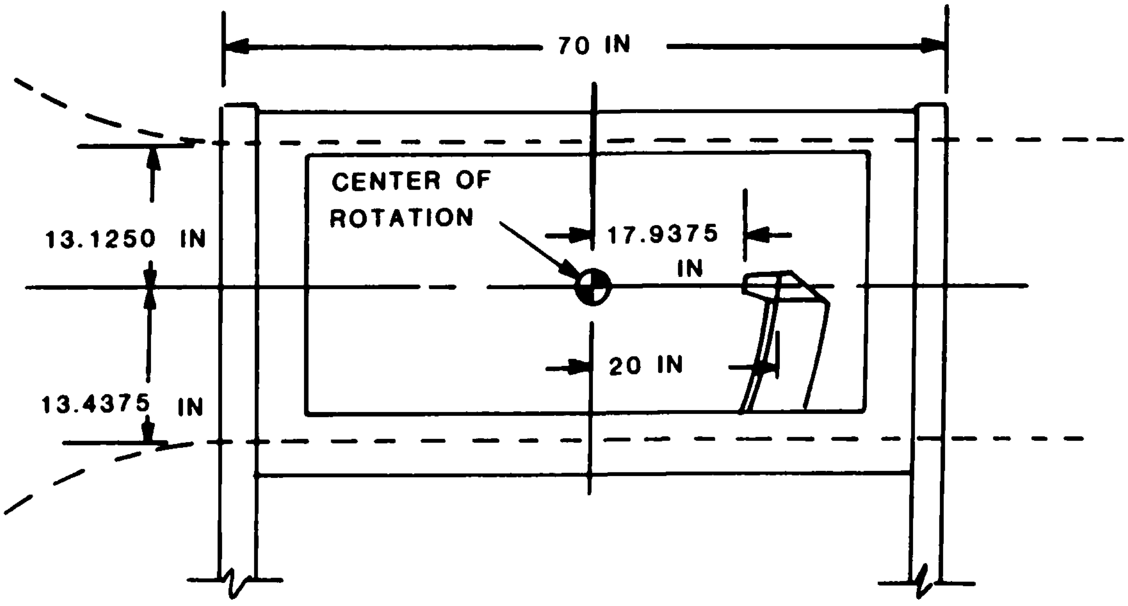

Figure 2. Model Support System.

The model used in the test section was a 1/18.4 scale T-38 with a NACA 65A004.8 (mod) airfoil for the wing sections. Some of the model dimensions are as follows:

length = 28.76 in

wing span = 16.45 in

MAC = 5.04 in

Wing planform area = 72.17 in^2

CG position = 19.4% MAC

The configurations tested included combinations of boundary layer trips, the ventral fin, and the clipped vertical tail. Two configurations are shown in Figure 3. In order to get both longitudinal and lateral directional data, angle of attack (alpha) sweeps and sideslip angle (beta) sweeps were performed using the model support system.

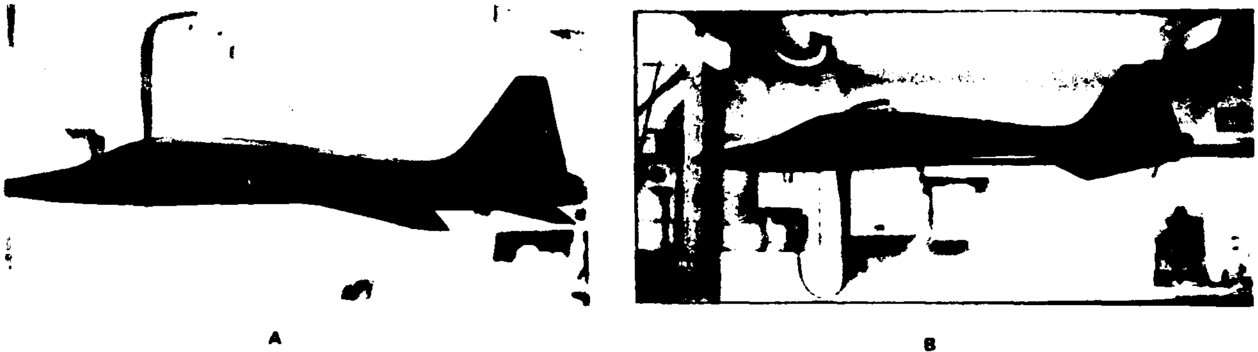

Figure 3. T-38 Configurations (a) normal,
(b) with Ventral Fin and Clipped Tail.

The purpose of testing the airplane with a clipped vertical tail was to try to return C_n to its original value. In other words, the tail was clipped to compensate for the increased weathercock stability of the airplane resulting from the addition of the ventral fin. Clipping the vertical tail should also cause a decrease in roll

AD-A157 215 AIR FORCE ACADEMY AERONAUTICS DIGEST(U) AIR FORCE 2/3
ACADEMY CO J E DEJONGH ET AL. APR 85 USAFA-TR-85-2

UNCLASSIFIED F/G 20/4 NL

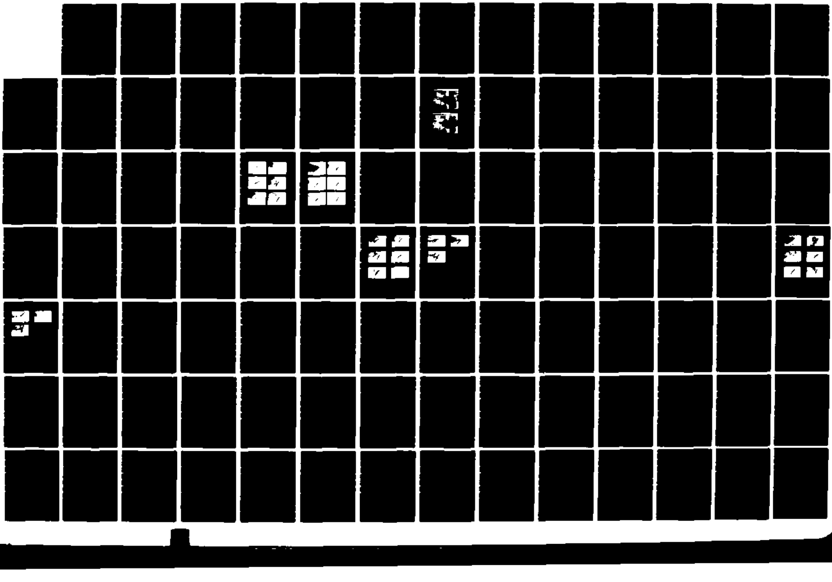

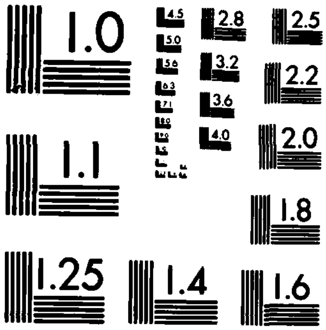
1.0
4.5
5.0
5.6
6.3
7.1
8.0
2.8
3.2
3.6
4.0
2.5
2.2
2.0
1.1
1.8
1.25
1.4
1.6

stability, C_l , which will probably be compounded by the ventral fin because these two surfaces are 180 degrees apart on the airplane. Because of the reduced surface area of the tail, the overall drag on the T-38 should decrease, unless the tail serves some purpose in reducing separation drag.

Force and moment data were acquired using a 0.75" diameter, six component steady-state internal strain-gage balance, seen in Figure 4. The force balance is mounted on the end of the sting support and is inserted into the model. It contains six internal strain-gages, which measure forces and moments on the model, and it transfers this data to a computer in the form of an electrical output. The specifications of the 0.75" force balance are shown in Figure 5. The test procedure included taking tare data, such as model weight and amplifier zero settings prior to each run. In addition, tunnel total and static pressure transducers were initially calibrated to determine the psi/mV ratio. Using this ratio along with the atmospheric conditions, tunnel velocity could be calculated. All data was acquired using a Digital PDP 11/45 computer data acquisition system.

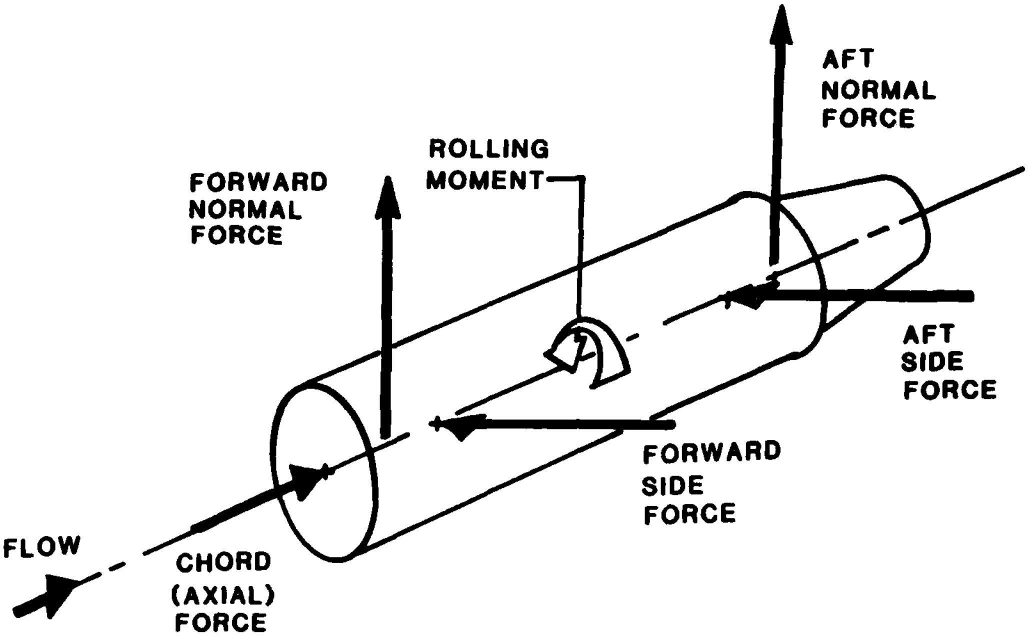

Figure 4. Six Component Force Balance with Positive Balance Loads.

IV. Discussion

In this section, I will discuss the results of the drag measurements and the effects that the ventral fin had on drag coefficient. In addition, I will discuss the static stability results and try to explain why the ventral fin apparently reduced the parasite drag coefficient. Some of the results obtained did not agree well with what theory predicted while others did.

A. Drag Measurements

The resulting reduction in drag coefficient due to the ventral fin can be seen from the summary of alpha-sweep data in Table 1 and Figures 6 through 15.

Figure 5 Bice

(All dimensions in inches)

	MK-II	MK-VIIIA
A	3.0	2.6
B	2.5	2.0
C	0.7498	0.999
D	4.655	4.655
E	3.83	3.83
F	0.825	0.825
G	3.7	3.7
H	1.9	1.9
I	1.8	1.8
J	0.125 (OD)	0.125 (OD)
K	0.06	0.06

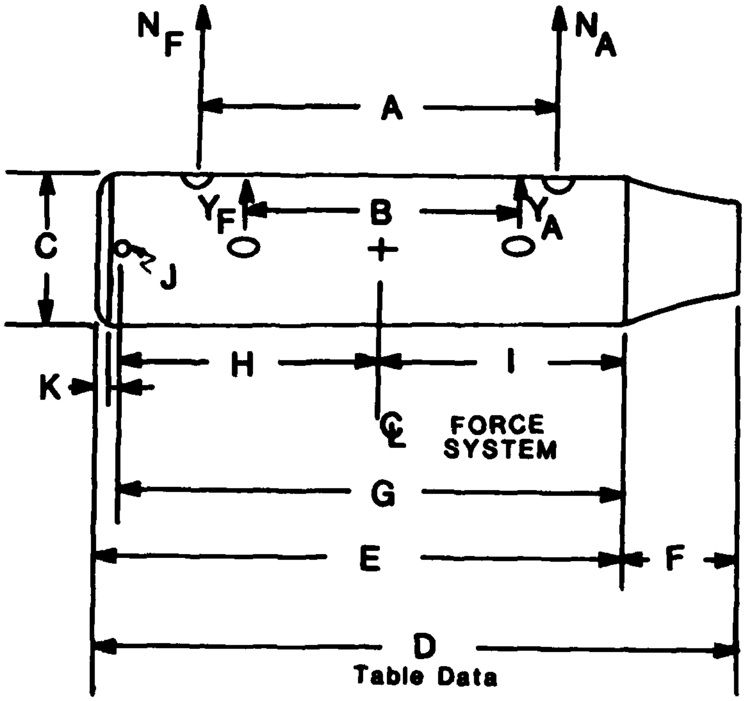

Figure 5. Force Balance Specifications.

Balance	Forward Normal Force	Aft Normal Force	Forward Side Force	Aft Side Force	Chord (Axial) Force	Rolling Moment
MK-II	+100 lbf	+100 lbf	+50 lbf	+50 lbf	+35 lbf	+60 in-lbf
MK-VIIIA	+400 lbf	+400 lbf	+200 lbf	+200 lbf	+75 lbf	+50 in-lbf

				$-5° \le \alpha \le +10°$		$-5° \le \alpha \le +5°$	
Run #	Boundary Trips	Ventral Fin	Clipped Tail	C_{Do}	K	C_{Do}	K
1*				.0254	.3115	.0316	.1700
2*	X			.0323	.2908	.0387	.1708
3*	X	X		.0309	.2708	.0373	.1587
7**	X		X	.0314	.2564	.0381	.1313
8**	X	X	X	.0352	.2492	.0407	.1453

$^{*}C_D = C_{D_o} + K(C_L - C_{L_{min}})^2$ where $C_{L_{min}} = C_L)_{\alpha = 0°}$

$^{**}C_D = C_{D_o} + KC_L^{\,2}$

Eyeball Curve Fit Values

Run #	$C_{Do(-5,+10)}$	$C_{Do(-5,+5)}$
1	.0325	.0325
2	.0358	.0350
3	.0340	.0348
7	.0363	.0367
8	.0400	.0400

Table 1: Alpha-Sweep Summary

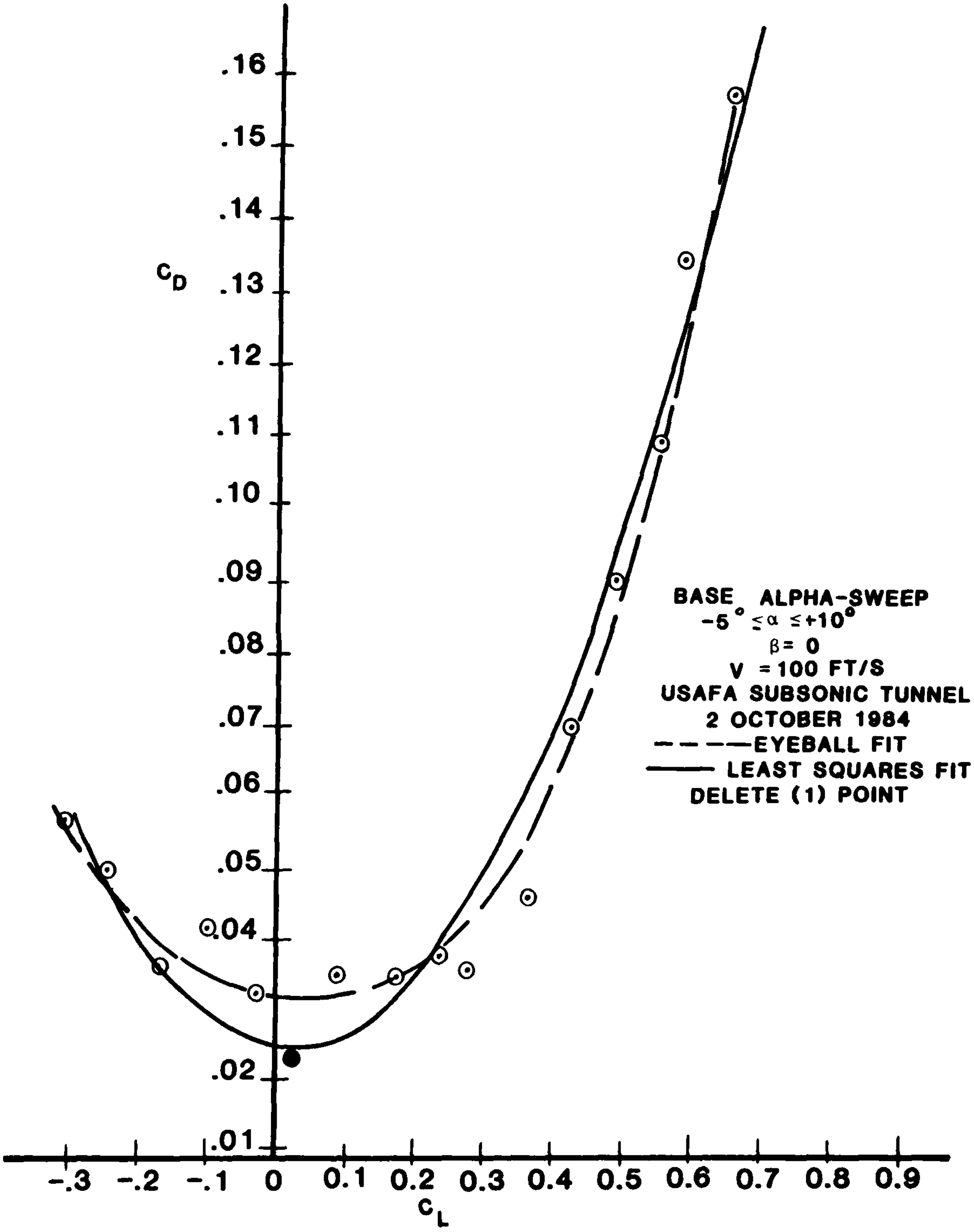

Figure 6. C_D vs C_L Base Sweep.

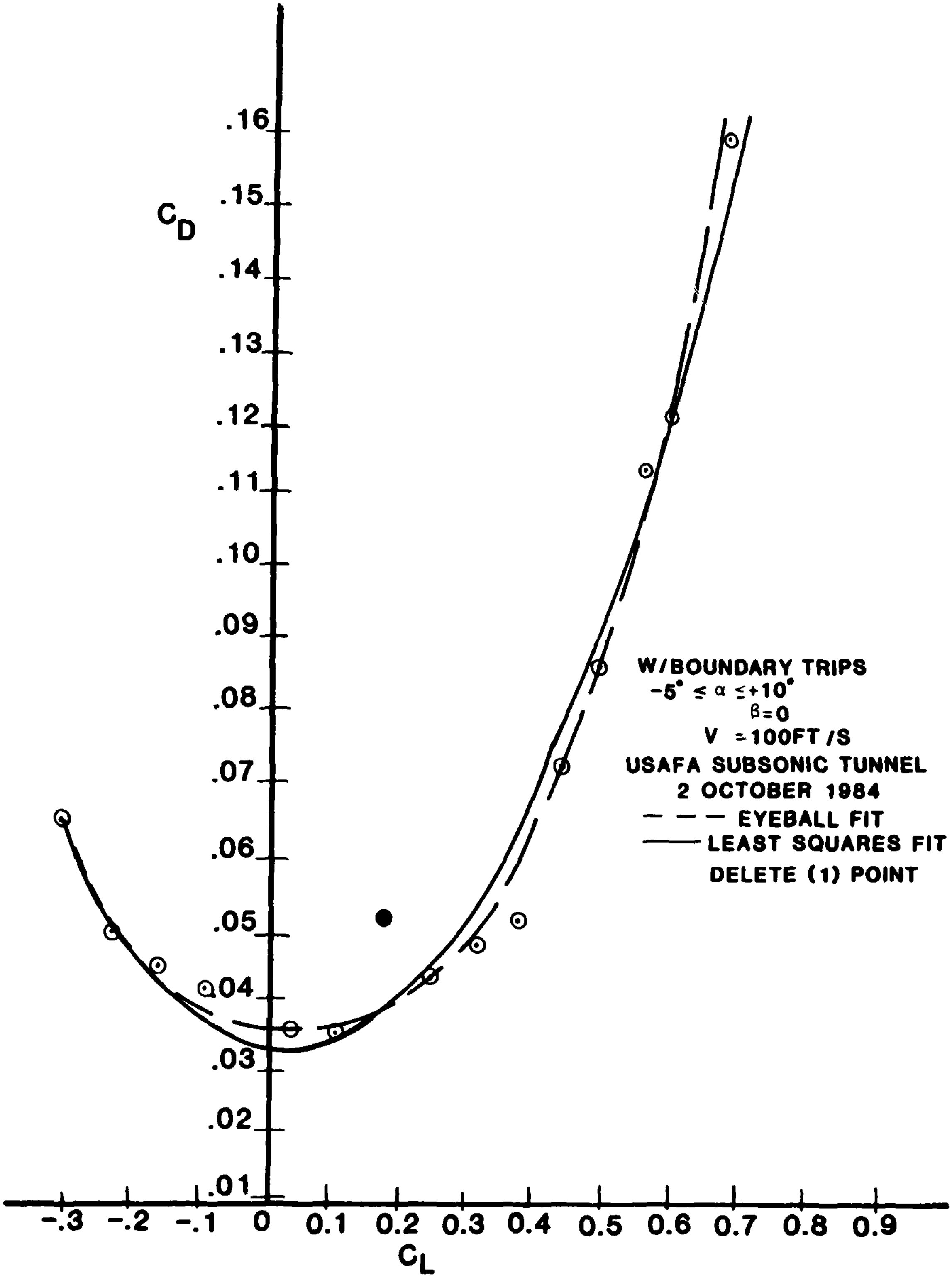

Figure 7. C_D vs C_L with Boundary Trips.

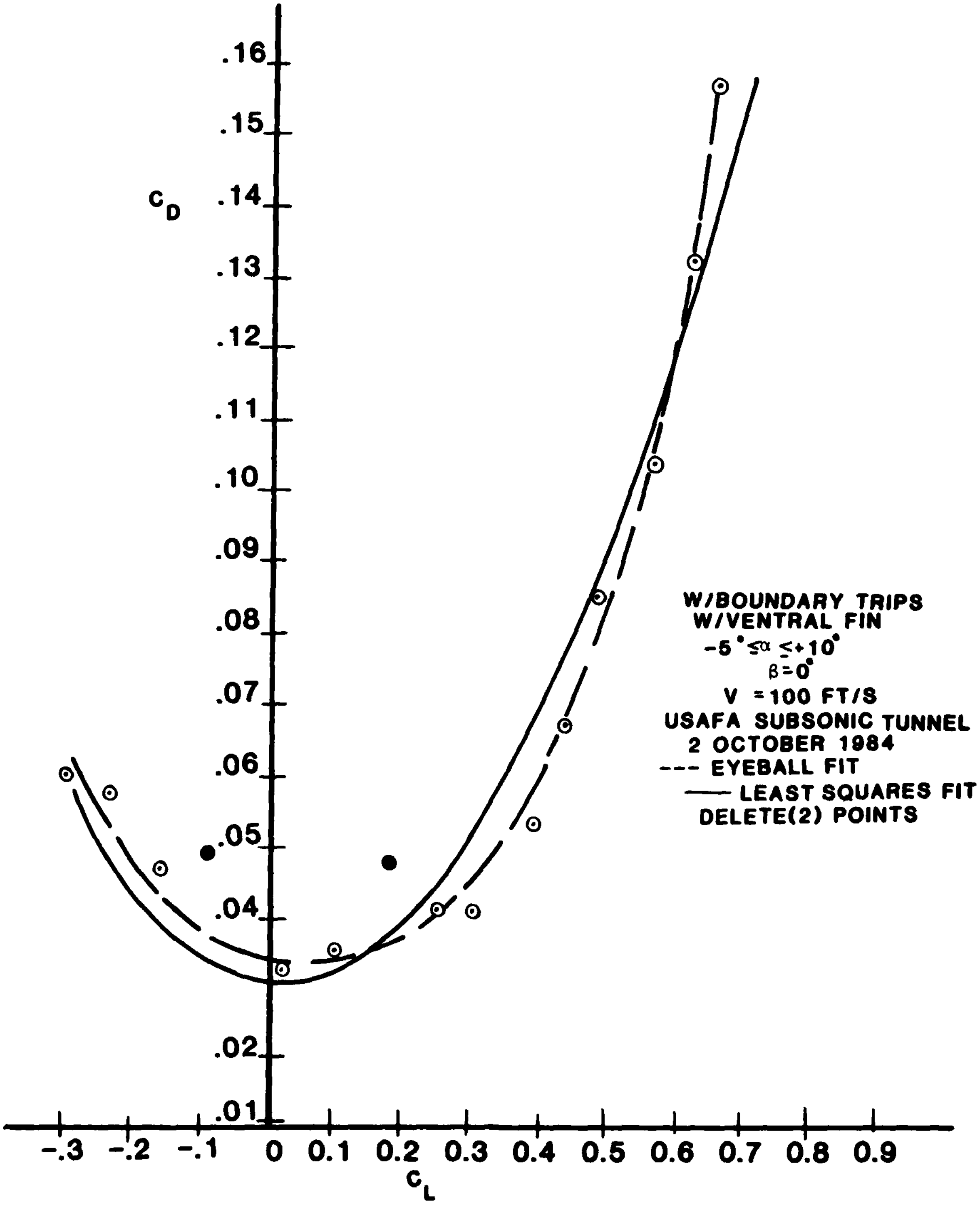

Figure 8. C_D vs C_L with Boundary Trips and Fin.

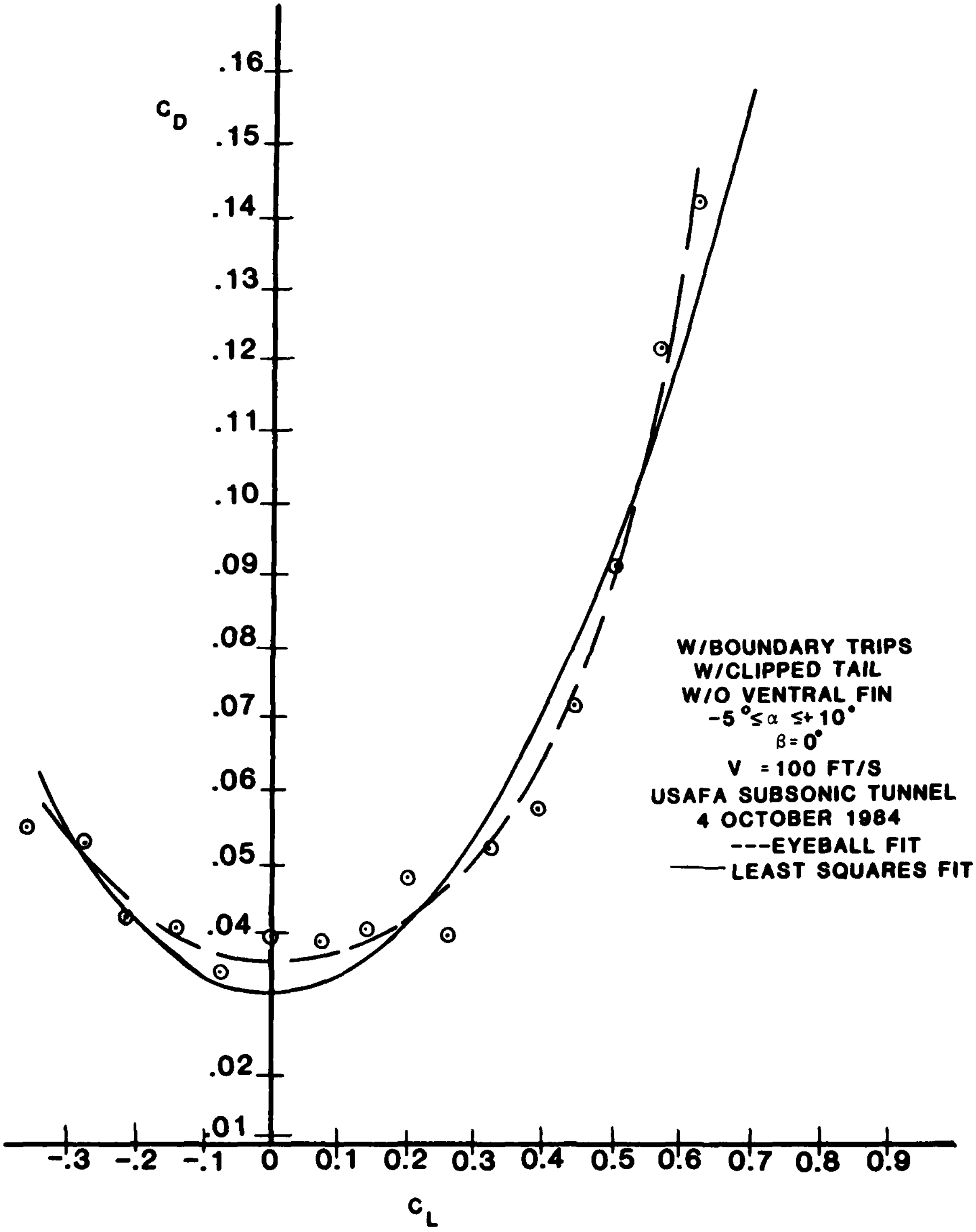

Figure 9. C_D vs C_L with Boundary Trips and Clipped Tail.

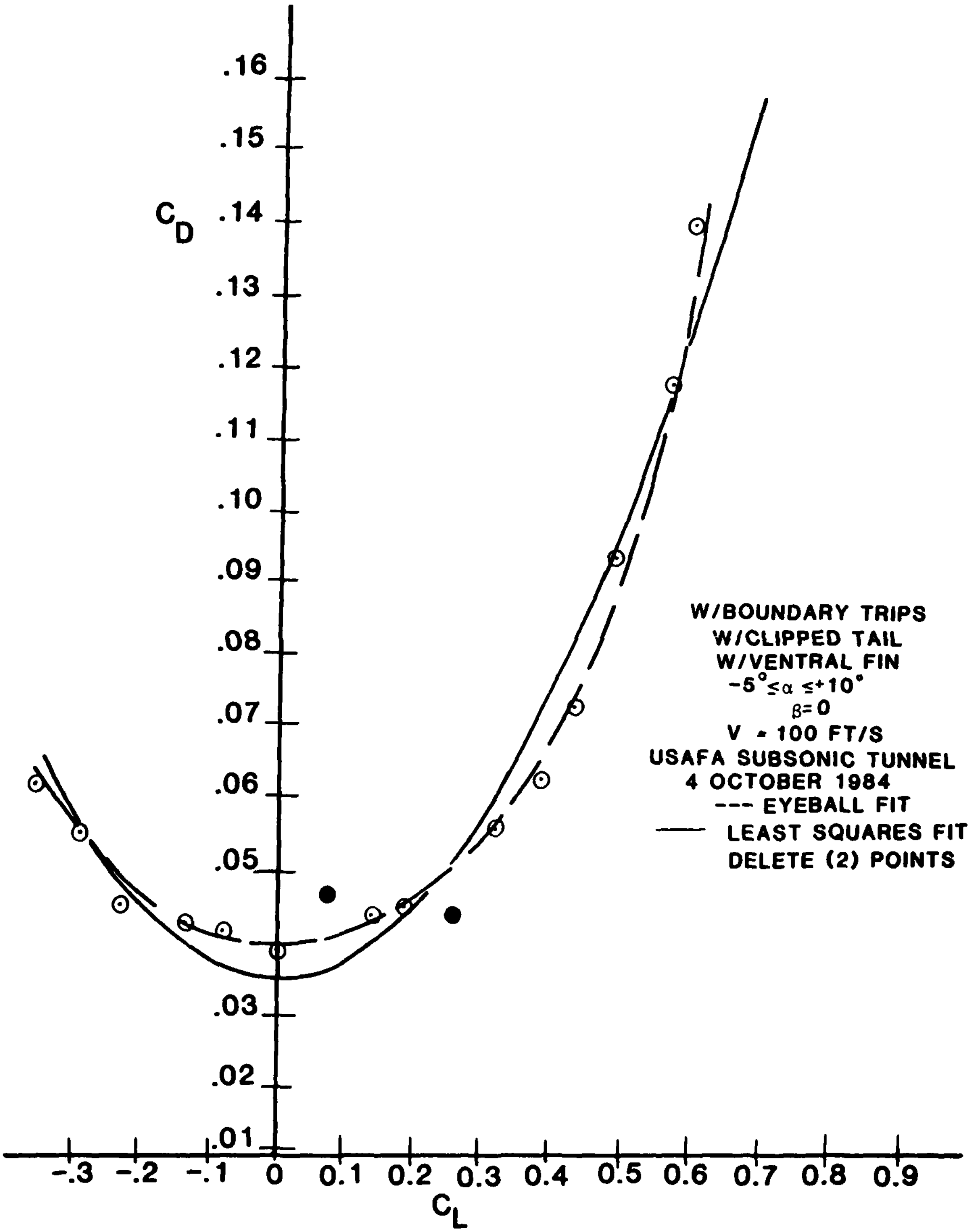

Figure 10. C_D vs C_L with Boundary Trips, Clipped Tail and Fin.

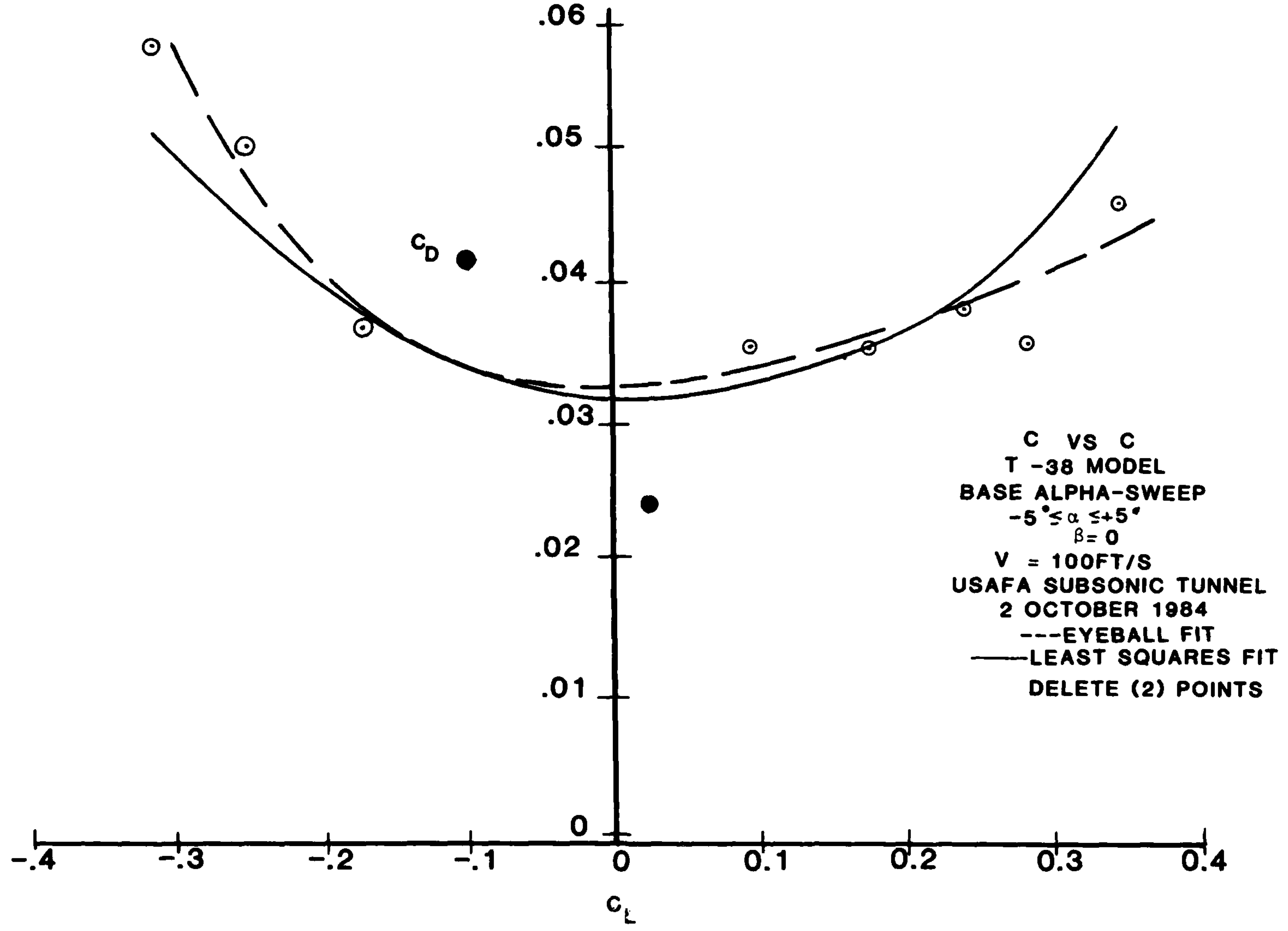

Figure 11. C_D vs C_L Base Sweep.

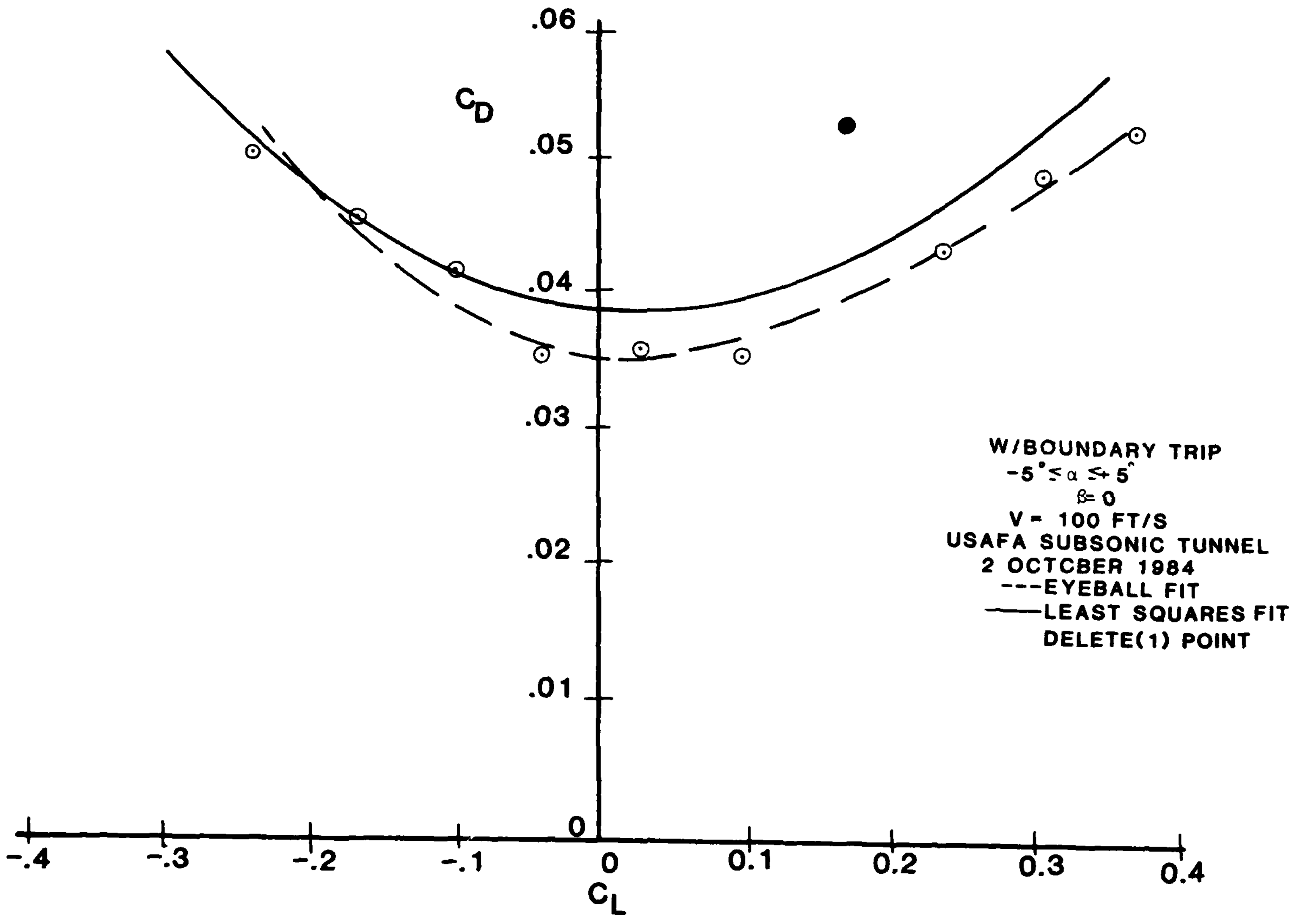

Figure 12. C_D vs C_L with Boundary Trips.

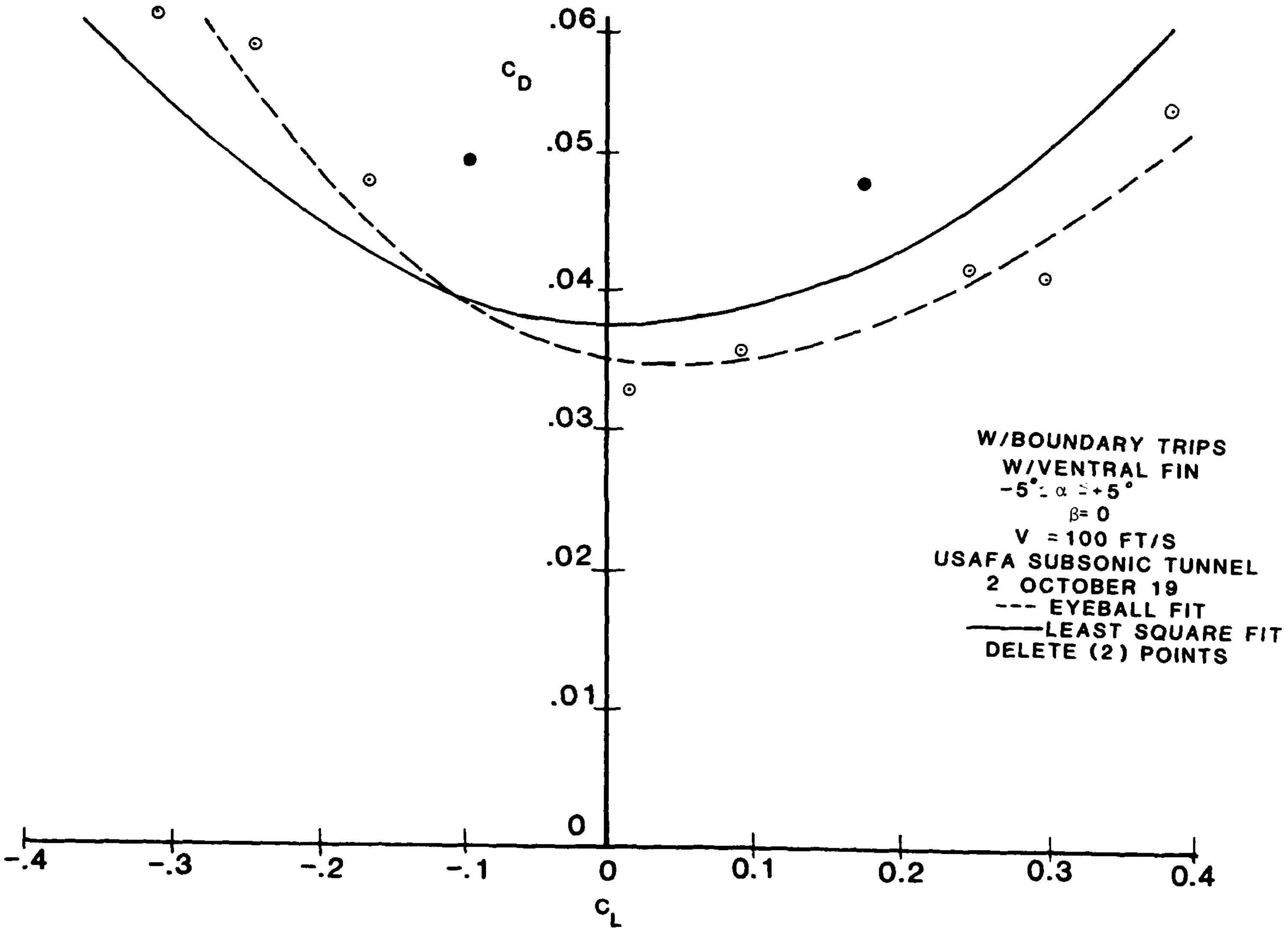

Figure 13. C_D vs C_L with Boundary Trips and Fin.

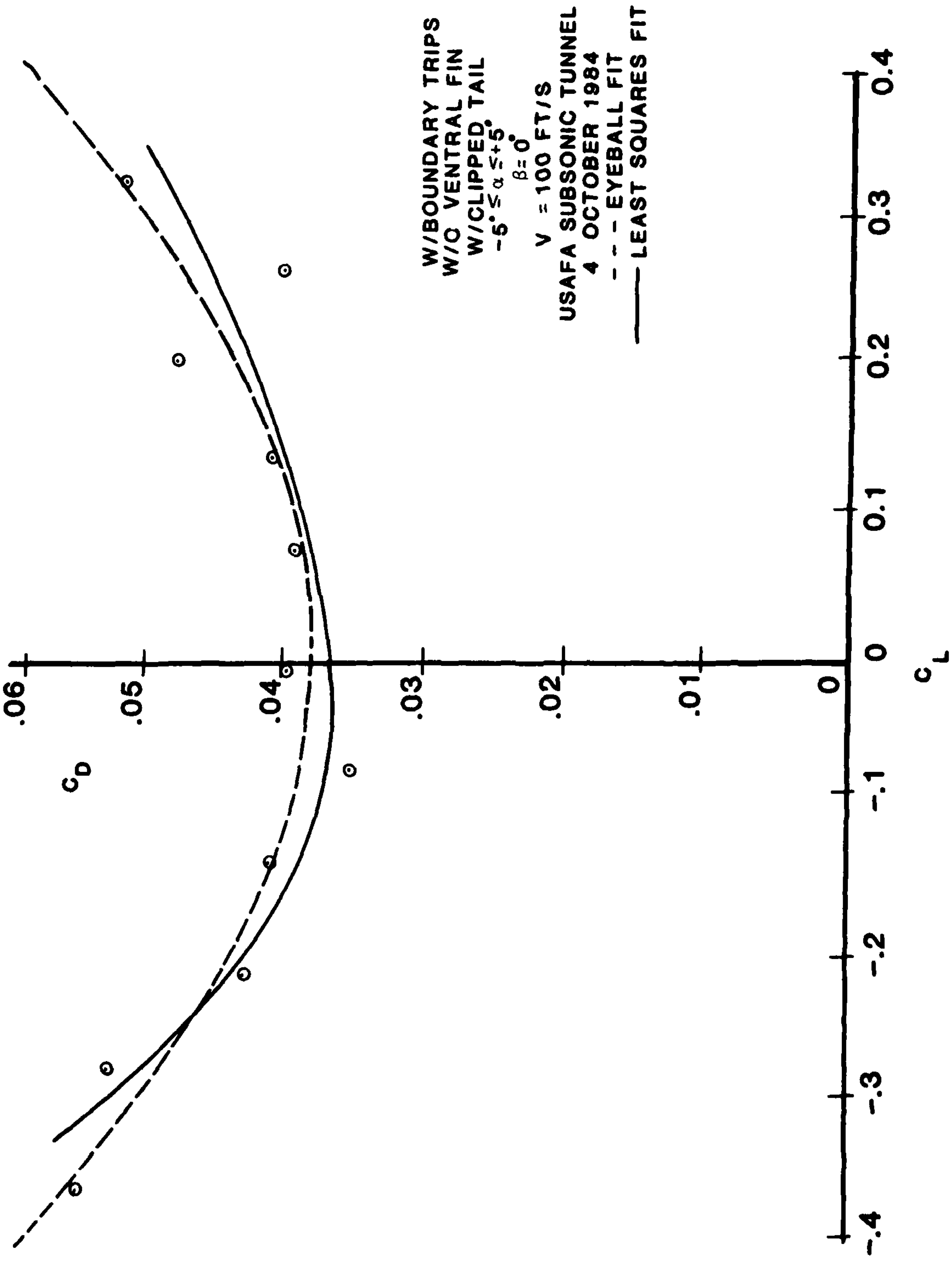

Figure 14. C_D vs C_L with Boundary Trips and Clipped Tail.

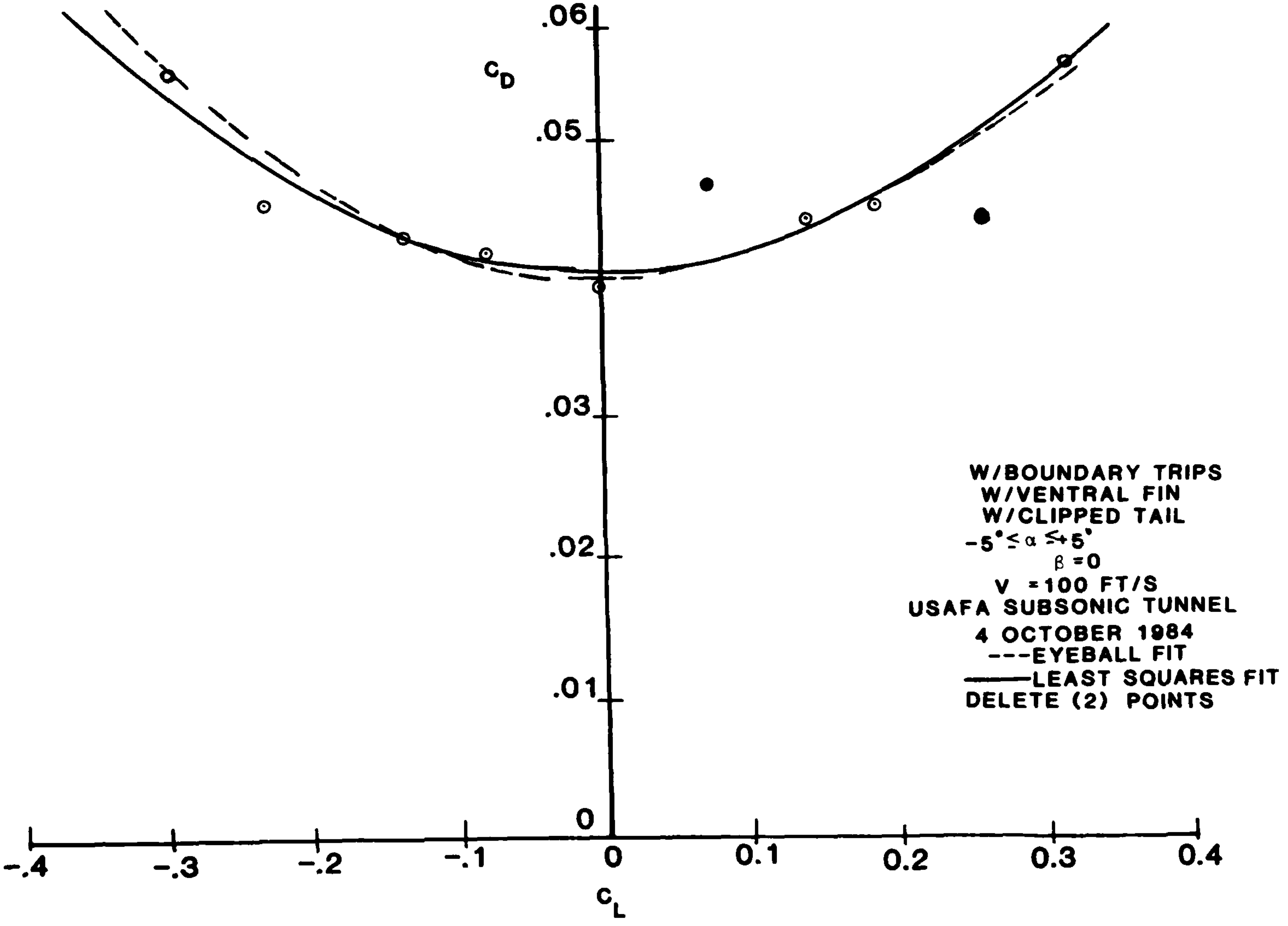

Figure 15. C_D vs C_L with Boundary Trips, Clipped Tail and Fin.

The values of C_{D_o} and K were calculated using linear regression techniques and then compared to the values of C_{D_o} determined by an eyeball curve fit of the data points. For the -5° to +10° alpha sweeps (runs 1,2,3,7, and 8) between a 14 and 18 drag count reduction in C_{D_o} exists due to the addition of the ventral fin. One drag count equals .0001 C_D. Note the differences in the value of K, differences which indicate that the lift distribution, or span efficiency factor, is being altered in some way. I attributed this to the effects of the walls of the wind tunnel interacting with the wings at the higher values of alpha (6° to 10°).

For this reason, I recalculated the values of C_{D_o} and K and got a smaller, more consistent range of values for K in the -5° to +5° alpha region. Since the purpose of this project was to determine the drag coefficient at low to intermediate C_L values, I decided that this would also give a more realistic idea of the drag count reduction. Analyzing the -5° to +5° region, the drag reduction varied between 2 and 14 drag counts. A look at the drag polars for all test runs shows a lot of variance in C_D at low values of C_L. This is due to the fact that drag forces on the order of only 0.2 lbs were being measured by the force balance which can handle up to 35 lbs in axial loading. In other words, the balance wasn't being exercised. The values for drag reduction stated in the two paragraphs above were for the T-38 configured with a normal vertical stabilizer. Further experimentation was done with the tail clipped off at the top.

Contrary to my expectations of a reduction in drag, the drag count increased significantly when the vertical tail was clipped (runs 7 and 8), leading me to believe that the vertical tail somehow reduces the amount of separation drag in the upper tail area. From the standpoint of mere speculation, reducing separation may also be the function of the ventral fin in reducing drag on the bottom side of the T-38.

B. Static Stability

The reason for clipping the tail was to compensate for the increased directional stability of the plane due to the ventral fin. Increased stability is not desirable after a certain point is reached because the maneuverability of the plane is degraded. Looking at Table 2, which summarizes the stability derivatives calculated during beta-sweep tests (runs 5 and 6), I found that the ventral fin did cause an increase in C_{n_β} as predicted, from 0.0038/deg to 0.0043/deg. Clipping the tail reduced this value to 0.0027/deg., indicating that too much of the vertical stabilizer was cut off in trying to return the C_{n_β} to its original value.

	$-10° \leq \beta \leq +10°$				$-5° \leq \beta \leq +5°$			
Run #	C_{n_β} (deg^{-1})	b_n	C_{l_β} (deg^{-1})	b_l	C_{n_β} (deg^{-1})	b_n	C_{l_β} (deg^{-1})	b_l
5	.0042	-.0044	-.0044	.0160	.0043	-.0014	-.0060	-.0112
6	.0038	-.0025	-.0037	.0151	.0038	-.0021	-.0053	-.0104
9	.0030	-.0044	-.0005	.0149	.0027	-.0042	-.0001	-.0123
10	.0026	-.0042	-.00135	.0162	.0023	-.0040	-.0009	-.0134

Run #	Boundary Trips	Ventral Fin	Clipped Tail
5	X	X	
6	X		
9	X	X	X
10	X		X

Table 2: Beta-Sweep Summary

The initial roll stability results were unexpected because the data indicated that the addition of a ventral fin was making C_{l_β} more negative, or stabilizing the aircraft in the roll axis -- something that is improbable according to theory. However, data for runs 5, 6, 9, and 10 consistently show that the addition of the ventral fin causes the value of C_{l_β} to decrease and become more negative. In other words, theory is being defied. How or why this is happening is still unclear. One trend which causes concern is the fact that the aircraft goes from being stable in the roll axis to being unstable when the vertical tail is clipped. Again, this indicates that the tail was clipped too much, just as the C_{n_β} data indicated.

Upon analysis of the data at zero alpha and beta, I found that the stability derivatives, C_{l_β} and C_{n_β}, indicated that the plane was asymmetrically loaded and mounted in the wind tunnel with a slight amount of negative sideslip. Looking at the data collected from all tests, I realized that this was a consistent trend at zero beta and alpha.

The central questions of this study on drag reduction remain unanswered. Why does the ventral fin reduce the drag on the T-38? What is the cause-effect relationship between the fin and the flow? Upon analysis, graphing, and reduction of the data acquired during testing, I came to several conclusions about the effects of the ventral fin on the T-38's drag and static stability. However, the reasons that some of these effects occur, especially the reduction in drag, are uncertain. Even after having talked to several aerodynamicists, I can at best simply speculate as to why this ventral fin causes a drag reduction. However, I am certain that this is a local phenomenon present only in the tail region. The ventral fin is either reducing the amount of separation in the tail area or moving the point of separation back.

C. Theories/Speculations

To further investigate the phenomenon and try to discover what was happening, oil flow tests were performed on the model in the same conditions as the wind tunnel data runs. Figure 16 shows the results of two oil flow tests.

From the pictures, it is evident that no strong vortices or turbulent wakes are being shed by the ventral fin nor were any present before the fin was added. I have speculated, however, that a slight portion of the wake from the tip of the fin may be interacting with the wake of the body causing the airflow to separate further aft and the drag to decrease. My reasoning here is that although the fin wake may not be strong enough to move the oil and show a vortex pattern, it may be influencing the flow in the tail region. I would suggest using smoke streams to get a better visualization of the phenomenon taking place in the tail area because smoke will be more sensitive to small changes in the flow pattern. Although this method would be sufficient as a qualitative test, a seven hole pressure probe or some type of external flow measuring device should be used to gather quantitative data about the flow field in this region.

The second speculation I have formed is that the ventral fin is acting as a flow-straightening device by preventing spanwise flow from occurring across the bottom of the tail. This spanwise flow could be caused by the vorticies generated by the engine inlets or wing-root intersections. Although the oil flow tests did not show any evidence of spanwise flow, it is possible that weak vortices were shed that did not show up in the oil tests. While the amount of drag reduction due to the fin is small, it is consistent and should be investigated

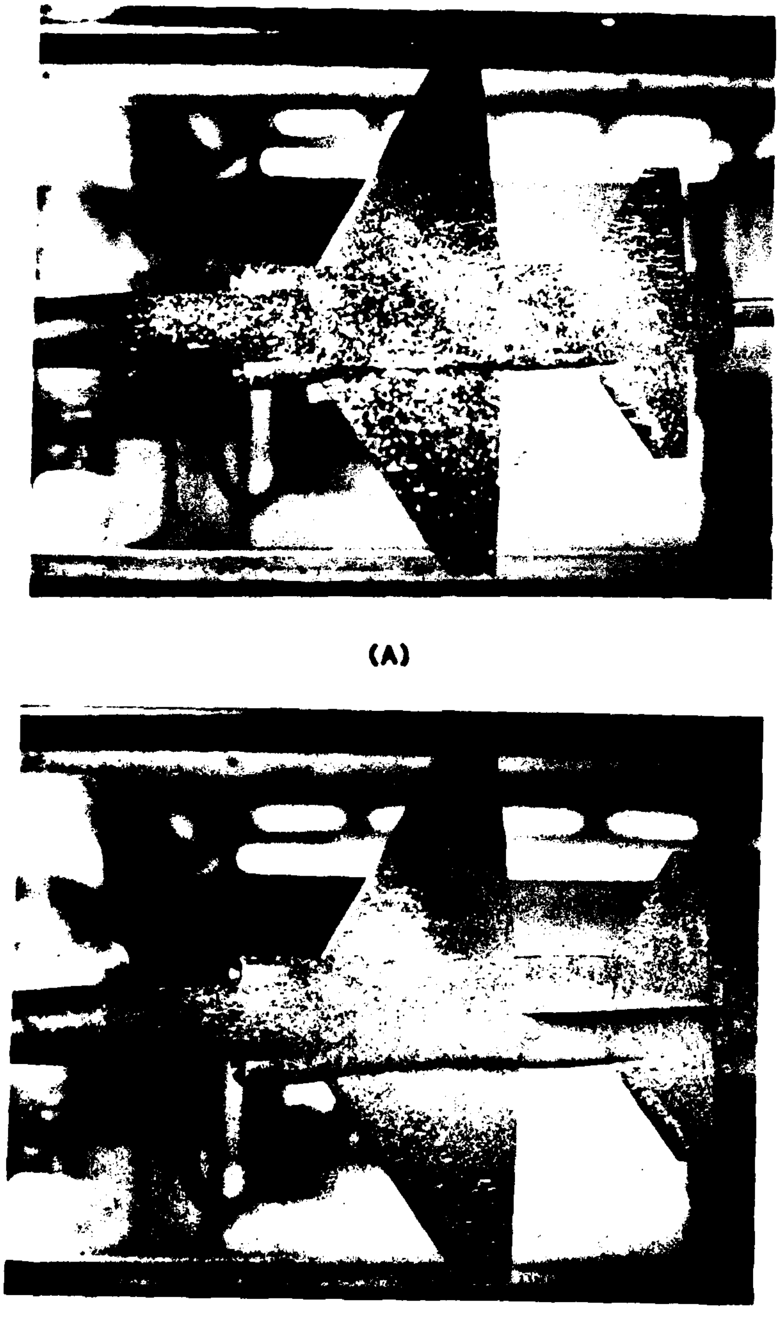

Figure 16: Oil Flow Test Results
(A) Normal T-38
(B) T-38 with Ventral Fin

further to find the exact nature of the fin's effect.

V. Conclusions

A. The ventral fin on the tail section of the T-38 was responsible for reducing the parasite drag on the airplane.

B. Lateral-directional stability derivatives are affected by the ventral fin. Directional stability is increased, as is lateral stability (which is contrary to theoretical predictions).

C. No theory has been conceived as to why the roll stability derivative is more stable with the addition of the ventral fin.

D. The vertical tail was clipped too much, causing a decrease in directional stability, the appearance of an unstable rolling moment coefficient, and an increase in parasite drag.

VI. Recommendations

A. Take more force and moment data to verify the ventral fin's potential in reducing drag.

B. Perform additional testing on the T-38 using a seven hole pressure probe to plot the flow field around the tail region, with and without the ventral fin.

C. Do further flow visualization studies using smoke streams.

D. Lengthen the clipped tail or keep the regular sized tail in order to keep the stability derivatives close to normal T-38 values.

Symbols

English Symbols

A	aspect ratio
b	wing span (ft)

c	wing mean aerodynamic chord, MAC, (ft)
D	drag force (lbf)
e	span efficiency factor
K	drag-due-to-lift-factor
L	lift force (lbf)
q	dynamic pressure (lbf/ft^2)
R_e	Reynolds number (V /μ)
S	wing planform area (ft^2)
V	velocity (ft/s)
C_D	total drag coefficient (D/qS)
C_{D_o}	parasite drag coefficient
C_{D_f}	friction drag coefficient
C_L	lift coefficient (L/qS)
C_l	rolling moment coefficient
C_n	yawing moment coefficient

Greek Symbols

α	angle of attack (deg)
β	angle of sideslip (deg)
ρ	density (slug/ft^3)
μ	coefficient of viscosity (slug/ft s)

References

1. Anderson, John D., Jr. Introduction to Flight, New York: McGraw-Hill Book Company, 1978.

2. Lang, James D., revised by J.C. Carling, Aircraft Performance, Stability and Control, USAF Academy, 1974.

AN EXPERIMENTAL INVESTIGATION OF AN AIRFOIL UNDERGOING LARGE AMPLITUDE PITCHING MOTIONS

J.M. Walker*, H.E. Helin**, AND J.H. Strickland***

Abstract

Flow visualization and near-surface hot-wire experiments were performed in the USAF Academy Aeronautics Laboratory 2ft x 3ft subsonic wind tunnel on an airfoil undergoing large amplitude pitching motions. The experiments were conducted using a 6-in. NACA 0015 airfoil at an airfoil Reynolds number of 45000 by pitching from 0° to 60° at various constant angular pitch rates. The two cases presented represent two different nondimensional pitching rates, α^+, equal to the pitch rate, $\dot{\alpha}$, nondimensionalized by the chord, c, and the freestream velocity, U_∞.

Data for the two cases, in which values of α^+ were equal to 0.2 and 0.6 show the dramatic effect of pitch rate on flow structure. Large scale vortical structures are seen in both cases but appear in different form at higher angles of attack for the larger α^+ value. These structures are very energetic, producing reverse flow velocities near the airfoil surface of one to two and one-half times the freestream velocity.

I. Introduction

In recent years the study of unsteady aerodynamics has intensified due to the need to more fully understand the aerodynamics of helicopters, axial flow turbines and compressors with inlet distortions, vertical axis wind turbines, and missiles and fixed wing aircraft undergoing rapid maneuvers. More recently the need to understand the unsteady flow behavior around lifting surfaces which have significant stalled regions on their surfaces has become apparent.

A number of studies have been done with regard to analytical approaches to the "dynamic stall" problem as evidenced by the reviews of McCroskey (Ref. 1 and 2). In general, these approaches include

---

*Major, USAF, AFIT Student, Univ. of New Mexico
**Lt., USAF, Task Manager/Unsteady Aerodynamics, Frank J. Seiler Research Laboratory
***Prof. of Mech. Engr., Texas Tech Univ., Lubbock, Texas

semi-empirical models (Ref. 2-6), boundary layer prediction schemes which can be used to predict some of the behavior associated with unsteady stall (Ref. 7-9), models which represent the separated shear layers as discrete vortices (Ref. 10-13), and full Navier-Stokes solutions (Ref. 14-15). To date, however, none of these analytical methods have been proven to be totally satisfactory for predicting the lift and drag on arbitrary airfoil sections undergoing arbitrary airfoil motions with the potential for dynamic stall. Part of this lack of credibility is rooted in the fact that dynamic stall data, which can be used to test these techniques, are still somewhat limited. In addition, the lack of data may be hiding a certain amount of the "physics" of the phenomenon which should be included in the less sophisticated approaches to make them more reliable.

Most of the experimental data obtained for unsteady separated flow over airfoils have been obtained from oscillating airfoils undergoing relatively small sinusoidal pitch oscillations (1° to 10°) about a relatively low mean angle of attack (0° -15°) as typified by the experiments reported by McCroskey and Philippe (Ref. 16), McAlister and Carr (Ref. 17), Martin, et al (Ref. 18), and Robinson and Luttges (Ref. 19). The types of data obtained in these studies include flow visualization data, hot-film and hot-wire data, and surface pressure measurements. Such airfoil motions are, of course, applicable to many of the fluid devices studied in the past. On the other hand, few experimental data are available for situations in which an airfoil undergoes very large angle of attack excursions taking it into deep dynamic stall. Applications such as the recently conceived "supermaneuverability" of fighter aircraft (Ref. 20) require a more thorough understanding of dynamically stalled airfoils at angles of attack which may exceed 45°. In addition, the motion of the airfoil for this application will perhaps be more closely related to a constant motion as opposed to a sinusoidal motion.

A very limited amount of experimental data has been obtained for airfoils undergoing constant pitching rate motions up to moderate angles of attack of at least 30°. These works include the study of Harper and Flanigan (Ref. 21), who obtained force balance data on a small aircraft model pitching up to 30°, the work of Ham and Garelick (Ref. 22), who obtained surface pressure measurements on an airfoil pitching up to 30°, and the work of Francis, et al (Ref. 23), who obtained surface pressure measurements on an airfoil pitching up to 60°. None of these works have included any flow visualization data or hot wire data. The flow visualization data and surface hot wire data presented in this paper are intended to partially fill this void.

II. Experimental Arrangement

All data were obtained in the USAF Academy Aeronautics Laboratory's low-speed 2ft x 3ft subsonic wind tunnel on a 6in. chord NACA 0015 airfoil. For this particular series of experiments the freestream velocity was maintained between 19.0 and 20.0 ft/sec which yields a Reynolds number based on the airfoil chord of approximately 45000. A computer controlled pitch oscillator described by Francis, et al (Ref. 24) was used to impart constant pitch rate motions to the airfoil between 0° and 60° angles of attack. For the two cases studied herein $\dot{\alpha}$ was held constant at 440°/sec and 1380°/sec which yielded values of $\alpha^+ \equiv \dot{\alpha}c/U_\infty$ equal to 0.2 and 0.6 respectively.

The basic flow visualization scheme makes use of a "smoke wire" stretched across the tunnel normal to the span and upstream of the pitching airfoil. A smoke producing oil (theoretical fog fluid) was coated on a .005 in. diameter tungsten wire which was in turn heated electrically to produce a large number of fine smoke streaks in the flow. These streaks were spaced fairly uniformly due to the regular spacing of oil droplets formed when the wire was coated. The smoke was illuminated by a high intensity strobe light placed downstream of the airfoil. A PDP 11 computer was programmed to control the smoke wire, the airfoil pitching motion, and the strobe flash in the proper timing sequence. A 35mm camera aimed parallel to the pitch axis was used to record the visual data.

In order to obtain near surface velocity measurements, seven hot-wires were mounted on the upper surface (suction side) of the airfoil as shown in Figure 1. The hot-wire sensing elements (TSI-10 hot films) were soldered to pairs of number 9 sewing needles which protruded above the airfoil surface approximately 3 percent (0.2 in.) of the chord length. The needle supports in turn were mounted in electrically insulated plugs machined flush with the airfoil surface. The probes were located along the chord line at 7, 20, 33, 47, 60, 78, and 87 percent chord. Velocity signals were obtained from the probes using a TSI model 1050 hot-wire anemometer system at a sampling rate of 1 KHz. Twenty five repetitions of each case were run to obtain ensemble averages of the velocity signal from each probe.

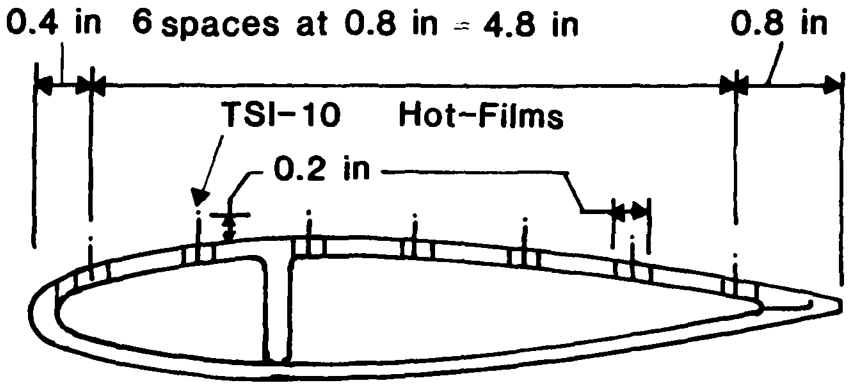

Fig. 1 Surface Hot-Wire Configuration

III. Experimental Results

The instantaneous angle of attack, α, of the airfoil as a function of time is shown in Figure 2 for the two pitching rates reported herein. The increase of α with time is very linear for $\alpha^+=0.6$ and fairly linear for $\alpha^+=0.2$, the maximum deviation being 2% and 4% respectively.

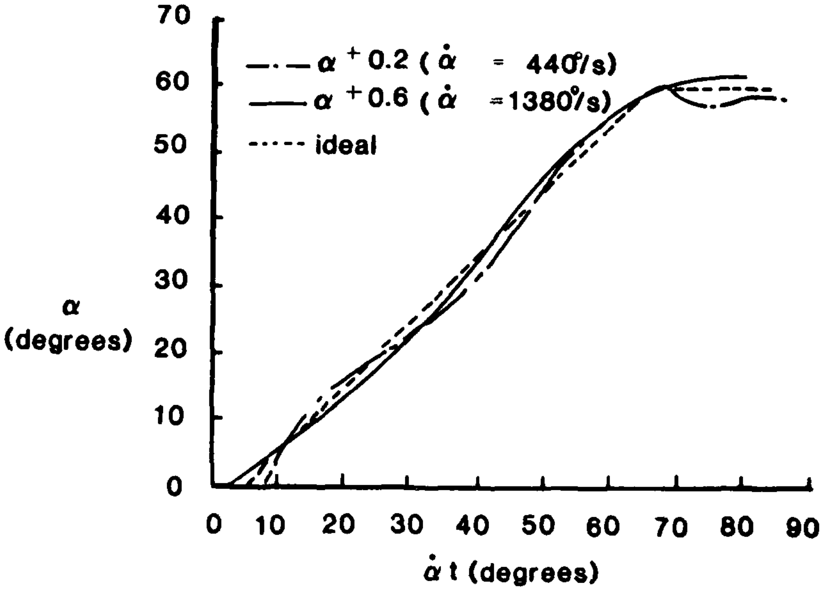

Fig.2 Variation of Pitch Angle With Time

A. Flow Visualization

Flow visualization data are shown in Figures 3 and 4 at selected angles of attack for the two pitching rates. The differences in flow structure are rather dramatic at similar angles of attack for the two cases. Data at the lower α^+ value in Figure 3 show a separation bubble beginning to form at the leading edge at an angle of attack of about 20°. This bubble quickly evolves into a leading edge vortex. This vortex increases in size until its diameter is on the order of half the chord length. While continuing to grow, the vortex begins to move away from the upper (suction) surface of the airfoil which has by then reached a high angle of attack (approximately 40°). Francis, et al (Ref. 23), whose data were taken under slightly different conditions from Figure 3, suggest that the maximum lift at the lower rate is produced at angles of attack between 30°-35°. The flow visualization data in turn suggests that maximum lift occurs when the vortex on the suction side is well developed and still relatively close to the surface.

Data at the higher α^+ value in Figure 4 shows the formation of two distinct vortices which appear to be of comparable importance although not necessarily of comparable strength. Initially there appears to be a region of boundary layer separation which moves from the trailing edge toward the leading edge. At an angle of attack near 30°, a leading edge vortex begins to form. At around 35° the leading edge vortex has grown large enough to retard the forward movement of the trailing edge separation zone. At an angle of attack near 40°, the forward progress of the trailing edge separation zone is halted entirely due to "reattachment" of the flow caused by the leading edge vortex. Furthermore, the clockwise vorticity, shed at the trailing edge due to increasing bound circulation, reattaches the flow at the trailing edge and produces a counter clockwise vortex in the trailing edge separation region similar to the leading edge vortex. As the angle of attack increases, both the leading edge and trailing edge vortices grow to nearly a half chord in diameter and remain relatively stable in their positions until the airfoil reaches its maximum angle of 60°. McAlister and Carr (Ref. 17) have noted similar behavior on airfoils undergoing harmonic oscillations although the effects were much less pronounced due to the low angles of attack in their study. They denote the leading edge vortex as the "dynamic stall vortex" and the trailing edge vortex as the "shear layer vortex." They also note that the "shear layer vortex" seems to disappear at high Reynolds numbers, leaving only the "dynamic stall vortex." The boundary layer separation and the disappearance of the trailing edge vortex at high Reynolds numbers simply indicates that the flow does not separate in the trailing edge region prior to the formation of the leading edge vortex.

B. Surface Velocity Data

Selected "near-surface" velocity data are shown in Figures 5 and 6 for the corresponding cases given in Figures 3 and 4 respectively. The primary purpose of the data taken from the seven hot-wire probes was to obtain insight into the strength of large scale vortices on the suction side of the airfoil by measuring the reverse flow near the wall (3% chord away from the wall). The direction of the flow is not apparent from examination of the single element hot-wire data without the aid of the flow visualization data. In some cases, even comparison of both types of data does not allow one to make a definitive decision concerning flow direction. In addition, the data are inaccurate for cases in which the velocity is close to zero due to the high turbulence intensity levels under those conditions. However, significant forward and reverse flow velocities are easily dectectable and are measurable with reasonable accuracy.

For the α^+ value of 0.2, maximum reverse flow velocities on the order of 140% of freestream were measured. The maximum reverse flow velocity occurs directly under the center of a vortex. The arrows in Figure 5 represent the approximate chordwise locations of the center of the vortex as it moves along and away from the airfoil. At an angle of attack of 24° a suction peak and regions of leading edge separation, reattachment, and trailing edge separation are indicated in both Figure 3a and 5a. At an α of 27°, Figures 3b and 5b show leading edge separation, a probable reverse flow region, and a reattachment region. The small reverse flow velocity obtained at sensor 4 is apparently due to the fact that the hot-wire is sticking up somewhat into the vortex core. Figures 3c and 5c show leading edge separation, a dramatic reverse flow region, and a short reattachment zone at α = 36°. Figures

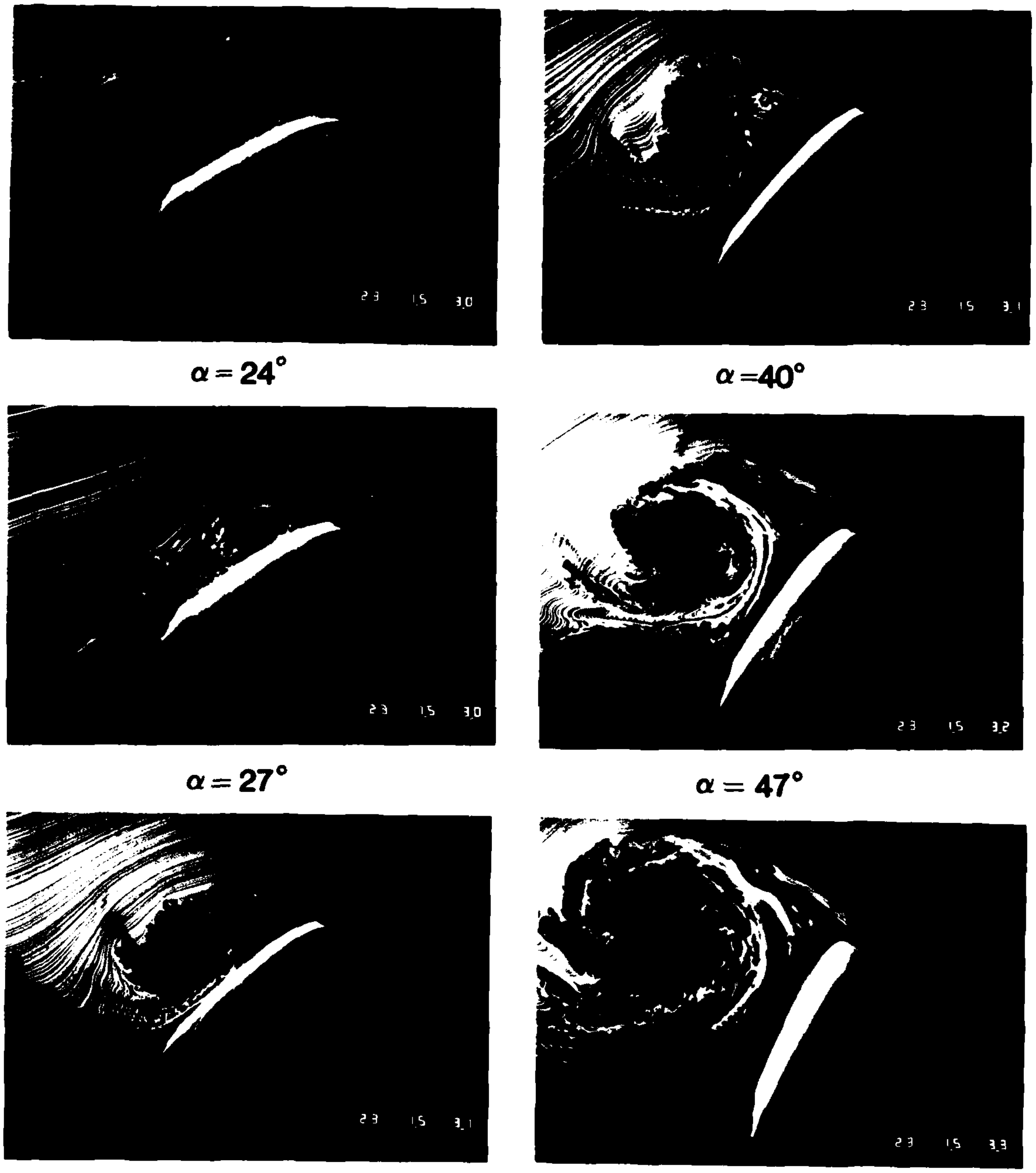

$\alpha = 24^\circ$ $\alpha = 40^\circ$

$\alpha = 27^\circ$ $\alpha = 47^\circ$

$\alpha = 36^\circ$ $\alpha = 59^\circ$

Fig.3 Flow Visualization Data (Re=45,000, $\alpha^{+}=0.2$, constant $\dot{\alpha}$ motion, pitch axis at 25% chord)

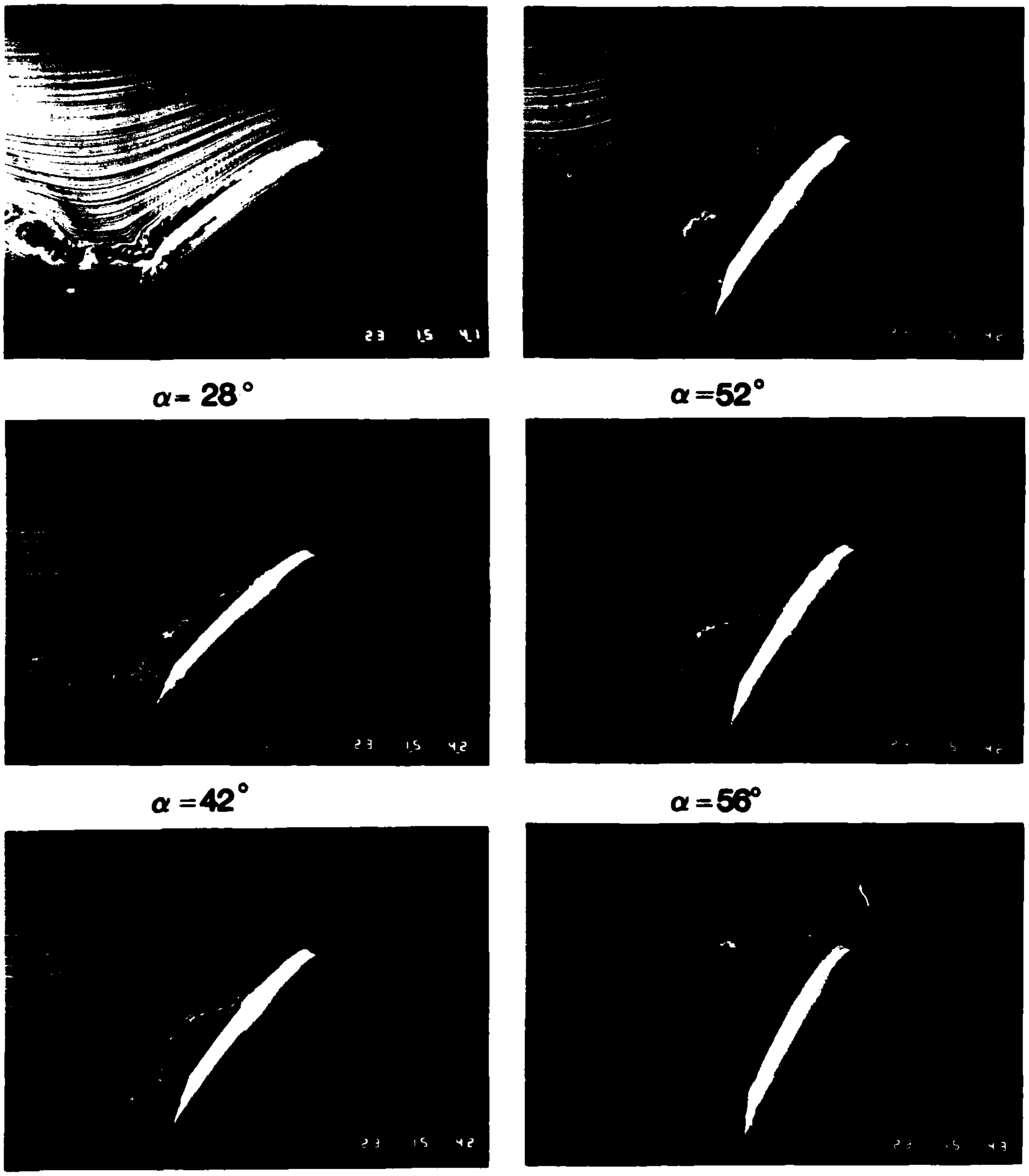

$\alpha = 28°$

$\alpha = 52°$

$\alpha = 42°$

$\alpha = 56°$

$\alpha = 47°$

$\alpha = 60°$

Fig.4 Flow Visualization Data (Re=45,000, $\alpha^{+}=0.6$, constant $\dot{\alpha}$ motion, pitch axis at 25% chord)

3d,e,f, and 5d,e,f show the vortex convecting downstream with the subsequent reduction in reverse flow velocities near the surface. It is interesting to note that since the airfoil is still pitching up, this vortex actually moves slightly forward in a reference frame fixed to airfoil.

For the α^+ value of 0.6, maximum reverse flow velocities on the order of 210% of the freestream velocity are observed. As before, the peak reverse flow velocities occur under the centers of the vortices, and the arrows in Figure 6 note the chordwise locations of the vortex centers. Figure 6a shows what would appear to be a typical surface velocity distribution for flow over an airfoil in which separation is just beginning to occur at the rear of the airfoil. It should be noted, however, that under steady flow conditions this situation would occur at angles of attack of less than 10° whereas in the present case the angle of attack is 28°. Figures 4b and 6b show the development of the two vortices as well as the stagnation or reattachment zone between them. Note that the leading edge vortex builds rather rapidly and initially produces a much higher reverse flow velocity than does the trailing edge vortex. By the time that the airfoil pitches to its maximum angle of 60°, however, the trailing edge vortex produces a reverse flow velocity of the same order as the leading edge vortex.

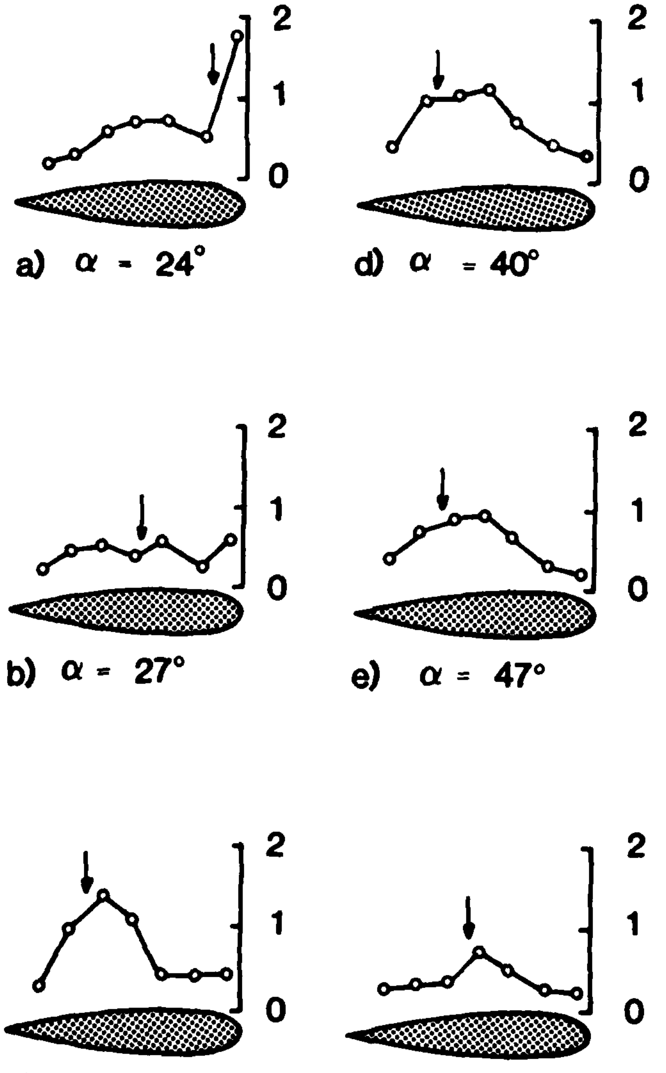

a) α = 24°

d) α = 40°

b) α = 27°

e) α = 47°

c) α - 36°

f) α - 59°

Fig.5 Absolute Velocity Ratio $|u|/u_\infty$ Obtained From Surface Hot-Wires Re=45,000, α^+0.2

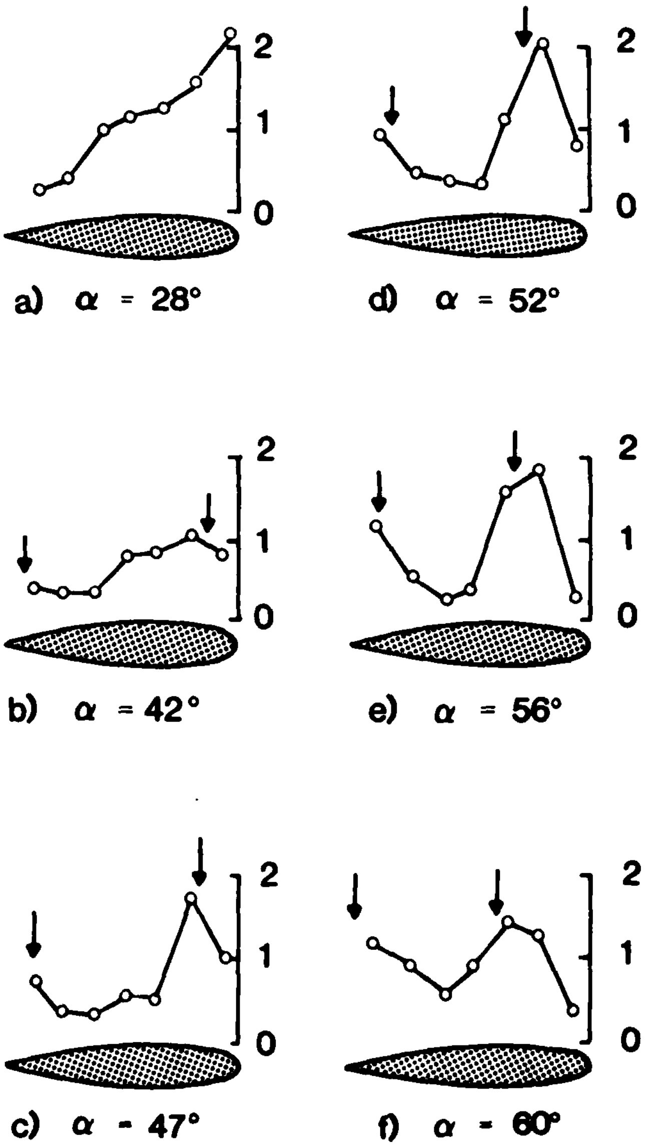

Fig.6 Absolute Velocity Ratio $|u|/u_\infty$ Obtained from Surface Hot-Wires Re=45,000, α^+ 0.6

IV. Conclusions

From the work presented herein, it can be seen that the flow structure is a strong function of the nondimensional pitching rate, α^+. The higher the value of α^+, the higher the angle of attack reached before the beginning of flow separation, the more energetic the suction peak, the more energetic the leading edge vortex, and the higher the reverse flow velocities near the surface of the airfoil. In addition, at the higher α^+ value, significant secondary vortical structures appear. For the two cases presented, $\alpha^+=0.2$ and $\alpha^+=0.6$, large reverse flow velocities on the order of 1 to 2 times the freestream velocity, respectively, near the suction surface of the airfoil, indicate the relative magnitudes of vortical energy present. Maximum reverse flow velocities occur for any given angle of attack directly under the center of the vortex. Other parameters which were not varied in this study, but which may also significantly affect the flow structure, are the pitch axis location (maintained at 25% chord in the present study), Reynolds number, and initial angle of attack.

V. Acknowledgements

The research described in this report was sponsored by the Frank J. Seiler Research Laboratory (AFSC) at the USAF Academy, Colorado Springs, Colorado. Summer faculty support was made available by the Air Force Office of Scientific Research (AFSC) under contract F49620-82-C-0035. The authors would like to gratefully acknowledge the efforts of Mr. Bob Hatfield in instrumenting the hot-wire airfoil model and refurbishing the pitching mechanism, Mr Russ Meinzer and Mr. Wolfgang Bank of the Department of Aerospace Engineering, University of Colorado for fabricating the flow visualization airfoil model and smoke generation system electronics respectively, and Ms. Leah Kelly of

FJSRL/NH for administrative and typing support. The enthusiastic support of Lt. Col. T.T. Saito and his staff, including Captain Vic Villhard for his computer graphics expertise, was vital to the accomplishment of this task.

References

1. McCroskey, W.J., "Recent Developments in Dynamic Stall," Proceedings of a Symposium on Unsteady Aerodynamics, University of Arizona, Vol. 1. pp. 1-33, 1975.

2. McCroskey, W.J. "Some Current Research in Unsteady Fluid Dynamics - The 1976 Freeman Scholar Lectures," J. Fluids Engineering, Vol. 99, pp. 8-38, 1977.

3. Ericson, L.E. and J.P. Reding, "Dynamic Stall Analysis in Light of Recent Numerical and Experimental Results," J. Aircraft, Vol. 13, No. 1, pp. 248-255, 1976.

4. Gormont, R.E., "A Mathematical Model of Unsteady Aerodynamics and Radial Flow for Application to Helicopter Rotors," U.S. Army AMRDL Technical Report 72-67, 1973.

5. Carta, F.O., "Unsteady Normal Force on an Airfoil in a Periodically Stalled Inlet Flow," J. Aircraft, Vol. 4, pp. 416-421, 1967.

6. Johnson, W., "The Effect of Dynamic Stall on the Response and Airloading of Helicopter Rotor Blades," J. Am. Hel. Soc., Vol. 14, pp. 68-79, 1969.

7. Nash, J.G., L.W. Carr, and R.E. Singleton, "Unsteady Turbulent Boundary Layers in Two-Dimensional Incompressible Flow," AIAA Journal, Vol. 13, pp. 167-173, 1975.

8. Dwyer, H.A. and W.J. McCroskey, "Crossflow and Unsteady Boundary Layer Effects on Rotating Blades," AIAA Journal, Vol. 9, pp. 1498-1505, 1971.

9. Telionis, D.P., "Calculations of Time-Dependent Boundary Layers," Unsteady Aerodynamics, R.B. Kinney (Ed.), Vol. 1, p. 155, 1975.

10. Ham, N.D., "Aerodynamic Loading on a Two-Dimensional Airfoil During Dynamic Stall," AIAA Journal, Vol. 6, pp. 1927-1934, 1968.

11. Katz, J., "A Discrete Vortex Method for the Non-Steady Separated Flow Over an Airfoil," J. Fluid Mech., Vol. 102, pp. 315-328, 1981.

12. Strickland, J.H., J.M. Oler, and B.J. Im, "Preliminary Results from the Unsteady Airfoil Model USTAR2," Proceedings of the Workshop on Unsteady Separated Flow, USAF Academy, Aug. 10-11, 1983 (in press).

13. Dvorak, F. and B. Maskew, "Prediction of Dynamic Stall Characteristics Using Advanced Nonlinear Panel Methods," Proceedings of the Workshop on Unsteady Separated Flow, USAF Academy, Aug 10-11, 1983 (in press).

14. Mehta, U., "Dynamic Stall of an Oscillating Airfoil," AGARD Fluid Dynamics Panel Symposium, Ottawa, Paper No. 23, Sept. 1977.

15. Hodge, J.K., A.L. Stone, and T.E. Miller, "Numerical Solution for Airfoils Near Stall in Optimized Boundary-Fitted Curvilinear Coordinates," AIAA Journal, Vol. 17, pp. 458-464, 1979.

16. McCroskey, W.J. and J.J. Philippe, "Unsteady Viscous Flow on Oscillating Airfoils," AIAA Journal, Vol. 13, No. 1, pp. 71-79, Jan. 1975.

17. McAlister, K.W. and L.W. Carr, "Water Tunnel Visualizations of Dynamic Stall," Journal of Fluids Engineering, Vol. 101, pp. 376-380, Sept. 1978.

18. Martin, J.M., R.W. Empey, W.J. McCroskey, and R.X. Caradonna, "An Experimental Analysis of Dynamic Stall on an Oscillating Airfoil," J. Am. Hel. Soc., Vol. 19, No. 1, pp. 26-32, Jan. 1973.

19. Robinson, M.C. and M.W. Luttges, "Unsteady Flow Separation and Attachment Induced by Pitching Airfoils," AIAA Paper 83-0131, Jan. 1983.

20. Herbst, W.B., "Supermaneuverability," Joint Automatic Control Conference, Univ. of VA, June 17-19, 1981; See also Workshop on Unsteady Separated Flow, USAF Academy, Aug. 10-11, 1983, published by the University of Colorado, Dept. of Aero. Engr.

21. Harper, P.W. and R.E. Flanigan, "The Effect of Rate Change of Angle of Attack on the Maximum Lift of a Small Model," NACA TN 2061, 1950.

22. Ham, N.D. and M.S. Garelick, "Dynamic Stall Considerations in Helicopter Rotors," J. Am. Hel. Soc., pp. 40-50, Apr. 1968.

23. Francis, M.S., J.E. Keesee, and J.P. Retelle, "An Investigation of Airfoil Dynamic Stall with Large Amplitude Motion," FJSRL-TR-83-0010, Oct. 1983.

24. Francis, M.S., J.E. Keesee, and J.P. Retelle, "A Two-Degree-of-Freedom Oscillator for Unsteady Aerodynamics Application," FJSRL-TR-81-0007, July 1981.

INTERRELATED EFFECTS OF PITCH RATE AND PIVOT POINT ON AIRFOIL DYNAMIC STALL

Hank E. Helin* and John M. Walker**

Abstract

Experimental investigations were conducted to study energetic dynamic stall vortices and the associated unsteady aerodynamics generated by a pitching NACA 0015 airfoil. The airfoil model was pitched from 0° to 60° at constant rates of 460°/s, 920°/s, and 1380°/s about its quarter-chord, half chord,and three quarter chord positions. Extensive 35mm still photographs and 16mm high-speed movies, both employing smoke wire flow visualization, documented the initiation and development of the time dependent dynamic stall phenomena. In addition, hot-wire anemometry measurements were made which provided for more quantitative analysis of the unsteady separated flowfields. Pitch rate and pivot point were shown to have interrelated effects on the development of the dynamic stall flowfield. In many cases similar "looking" flowfields were generated by different combinations of pitch rate and pivot point. However, significant differences were observed in the near-surface velocity profiles.

I. Introduction

The energetic nature of the unsteady flowfields generated by pitching airfoils has been a topic of study for much of the 20th Century (Ref. 1). The vast number and interaction of variables involved have significantly complicated both theoretical and experimental efforts to understand the fluid mechanics and the development of reliable prediction methods. Most theoretical studies revolve around attempts to relax assumptions postulated in steady thin airfoil theory. In general, the results from these studies have been somewhat restricted and significant progress has been elusive. This is due in part to the lack of broad scope experimental data which are needed to set modeling parameters and as a basis for checking theoretical calculations. The general thrust of

---

*Lt., USAF, Instructor, Dept of Aeronautics, USAF Academy, Co.

**Major, USAF, Aeromechanics Div., FJSRL, USAF Academy, Co.

experimental unsteady aerodynamic research has been to reduce the undesirable effects associated with dynamic stall. Many of the parameters involved have been restricted to model specific areas and types of problems. However, with the more recent realization that the extremely energetic nature of unsteady flows might be exploited and utilized to enhance performance, the scope of research efforts has been expanded significantly (Ref. 2).

Unsteady aerodynamic effects generated by pitching or oscillating airfoils are generally classified under the heading of "Dynamic Stall." Inherent in this phenomenon is the development of a dynamic stall vortex which occurs as the lifting surface dynamically surpasses its static stall angle of attack. Large unsteady aerodynamic forces are generated, from which the lift, drag, and moment coefficients greatly exceed their maximum static counterparts (Ref. 3). The unsteady effects of dynamic stall are dominated by turbulent flow and the production of large scale vortices. The more general methods employed in analyzing dynamic stall involved tests with airfoils driven through moderately large amplitude, slow oscillations in angle of attack. This was consistent with attempts to understand and eliminate the undesirable effects associated with dynamic stall on helicopter rotors. In contrast, recent efforts are now also exploring the possibilities of utilizing the unsteadiness of the flowfield to enhance performance. These studies have examined new parameter combinations including much higher oscillation/pitch rates (Ref. 2). Studies have been performed to analyze the repetitive interaction of the dynamic stall vortices as a means of maintaining flow attachment (and hence, greatly increasing lift) at high angles of attack (Ref. 4). In addition, extensive studies have also been done to correlate this phenomenon as a function of the driving parameters involved, that is, pivot location, airfoil shape, Reynolds number, and mean angle of attack (Ref. 5).

Large, energetic vortical structures have been shown to be an important correlate of oscillating/pitching airfoils, and current research activities have documented their dramatic impact on airfoil lift and drag characteristics (Ref. 6 and 7). In addition, the impetus to exploit the energetic nature of large vortices as a potential to enhance performance has already been demonstrated (Ref. 1). Clearly, before such a realistic utilization is possible, extensive studies must be performed to expand our knowledge concerning fundamental aspects. Questions regarding the direct relationship between the time dependent fluid dynamics and associated airfoil/flowfield interaction, have yet to be answered. Before attempts to utilize these phenomena are made, the flowfield dependence upon the driving parameters of airfoil geometry and dynamics must be fully understood. The present study focuses on only a small part of this problem: the relationships between the pitch rate, pitch axis, and resultant vortex development.

II. Methods

Experiments were conducted using a NACA 0015 airfoil model in the USAF Academy's subsonic wind tunnel. Two experimental techniques were employed: 1) smoke-wire flow visualization using 35mm still and 16mm high-speed movie cameras, and 2) near-surface hot-wires mounted in a staggered array on the airfoil's surface.

The airfoil model was a NACA 0015 extruded aluminum section with a 6" chord and 22" span. The airfoil was pitched from 0° to 60° by a single-degree-of-freedom oscillator employing a DC stepping motor and a computer driven index controller. Airfoil angular position was measured by a linear potentiometer mounted on the oscillator. System performance checks documented cycle to cycle repeatability with a maximum standard deviation of 0.5° over a 25 run ensemble average.

The USAF Academy's subsonic wind tunnel has a 2'x3' test section. All testing was conducted at a freestream velocity of 20 ft/s, which, with the 6" NACA 0015, resulted in an airfoil Reynolds number of 45,000. The turbulence intensity level of the tunnel in this velocity range has been documented at less than 0.1%. The low turbulence level and the low velocity were necessary for high quality detailed flow visualization.

Flow visualization was obtained using a .005" tungsten wire coated with theatrical fog fluid. An electrical current was applied to the wire, which produced a set of fine streaklines across the test section. These streaklines were photographed using a high intensity arc-lamp strobe light, with a flash duration of 7 μs, coupled with a 35mm camera and a 16mm high-speed movie camera. The 35mm photographs are phase-locked single exposures on 400 ASA TRI-X film developed at 1200 ASA. Only one photograph could be taken during a pitch motion, a procedure which required multiple motion sequences with each successive photograph at an incremented angle of attack. The 16mm high-speed camera system, however, allowed multiple photographs over one motion cycle, which provided for detailed studies of the flowfield evolution as a function of time. The entire oscillator/smoke-wire/flash/camera system was controlled and synchronized using a PDP 11/45 and PDP 11/03 computer system.

Near surface velocity measurements were made using seven hot-wires mounted on the upper (suction) surface of the airfoil. The hot-wire sensing elements (TSI-10 Hotfilms) were fixed at .2" above the surface and equally spaced at .8" increments. The sensor positions were:.4", 1.2", 2.0", 2.8", 3.6", 4.4", and 5.2" on the 6" chord airfoil. Velocity signals were obtained using a TSI 1050 anemometer system coupled with the Laboratory Peripheral System package of the PDP 11/45 computer. The velocities at the various sensor locations, with the airfoil at 0° angle of attack, were compared with a freestream hot-wire to obtain normalizing coefficients. The measured velocities over the airfoil surface were in turn normalized to a percent of freestream, for analysis. The sampling rate varied with the pitch rate employed but was always above 1 KHz.

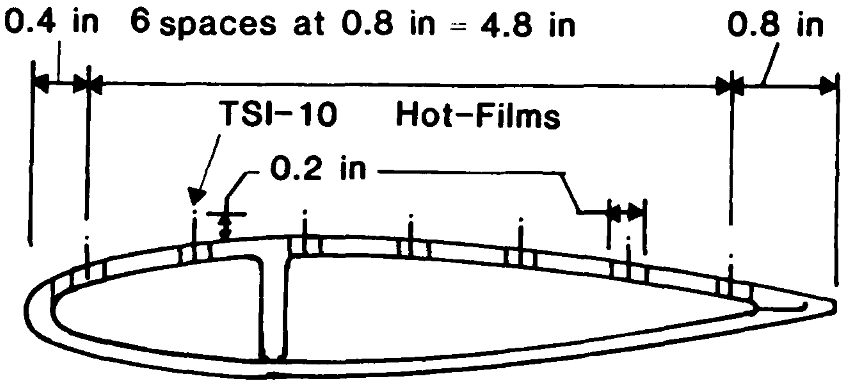

Fig.1 Surface Hot-Wire Configuration

III. Results

A well known effect of oscillating or pitching an airfoil is that the static stall angle can be exceeded by some amount before dynamic stall occurs. Dynamic stall is preceded by the separation of flow near the trailing edge. This forms a separated region over the airfoil which grows rapidly as its initiation point moves up from the trailing edge toward the leading edge. The initiation, development, and even the strength of the dynamic stall vortex, have been shown to be a complex function of the driving parameters. This function is far from being fully understood. Rather than complicate the scheme further by using periodic motions, which set up a hysteresis loop, constant pitch motions from 0° up to an angle of attack of 60° were employed. Once the maximum angle was reached, the airfoil was stopped, allowing the unsteady flowfields to develop freely.

A steady state study of static stall conditions for the NACA 0015 airfoil was conducted. As the airfoil's angle of attack was slowly incremented toward the static stall angle under steady flow conditions, a trailing edge separation zone formed and moved up the suction surface of the airfoil until, at an angle of attack of 12°, flow was separated over fifty percent of the airfoil chord. This was readily determined by smoke flow visualization. This steady flow stall criterion will be used to compare the delay in onset of dynamic stall with regard to angle of attack and the initiation of the dynamic stall vortex. Qualitative analyses of flow visualization are based upon the initiation of the dynamic stall vortex, its temporal position with respect to the airfoil angle of attack -- which is dependent on the pitch rate employed -- and its spatial position with respect to the airfoil chord. These analyses are compared and correlated with the near surface velocities measured with the hot-wires.

Table 1 shows the combination of pitch rates and pitch axes that were employed. These combinations of driving variables allowed for analyses of the initiation and development of unsteady dynamic stall flowfields based upon chord angular displacement with respect to time, airfoil leading edge angular velocities, and the interrelated effects of chord and leading edge angular velocities.

	PITCH RATE		
	460°/s	920°/s	1380°/s
0.25c	X	X	X
0.5c		X	
0.75c		X	

Table 1. Pitch Rates and Pitch Axes

A. Increased Pitch Rate, Fixed Pitch Axis

With the pitch axis fixed at 0.25 c, the dramatic effects of increased pitch rate are visually documented in Figure 2. As the pitch rate was increased from 460°/s to 920°/s, and finally to 1380°/s, the initiation of the dynamic stall vortex was delayed to higher angles of attack. This delay is not a linear function of the pitch rate. The effects of an increment in pitch rate are more prominent at lower rates than at higher rates. At a pitch rate of 460°/s, the dynamic stall vortex began to form around $\alpha = 22°$. At double the pitch rate, 920°/s, it began forming at $\alpha = 31°$. However, an increase to 1380°/s only pushed the dynamic stall vortex initiation to $\alpha = 34°$. Another dominant feature is the spatial position of the vortex with respect to the airfoil. At the lower pitch rates the vortex formed much earlier in the pitch cycle and moved rapidly downstream. As the pitch rate increased, the dwell time, that is, the time that the vortex remained close to and over the airfoil, also increased. In all cases, the dynamic stall vortex remained energetic and continued to rotate until well downstream of the airfoil. This is not readily discernible from still photographs taken over multiple cycles but was clearly evident in the high-speed 16mm movies taken over a single cycle.

a) 30°, 460°/s b) 45°, 460°/s

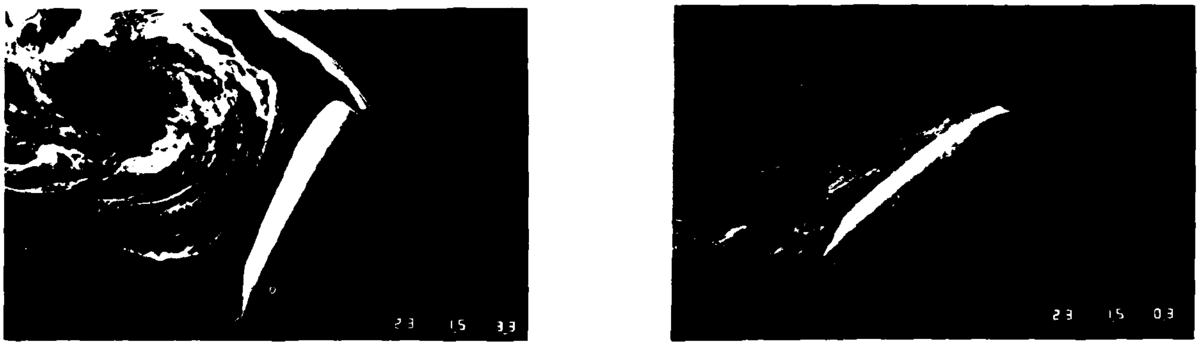

c) 60°, 460°/s d) 30°, 920°/s

e) 45°, 920°/s f) 60°, 920°/s

Fig.2 Pitch Rates of 460°/s, 920°/s, and 1380°/s with Pictures at 30°, 45°, and 60° for Each Rate. Pitch Axis Constant at 0.25c.

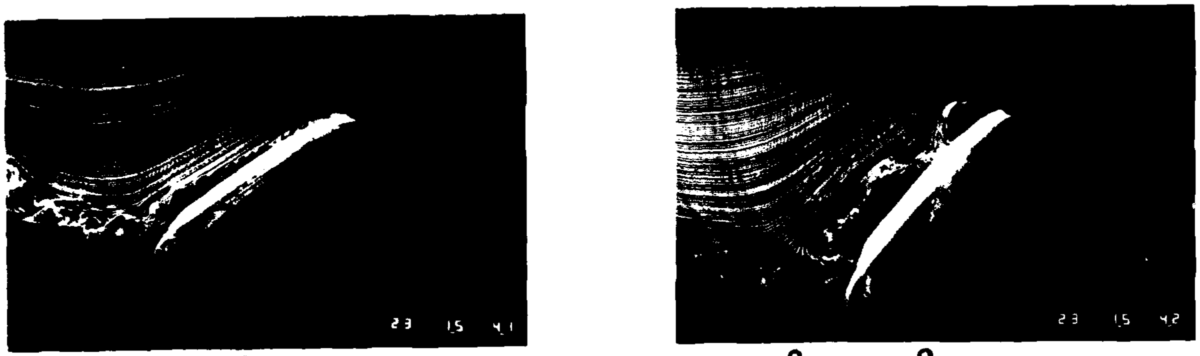

g) 30°, 1380°/s

h) 45°, 1380°/s

i) 60°, 1380°/s

Fig.2 continued

The 16mm movies taken at 500 frames per second visualized the dramatic differences between streaklines and streamlines for a time dependent flowfield. Many of the contorted streaklines developed early as the vortex was forming, and then were carried along as historical patterns. However, the energetic rotation of the vortex was easily seen from frame to frame and the streaklines are indicative of the vortex position and temporal development. In addition, the movies document the direction of the flow at different points in the flowfield. This was very useful in determining rotational directions and reverse flow areas over the surface.

When the movies are compared to the still photographs and hot-wire data, with respect to angle of attack, a quantitative analysis of the flowfield and vortex development is easily made. Since the hot-wire sensors are close to the surface, they indicate the magnitude of the flow which is essentially parallel to the surface. And when correlated with the flow visualization, the direction of the flow along the surface is readily discernible much of the time. Peaks in the profiles match with the spatial positions, as observed in the flow visualization of the vortex centers over the airfoil. Figure 3 shows the velocities in percent freestream at the first sensor location for the three different pitch rates. Peaks in the velocity profiles at the first sensor agree with the vortex initiation angles documented in the flow visualization. Interestingly, up to the point of vortex initiation, the slope of the velocity profiles, as a function of the angle of attack, is relatively independent of the pitch rate. Of further interest, the maximum velocity of the first sensor was also independent of the pitch rate as evidenced by the near equal magnitudes of the peaks in Figure 3. However, the relative magnitudes of the velocities at stations further aft are different for changes in pitch rate.

Correlation of peaks in the velocity profiles with observed vortex positions from the flow visualizations showed that the maximum velocities increase as the pitch rate was increased. An example of this is in Figure 4, which shows the magnitude of the velocity at sensor number 2 on the suction surface of the airfoil for two different pitch rates. These higher velocities and the fact that the flow visualization also showed more cohesive appearing vortices as the pitch rate was increased, are a direct inference that vortex strength increases as a function of increasing pitch rate. This readily suggests that the increased dwell time at the higher pitch rates is directly coupled to the increased energetic and cohesive nature of the dynamic stall vortices at the higher pitch rates.

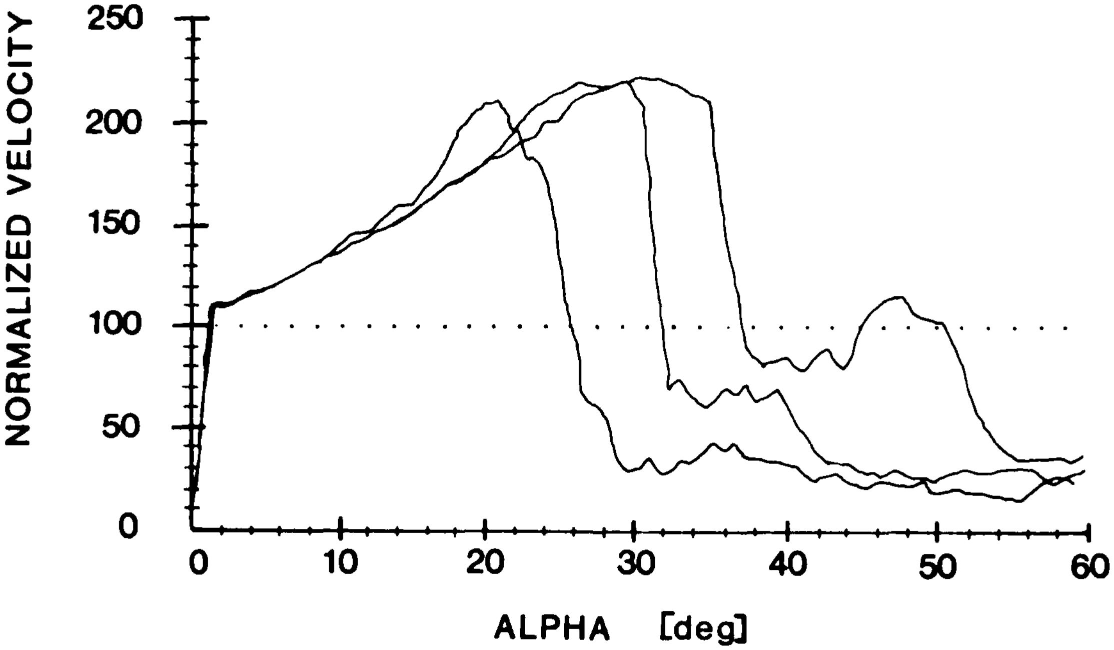

Fig.3 Magnitude of the Velocities at Sensor Number One, in Percent Freestream, for Pitch Rates of 460°/s, 920°/s and 1380°/s. Pitch Axis is 0.25c.

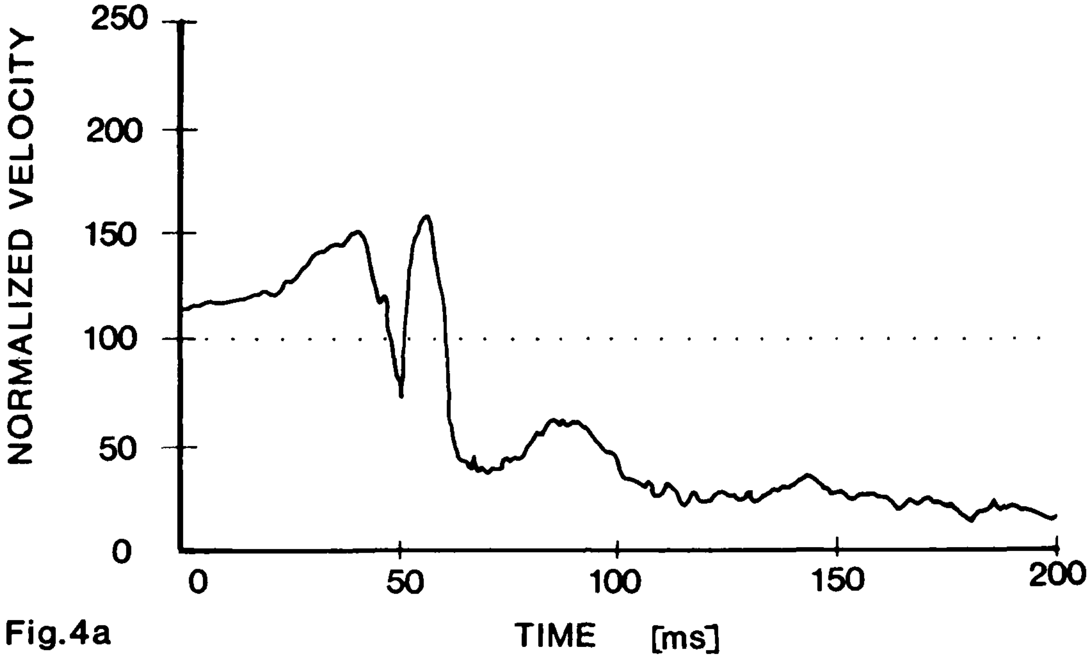

Fig.4a

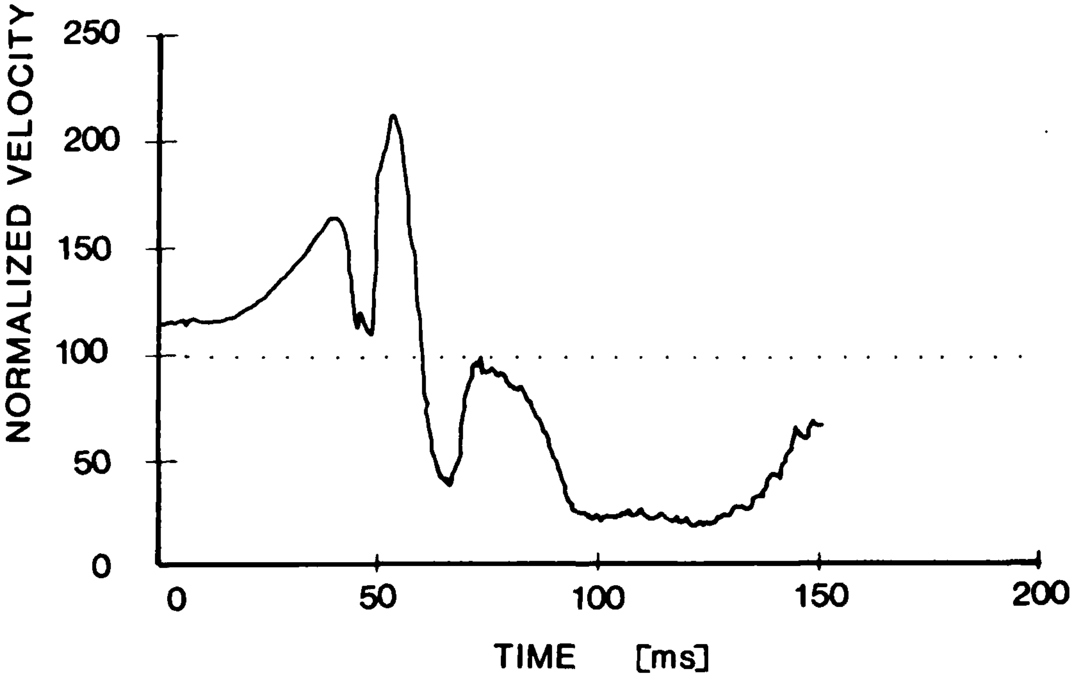

Fig.4b Magnitude of the Velocities over the Airfoil Surface, in Percent Freestream, at Sensor Number Two. Pitch Axis is .25c. Pitch Rate is a) 920°/s, b) 1380°/s.

B. Increased Pitch Axis, Pitch Rate Constant

As shown by the flow visualization photographs in Figure 5, the effects of moving the pitch axis further along the chord are similar to those discovered for increasing pitch rate. As the distance from the leading edge was increased from 0.25 c to 0.5 c and finally 0.75 c, the onset of dynamic stall was again delayed. Once the leading edge vortex was generated, its evolution and growth characteristics during the remaining portion of the pitch cycle, and with time, appeared constant.

Although the initiation of the dynamic stall vortex was delayed to very high angles of attack, the subsequent rapid development and movement of the vortex over the airfoil was very similar, with no appreciable increase in dwell time regardless of the pitch axis location. This is in contrast to the coupled effect of delayed initiation and increased dwell time as pitch rate was increased. In addition, there is not a perceivable increase in coherent appearance with increased pitch axis distance as there was with increased pitch rate (Figures 2 and 5). Again, the high-speed 16mm movie documented the energetic nature of the dynamic stall flowfield, showing continued growth and significant rotation throughout the time the vortex was in the vicinity of the airfoil.

Dynamic stall at the first hot wire sensor, evidenced by a sharp decrease in the magnitudes of the velocities shown in Figure 6, occurs at 30°, 36°, and 42° for pitch axies of 0.25 c, 0.5 c and 0.75 c, respectively. This represents a relatively linear increase in stall delay as a function of increased pitch axis distance. Figure 6 is also illustrative of significant differences in the velocity magnitude profiles at the first sensor location. There is a definite decrease in the slope with respect to the angle of attack as the pitch axis distance from the leading edge was increased. Also, the peak velocity at the first sensor decreased as pitch axis was increased -- more so from 0.25 c to 0.5 c than from 0.5 c to 0.75 c. These two phenomena are completely different from observations at increasing pitch rate (Figure 3).

As mentioned in the flow visualization discussion, the development of the stall flowfield appears quite similar, except for an increase in the dynamic stall angle, regardless of the pitch axis employed. The remarkable similarities in the velocity profiles as a function of time, at sensor number three, are shown in Figure 7 for the three pitch axes. As pitch axis distance was increased, the initial slopes decreased slightly (noted before at sensor number one), the maximum magnitude of the peaks decreased slightly, and dynamic stall was delayed. However, the general shapes of the profiles are overwhelmingly similar and are merely shifted an increment of time as the pitch axis is moved aft.

a) 30°, .25c

b) 45°, .25c

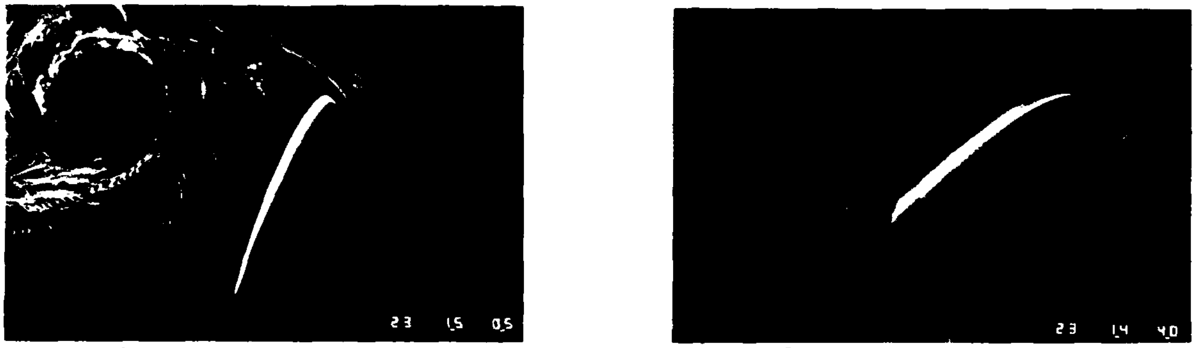

c) 60°, .25c

d) 30°, .5c

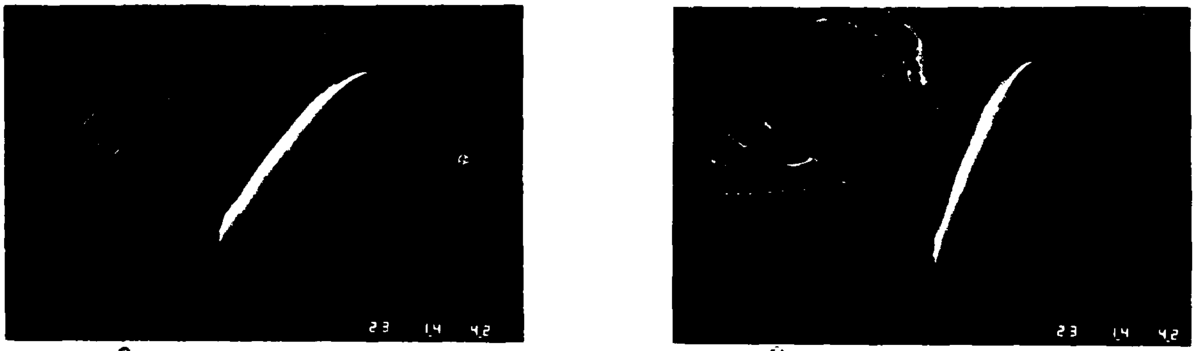

e) 45°, .5c

f) 60°, .5c

Fig.5 Pitch Axes of 0.25 c, a 0.5 c and 0.75 c with Pictures at 30°, 45° and 60° for each axes. Pitch Rate Constant at 920°/s.

g) 30°, .75c

h) 45°, .75c

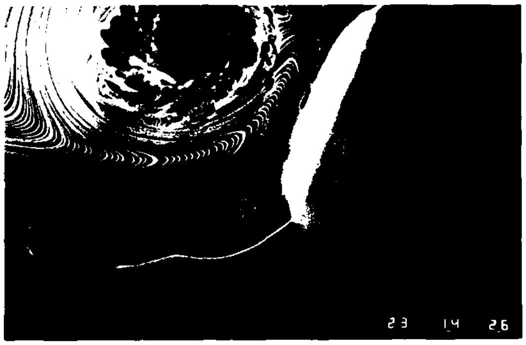

i) 60°, .75c

Fig.5 continued

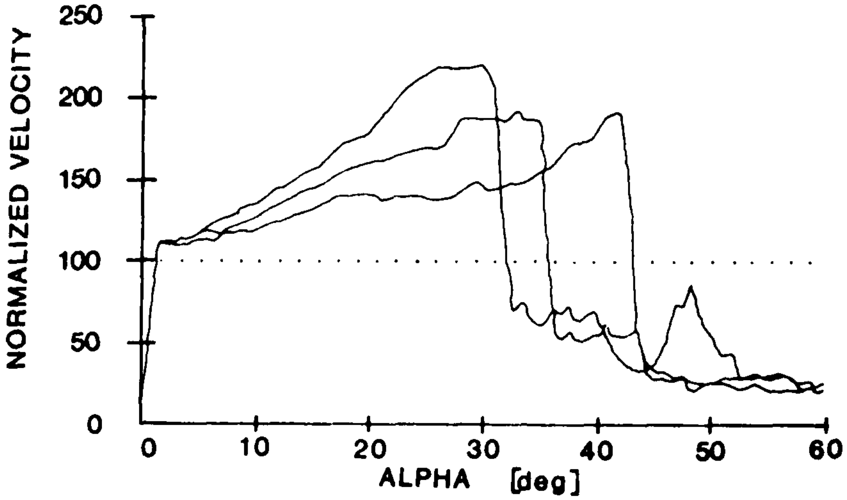

Fig.6 Magnitude of the Velocities at Sensor Number One, in Percent Freestream, for Pivot Axes of 0.25 c, 0.5 c and 0.75 c Pitch Rate is 920°/s.

IV. Discussion

Studies of an airfoil pitched from 0° to 60° angle of attack at various pitch rates about different pitch axes have shown the development of a complex interactive flowfield. The most prevalent feature was the formation of an energetic dynamic stall vortex which was both spatially and temporally dependent on the driving parameters. The dynamic stall phenomenon was extremely reproducible. In light of this reproducible nature, single shot photographs, rather than motion cycles, and ensemble averaged hotwire profiles were used to quantify flowfield development. In addition, high speed movies documented the energetic rotation and travel of the dynamic stall vortex as it developed. The presence of the dynamic stall vortex was observed to have significant effect on the velocity distribution over the airfoil surface at angles of attack well beyond the normal static stall.

As the dynamics of the airfoil motion were changed, the following impacts on the dynamic stall process were observed:

1) Pitch Rate

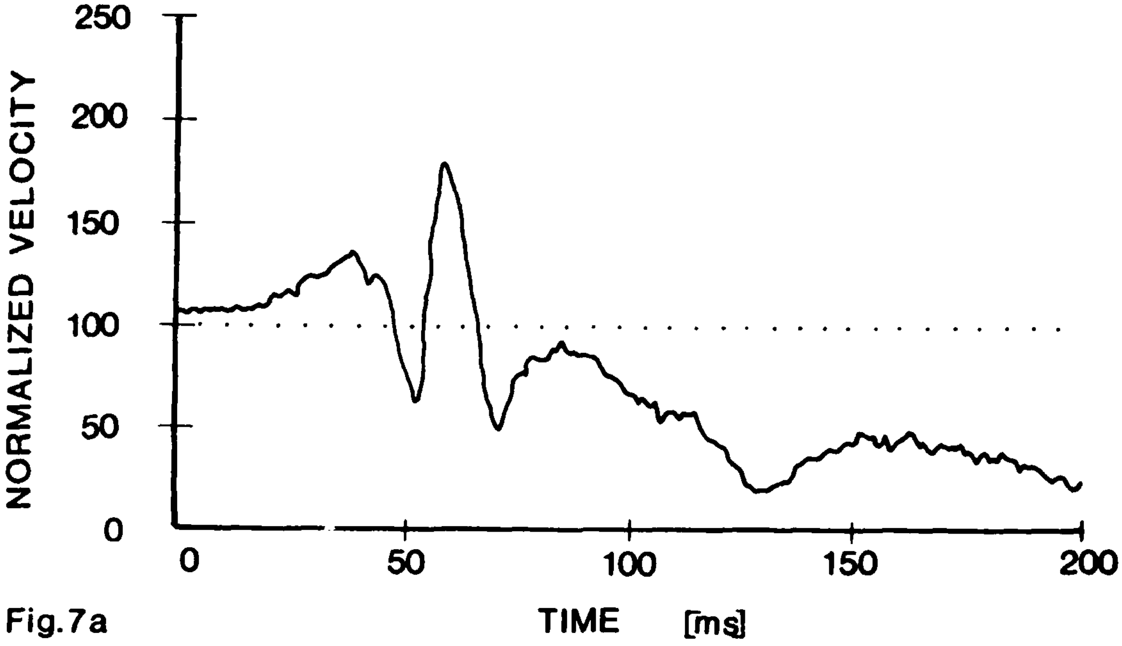
NORMALIZED VELOCITY
250
200
150
100
50
0
0
50
100
150
200
TIME [ms]

Fig.7a

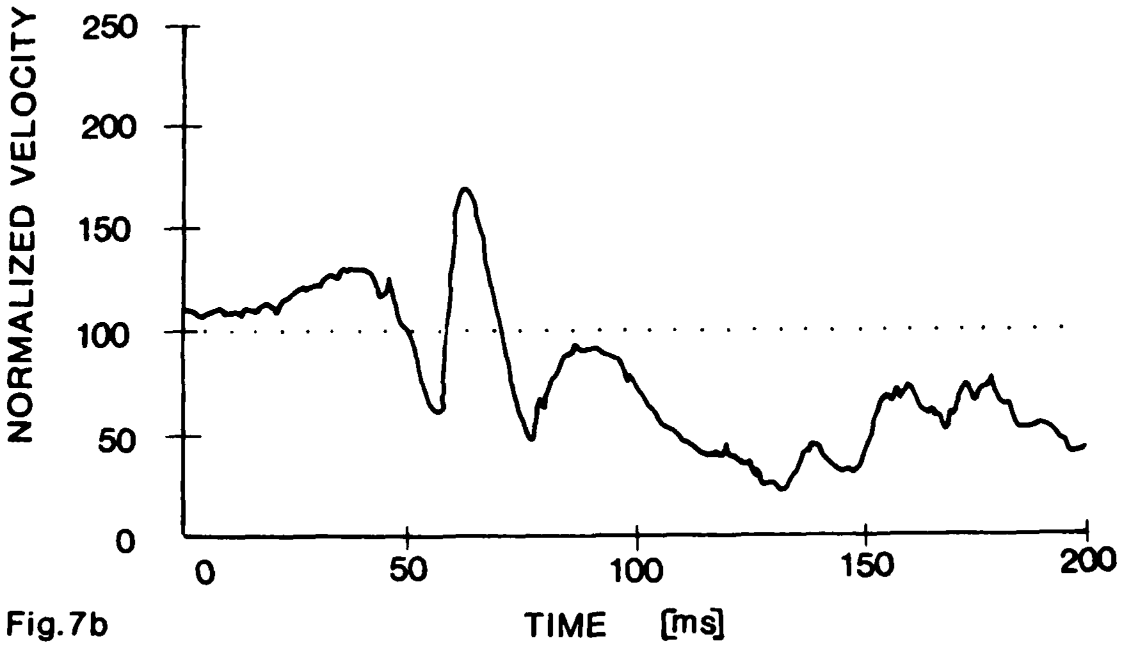
NORMALIZED VELOCITY
250
200
150
100
50
0
0
50
100
150
200
TIME [ms]

Fig.7b

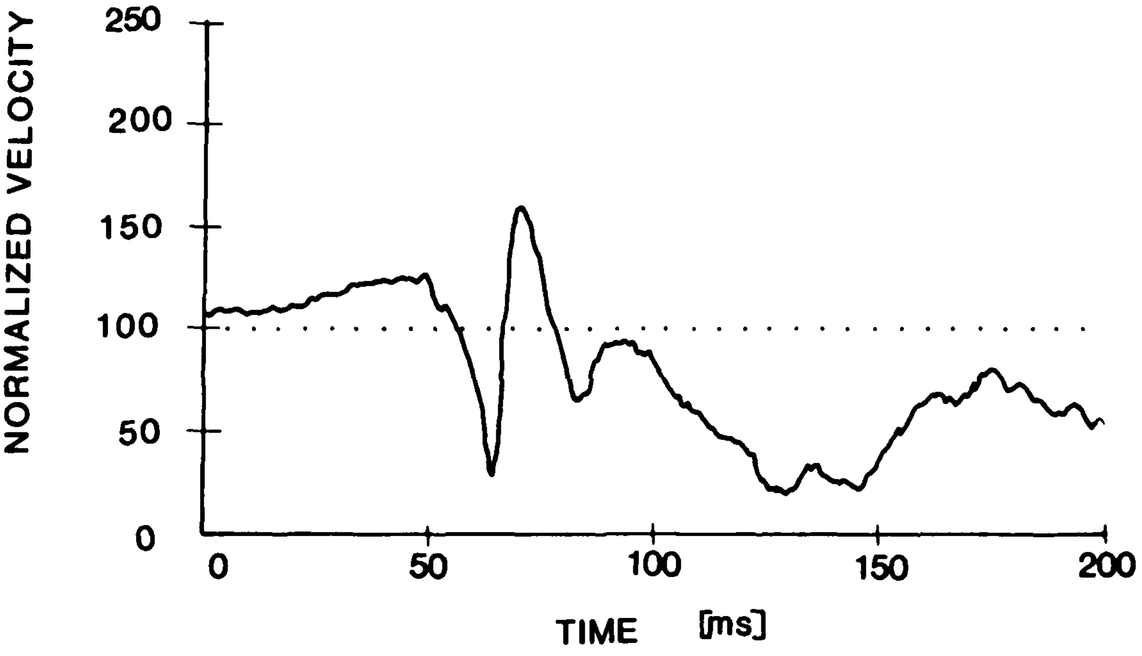

Fig.7c Magnitude of the Velocities over the airfoil surface, in Percent Freestream, at Sensor Number Three. Pitch Rate is 920°/s. Pitch Axis is a) 0.25c, b) 0.5c, c) .75c.

It is clearly evident that as the pitch rate is increased, the angle of attack at which dynamic stall occurs is also increased. This effect is nonlinear and more prevalent at increments in low pitch rates than at the higher rates. In fact, although using a different range of parameters, Gormont suggests that the angle of attack at which dynamic stall occurs varies with the square root of the pitch rate (Ref 8). In addition, the slope of the velocity profile with respect to angle of attack, close to the surface and near the leading edge, does not change as the pitch rate is increased. Also, the corresponding peak velocities near the leading edge change very little. There are direct indications that increased pitch rates form more coherent and energetic dynamic stall vortices. As the vortices become more energetic, (as was shown by increased velocity magnitudes in the profiles aft of the leading edge), they remain over the airfoil for a longer period of time. This would dramatically influence the time averaged aerodynamic forces on the airfoil at high angles of attack.

2) Pitch Axis

Moving the pitch axis toward the trailing edge emulates some of the effects of an increased pitch rate. Dynamic stall occurs at correspondingly higher angles of attack, and the large dynamic stall vortex again has significant impact on the velocities over the airfoil surface. However, differences do exist in the velocity profiles and vortex dynamics from those noted for an increased pitch rate. The slope of the velocity magnitude profiles at the first sensor changed substantially; the velocity increased at a slower rate and did not reach as high a peak when the pitch axis was moved toward the trailing edge. Also, the dynamic stall vortex, once initiated, evolved rapidly and moved quickly downstream regardless of the pitch axis. Substantial similarities were seen in the velocity magnitude profiles of the mid-chord region for the various pitch axis locations. The profiles had the same relative peaks and magnitudes with the only difference being a slight temporal increment as the pitch axis was moved aft.

These observed phenomena show the dramatic effects of pitch rate and pitch axis on the dynamic stall process. Clearly, more quantitative aerodynamic measurements are needed to precisely select an optimal parameter combination to enhance performace. Experimental studies to quantify these and other effects are underway using more extensive hot-wire techniques and minature surface mounted pressure transducers.

References

1. McCroskey, W.J., "Unsteady Airfoils," Annual Review of Fluid Mechanics, 1982, pp. 285-311.

2. Robinson, M.C. and M.W. Luttges, "Unsteady Separated Flow: Forced and Common Vorticity About Oscillating Airfoils," Workshop on Unsteady Separated Flows, 10-11 Aug. 1983, U.S. Air Force Academy. Proceedings pp. 117-126.

3. Carr, L.W., K.W. McAlister, and W.J. McCroskey, "Analysis of the Development of Dynamic Stall Based on Oscillating Airfoil Experiments," NASA TN D-8382, Jan. 1977.

4. Robinson, M.C. and M.W. Luttges, "Vortex Generation Induced by Oscillating Airfoils: Maximizing Flow Attachment," 8th Biennial Symposium on Turbulence, Rolla, MO. 26-28 Sept. 1983, pp. 13.1-13.10.

5. Robinson, M.C. and M.W. Luttges, "Unsteady Flow Separation and Reattachment Induced by Pitching Airfoils," AIAA Paper No. 83-0131, Jan. 1983, pp. 1-14.

6. McCroskey, W.J., et. al., "Dynamic Stall Experiments on Oscillating

Airfoils," AIAA Paper No. 75-125, Jan. 1975.

7. Martin, J.M., R.W. Empey, W.J. McCroskey and F.X. Cardonna, "Experimental Analysis of Dynamic Stall on an Oscillating Airfoil," Journal of the American Helicopter Society, Vo. 19, No. 1, Jan. 1973, pp. 26-32.

8. Gormont, R.E., "A Mathematical Model of Unsteady Aerodynamics and Radial Flow for Application to Helicopter Roters," U.S. Army AVRDL Technical Report 72-67, 1973.

SECTION III.

Fluid Dynamics

AN EXAMINATION OF CURVE SMOOTHING USING DIGITAL FILTER THEORY

Paul I. King,* and Martin L.G. Oldfield**

Abstract

The theory of digital filters is used to explain the effect of applying a smoothing function to data which contains unwanted frequency components. The smoothing of a curve is viewed as the convolution of the raw data with the impulse response values of a finite impulse response, non-recursive filter. By the convolution theorem the frequency response of the smoothed curve is then the product of the response of the raw data and the frequency response of the filter. Two filter impulse responses are examined, the windowed moving average and the moving least square polynomial. The windowed moving average is easy to use and for the same number of smoothing coefficients produces a qualitatively smoother curve. For studying transient peak data the least square polynomial is the best choice.

I. Introduction

In recent years the development of high speed analog-to-digital (A/D) recording devices has solved the problem of sampling and storing certain measurements of physical phenomena at appropriate rates for detailed postmortem analysis. At the same time the evolution of fast Fourier transform algorithms along with the development of digital filter theory has given engineers and scientists powerful mathematical and computational tools for the analysis of complex waveforms inherent in the recorded data.

It is not uncommon nowadays to acquire a large amount of data in a short period of time such as is shown in Figure 1. This figure shows the results of pressure measurements made in a turbulent boundary layer. The turbulent fluctuations represent a numerically noisy signal and it is difficult to extract meaningful information from this raw

---

*Major, USAF, Assistant Professor of Aeronautics, DFAN

**Lecturer, Oxford University, England

data. A common technique is to numerically smooth the data so that qualitative analysis is facilitated and numerical differentiation is made possible. What follows is an examination of smoothing viewed as a process of filtering raw data -- that is, a process in which one retains (passes) relevant data and discards (attenuates) spurious or irrelevant data.

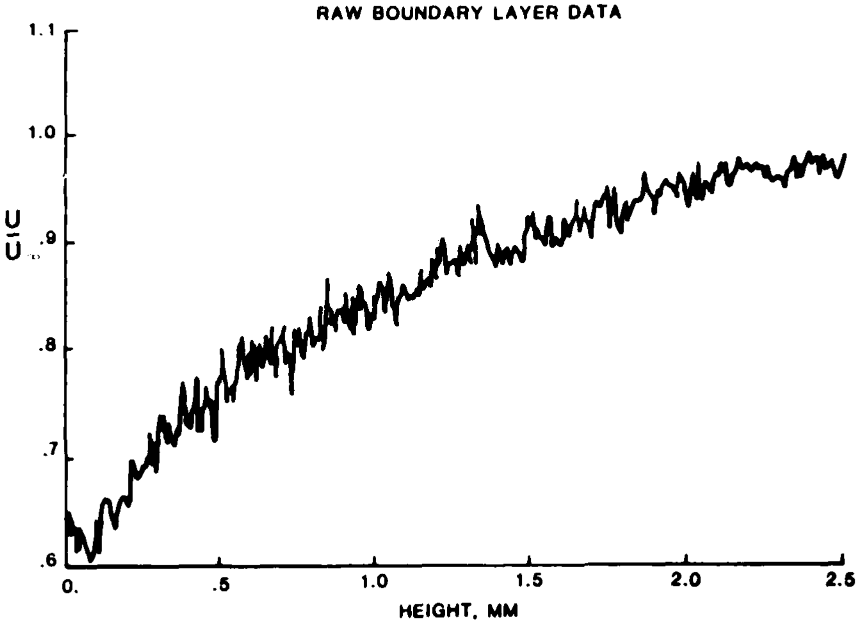

Figure 1. Raw Data from High Speed Data Acquisition

The filtering (smoothing) of data after the experiment holds many advantages including affording one the time to examine data away from the hectic environment of the experiment itself. More importantly one can structure the filter network (smoothing function) so as to avoid the problems intrinsic to real-time analog filtering. The ability to look ahead in time allows the digital filter to avoid the time delay and phase shift common to analog filters.

This paper discusses the considerations important to the selection of a smoothing function for a particular application. In doing so the frequency response of the function must be considered and thus some familiarization with transform analysis and convolution must be gained. In particular two filter functions are examined: the simple running average and the running least square polynimial fit.

II. The Smoothing Function Viewed as a Filter

In the following analyses, the data are assumed to be a function of a single variable, such as amplitude vs time or amplitude vs distance. For discussion purposes it is assumed that amplitude is the ordinate value, and time or distance is the value on the abscissa axis. The discussion on frequency analysis is applicable to any function of a single variable.

One can view the unsmoothed data as a synthesized signal composed of oscillating waves of varying amplitude and phase, superimposed on a time varying mean signal whose form and magnitude is to be determined. The synthesized signal is sampled in uniform time or spacial increments. The samples form a sequence x(nT) or simply x(n) where

$$x(n) = x(t)\Big|_{t=nT} \qquad -\infty<n<\infty \tag{1}$$

and T is the sampling interval (Ref. 1.).

The problem in curve smoothing is finding an appropriate filter to act on the sampled data after the fact and produce a result having the desired frequency characteristics. The features of this problem are shown in block diagram form in Figure 2. Here one assumes linearity as well as a correspondence between the input and output signals. This correspondence is defined by the convolution (smoothing formula),

$$y(n) = \sum_{m=-\infty}^{m=\infty} x(n-m)C_m \tag{2}$$

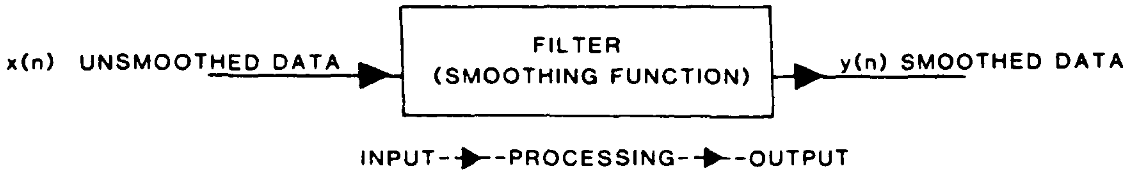

Figure 2. The Smoothing Function Viewed as a Filter

The value y(n) is the smoothed value formed by the convolution of the unsmoothed values, x(n-m), with the convolution variables C_m. These variables, C_m, are explained in the theory of digital filtering as the impulse response of a linear finite impulse response (FIR) filter (Ref. 1).

The convolution summation shown above produces a moving weighted average of the input data. One example of such a moving weighted average is the set of convolution variables C_m = constant = 1/N, where N represents the length of the convolution interval. This is a finite convolution formed by a truncated smoothing formula composed of N terms, N usually being an odd integer. The weighted value y(n) replaces the original data value x(n). The smoothed values are

$$y(n) = 1/N \sum_{m=-\frac{(n-1)}{2}}^{m=\frac{(n-1)}{2}} x(n-m) \qquad (3)$$

This is the simple running average of which more will be said later.

As shown in Equation 3, y(n) depends only on values of the input samples. This type of correspondence defines the coefficients of what is commonly called a non-recursive FIR filter.

As with any filtering process, analog or digital, the characteristics of the filter must be analyzed. All filters will distort and/or remove information from the input signal. It is convenient to think of the filter's action on the data as involving a transfer function in the sense that information is processed in order to produce an output. The filter coefficients, C_m, are the coefficients of the transfer function and are thereby related to the response of the filter.

III. The Fourier Transform and Convolution

To examine the response of the filter, it is necessary to review certain characteristics of discrete data as observed in the time (real)domain and the frequency domain -- the transformed time domain. The two regions are mapped by the Fourier transform. A continuous time based signal, h(t), is transformed to the frequency domain with amplitude H(f) via this Fourier transform,

$$H(f) = \int_{\infty}^{\infty} h(t)e^{-j2\pi ft}\,dt \qquad (4)$$

H(f) is the frequency response of the signal h(t) and is generally a complex value, indicating that both amplitude and phase must be determined for any frequency. If the continuous signal is sampled N times with sampling interval T, the tranform has discrete values computed as (Ref. 3),

$$H(n/NT) = \sum_{K=0}^{N-1} h(kT)e^{-j2\pi nk/N} \qquad (5)$$

A shorthand notation for this mapping process is

$$h(kT) <> H(n/NT) \tag{6}$$

The Fourier transform is used to study the effects of a smoothing function in conjunction with a powerful analytical tool, the convolution theorem.

Convolution of two continous signals, x(t) and h(t), is defined as

$$y(t) = \int_{-\infty}^{\infty} x(\tau)h(t-\tau)d\tau \tag{7}$$

where y(t) is the result of summing the product of signal $x(\tau)$ with the lagged signal $h(t-\tau)$. This is written in notational form

$$y(t) = x(t) * h(t) \tag{8}$$

The convolution integral is best understood in a graphical sense. The signal h(t) is folded, or rotated, about the ordinate axis and displaced an amount t. The overlap region of $x(\tau)$ and $h(t-\tau)$ is then multiplied point for point and the products summed to yield y(t). Recall that this is similar to the process used to obtain the smoothed values y(n) in Equation 2.

If one is processing data acquired in discrete form, the convolution integral (summation) for period N is written

$$y(kt) = \sum_{i=0}^{N-1} x(iT)h((k-i)T) \tag{9}$$

or in notational form,

$$y(kt) = x(kt) * h(kt) \tag{10}$$

A mathematical relationship, the convolution theorem, relates the Fourier transform and the convolution integral. In notational form this is written

$$X(t) * h(t) <> X(f)H(f) \tag{11}$$

IV. The Smoothing Function's Relationship to Frequency Response

As suggested by Equation 11, the Fourier transform of the convolution product is the product of the individual transforms. Thus convolution in the time domain is mathematically equivalent to multiplication in the frequency domain. This can be related to the filtering process.

Filtering is usually represented in the frequency domain as the product of the signal response with the filter response as shown in Figure 3. From the convolution thereom, this is equivalent in the time domain to convolution of the signal with the inverse transform of the filter frequency response. When a filter is subjected to an impulse input, the Fourier transform of its time response to the impulse is the filter's frequency response. Therefore, the inverse transform just referred to is called the filter impulse response. It is evident that the smoothing process can be analyzed by examining either the smoothing function time characteristics, or its frequency response in the transformed domain. Furthermore, if one can specify the desired frequency response of the filter, one can, in theory, invert the response to obtain the time domain values, C_m. These ideas form the basis of digital filtering theory.

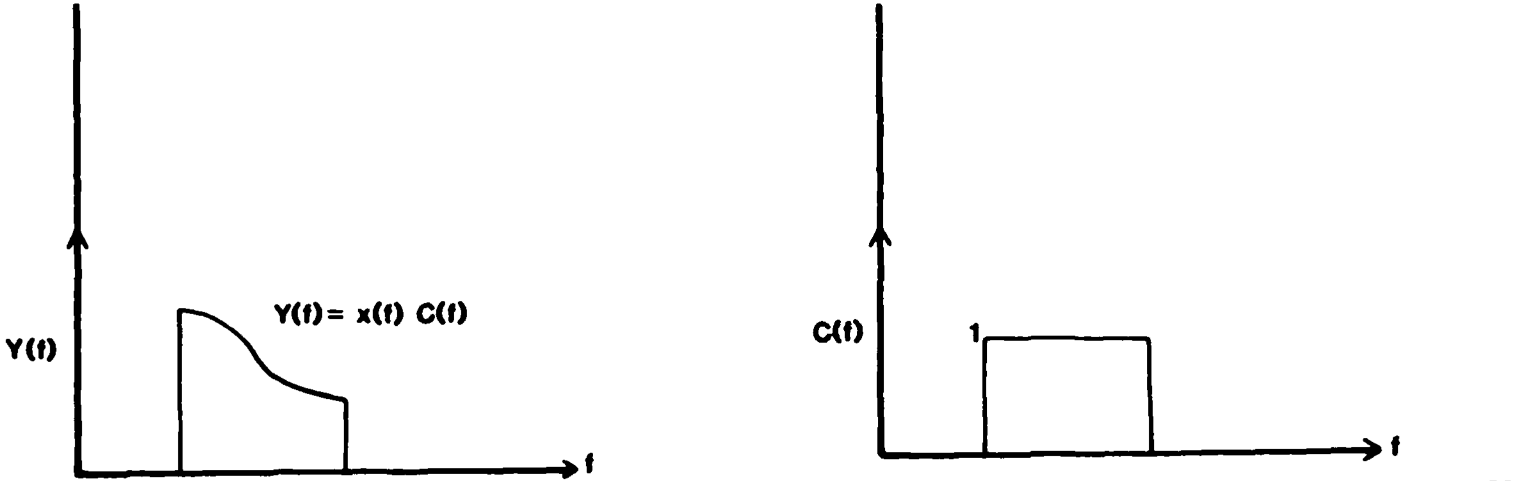

A. FOURIER TRANSFORM OF FILTERED SIGNAL

B. FOURIER TRANSFORM OF IDEAL BANDPASS FILTER

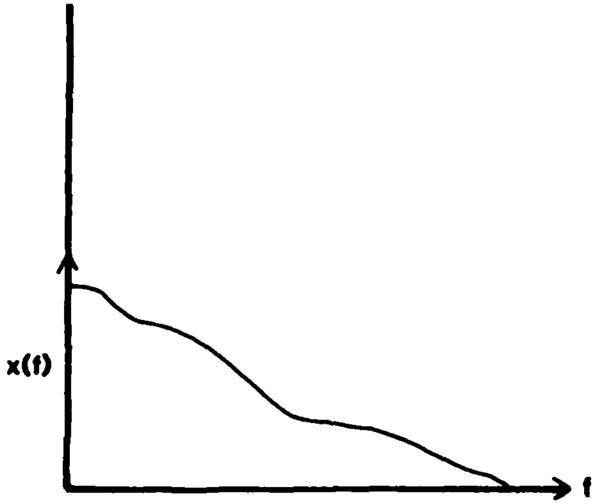

C. FOURIER TRANSFORM OF RAW SIGNAL

Figure 3. Analog Filtering as Viewed in the Frequency Domain

Stearns (Ref. 4) shows that the frequency response of a numerical smoothing function is the discrete Fourier transform of some function C(t) which has been sampled and stored as C(mT) or simply C_m. He demonstrates that the convolution variables, C_m, as shown earlier (Equation 2) do indeed represent the impulse response of the filter. Substituting these values for h(kT) in Equation 5, the discrete frequency response is

$$C(n/NT) = \sum_{m=0}^{N-1} C_m e^{-j2\pi nm/T} \qquad (12)$$

Conversely, if the frequency characteristics, C(n/NT), are known or specified, then one obtains the filter synthesis formula (Ref. 3).

$$C = 1/N \sum_{n=0}^{N-1} C(n/NT) e^{j2\pi nm/T} \qquad (13)$$

V. Choosing an Appropriate Filter Function

At this point, it is instructive to examine the frequency response of some candidate smoothing functions. Figures 4a and 5a represent the impulse responses of two common filters, the moving average, and ideal filter respectively.

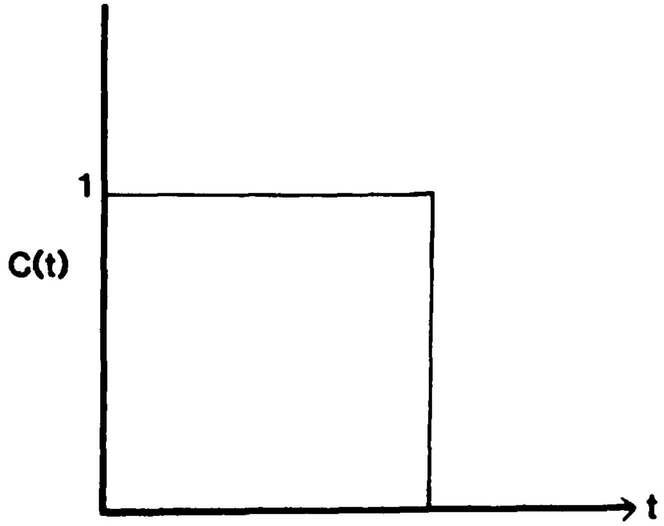

A. FILTER FUNCTION

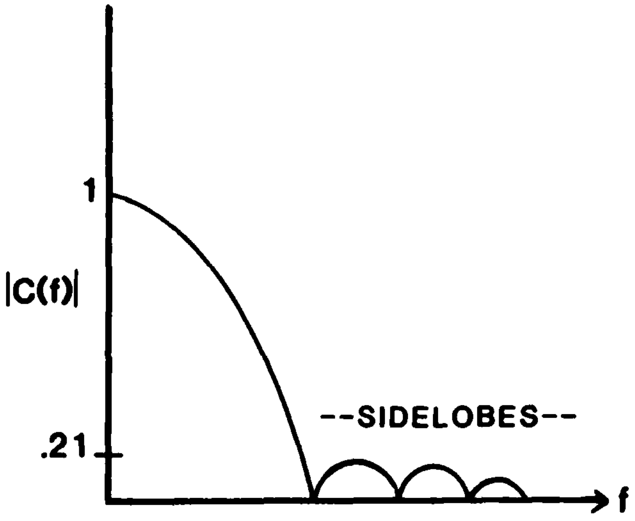

B. FOURIER TRANSFORM

Figure 4. The Simple Moving Average Filter Function

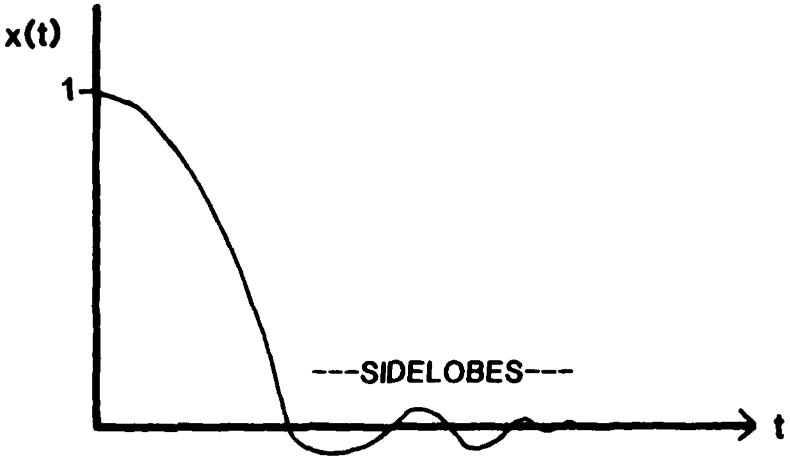

A. INVERSE FOURIER TRANSFORM

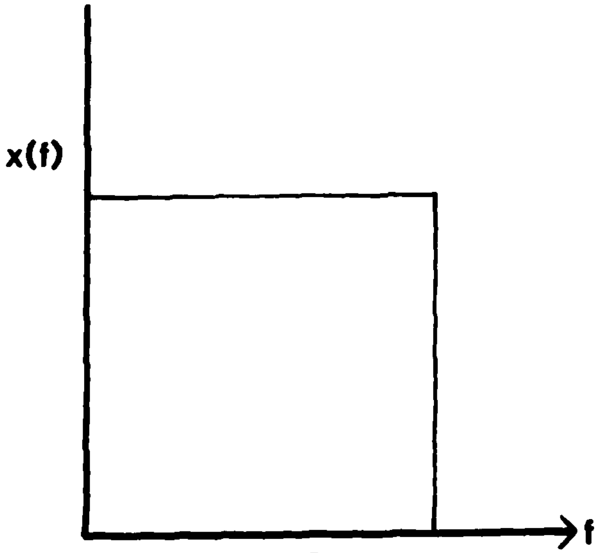

B. IDEAL FILTER

Figure 5. Time Response Required for Ideal Filter

As mentioned earlier, the simplest function is the moving average, which in the time domain is a rectangular truncation function. The function and its transform are shown in Figure 4 (only positive frequencies are shown). The sidelobes in the frequency domain are due to truncation *in the time domain* and are *indicative* of what happens when truncation occurs in either the time or frequency domain (see Figure 5). The moving average thus introduces undesirable frequency characteristics, and one is motivated to search for a more suitable function.

An obvious selection would seem to be the so called *ideal filter* for which frequency response is the rectangular truncation function as shown in Figure 5b. The impulse response of the ideal filter has sidelobes which extend to infinity and which are caused by the truncation (sharp cutoff) in the frequency function. To accurately represent such a function would require a series of *infinite length*. To obtain a practical convolution series one usually would truncate the infinite series after n terms as an approximation to the full series. However, truncation after the nth term will cause the well known Gibb's phenomenon, an overshoot and oscillatory frequency response (Figure 6 and Ref. 4).

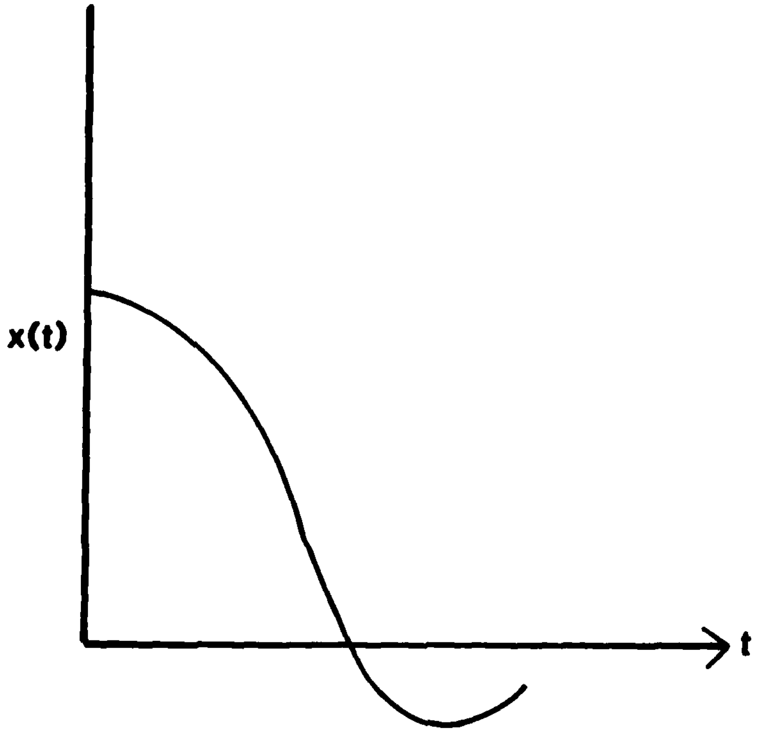

A. TRUNCATED IMPULSE RESPONSE

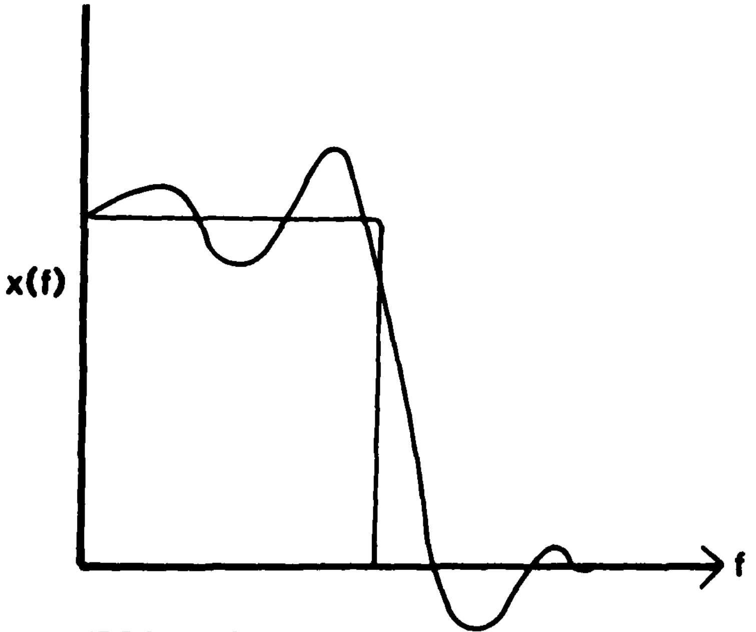

B. FREQUENCY RESPONSE

Figure 6. Gibb's Phenomenon

In summary, there are two problems associated with choosing a filter function which will yield the desired results and which is mathematically realizable. First, it is always necessary for any realizable function to be limited in time. That is, it must be of finite length (a truncated function); the values C_m must equal zero beyond a specified upper limit on m. As shown above, this will lead to oscillatory and undesirable frequency characteristics in the frequency domain. Second, it is necessary for the sidelobes of the impulse response to be as small as possible. This implies that the frequency response cannot have a sharp cutoff. Figure 5 shows that a sharp cutoff necessitates sidelobes of significant magnitude in the impulse response coefficients. These two problems would seem to preclude the use of the ideal filter function or simple running average in their usual form.

VI. Windowing

The solution to these problems is to window the filter function coefficients (Ref. 1). That is, weight the coefficients in some manner to reduce the end effects caused by truncation. Two approaches are recommended. The first (Ref. 4) is to window the truncated impulse response series shown in Figure 6. This series represents the approximate impulse response of the ideal bandpass filter. As shown in Figure 7, by using an appropriate window function (discussed below) it is possible to reduce frequency domain ripple (Gibb's phenomeon). Windowing also diminishes the strength of the sidelobes which results in a loss of sharpness of the frequency cutoff.

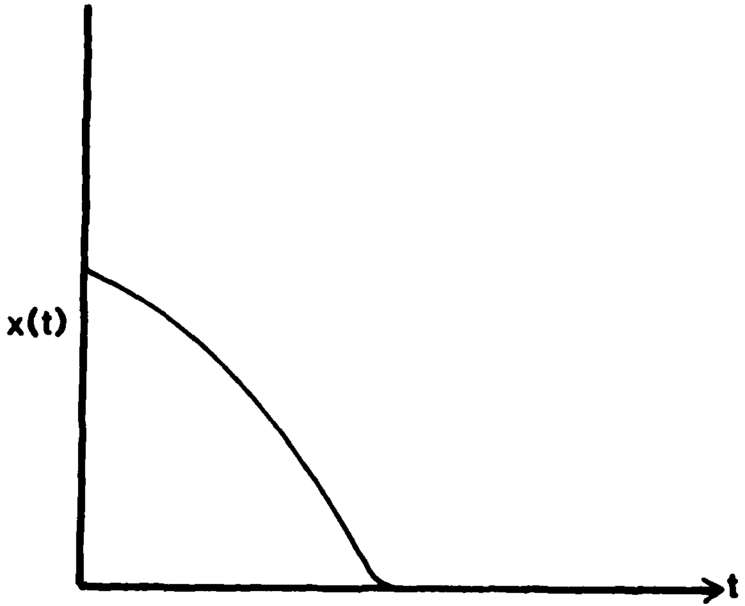

A. WINDOWED IMPULSE RESPONSE

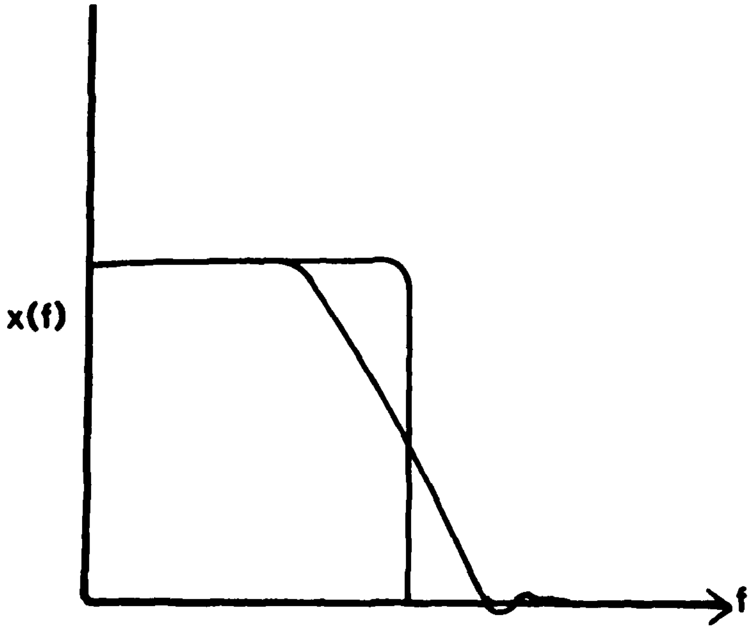

B. FREQUENCY RESPONSE

Figure 7. Effect of Windowing on Approximated Ideal Filter

A second and mathematically simpler method is to window the running average coefficients $C_m = 1/N$. The same benefits accrue as in windowing the ideal filter, but a further loss in cutoff sharpness results. However, the ease of the method outweighs this problem, and for the purposes of discussion this method will be the one referred to for the remainder of this paper.

Many window functions exist (Ref. 1), but for discussion purposes only the two most often used for data smoothing will be examined here. The first is the cosine bell or Hamming window. This function can be expressed in discrete form as

$$h(n) = \alpha + (1-\alpha)\cos 2\pi n/N \tag{14}$$

where h(n) represents discrete values of the window function. The best α is 0.54 (Ref. 1).

Using this α and multiplying by the coefficients of the running average function, one obtains the coefficients of the windowed running average function as

$$C_m = (1/.54N)(.54 + .46\cos 2\pi m/N) \tag{15}$$

The value 0.54 has been placed in the denominator for the purpose of scaling the frequency response to the value one at zero frequency.

Another often used window function is the least squares polynomial developed by Savitzky and Golay (Ref. 2). This method involves fitting an mth order polynomial through the data using the least squares criteria for each interval of 2n+1 points in the smoothing convolution. The new central value of the group is the value that lies on the fitted curve at the corresponding data location.

Savitzky and Golay (Ref. 2) have tabulated the values of the convoluting variables, C_m, for a number of polynomials and their derivatives beginning with a quadratic-cubic polynomial. (The quadratic and cubic polynomials have identical convolution coefficients.) This polynomial is adequate for most work since "any smooth curve will look more or less like a quadratic in the vicinity of a peak or like a cubic in the vicinity of a shoulder" (Ref. 2). The smoothing coefficients for this function are

$$C_m = \frac{3\ (5m(N+1-m)-1/2(N+2)(N+3))}{(N-2)N(N+2)} \qquad (16)$$

where N is an odd number representing the length of the function and m varies from one to N. One advantage of the least squares polynomial method is the relative simplicity of the derivative functions. The smoothing coefficients for the first derivative quadratic function are

$$C_m = m - 1/2(N+1) \qquad (17)$$

The discrete Hamming and quadratic-cubic least square functions are displayed in Figure 8. The two values of N shown, 65 and 129, were chosen for mathematical ease in computing discrete Fourier transforms by computer. These two functions possess the desired impulse characteristics of a mathematically suitable smoothing function -- finite length and reduced sidelobes. The discrete Fourier transform of these functions are shown in Figure 9. As indicated in the figure, the frequency response of these functions are also finite functions with reduced sidelobes. Also indicated in Figure 9, for two functions of the same length, the Hamming function has a lower cutoff but attenuates the higher frequencies more than the least squares function.

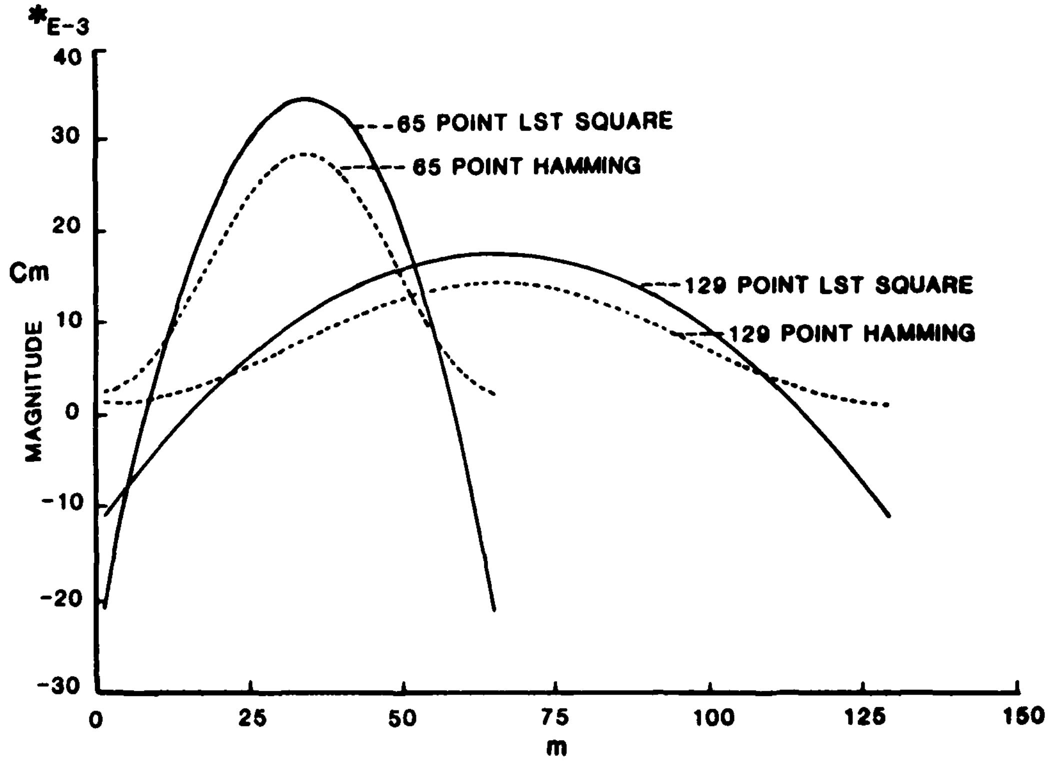

Figure 8. Comparison of Convolution Coefficients for Two Windowed Functions

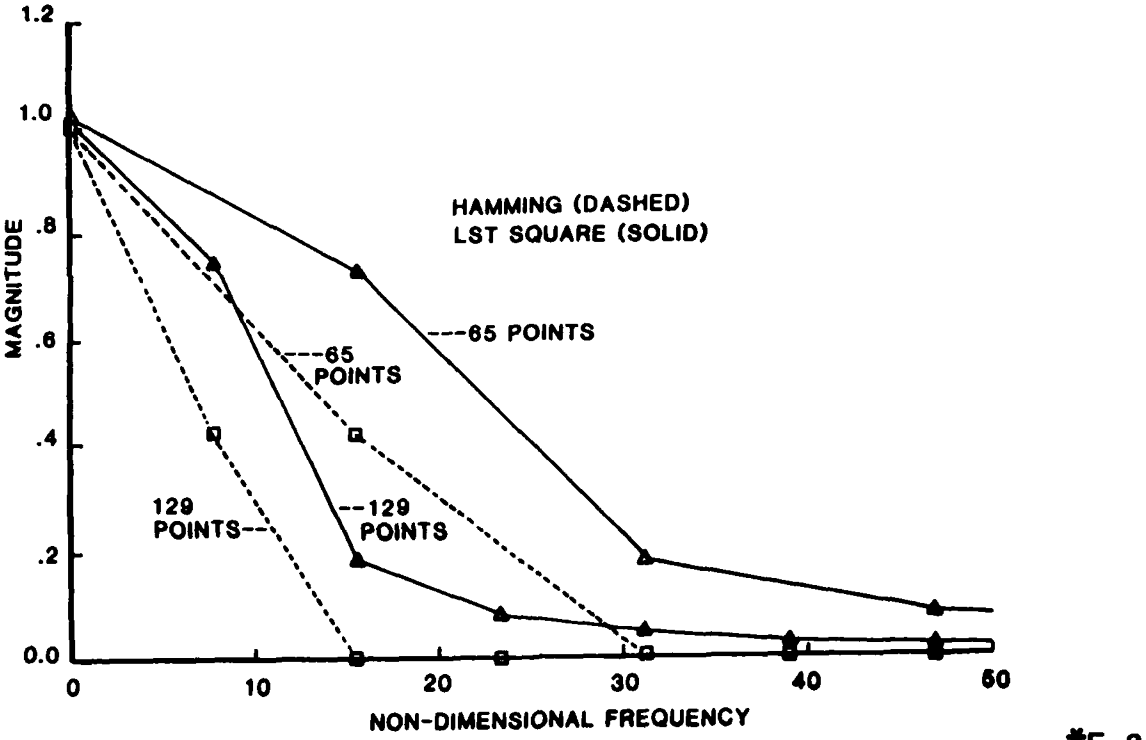

Figure 9. Frequency Response of Two Filter Functions

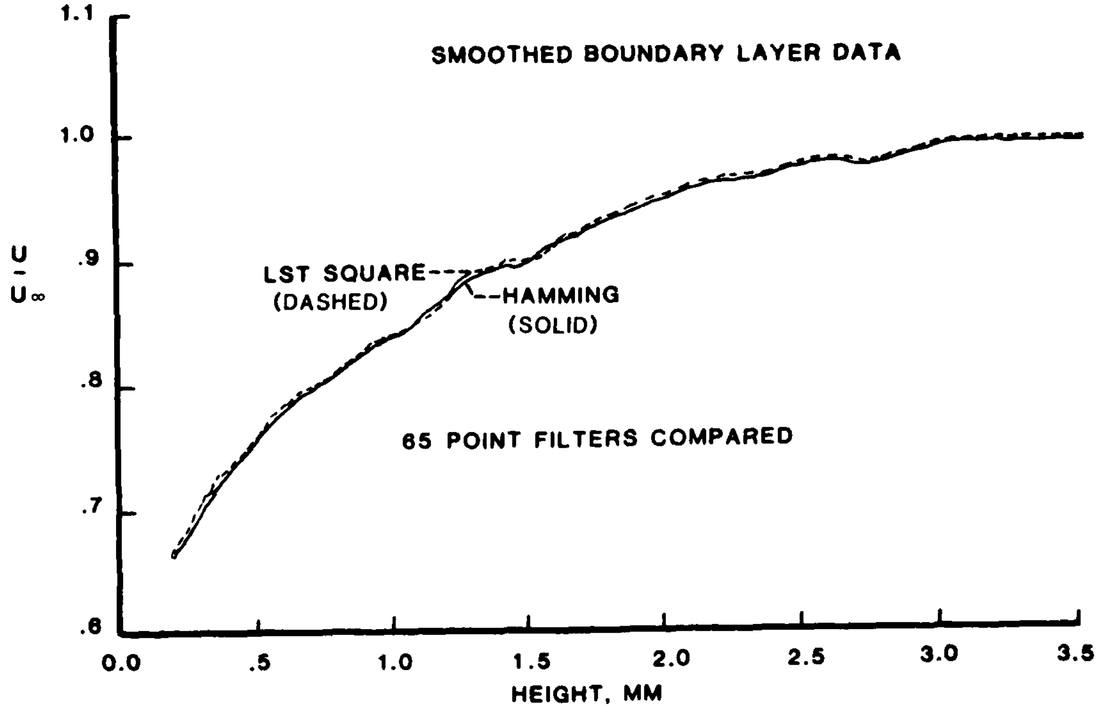

Figure 10. Smoothed Data from Figure 1

The results of using 65-point functions to smooth the data from Figure 1 are shown in Figure 10, in which the raw data has been omitted. One can see that the two functions produce a similar mean curve; however, the least square result contains more ripples while the Hamming window result is attenuated more in the region where the mean is changing rapidly. In Figure 9, one can observe that the 65-point Hamming result is similar to the 129-point least square result. This would seem to indicate that an N-point Hamming smoothing is similar to a 2N-point least square smoothing. If one were truncating unsmoothed end points, the Hamming function would allow for a larger number of retained end points. This is demonstrated in Figure 11, in which smoothing has been carried out on the data of Figure 1. Using the 65-point and 129-point functions for each smoothing operation, N-1 points have been truncated, half at each end. (The data was not smoothed to the full right hand end in order to conserve computer time.) The results of the 65-point Hamming smoothing are qualitatively similar to the 129-point least square smoothing.

Figure 11. Comparison of Data Smoothed by Different Functions

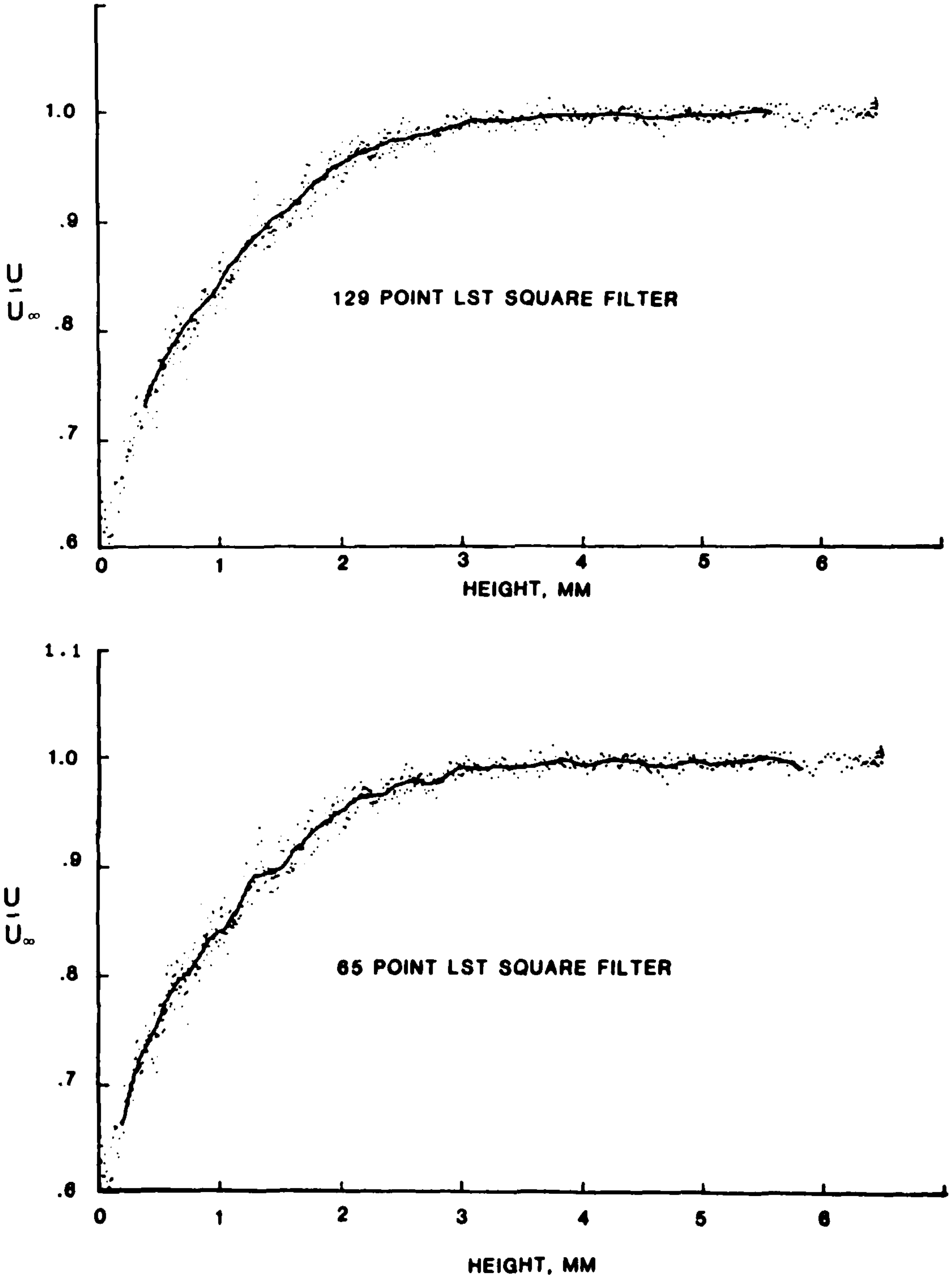

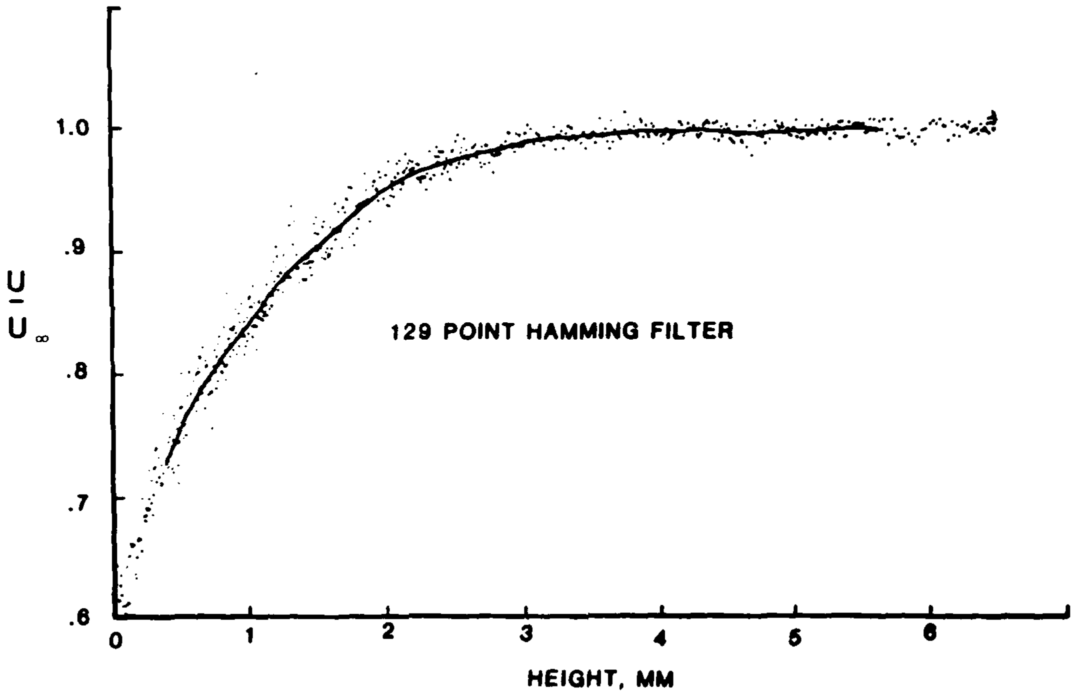
1.0
.9
.8
.7
.6
$\frac{U}{U_\infty}$
129 POINT HAMMING FILTER
0
1
2
3
4
5
6
HEIGHT, MM

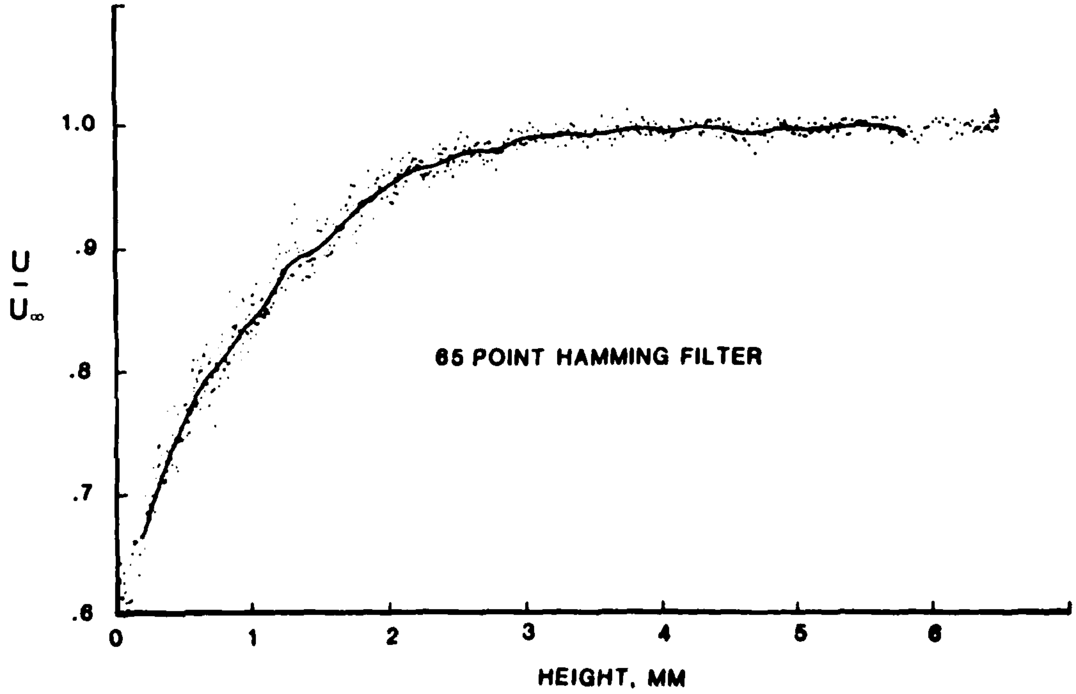
1.0
.9
.8
.7
.6
$\frac{U}{U_\infty}$
65 POINT HAMMING FILTER
0
1
2
3
4
5
6
HEIGHT, MM

VII. Length of Smoothing Function

Once one has decided to use a smoothing function, the length (number of points) must be determined. This will be governed by the type of data one is examining and the amount of data that one can afford to lose at the end points. Addressing the latter point first, it is recognized that for a 2n+1 convolution function the central point (n+1 th point) is replaced by the convolution summation, and at either end of the data set, n points cannot be smoothed. For example, in using a nine point function, eight points are unsmoothed for each pass of the smoothing function, four at each end. Many theories exist on how to treat these end points. One is to use a shorter function on the end points than that used on the central portion of the data. A second solution is simply to truncate the end points after each smoothing convolution. There is no general answer to this question; it must be decided based upon the smoothing effects desired.

The length of the smoothing function will depend on whether one wants to examine the mean of the data, the peak waveforms, or a combination of the two. A filter function used to identify the mean would reduce the standard deviation of the data about the mean. According to a study by Enke and Nieman (Ref. 5) this filter function should be as long as possible but small enough so that not more than one inflection in the observed data is included in any convolution interval of 2n+1 points.

In order to study peaks in the data, the smoothing function should cause as little distortion in waveform shape as possible and at the same time increase the ratio of peak values to signal noise. Enke and Nieman suggest that this type of data is best filtered by a function in which width at half-peak height equals that of the peaks in the data and in which the function length, 2n+1, is twice that of the afforementioned width. This is closely approximated by a quadratic-cubic function. This criteria will lead to shorter functions than those used to simply identify mean values and will produce a compromise between noise reduction and signal distortion. To choose a function with which to smooth data in which both mean values and peaks are of interest will require a judgement based on the relative importance of the signal mix.

VIII. Conclusions

In summary, the Hamming function would seem to provide for the least end point truncation and be best suited for smoothing data in which the mean is of highest interest. The least squares function on the other hand appears to have a sharper frequency rolloff and thus is well suited to data in which peak values and waveform shape are of interest. The choice made to smooth the boundary layer data shown in Figure 1 was governed by a consideration of the loss of end points in the data. Thus the Hamming function was chosen to provide the best smoothed results for this data.

Regardless of the choice of smoothing functions, it is important that the effects of the smoothing procedure be understood. When one views the procedure as one of filtering the data with a low pass filter, it is evident that not only can data be obscured or even lost but spurious data can be introduced (the Gibb's phenomenon). The use of a windowed function offers the best solution to the smoothing problem. This paper has compared two popular functions: the Hamming (or windowed retangular function) and the moving least square polynomial.

References

1. Rabiner, L.R. and B. Gold, Theory and Application of Digital Processing, Prentice-Hall Inc., 1975.

2. Savitzky, A. and M.J.E. Golay, "Smoothing and Differentation of Data by Simplified Least Squares Procedures," Analytic Chemistry, 36, No. 8, July 1964, pp. 1627-1639.

3. Brigham, E.O., The Fast Fourier Transform, Prentice-Hall Inc., 1974.

4. Sterns, S.D., Digital Signal Analysis, Hayden Book Company Inc., 1975.

5. Enke, C.G., and T.A. Nieman, "Signal-to-Noise Ratio Enhancement by Least Squares Polynomial Smoothing," Analytic Chemistry, 48, No. 8, July 1976, pp. 705A-712A.

SECTION IV.

Flight Mechanics

FLIGHT TEST MEASUREMENT OF THE AERODYNAMIC EFFECT OF THRUST LEVEL ON LIFT AND DRAG

T.R. Yechout*

Abstract

A flight test technique has been developed under NASA Dryden sponsorship to define the aerodynamic effect of thrust level on aircraft lift and drag characteristics. Conventional stabilized "speed power" tests require that the thrust be adjusted for each test condition and, as a result, the effect of thrust on aerodynamic characteristics cannot be easily identified. The technique utilizes quasi steady-state maneuvers at selected power settings throughout the Mach range of the aircraft to define lift and drag coefficient variation as a function of angle of attack, Mach number, and power setting. A twenty hour verification flight test program was accomplished using a Learjet Model 35 aircraft. Significant power effects were identified which should be anticipated on any aircraft with jet engines mounted on the aft fuselage above the inboard wing section.

I. Introduction

In-flight definition of the aerodynamic effect of thrust level on lift and drag characteristics has not been accomplished in the past. Normally, lift and drag measurements are made using a series of stabilized points throughout the aircraft flight envelope. A wide range of engine power settings are used to achieve the stabilized conditions from which lift and drag may be determined given an in-flight thrust and airflow model along with normally instrumented aircraft parameters such as weight and angle of attack. Unfortunately, the flow field around the aircraft may be significantly altered by the airflow through engine(s) which will result in the lift and drag characteristics being directly dependent on engine power. If the stabilized point method is used on an aircraft with significant power effects, use of the resulting data to predict non-stabilized

---

*Lt. Col., USAF, Associate Professor, Dept. of Aeronautics, USAF Academy,Co.

(i.e. excess thrust not equal to zero) performance characteristics will be susceptible to significant error. A flight test technique has been developed to efficiently evaluate the effect of engine power setting on the lift and drag characteristics of an aircraft. The technique utilized quasi steady-state maneuvers (level accelerations and decelerations) at selected power settings throughout the Mach range of the aircraft to define lift and drag coefficient variation as a function of angle of attack, Mach number, and power setting. The technique was developed and evaluated during a twenty hour flight test program using a Learjet Model 35 aircraft. This effort was part of an overall research program which concentrated on modeling aircraft performance throughout the flight envelope. The use of quasi steady-state maneuvers not only allowed definition of power effects on lift and drag, but also provided a very time efficient approach to overall in-flight aircraft performance definition when compared to the stabilized point method.

II. Concept

Development of the lift and drag characteristics from quasi steady-state maneuvers began with consideration of the forces acting on the aircraft. The aircraft force balance equations resolved parallel and perpendicular to the flight path (assuming zero sideslip, wings level, and constant mass) are, from Figure 1,

$$F_x = ma_x \tag{1}$$

$$F_g \cos(\alpha+\lambda) - F_r - D = W\left(\frac{a_x}{g} + \sin\gamma\right) \tag{2}$$

$$F_z = ma_z \tag{3}$$

$$L + F_g \sin(\alpha+\lambda) = W(\frac{a_z}{g} + \cos\gamma) \qquad (4)$$

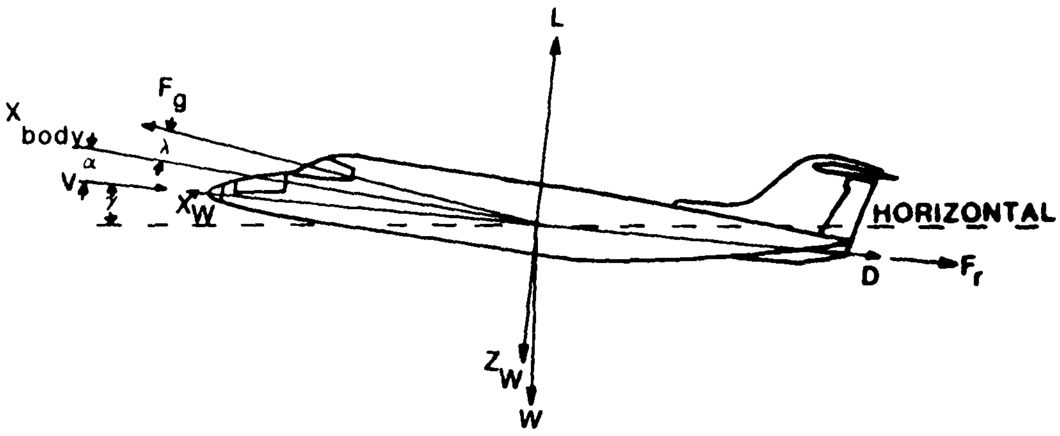

Figure 1. Aircraft Force Balance Diagram

As discussed in Reference 1, the flight path load factors resolved along the x and z wind axes are

$$n_x = \frac{a_x}{g} + \sin\gamma \qquad (5)$$

$$n_z = \frac{a_z}{g} + \cos\gamma \qquad (6)$$

The force balance equations may then be expressed

$$F_g \cos(\alpha+\lambda) - F_r - D = Wn_x \qquad (7)$$

$$L + F_g \sin(\alpha+\lambda) = Wn_z \qquad (8)$$

and the relationships for lift and drag coefficient are

$$C_L = \frac{Wn_z - F_g \sin(\alpha+\lambda)}{(1/2)\gamma' p_a M^2 S} \tag{9}$$

$$C_D = \frac{F_g \cos(\alpha+\lambda) - F_r - Wn_x}{(1/2)\gamma' p_a M^2 S} \tag{10}$$

Equations 9 and 10 express lift and drag coefficients in terms of wind axes accelerations, the engine model parameters of gross thrust and ram drag, and normally recorded flight test parameters such as angle of attack, ambient pressure, weight, and Mach number. The equations are compatible with quasi steady-state maneuvers in which excess thrust is not equal to zero and flight path accelerations are present. Wind axis accelerations were determined from accelerometers mounted along the body axis of the aircraft using the appropriate angular transformations. A unique inflight thrust and airflow prediction technique, termed "Thrust Modeling," was developed as part of the overall program to define the gross thrust and ram drag terms in Equations 9 and 10. The technique consisted of correcting the engine deck predictions of thrust and airflow to match the performance of the actual engines installed in the aircraft using a three step approach:

1) Simplified representation of engine deck predicted thrust, fuel flow, and airflow in corrected form,
2) Correction of the engine deck model, developed in step one, to the individual characteristics of each engine based on a static thrust run,
3) In-flight correction of thrust and airflow predictions based on actual test fuel flow, an accurate specific fuel consumption prediction and a balance of the thrust momentum equation.

The final equations in simplified form for thrust and airflow were:

$$F_{g_{test}} = \frac{W_{f_{test}} F_{g_{deck}}}{\eta W_{f_{deck}}} \qquad (11)$$

$$W_{a_{test}} = W_{f_{test}} \left[\frac{W_{a_{deck}}}{\eta W_{f_{deck}}} + \frac{1}{\eta} - 1 \right] \qquad (12)$$

where η was the ratio of static thrust run specific fuel consumption to engine deck specific fuel consumption defined as a function of corrected RPM. A complete development of this technique is presented in Reference 2. Thrust and air flow prediction accuracies were believed to be three to five percent or better based on data obtained from the Lear 55, F-104G, F-111, and YF-12 programs (Refs. 2, 3, 4, and 5). This prediction technique offered several advantages over the most commonly used methods as discussed in Reference 2.

Two corrections were made to lift coefficient for elevator trim effects resulting from 1) the thrust moment about the center of gravity (c.g.) and 2) a non-standard c.g. These corrections standardized the lift coefficient data to a common baseline.

In the first case, the effect of the associated moments created by the thrust (F_g) and ram drag (F_r) about the c.g. were removed. From Figure 2, this moment is given by

$$\Delta M_{thrust} = -F_g Z_{thrust} + F_r h_r \qquad (13)$$

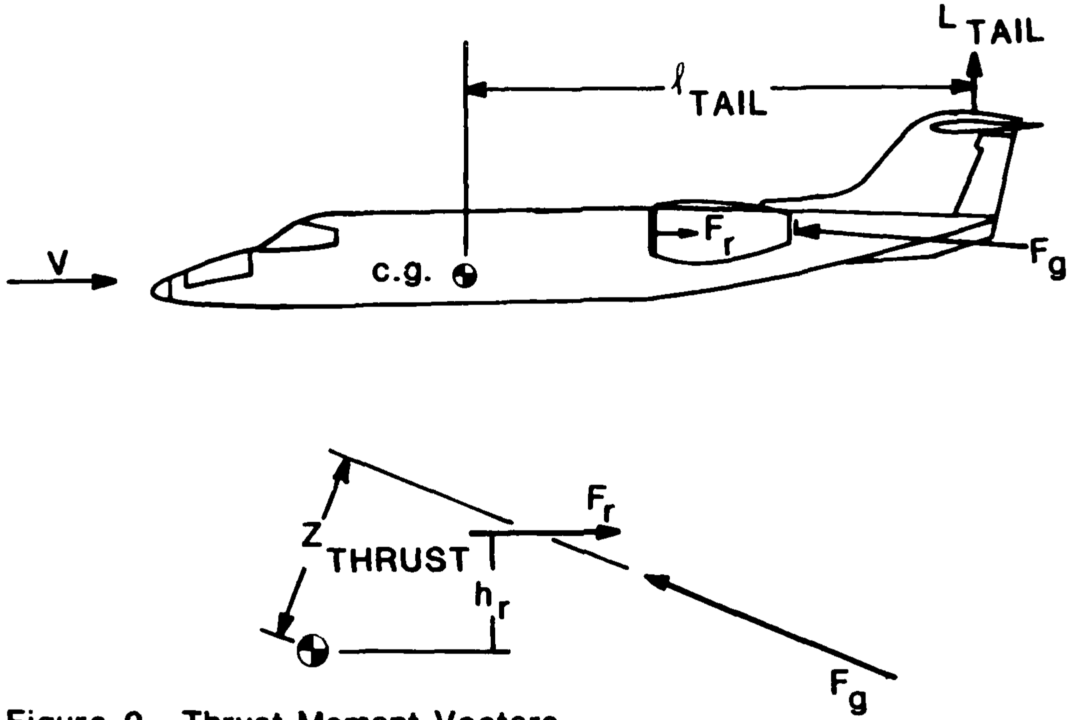

Figure 2. Thrust Moment Vectors

To counteract this moment, an incremental lift at the tail is needed, such that

$$-\Delta L_{tail}\ \ tail - F_g Z_{thrust} + F_r h_r = 0 \tag{14}$$

and the change in lift coefficient which must be added to C_L is $-\Delta L_{tail}\ qS$ or

$$\Delta C_{L_{\substack{thrust\\moment}}} = \frac{(F_g Z_{thrust} - F_r h_r)}{\ell_{tail} qS} \tag{15}$$

The trimmed lift coefficient (C_{L_T}) then becomes

$$C_{L_T} = C_L + \Delta C_{L_{\substack{thrust\\moment}}} \tag{16}$$

The distance Z_{thrust} is a function of c.g. and airframe geometry, while h_r and ℓ_{tail} are also functions of angle of attack.

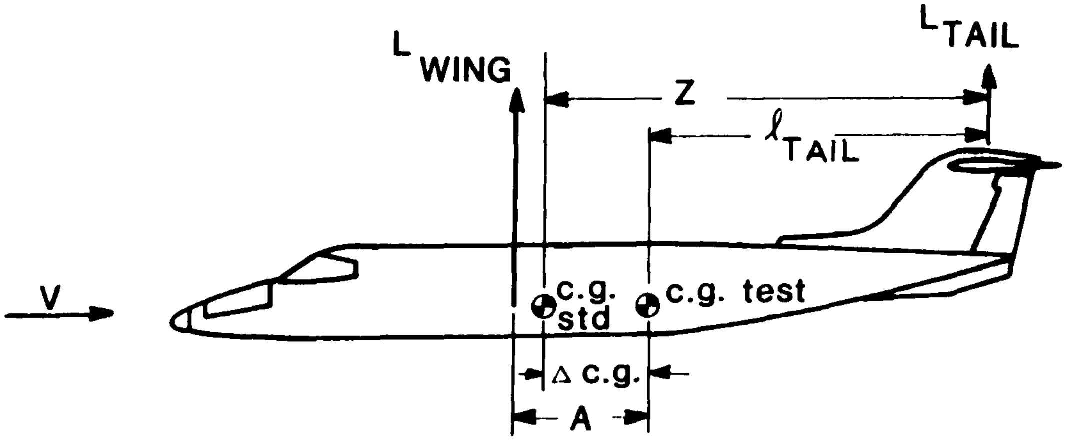

Figure 3. Moment Arms for C.G. Standardization

C_{L_T} was also standardized to a particular c.g. location. From Figure 3, this correction begins with a moment balance

$$AL_{wing} = L_{tail}\,\ell_{tail} \quad \text{(test c.g.)} \tag{17}$$

$$L_{wing}\,(A - \Delta c.g.) = Z(L_{tail} + \Delta L_{tail}) \quad \text{(standard c.g.)} \tag{18}$$

where L_{tail} is the change in tail lift required for a standard c.g. Since

$$Z = \ell_{tail} + \Delta c.g.,$$

$$L_{tail}\,\ell_{tail} - L_{wing}\,\Delta c.g. = (\ell_{tail} + \Delta c.g.)\,L_{tail} + (\ell_{tail} + \Delta c.g.)\Delta L_{tail}. \tag{19}$$

With the total aircraft lift (L) given by

$$L = L_{wing} + L_{tail} \tag{20}$$

for the test condition, Equation 19 becomes

$$-L(\Delta c.g.) = (\ell_{tail} + \Delta c.g.)\Delta L_{tail}, \tag{21}$$

and

$$\Delta L_{tail} = \frac{-L(\Delta c.g.)}{\ell_{tail} + \Delta c.g.} \tag{22}$$

In coefficient form

$$\Delta C_{L_{c.g.}} = \frac{-C_{L_T}(\Delta c.g.)}{(\ell_{tail} + \Delta c.g.)} \tag{23}$$

and the standardized lift coefficient corrected for thrust moment effects and to a standard c.g. is

$$C_{L_S} = C_{L_T} + \Delta C_{L_{c.g.}}. \tag{24}$$

A correction to the drag coefficient was made for skin friction variation as a function of Reynolds number to standardize the drag coefficient data to a particular altitude. Schlichting's formula for the skin friction coefficient assuming turbulent flow (Ref. 6) was used.

$$C_f = \frac{.455}{(\log_{10} R_e)^{2.58}(1 + .144M^2)^{.65}} \tag{25}$$

$$R_e = \frac{\rho V \ell}{\mu} \quad \begin{array}{l} \ell = \text{characteristic length} \\ \mu = \text{viscosity coefficient} \end{array} \tag{26}$$

AD-A157 215   AIR FORCE ACADEMY AERONAUTICS DIGEST(U) AIR FORCE   3/3
ACADEMY CO J E DEJONGH ET AL. APR 85 USAFA-TR-85-2

UNCLASSIFIED   F/G 20/4   NL

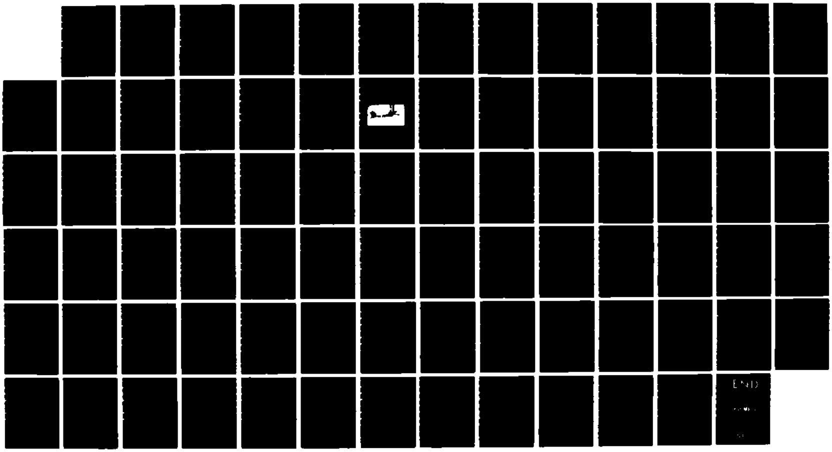

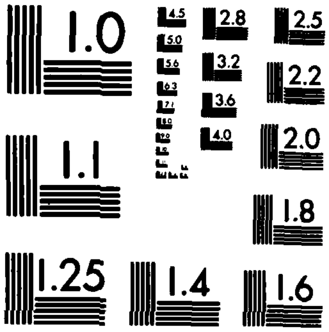

MICROCOPY RESOLUTION TEST CHART
NATIONAL BUREAU OF STANDARDS-1963-A

The drag coefficient due to skin friction is then

$$C_{D_{SF}} = C_f \left(\frac{\text{Wetted Area}}{S} \right) \qquad (27)$$

where the drag on the aircraft is obtained by adding the drag on each of the components shown in Table 1. The Reynolds number calculation of Equation 26 requires the characteristic length, and the drag coefficient calculation of Equation 27 requires the applicable wetted area. The skin friction drag contributions were then standardized to an altitude of 25000 feet by computing $C_{f_{25000'}}$ and $C_{D_{SF_{25000'}}}$ and defining the incremental change in drag coefficient due to skin friction variation for off-standardized conditions as

$$\Delta C_{D_{SF}} = C_{D_{SF_{25000}}} - C_{D_{SF}} \qquad (28)$$

This methodology was used for each of the aircraft components; and the total skin friction drag correction, $C_{D_{SF_{total}}}$, was obtained by summing the contribution of each component.

$$\begin{aligned} \Delta C_{D_{SF_{\text{total}}}} = {} & \Delta C_{D_{SF_{\text{fuselage}}}} + \Delta C_{D_{SF_{\text{wing}}}} + \Delta C_{D_{SF_{\text{h.tail}}}} \\ & + \Delta C_{D_{SF_{\text{v. tail}}}} + \Delta C_{D_{SF_{\text{pylon}}}} + \Delta C_{D_{SF_{\text{nacelles}}}} \\ & + \Delta C_{D_{SF_{\text{ventral fin}}}} + \Delta C_{D_{SF_{\text{tank}}}} + \Delta C_{D_{SF_{\text{tank fin}}}} \end{aligned} \qquad (29)$$

The standardized drag coefficient, C_{D_S}, is then

$$C_{D_S} = C_D + \Delta C_{D_{SF_{\text{total}}}} \tag{30}$$

An altitude of 25000 feet was chosen for standardization since it was approximately in the middle of the altitude envelope of the aircraft.

Fuselage
Wing
Horizontal tail
Vertical tail
Engine pylons
Engine nacelles
Ventral fin
Tip tanks
Tank fins

Table 1: Aircraft Components Used to Calculate Skin Friction Drag

C_{L_s} and C_{D_s} versus angle of attack characteristics were defined from a series of test points obtained during acceleration and deceleration maneuvers. These characteristics were defined as a function of power setting and Mach number. The needed lift coefficient range was obtained through variation of the weight-pressure ratio (W/δ) as discussed in the Test Procedure section. By determining the lift and drag characteristics as a function of power setting, the power-dependent effects could be defined when comparing data for the same Mach number and angle of attack.

III. Test Procedure

Quasi steady-state acceleration/deceleration maneuvers provided the necessary data to define lift and drag characteristics. These maneuvers were conducted at nearly constant altitude using the altitude hold mode of the autopilot. Normally less than a 60 foot excursion from the start altitude was experienced during a maneuver. Eight "cardinal" power settings were evaluated consisting of 95, 90, 85, 80, 75, 70, 60, and 50 percent low pressure fan RPM (N_1). The N_1 was chosen as the variable to represent power because of the relatively high bypass ratio of the engines and the resulting high correlation to engine airflow. An acceleration/deceleration was conducted at a cardinal power setting by holding N_1 to within 1/2 percent during a maneuver. A range of the weight-pressure ratio parameter (W/δ) within the aircraft envelope was designated to provide a lift coefficient variation for a given Mach number so that Mach effects could be defined. Eight values of W/δ were evaluated as shown in Table 2. These eight values of W/δ provided eight evenly spaced points on a constant Mach drag polar in the mid-Mach range. At each value of W/δ, an acceleration/deceleration sequence was performed, which included maneuvers at all cardinal power settings above idle. As W/δ increased, the number of available power settings decreased because the idle RPM increases with altitude. For example, at 40,000 feet only the 95, 90, and 85 percent power settings could be evaluated. As a result, the largest amount of data was obtained for the higher power settings.

W/δ	Nominal Altitude
22,000	10.000 ft
40,000	23,000 ft
47,000	26,000 ft
53,000	29,000 ft
60.000	32,000 ft
67,000	35,000 ft
73,000	38,000 ft
80,000	40,000 ft

Table 2: Performance Modeling Maneuvering Sequences

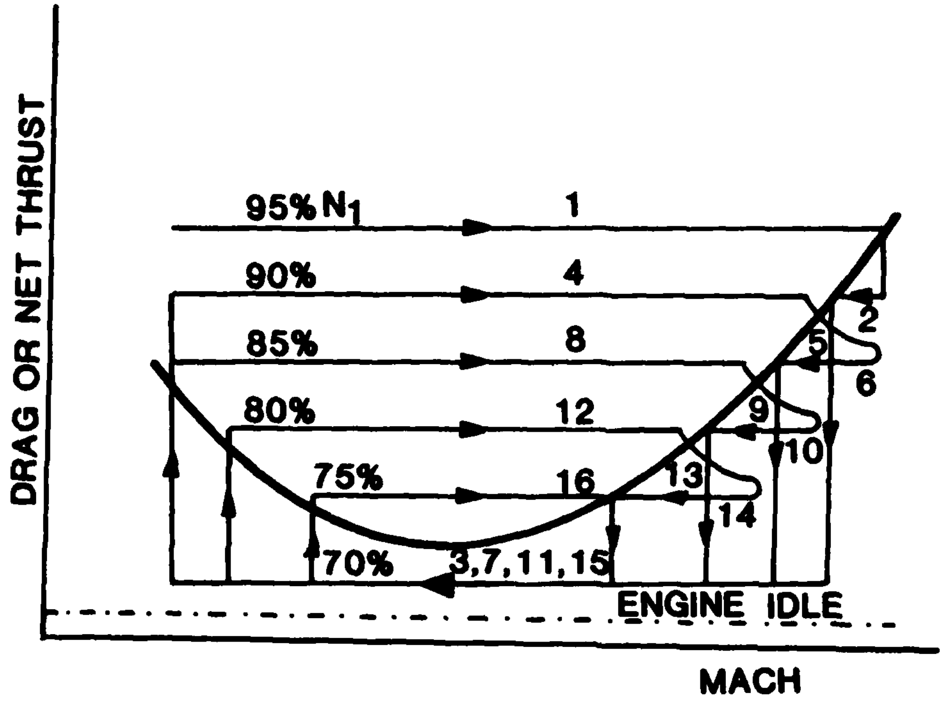

Figure 4. Typical Maneuvering Sequence

Sequence	Power Setting	Maneuver	Data Recorded
1	95	Accel	Yes
2	90	Decel	Yes
3	70	Decel	Yes
4	90	Accel	Yes
5	95	Accel	No
6	85	Decel	Yes
7	70	Decel	Yes
8	85	Accel	Yes
9	95	Accel	No
10	80	Decel	Yes
11	70	Decel	Yes
12	80	Accel	Yes
13	95	Accel	No
14	75	Decel	Yes
15	70	Decel	Yes
16	75	Accel	Yes

A typical maneuvering sequence, illustrated in Figure 4, assumes that the drag curve and engine idle level are as shown for a particular W/δ configuration. A sequence began by slowing the aircraft to an acceptable minimum speed (for the Lear 35 this was an airspeed slightly above stick shaker speed) at an altitude based on the target value of W/δ. A 95 percent acceleration was then performed. When the acceleration had slowed to approximately a quarter knot per second, the throttles were retarded to 90% and a deceleration was performed until a stabilized point was approached. The sequence then continued as shown in Figure 4. Altitude adjustments were made at convenient times in the sequence to maintain W/δ within approximately 1 percent as weight decreased. Although not specifically shown in the Figure 4 diagram, a high power setting for sequence 9 was used to accelerate past the last stabilized condition so that the deceleration as shown in sequence 10 could be obtained. Although a stabilized "speed power" point was generally not obtained, the Mach number for which the drag and net thrust curves intersected could easily be estimated based on the Mach region in which the acceleration and deceleration for a particular power setting were terminated. The general guideline used was to accelerate far enough past the last stabilized condition so that the engine RPM would achieve stabilization on the subsequent deceleration before reaching the Mach number of the last stabilized point. Data were taken periodically throughout an acceleration/deceleration rather than continually to keep the volume of data to a manageable level. Ideally, approximately a twenty-second burst of data was recorded as the aircraft passed through each .05 Mach increment. The actual test sequence performed at each W/δ condition depended directly on the location of the drag curve with respect to the net thrust levels. For example, if two cardinal power settings were located between engine idle and the bottom of the drag curve, then at least one deceleration would be performed at each of these power settings. The maneuver sequence was designed to acquire the needed data in a time-efficient manner and also to be easily accomplished by the flight crew. It clearly met these objectives. For planning purposes, approximately 45 minutes were required to accomplish a maneuvering sequence at one value of W/δ for this aircraft.

IV. Results

The C_{L_s} versus angle of attack characteristics for the Lear 35 fell into two distinct categories. Above .65 Mach, power effects were negligible but distinct Mach effects were identified. A summary of the standardized lift coefficient characteristics in this high Mach region is presented in Figure 5, in which an increase in Mach number resulted in an increase in C_{L_s} as well as the slope C_{L_α}. The extrapolated portions of each curve are identified by the uniform dashed lines as indicated. Below .65, Mach effects were negligible, but power effects were found as presented in Figure 6. At power settings above 60%, a small but significant increase in C_{L_s} was observed. At 70% power, an approximate .01 increase in C_{L_s} resulted throughout the angle of attack range when compared to the data from the 60% power curve. As power was increased to 75% and above, an additional increase of approximately .01 over the 70% curve was found. The data scatter experienced when defining the C_{L_s} versus α curves presented in Figures 5 and 6 was $\pm.02$ maximum (based on C_{L_s}) with approximately 95 percent of the data falling within $\pm.01$ of the defined curves.

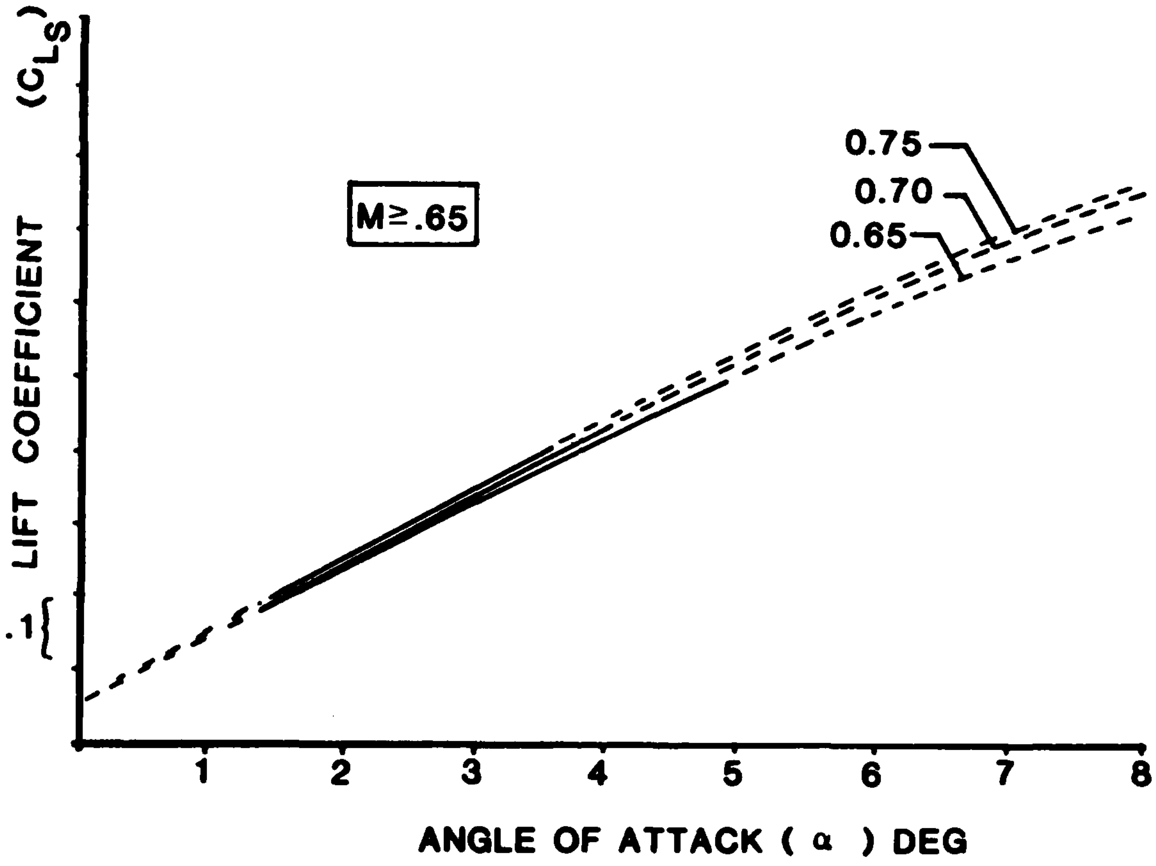

Figure 5. Lift Coefficient Characteristics, M ≥ .65

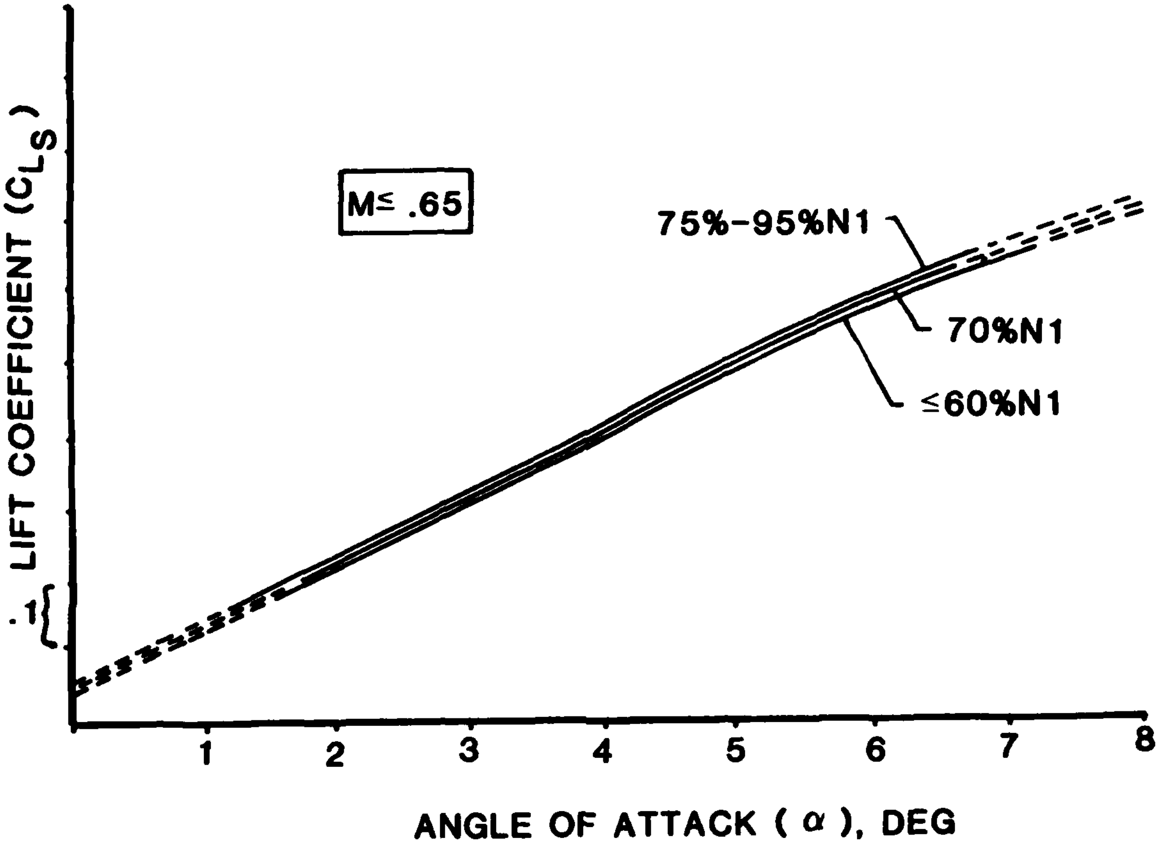

Figure 6. Lift Coefficient Characteristics
M ≤ .65

The power effects on C_{L_s} are thought to be directly related to the close proximity of the engine inlets above the inboard upper wing surface as profiled in Figure 7. Either of twp effects could be present. First, the flow field around the wing/nacelle may be fairly normal at high engine speed; however, at low engine speed, inlet spillage reduces the lift over the inboard section of the wing by retarding the flow. Second, above 60% power, the increased airflow through the engine may alter the flow field in the engine nacelle/wing root area so that the overall circulation around the inboard wing section is increased, resulting in a corresponding increase in lift. This increase in lift does not continue with increasing power settings above 75% but rather remains constant at approximately the 75% value. The increased airflow through the engine with increasing power may produce an increase in lift on the forward portion of the inner wing but may also result in flow starvation and separation near the trailing edge, producing an offsetting effect. Obviously, a flow field survey in the engine nacelle/wing root area is needed to help explain these power effects. Flow tufting in this area would be an excellent first step in understanding the power effects observed and could easily be accomplished concurrently with the quasi steady-state maneuvers used for performance modeling.

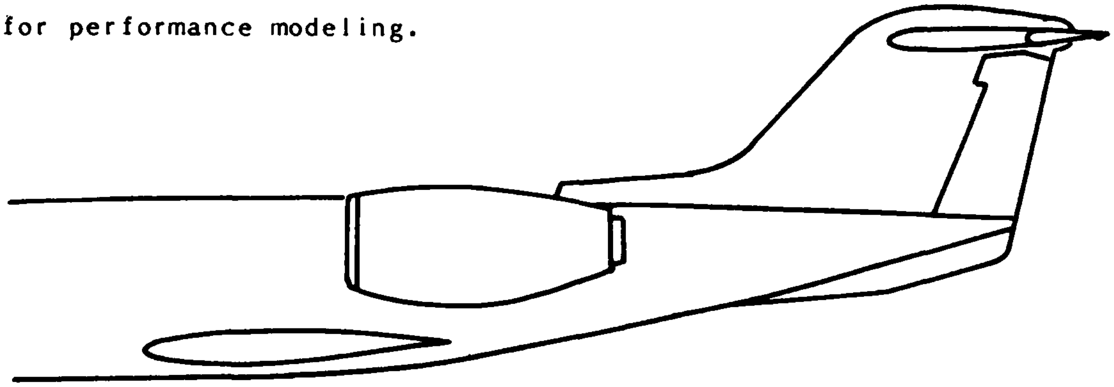

Figure 7. Engine/Airframe Configuration

As with lift coefficient, C_{D_s} versus angle-of attack characteristics fell into two distinct and consistent categories. For .6 Mach and above, power effects were not observed but Mach effects were identified. A summary of the standardized drag coefficient characteristics in the high Mach region is presented in Figure 8 where an increase in Mach number generally resulted in an increase in C_{D_s} for a given angle of attack. As shown in Figure 8, the largest increase in C_{D_s} with Mach number was projected above four degrees angle-of attack. For .55 Mach and below, Mach effects were not significant but power effects were found. As presented in Figures 9 and 10, C_{D_s} generally decreased as power decreased with approximately a 45 drag count band between 90% and 50% power in the mid angle-of-attack region. The 95% power curve intersected and crossed over the 90% curve at two locations and dropped below the 90% curve in the mid angle-of-attack region as shown. The data scatter experienced when defining the C_{D_s} versus α curves presented in Figures 8, 9, and 10 was ± .003 maximum (based on C_{D_s}) with approximately 95 percent of the data falling within .001 of the defined curves.

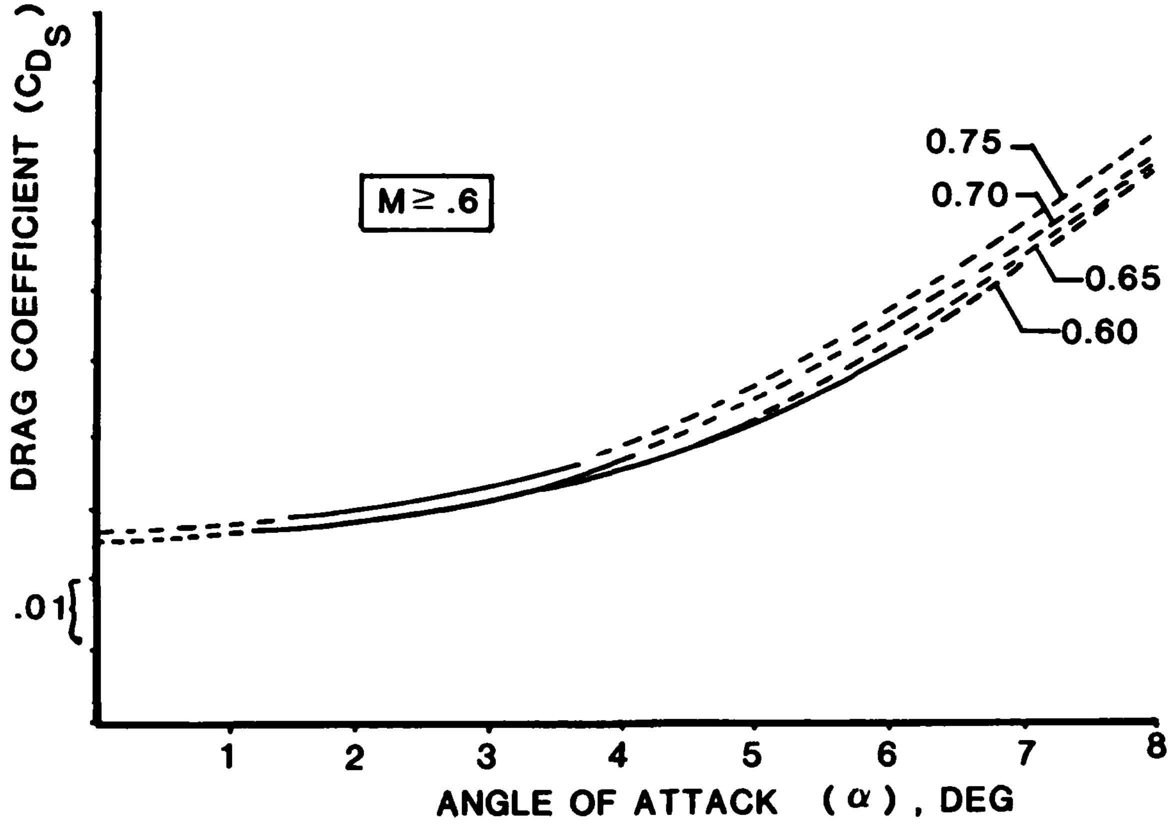

Figure 8. Drag Coefficient Characteristics, M ≥.6

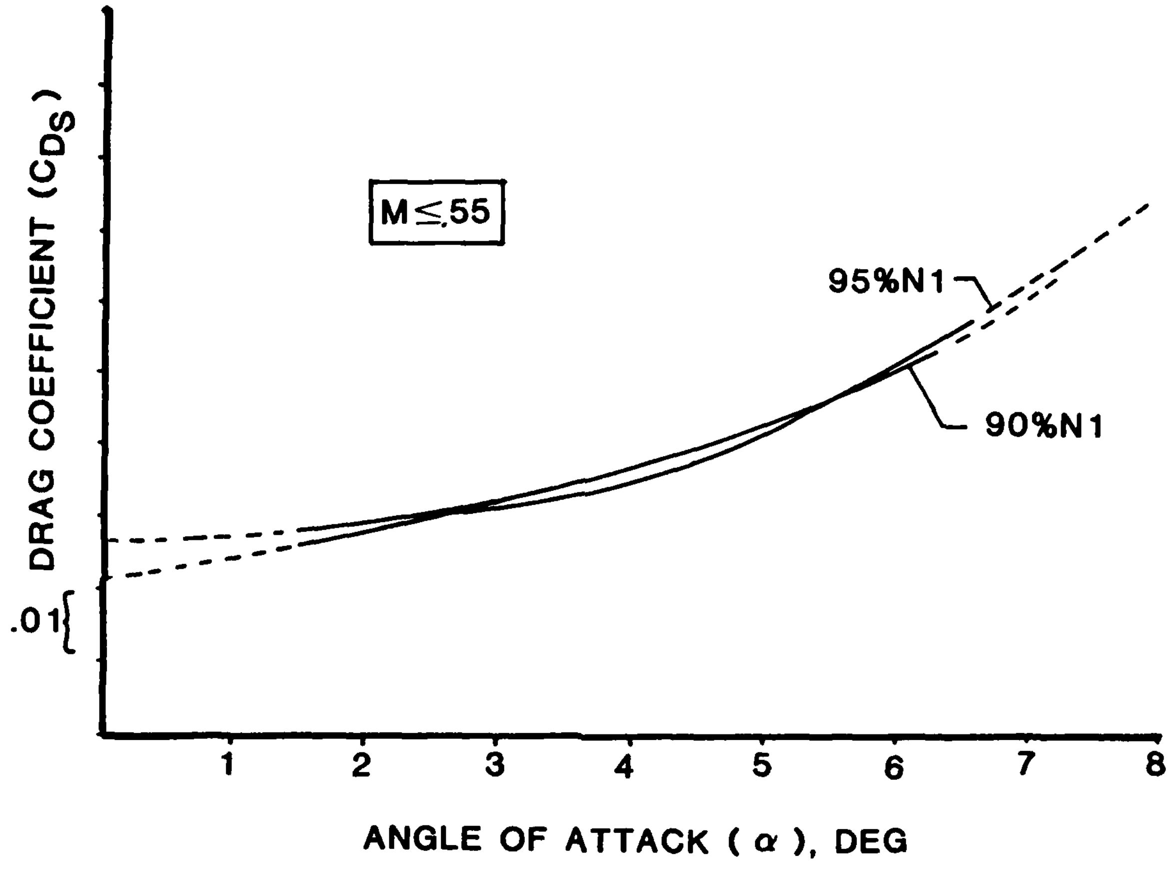

Figure 9. Drag Coefficient Characteristics

M≤.55, 90% and 95% N_1

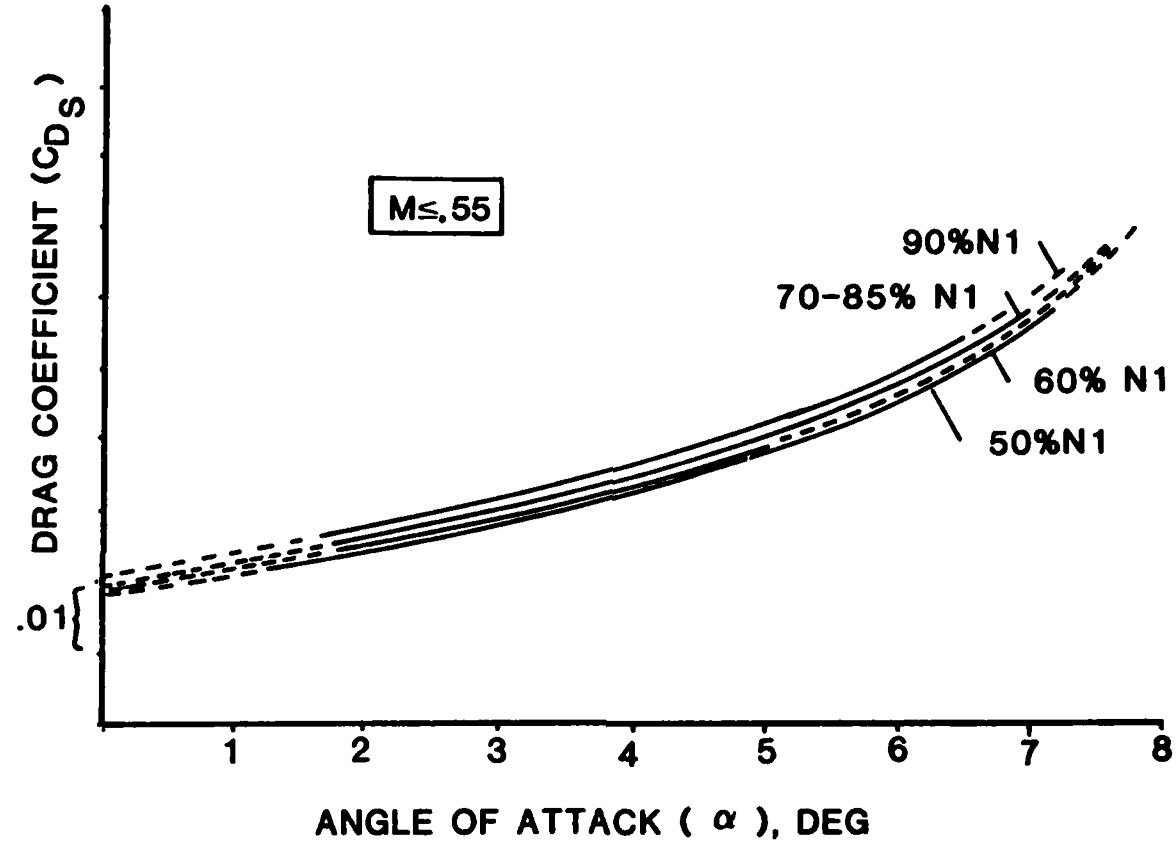

Figure 10. Drag Coefficient Characteristics, M ≤ .55, 50%-90%N_1

As with the lift coefficient curves, the complex flow interaction in the nacelle/wing root area must be analyzed to understand these characteristics. Normally it would be expected that lower drag would occur at higher power settings due to reduced inlet spillage. This trend is seen in the mid angle-of-attack region for 90% and 95% power (Figure 9). However, this is obviously not the only factor affecting the drag. Another possible interaction may be an increased pressure on the aft facing wing and fuselage surfaces (a drag reduction) resulting from increased inlet spillage at the lower power settings. The close proximity of the engine nacelle to these surfaces makes this possibility quite feasible. In Figure 9, the crossover experienced by the 95% curve in the higher angle-of-attack region (lower speed) indicates that the increased pressure phenomenon may become predominant as the projected area of aft facing wing and fuselage surfaces increases with angle-of-attack and as propagation of the inlet spillage air also increases with lower speed. Another contributing factor may be increasing flow starvation and separation near the trailing edge of the wing with increasing power, as discussed in the lift section. This would account for the increased drag observed with increased power. The absence of power effects on drag at .6 Mach and above is probably due to the low propagation of inlet spillage air at higher speeds. Again, a flow field survey in the wing root/nacelle area would help clarify the causes of the identified drag characteristics.

A selected number of steady-state (speed power) points were flown for comparison. Excellent agreement was obtained between the steady-state points and the curves presented in Figures 5 through 10. The maximum deviation for C_{L_s} was .01 and for C_{D_s} was .001 which was clearly within the observed data scatter. The maximum magnitudes of the thrust moment, c.g. and skin friction corrections were also determined for the flight test conditions evaluated. The maximum values for $\Delta C_{L_{\text{thrust moment}}}$, $\Delta C_{L_{c.g.}}$ And $\Delta C_{D_{SF}}$ were .003, .005, and .0012 respectively, which indicate that these corrections had a relatively small but still significant effect on the data.

V. Conclusions

An in-flight technique was developed to define the aerodynamic effect of thrust level (power effects) on aircraft lift and drag characteristics. A time efficient test approach was used which relied primarily on level acceleration and deceleration maneuvers. Flight test results for the Learjet Model 35 aircraft showed that power effects were very significant and must by considered if the data is to be used for predictions of aircraft performance under non-steady flight conditions. The power effects found on the Lear 35 were believed to be directly related to the complex flow field in the wing root area resulting from the overwing mounting of the engines. The approach developed in this program should generally be applicable to a large range of both jet and propeller powered aircraft.

Nomenclature

a_x	acceleration along x wind axis
a_z	acceleration along z wind axis
A	moment arm about test c.g. for L_{wing}
C_D	drag coefficient
C_{D_s}	drag coefficient corrected for skin friction variation (Eq. 7)
C_L	lift coefficient
C_{L_s}	lift coefficient corrected for thrust moment effect and non-standard c.g. (Eq. 4)

C_{L_T}	lift coefficient corrected for thrust moment effect
C_f	skin friction coefficient
F_g	gross thrust
F_r	ram drag
F_x	forces along x wind axis
F_z	forces along z wind axis
g	acceleration of gravity
h_r	moment arm for F_r
L	lift
ℓ_{tail}	moment arm about test c.g. for L_{tail}
M	Mach number
m	aircraft mass
N_1	low pressure fan RPM
n_x	x wind axis load factor
n_z	z wind axis load factor
P_a	ambient pressure
q	dynamic pressure
R_e	Reynolds number
S	wing reference area
W	aircraft weight
W_a	air flow
W_f	fuel flow
x	longitudinal axis
z	normal axis
Z	moment arm about standard c.g. for L_{tail}
Z_{thrust}	moment arm for F_g
α	angle of attack
γ	flight path angle

γ'	ratio of specific heat for air
λ	thrust inclination angle
δ	pressure ratio
ρ	air density

References

1. Simpson, W.R., "The Accelerometer Methods of Obtaining Aircraft Performance from Flight Test Data," Center for Naval Analysis, Professional Paper 245, June 1979.

2. Braman, K.B., W.G. Schweikhard, and T.R. Yechout, "Thrust Modeling, A Simplified Thrust and Airflow Prediction Technique for Flight Test Performance Measurements," AIAA Paper 83-2751, November 1983.

3. Marshal, R.T. and W.G. Schweikhard, "Modeling of Aircraft Performance from Flight Test Results and Validation with an F-104G Airplane," NASA Dryden Flight Research Center, NASA Tn D-7137, 1973.

4. Redin, P.C., "Application of a Performance Modeling Technique to an Airplane with Variable Sweep Wings," NASA Dryden Flight Research Center, NASA Technical Paper 1855, 1981.

5. Redin, P.C., "A Performance Model of the YF-12C Airplane," YF-12 Experiments Symposium, NAA CP-2054, Vol. 3, 1978, pp. 409-534.

6. Schlichting, H., "Turbulent Boundary Layers at Zero Pressure Gradient," <u>Boundary Layer Theory</u>, 7th Edition, McGraw-Hill, New York, 1979, pp. 635-665.

FLIGHT CONTROL SYSTEM DESIGN FOR A COMPUTER CONTROLLED AIRCRAFT WITH LIMITED SENSORS

Thomas P. Webb*

Abstract

A complete flight control system for a small computer controlled aircraft was designed using only yaw rate, heading, lateral load factor, airspeed, altitude, and rate of climb feedback. This multi-input multi-output control problem was done using the classical root locus technique on a linearized system model. The performance of the flight control system was then checked using a 12 degree-of-freedom nonlinear simulation. The simulation results revealed surprisingly good performance, considering the limitation on sensors.

I. Introduction

The Department of Electrical Engineering at the United States Air Force Academy is attempting, through one of its senior design courses, to design, build, and fly a computer controlled aircraft. The Department of Aeronautics was asked to help design the flight control system to be implemented by the on-board digital computer. The project involved building and testing a wind tunnel model of the aircraft to determine its aerodynamic characteristics, performing mass tests on the actual aircraft to determine inertia characteristics, developing a 12 degree-of-freedom nonlinear aircraft simulation program, and designing the actual flight control system. This report describes only the last task.

II. Aircraft Description

The aircraft acquired by the Electrical Engineering Department is an off the shelf hobby radio controlled airplane called the "Big Stick" sold by Hobby Shack in kit form. This particular aircraft was chosen for its large size and docile handling qualities. The aircraft is

---

*Major, USAF, Assistant Prof., Dept. of Aeronautics, USAFA.

configured for normal radio controlled operation to allow for initial testing, manual backup/overide for safety, and manual takeoffs and landings. The aircraft is propeller powered by a 2.5 brake horsepower (BHP) two-stroke-cycle gasoline Quadra 35 engine. The aircraft (see Fig. 1) has a wingspan of 8.73 feet. The estimated weight with full fuel and computer on board is 30 pounds. The tricycle landing gear configuration, as shown in the picture, was later modified to conventional (tail wheel) for structural reasons and to facilitate operation on grass.

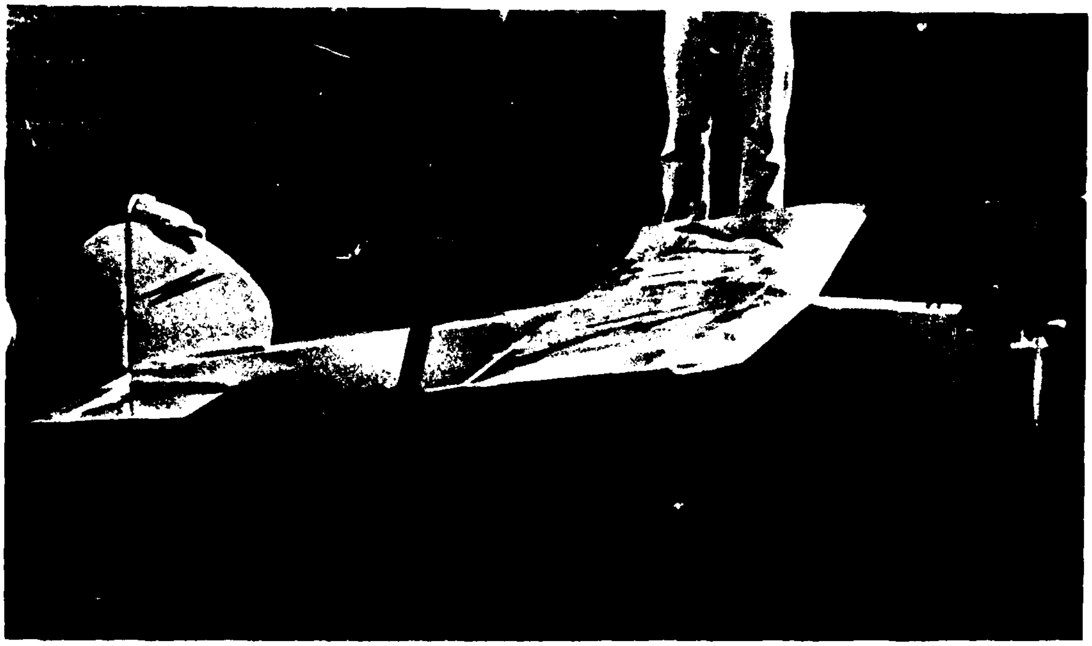

Figure 1. The Big Stick Airplane

The aircraft is controlled by conventional ailerons, rudder, elevator, and throttle. Drawings for the .122 scale wind tunnel model are contained in Appendix A.

III. The Control Problem

The purpose of the flight control system is to make the aircraft fly an arbitrarily specified (and not necessarily straight) path given continuous information on the current state of the aircraft through a limited number of sensors. The design of the flight control system was formulated as a multi-input multi-output feedback control problem. The actual parameters to be controlled were specified as altitude (h), airspeed (V), and heading (ψ).

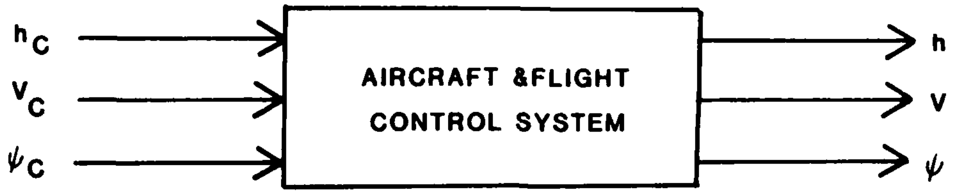

Figure 2. The Control Problem

Referring to Figure 2, the control problem can be visualized as one of driving the values of h, V, and ψ to those of h_c, V_c, and ψ_c, respectively, where c denotes the commanded value.

The flight control system makes inputs to the aircraft by adjusting the settings or deflections of the elevator (δ_e), throttle (δ_T), ailerons (δ_a), and rudder (δ_r). These control settings depend on the sensor measurements, which contain information about the actual state of the aircraft, and the commanded values of altitude, airspeed, and heading. This process is depicted in Figure 3.

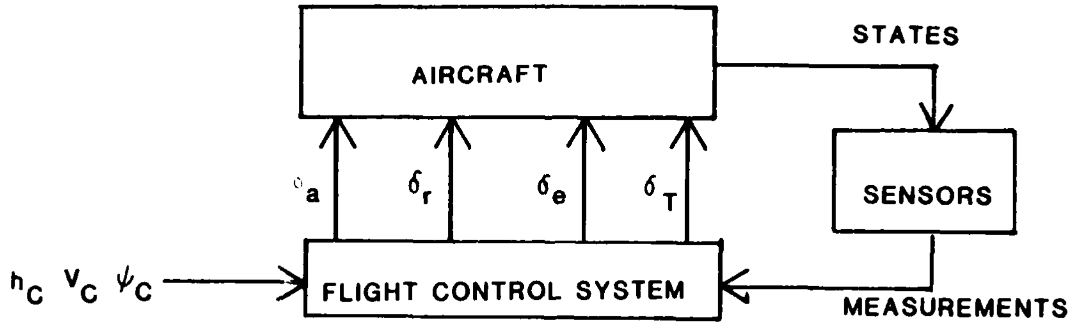

Figure 3. Control Process

The control system design problem, stated simply, was to find an algorithm to convert the commands and sensor measurements into the proper control settings to make the aircraft fly according to the commands.

Due to cost constraints, the sensors available for the project were limited to a yaw rate gyro, a lateral accelerometer, a heading indicator, an altimeter, and an airspeed meter. This is a very limited set of measurements considering the job required; therefore, it was feared that design of a satisfactory control system might prove impossible. For instance, note that there are no position gyros. This means that the control system is required to roll the aircraft in and out of turns with no feedback whatsoever as to the bank angle of the aircraft. Almost all three-axis autopilots in use today have position gryos for yaw, pitch, and roll angle measurements.

For design purposes, the measurements available to the flight control system were:

n_y	lateral load factor
r	yaw rate
	heading

h	altitude
V	airspeed
$\dot{h}$	rate of climb (to be derived by numerically differentiating h)

IV. Design Procedure

"Classical" control theory methods (LaPlace tranforms and root loci) were used in the design of this control system as opposed to "modern" optimal control techniques (although the state-space matrix representation was borrowed from modern theory).

Two important simplifications were made and carried throughout the entire design procedure. The first was that the control system was continuous instead of discrete. (Recall that the control system is to be implemented by a digital computer.) This assumption is not too unreasonable provided the cycle time of the computer is quite a bit faster than the aircraft response. The second simplification was that of perfect sensors. This means that the measurements of the aircraft's state provided to the control system are true and uncorrupted by noise. This simplification may or may not be valid, depending on the quality of the sensors. As is the case in many feedback control design problems, the sensors were of minor concern during the design process, but their performance will make or break the flight control system when it is implemented in the actual aircraft.

The design procedure consisted of four major steps:

1. Determining the control system structure
2. Formulating the complete system linear model
3. Selecting the control system gains
4. Checking the control system performance in a nonlinear simulation.

A. Control System Structure

The control system structure or framework was arrived at by paralleling the way a pilot flys an aircraft in instrument conditions without attitude information. (This type of flying is referred to as "needle, ball, and airspeed" flying and is normally only done as an emergency procedure following an attitude indicator failure.) The structure is shown in the block diagram in Figure 4.

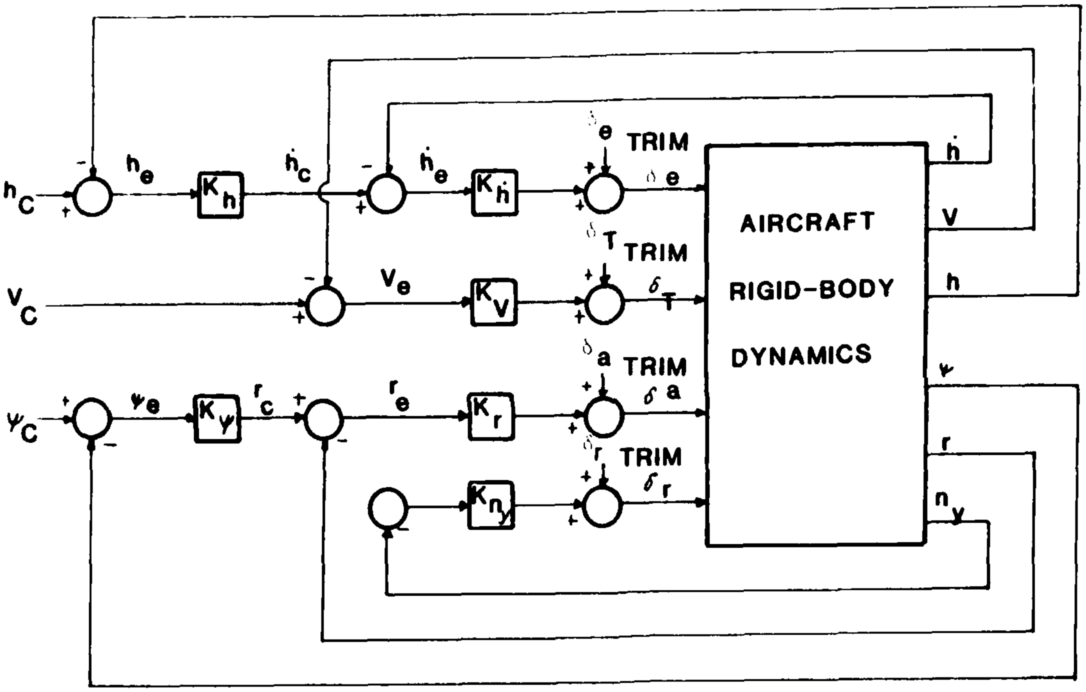

Figure 4. Flight Control System Structure (Basic)

In the block diagram (Figure 4) the squares with K's in them function to multiply the input signal by the constant, K, which is called a gain. The circles represent summers that subtract and add signals. The subscript, c, denotes a commanded value, as before. The e subscript denotes an error value which is the difference between the commanded value and the actual value. The trim control values were added to allow the control system to operate relative to some reference steady-state condition and also to allow for compensation of items impossible to account for in the math model, such as wing warp, propeller torque, etc.

To see how the system works, let's look at the aileron (δ_a) control loop which is driven by heading (ψ). Suppose ψ_c is 015 degrees (.262 rad.) but the actual heading, ψ, is 0 degrees or north. ψ_e then is .262 rad. This will result in a commanded yaw rate (r_c) of ψ_e x K_ψ rad/s. If the aircraft currently has zero yaw rate, r_e will also be ψ_e x K_ψ rad/s. From the diagram, δ_a will now be r_e x K_r more than $\delta_{a_{trim}}$. This will cause the aircraft to bank to the right and develop a positive yaw rate. As r approaches r_c, r_e gradually decreases and the aileron deflection is reduced. The aircraft is now turning. *As ψ approaches ψ_c, r_c decreases and r_e goes negative.* This deflects the ailerons in the opposite direction to gradually roll the aircraft out as ψ_c is approached. It is instructive to note that r is not exactly equal to the rate of change of ψ. However, it is close for small bank angles. (The same situation exists for the pilot flying needle, ball, and airspeed.) Heading is usually controlled much more effectively through bank angle but that measurement is not available. The other loops work in much the same fashion. The rudder is used solely to keep the aircraft coordinated, that is, to null out any lateral load factor. The pilot does this the same way by watching the ball (skid/slip indicator).

The control structure was later modified to include a yaw damper when the aircraft equations showed a highly oscillatory dutch roll mode (lightly damped oscillations in yaw). As can be seen in Figure 5, this modification consists of feeding the yaw rate back through the rudder to damp out the yaw oscillations. The washout component is a high pass filter that prevents the rudder from fighting the commanded yaw rate. Although the yaw damper gain, K_{YD}, was included in the following analyses, the washout filter was not.

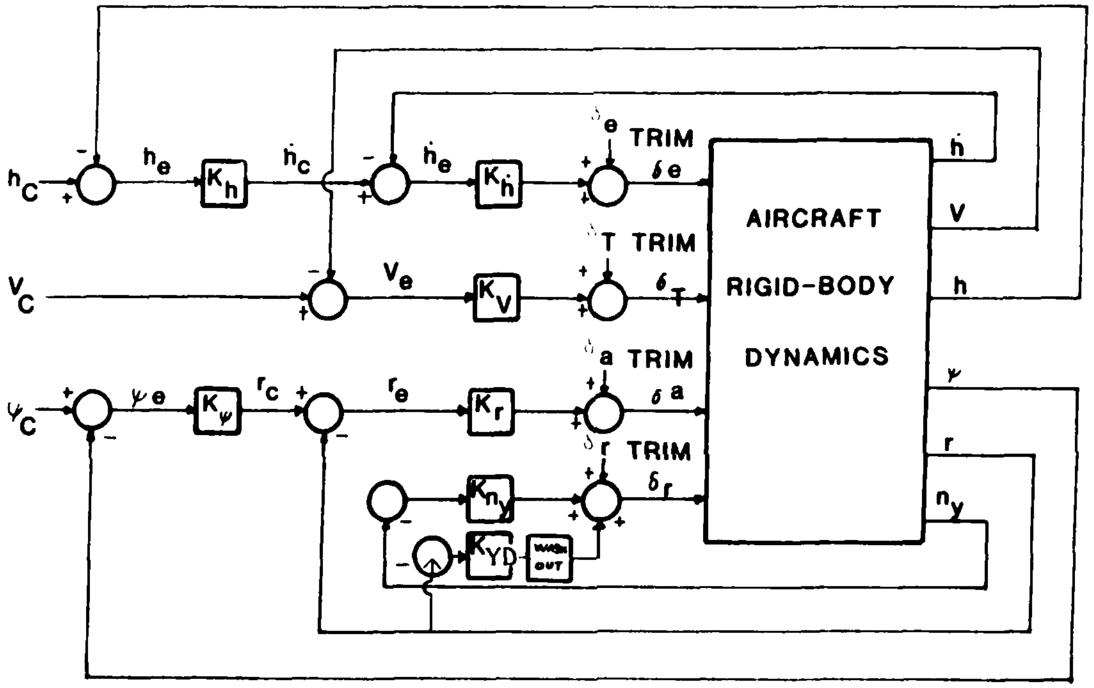

Figure 5. Flight Control System Structure (Modified)

With the control structure defined, the problem remaining was to determine the values of the gains.

B. Linearized System Model

The method used to determine the control gains required a linear system model, that is, a system described by linear differential equations. The linear model for the aircraft was derived using the methods of Reference 1. The necessary aerodynamic data was obtained by wind tunnel testing conducted in the Air Force Academy's low speed wind tunnel by Cadets First Class Charles T. Myers and Daniel A. Draeger and by estimation methods contained in Reference 5. The required mass data was obtained by Cadet First Class Thomas A. O'Berg through inertia testing of the actual aircraft. All of the aircraft data used are contained in Appendix B. The actual aircraft model is assembled in Appendix C.

The aircraft equations of motion were linearized about a steady-state flight condition of straight and level at 7500 feet, standard day, and a true airspeed of 73.33 ft/s (50mph). The usual two independent sets of coupled equations were obtained and are listed below in matrix form.

Longitudinal:

$$\begin{bmatrix} \dot{q} \\ \dot{\theta} \\ \dot{u} \\ \dot{\alpha} \\ \dot{h} \end{bmatrix} = \begin{bmatrix} -3.733 & 0 & .01189 & -1.341 & 0 \\ 1 & 0 & 0 & 0 & 0 \\ 0 & -32.2 & -.2566 & 10.01 & 0 \\ .9193 & 0 & -.01169 & -4.642 & 0 \\ 0 & 73.33 & 0 & -73.33 & 0 \end{bmatrix} \begin{bmatrix} q \\ \theta \\ u \\ \alpha \\ h \end{bmatrix} + \begin{bmatrix} -.2033 & 0 \\ 0 & 0 \\ -.0257 & 5.63 \\ -.0057 & 0 \\ 0 & 0 \end{bmatrix} \begin{bmatrix} \delta_e \\ \delta_T \end{bmatrix}$$

where: q = pitch rate in rad/s

θ = pitch angle change from steady-state in rad.

u = change in velocity component along longitudinal axis in ft/s

α = angle of attack change in rad.

h = altitude change from steady-state in ft.

δ_e = elevator deflection change from trim in deg.

δ_T = throttle change from trim in brake horsepower (BHP)

Lateral-directional:

$$\begin{bmatrix} \dot{\beta} \\ \dot{p} \\ \dot{r} \\ \dot{\phi} \\ \dot{\psi} \end{bmatrix} = \begin{bmatrix} -.5366 & -.000278 & -.9875 & .439 & 0 \\ -33.18 & -8.55 & 2.41 & 0 & 0 \\ 16.7 & .72 & -.448 & 0 & 0 \\ 0 & 1 & 0 & 0 & 0 \\ 0 & 0 & 1 & 0 & 0 \end{bmatrix} \begin{bmatrix} \beta \\ p \\ r \\ \phi \\ \psi \end{bmatrix} + \begin{bmatrix} 0 & .00274 \\ 10.14 & .48 \\ -1.17 & -.157 \\ & \\ 0 & 0 \end{bmatrix} \begin{bmatrix} \delta_a \\ \delta_r \end{bmatrix}$$

where: β = sideslip angle in rad.

p = roll rate in rad/s

r = yaw rate in rad/s

ϕ = roll angle in rad.

ψ = heading change from steady-state in rad.

δ_a = aileron deflection change from trim in deg.

δ_r = rudder deflection change from trim in deg.

Note that velocity, altitude, and heading (u, h, ψ) are now pertubation values from the reference flight condition. For example, an altitude of 7000 feet would be represented by $h = -500$ ft. Figure 5 is still perfectly valid if the command values are also pertubation values.

Each of these equations can be written in the standard state variable form as:

$$\dot{\bar{x}} = [A]\,\bar{x} + [B]\,\bar{u} \tag{3}$$

where $\bar{x}$ is defined as the state vector and $\bar{u}$ is defined as the control vector. The components of the state vector (such as h and r) are called states. [A] and [B] are referred to as the system and control matrices, respectively.

These matrix equations describe the aircraft only. It is necessary to combine the control system and the aircraft or "close the loop". Referring to Figure 5, it can be seen that the control inputs will be linear, algebraic combinations of the measurements and the commands. (As mentioned earlier, we are ignoring the washout filter.) The measurements, in turn, are all either states themselves or linear, algebraic combinations of the states. Equation 1 shows that this is true for the measurement $\dot{h}$. This is also true for n_y[1]. V is closely approximated by u. It is possible, then, in both the longitudinal and lateral-directional cases to express the controls as:

$$\bar{u} = -[F]\,\bar{x} + [B']\,\bar{u}_c \tag{4}$$

where [F] is called the feedback matrix and [B′] is called the input matrix. The vector $\bar{u}_c$ is the command which is defined as $[h_c, V_c]^T$ for the longitudinal case and $[\psi_c, 0]^T$ for the lateral-directional case.

From Figure 5 and Equation 1 and 2 the feedback and input matrices were determined to be as follows:

For the longitudinal model:

$$[F] = \begin{bmatrix} 0 & 73.33K_{\dot{h}} & 0 & -73.33K_{\dot{h}} & K_h K_{\dot{h}} \\ 0 & 0 & K_V & 0 & 0 \end{bmatrix} \tag{5}$$

$$[B'] = \begin{bmatrix} K_h K_{\dot{h}} & 0 \\ 0 & K_V \end{bmatrix} \tag{6}$$

---

[1] n_y is lateral load factor which is equal and opposite to nongravitational lateral acceleration, normalized to the acceleration of gravity, g. It can be shown from Reference 1 and Appendix C that for the linearized approximation,
$n_y = 1.222\beta + .000634p - .0285\,r - .00624\delta_r$, which is a linear, algebraic combination of the states. (δ_r is a combination of the states only, since there are no commands that feed into the rudder.)

For the lateral-directional model:

$$[F] = \begin{bmatrix} 0 & 0 & K_r & 0 & K_\psi K_r \\ \dfrac{1.22K_{ny}}{1-.00624K_{ny}} & \dfrac{.000634K_{ny}}{1-.00624K_{ny}} & \dfrac{K_{YD} - .0285K_{ny}}{1-.00624K_{ny}} & 0 & 0 \end{bmatrix} \quad (7)$$

$$[B'] = \begin{bmatrix} K_\psi K_r & 0 \\ 0 & 0 \end{bmatrix} \quad (8)$$

By substituting (4) into (3), we obtain

$$\dot{\overline{x}} = [A]\,\overline{x} + [B]\,\left\{-[F]\,\overline{x} + [B']\,\overline{u}_c\right\}. \quad (9)$$

Combining terms gives

$$\dot{\overline{x}} = [A - BF]\,\overline{x} + [BB']\,\overline{u}_c \quad (10)$$

The complete linearized system model (or closed-loop system), then, consists of two independent equations of the form of Equation 10 -- one for longitudinal motion and one for lateral-directional motion. The vectors and constant matrices have been defined for each case.

C. Determination of Control System Gains

The core of the feedback control problem is the selection of the control gains. In this project, that means finding values of K_h, $K_{\dot{h}}$, K_V, K_ψ, K_r, K_{ny}, and K_{YD} that give satisfactory response to aircraft heading, altitude, and airspeed commands in the presence of disturbances such as wind gusts.

The response of any linear dynamic system is characterized by the roots of its characteristic equation (also called system poles or eigenvalues). Root loci were used in this project to select the gains. A root locus is a complex plane plot showing how a pole varies as a gain is changed. By way of review, the sign of the real part of the pole indicates the stability of its associated mode (- for stable, + for unstable, 0 for neutral) and the imaginary part indicates the oscillation frequency (aperiodic if real). Complex poles occur in conjugate pairs. The magnitude of the pole (distance from origin) indicates the speed of the associated mode. For example, in Figure 6, poles 1, 2, and 5 are aperiodic. Poles 1 and 5 are stable while 2 is unstable. The mode associated with pole 5 will die out faster than the one associated with pole 1. The complex conjugate pairs 3 and 4 represent oscillatory modes. Mode 3 is stable and 4 is unstable.

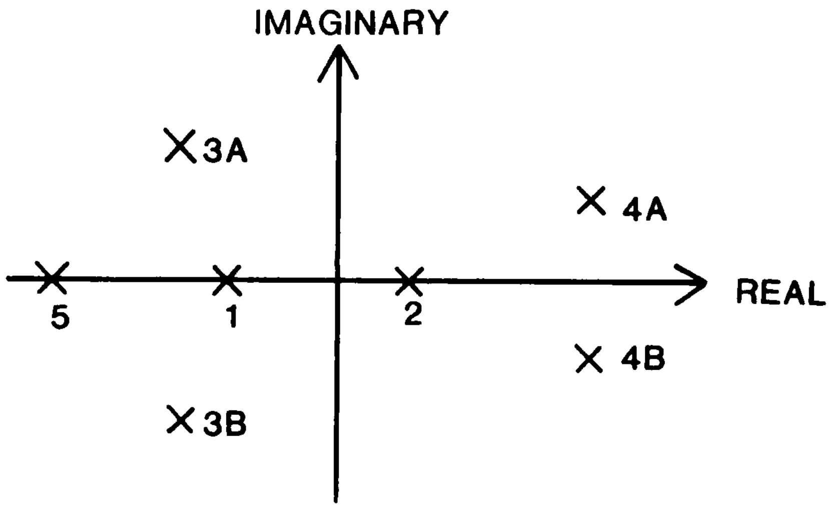

Figure 6. Poles on the Complex Plane

It can be shown (Ref. 4) that the characteristic equation of a system described by Equation 3 is det(λ[I] - [A]) = 0 where λ is an arbitrary scalar number and [I] is an identity matrix. The solutions of the equation for λ are the poles. We are interested in the poles of the closed-loop system, Equation 10. These can be determined by solving det(λ[I] - [A-BF]) = 0. The F matrix, of course, depends on the gains.

The root loci were constructed by varying the gains and solving for the poles after each change. This process had to be computerized. Separate programs were written on an Apple microcomputer for the longitudinal and lateral-directional cases. The results are discussed in the next section.

D. Nonlinear Simulation

A 12 degree of freedom nonlinear Big Stick simulation program was written for the Burroughs 6900 computer at the Air Force Academy by Cadet First Class Daniel A. Draeger. A hard copy is included in Appendix D. This simulation provides a much more accurate mathematical model of the aircraft than the linearized equations which were used to determine the control gains. Basically, the program numerically integrates the nonlinear aircraft equations of motion from Reference 1, modified to include the control system, and plots out any of the state variables versus time. The nonlinear equations do not decouple into longitudinal and lateral-directional sets.

The simulation was run to see how the control gains, selected under the linear assumption, would actually perform in the real, nonlinear world. The effects of such elements as control deflection limits and changes in air density could be observed. The simulation was also used to check the limiting values for r_c and $\dot{h}_c$. These are cutoff values which had to be incorporated into K_h and K_ψ to prevent the aircraft from stalling itself out or entering a steep dive in the case of a big change in h_c or rolling inverted when ψ_c changed. A side benefit of the simulation is that it provides a check on the previous calculations. Performance should be close to the linear prediction around the steady-state condition.

The simulation results for the selected gains are presented in the next section.

V. Results

A. Root Loci

In multi-loop feedback systems, such as the one being dealt with in this report, the gains affect the system poles in an interrelated and complex fashion. A "shotgun" (trial and error) approach was used to initially find a neighborhood of gains that appeared to give reasonable poles. The gains were then varied in a more systematic fashion to refine the gain selection. Gains were selected on the basis of the speed and stability of the resulting poles. This was done separately for the longitudinal and lateral-directional cases.

1. Longitudinal case

The three longitudinal gains selected were: $K_{\dot{h}}=-.2$ deg/ft/s, $K_h=.2$ ft/s/ft, and $K_V=.1$ BHP/ft/s. Figure 7 shows a segment of the longitudinal root loci plot that indicates how the poles are affected by the gains around the selected values. Only the upper left quadrant of the complex plane is shown since any values in the right half plane are unstable and unacceptable and since the bottom half plane is a mirror image of the top. The actual values of the poles plotted are contained in the computer printout in Appendix E.

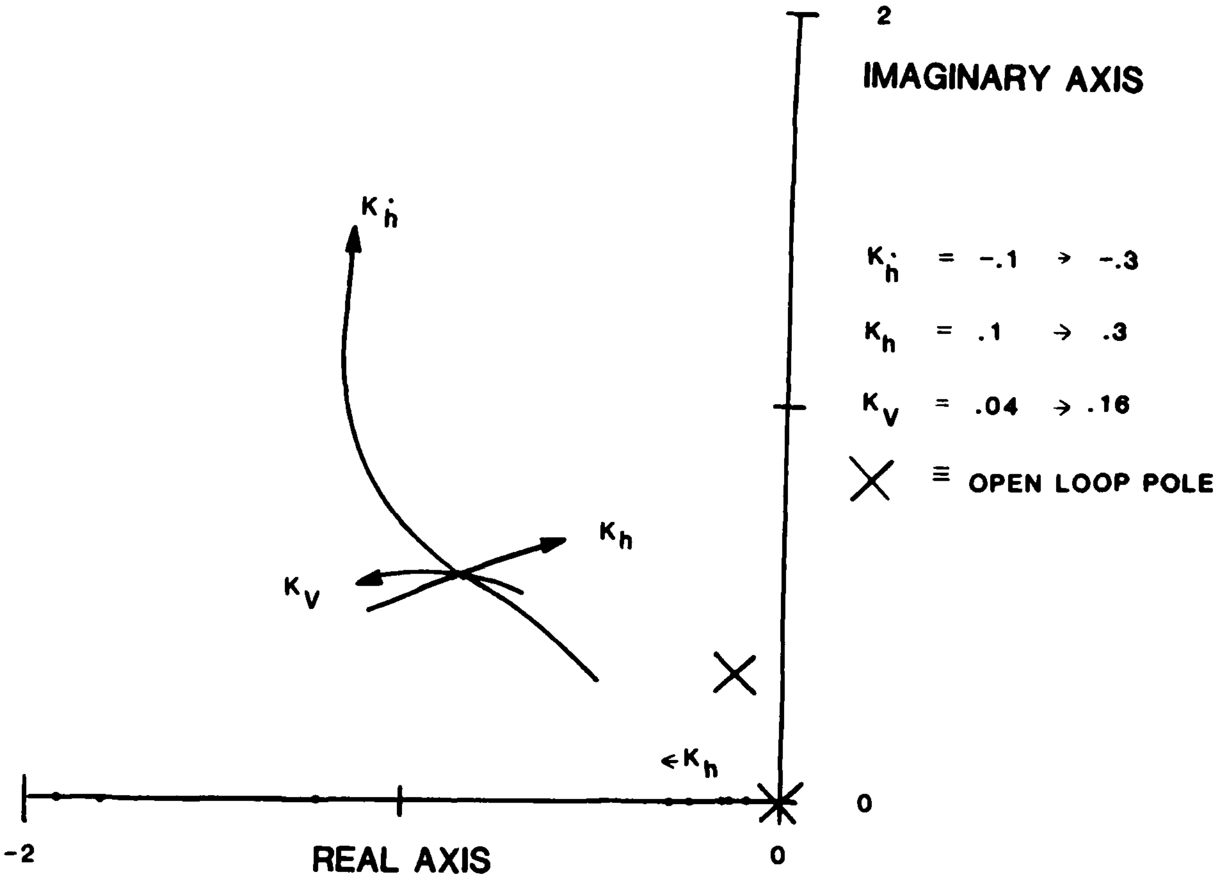

Figure 7. Longitudinal Root Loci

2. Lateral-directional case

The four lateral-directional gains selected were: K_{ny}=30 deg/g, K_r=1 deg/rad/sec, K_ψ =.1 rad/s/rad, and K_{YD}=-20 deg/rad/s. Figures 8 and 9 are the lateral-directional root loci plots. Figure 9 is a blow-up of the area around the origin in Figure 8. Again, a computer printout of the poles for each set of gains plotted is contained in Appendix E.

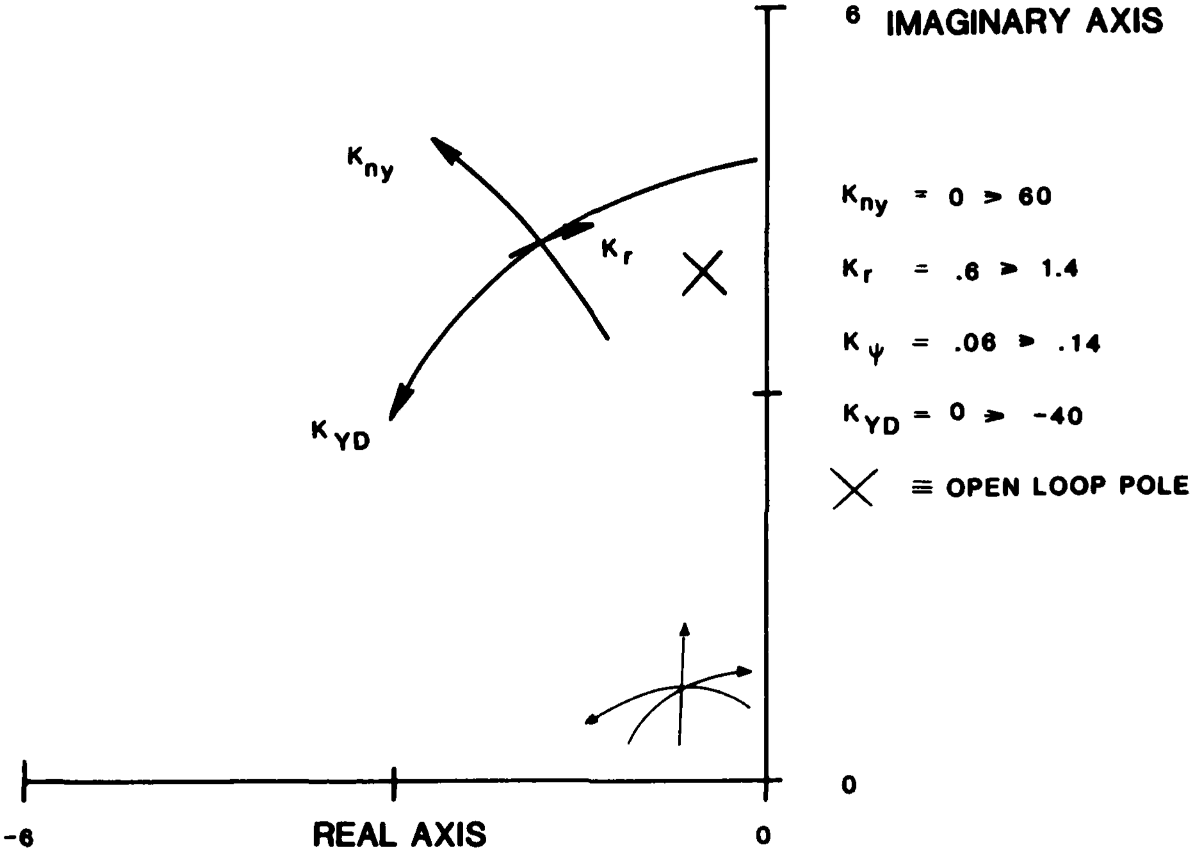

Figure 8. Lateral-Directional Root Loci

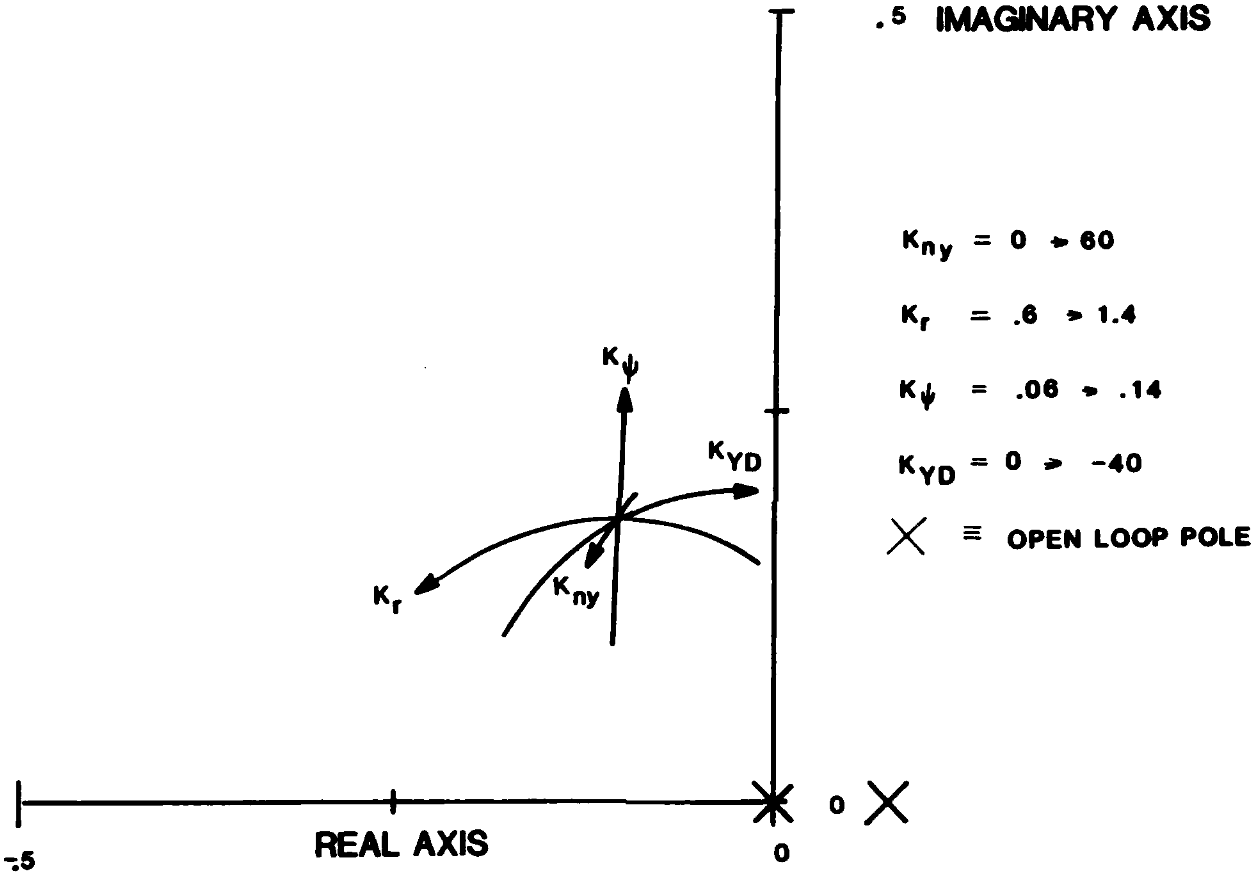

Figure 9. Lateral-Directional Root Loci (Blow-up)

B. Simulation

Simulations with the selected gains were run using the nonlinear simulation program of Appendix D. Limitations on control deflections and on some of the gains were added for reasons discussed in the last section. Four flight maneuvers were simulated. The initial conditions for each maneuver were the steady-state reference condition (straight and level with $\psi=0$, V=73.33 ft/s, and h=7500 ft). The four maneuvers were:

(1) level turn

(2) straight climb

(3) level, straight acceleration

(4) combination turn, descent, and deceleration

1. Nonlinear limits

The following control limits were used in the simulation based on estimated aircraft limits:

control	min.	max.
δe	-15 deg	15 deg
δT	0 BHP	3 BHP
δa	-15 deg	15 deg
δr	-15 deg	15 deg

Limits on commanded rate of climb ($\dot{h}_c$) were selected as ±11.5 ft/s. This corresponds to climb and descent angles of nine degrees. The climb would require about 2 BHP at steady-state. The commanded turn rate limit was selected as ±.12 rad/s. This equates to a bank angle of about 15 degrees and a turn radius of about 625 feet.

2. Level turn simulation

A level turn to a heading of 090 deg (1.57 rad) was commanded. The aircraft response is plotted in Figures 10-13. The slow oscillatory mode predicted in root loci Figure 9 can be seen in Figures 10 and 11 as the aircraft overshoots the commanded heading and corrects back. Note how this lateral-directional mode couples over into the longitudinal variables h and u in this nonlinear simulation (Figures 12 and 13). The aircraft does stabilize on its new heading in less than a minute after overshooting about 20 degrees. The altitude is held within 25 feet and the airspeed within 2 ft/s.

3. Straight climb simulation

A straight climb to 8000 feet was commanded. The aircraft response is plotted in Figures 14 and 15. Figure 14 shows that the aircraft enters a steady climb of approximately 10 ft/s. Approaching 8000 ft, it levels off nicely with little or no overshoot. Notice from Figure 15 that the control system is unable to keep the airspeed at the commanded value during the climb. Instead, the airspeed stabilizes at a value of about 6 ft/s below the commanded value. Due to the fact that there is no acceleration feedback, some steady-state error in velocity will always exist when not at the reference condition. (In the control literature, this is known as "type zero" behavior and is predictable from the linear analysis.) When the aircraft levels off, the control system is able to increase the airspeed back up to approximately the commanded value.

4. Level acceleration simulation

An acceleration to 90 ft/s was commanded. The aircraft response is plotted in Figure 16. As in the straight climb, a steady-state error of about 6 ft/s exists.

5. Multi-command simulation

To see how the aircraft would react to simultaneous commands, inputs of ψ_c=-1.05 rad (300 deg), h_c=7000 feet, and V_c=60 ft/s were made. The results are shown in Figures 17-20. As Figure 17 shows, the heading again overshoots but returns to the commanded value. From Figure 18 we can see that the aircraft levels off at a value slightly below 7000 feet. Figure 19 shows that the velocity goes through some gyrations. It stabilizes at about 70 ft/s in the descent and then reduces to about 62 ft/s when the aircraft pulls out of its dive. Figure 20 is a plot of the throttle activity during this maneuver. It shows the throttle at idle from the 5 to 13 second point. The power comes back in to about .05 BHP during the descent and then comes up to about .8 BHP after the aircraft levels out.

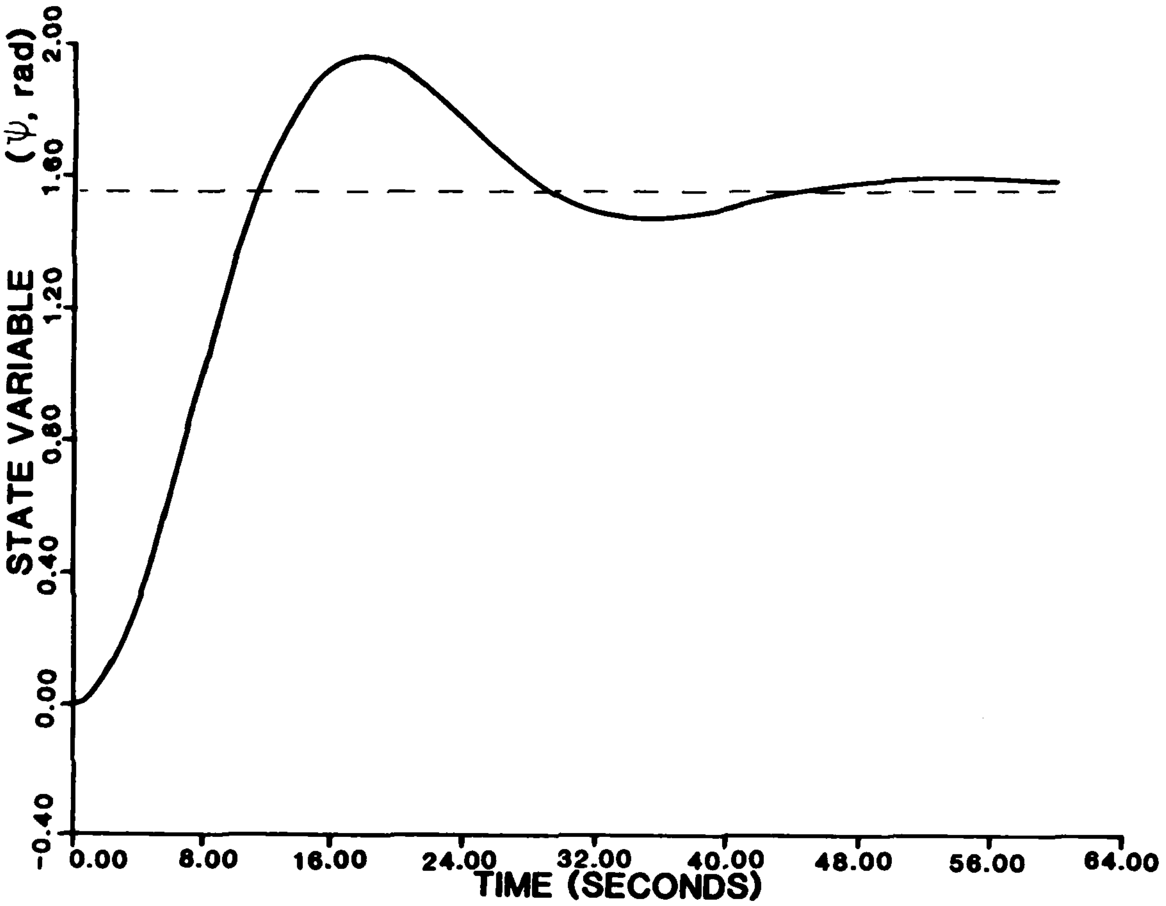

FLIGHT HISTORY

Figure 10. Level Turn Simulation - ψ

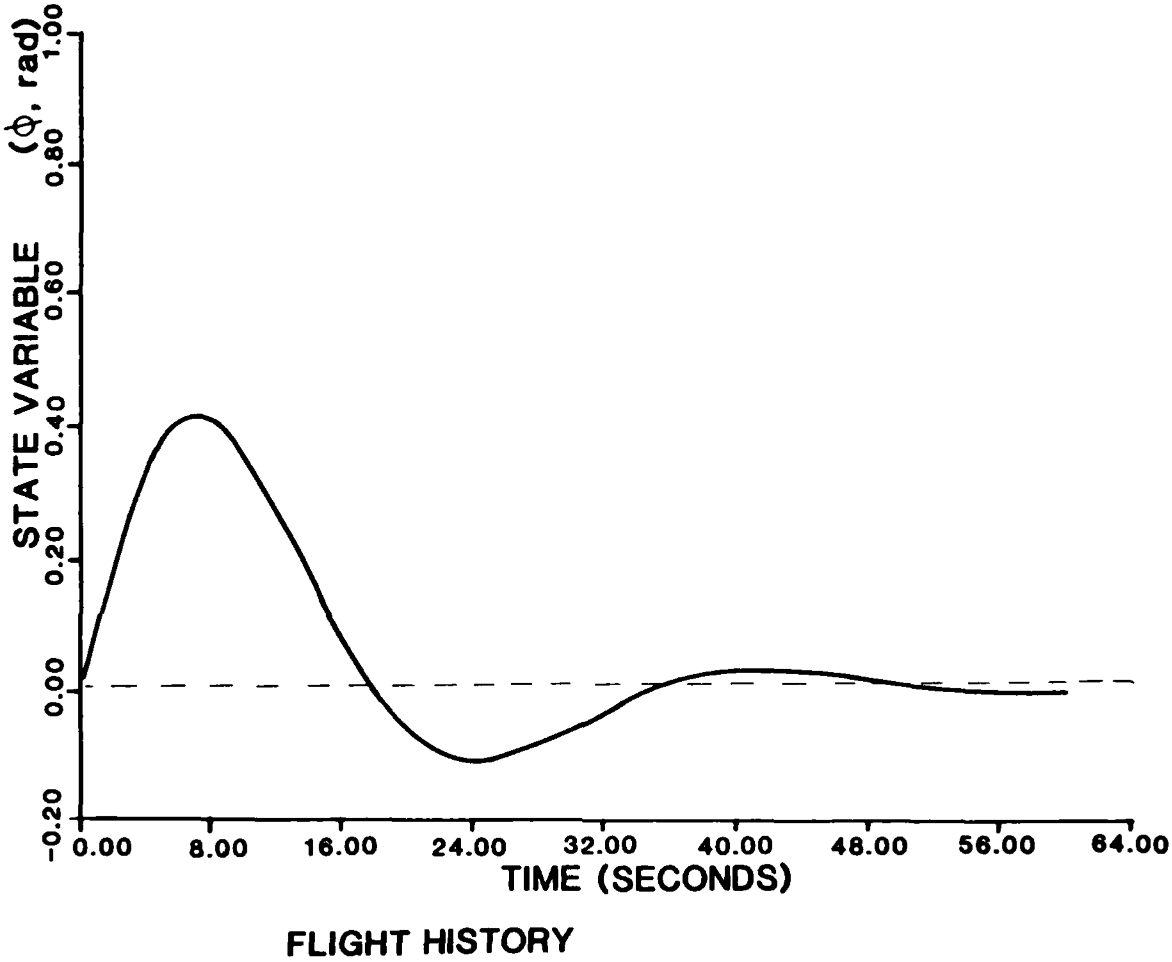

Figure 11. Level Turn Simulation - ϕ

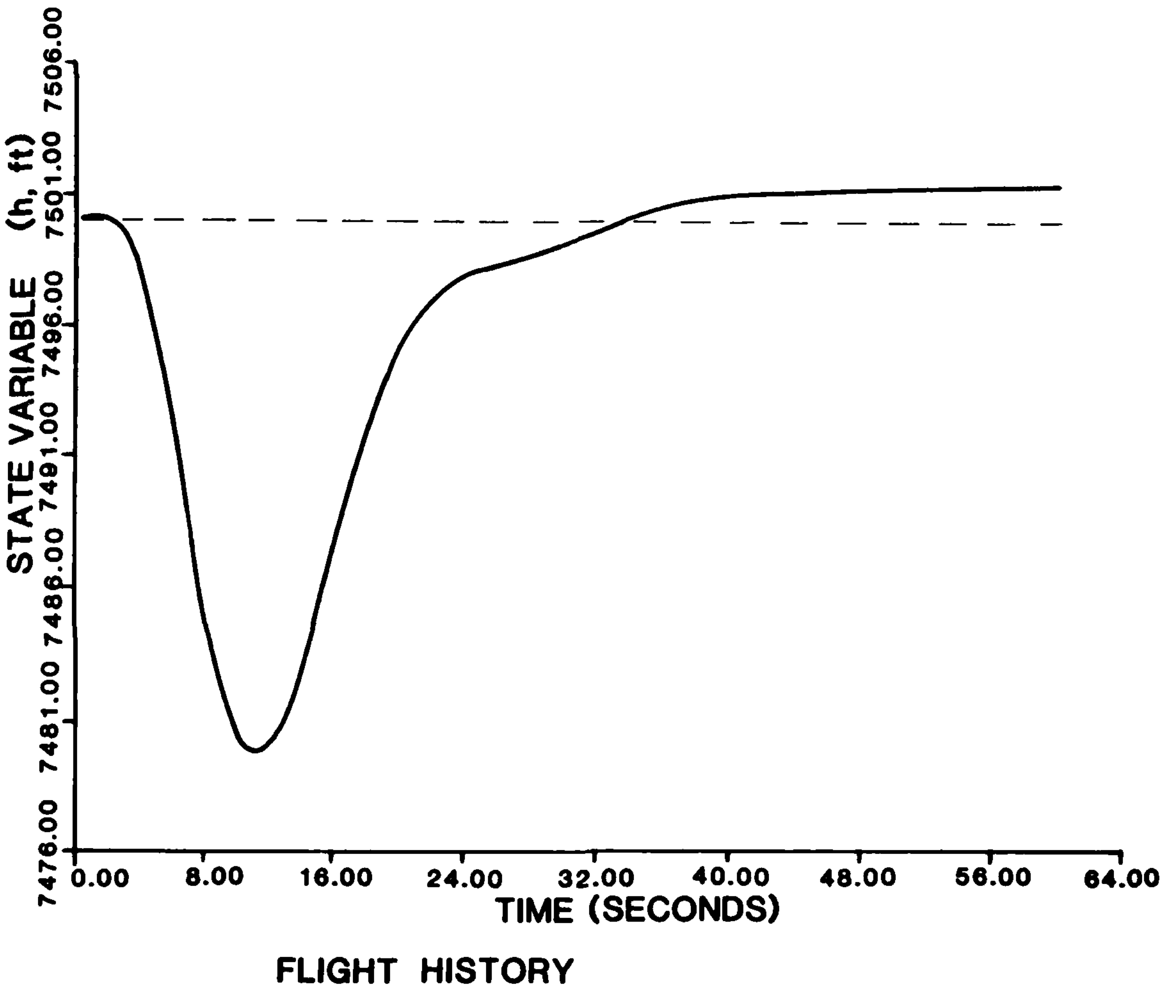

Figure 12. Level Turn Simulation - h

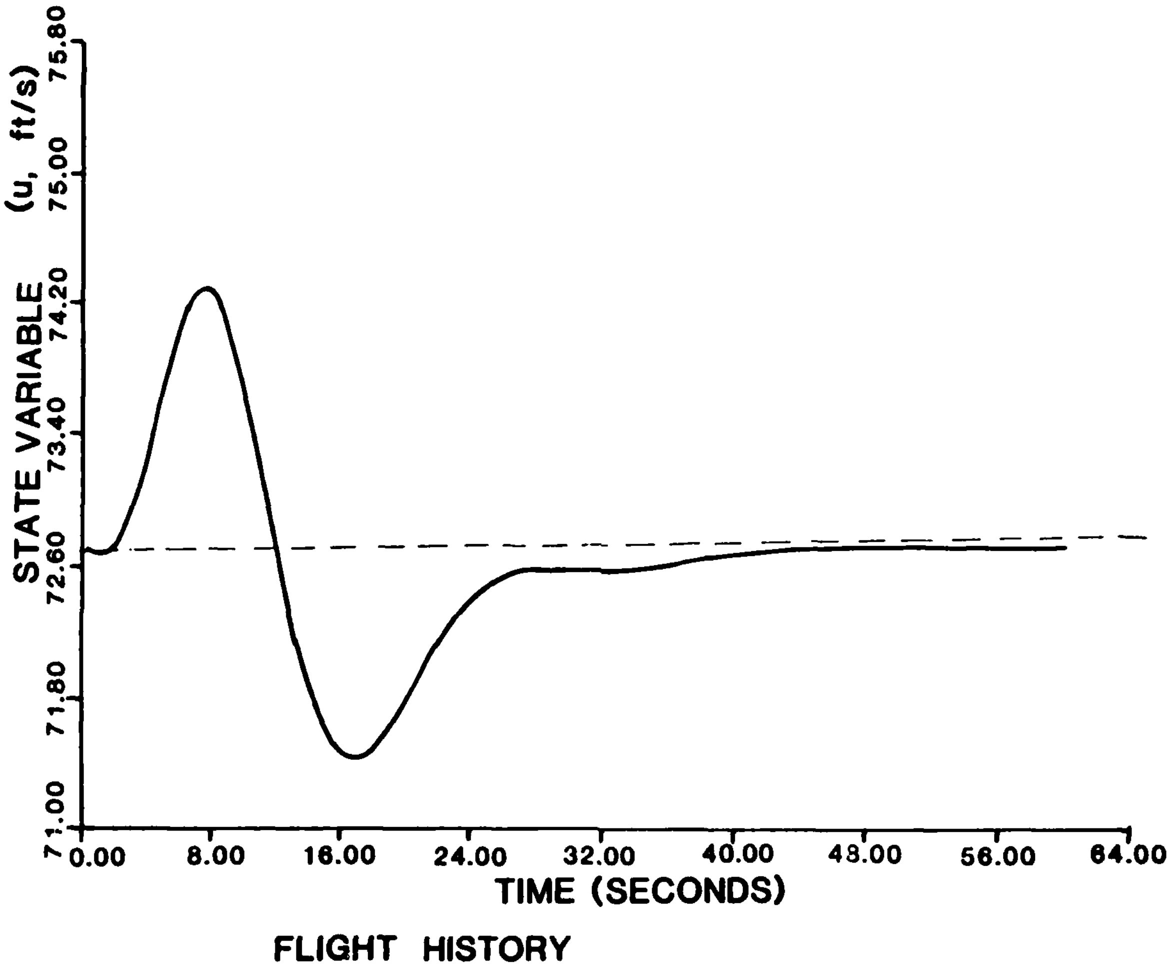

Figure 13. Level Turn Simulation - u

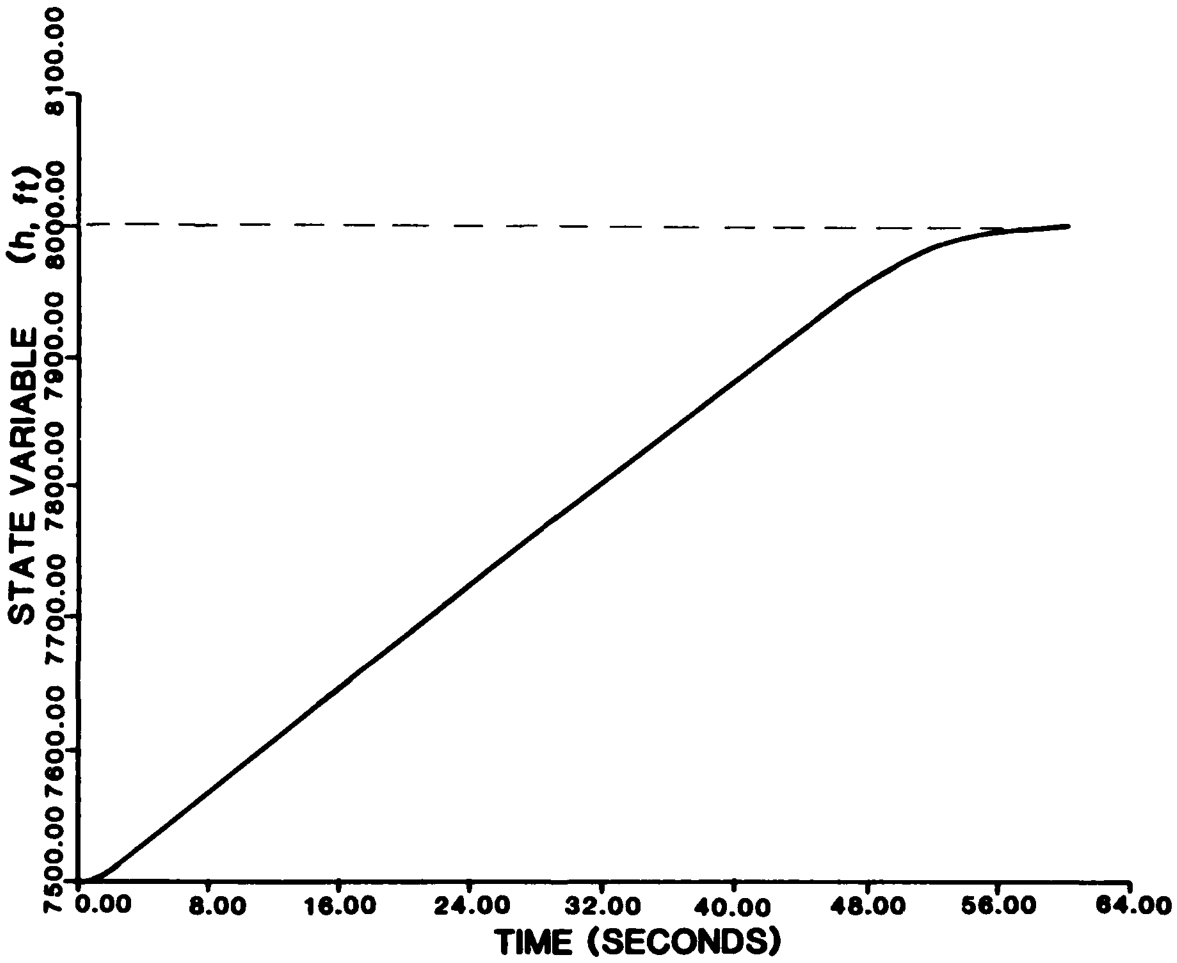

FLIGHT HISTORY

Figure 14. Straight Climb - h

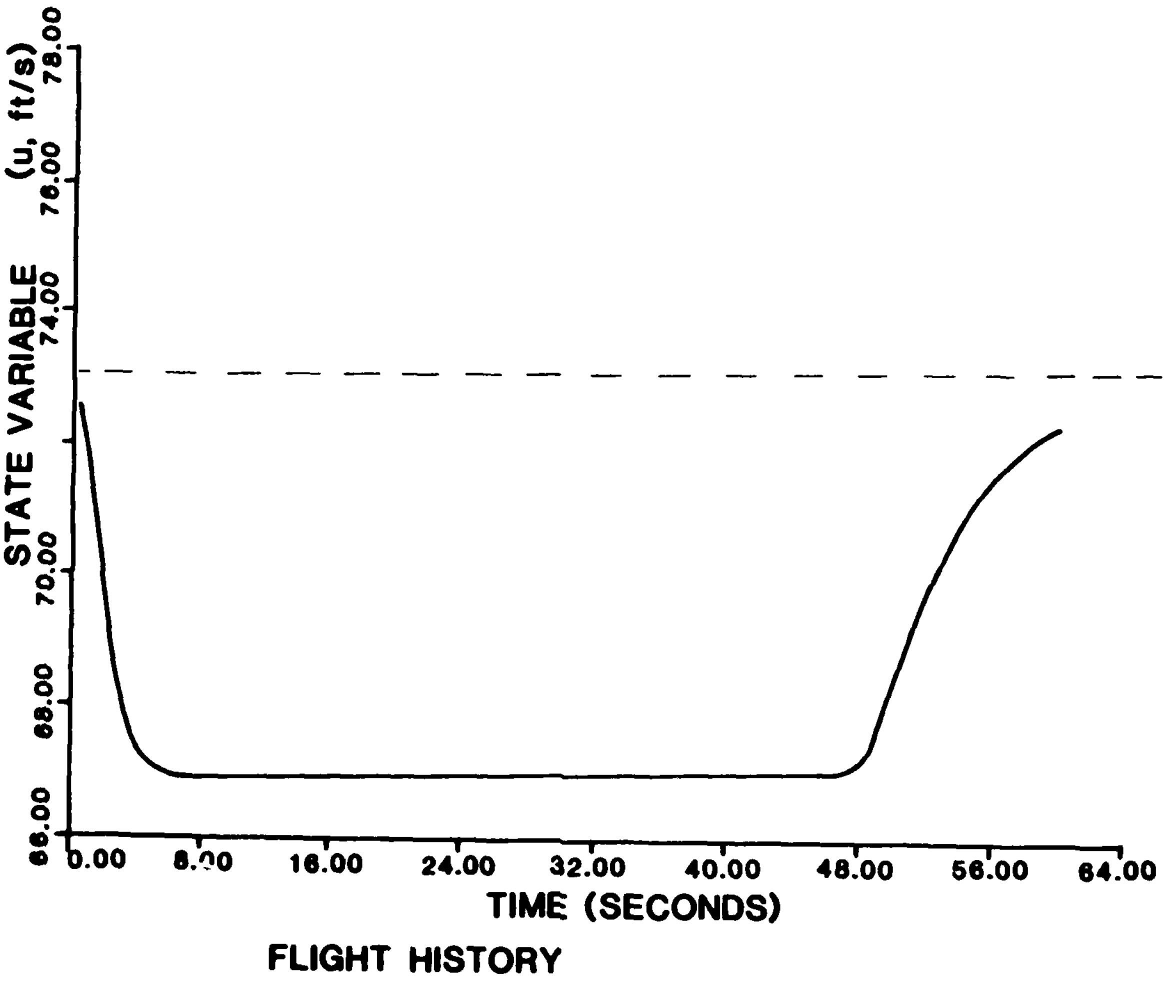

Figure 15. Straight Climb Simulation – u

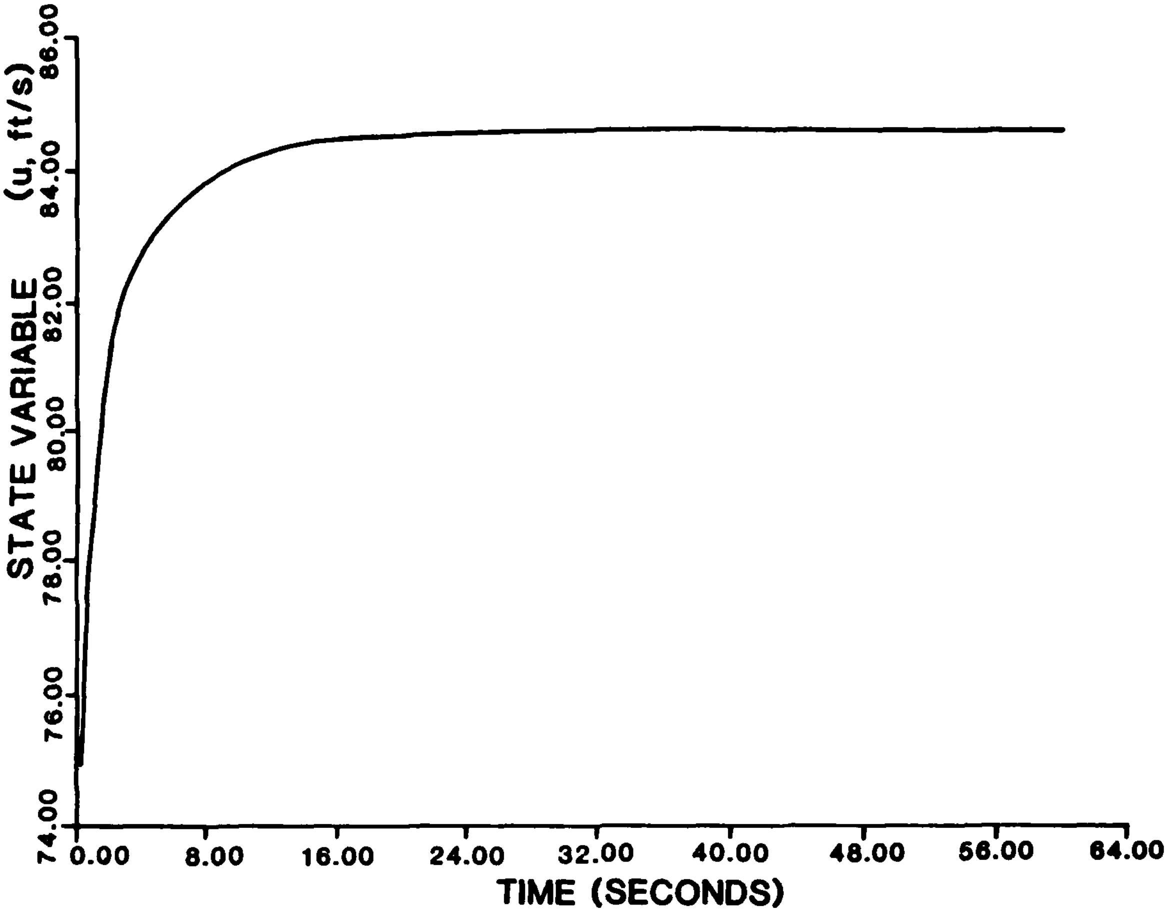

FLIGHT HISTORY

Figure 16. Level Acceleration Simulation - u

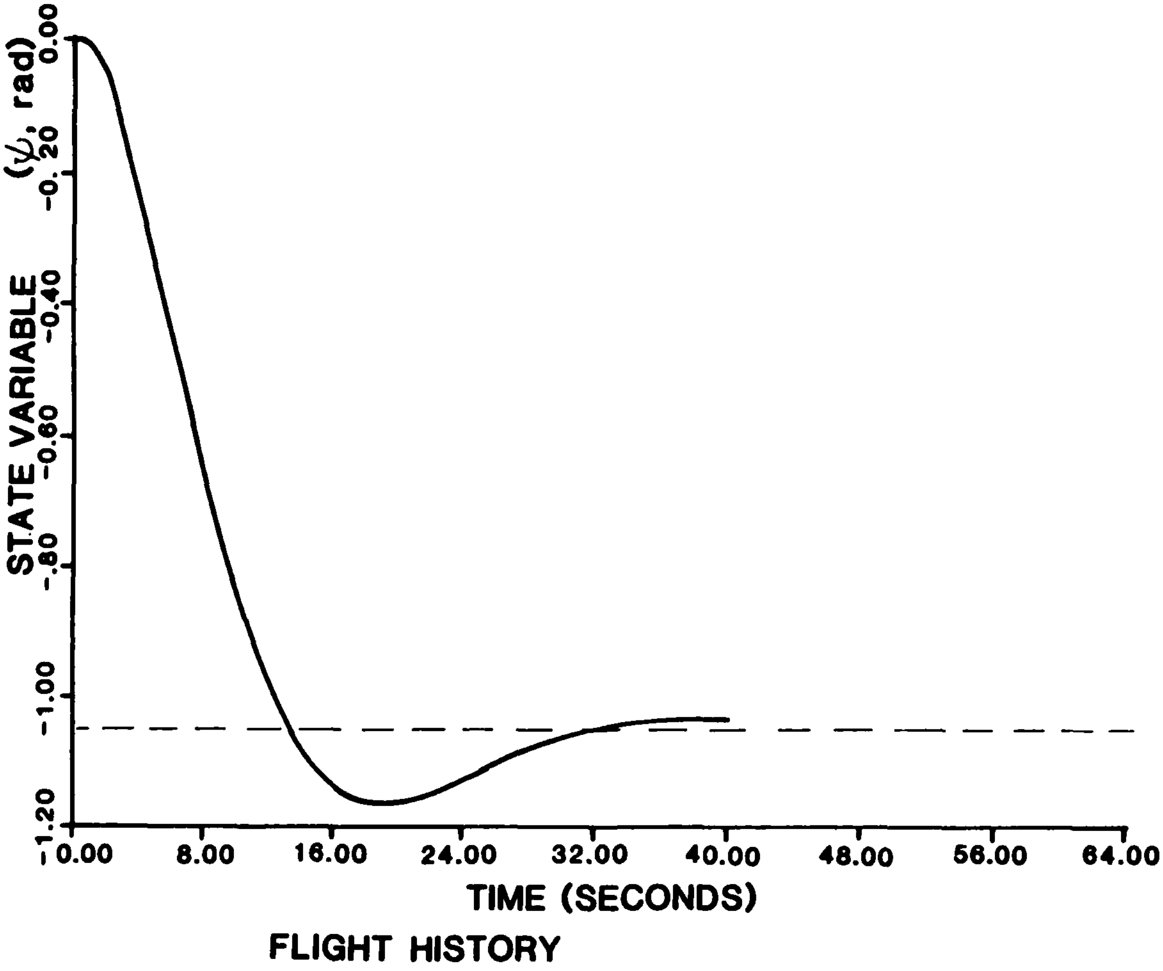

Figure 17. Multi-command Simulation - ψ

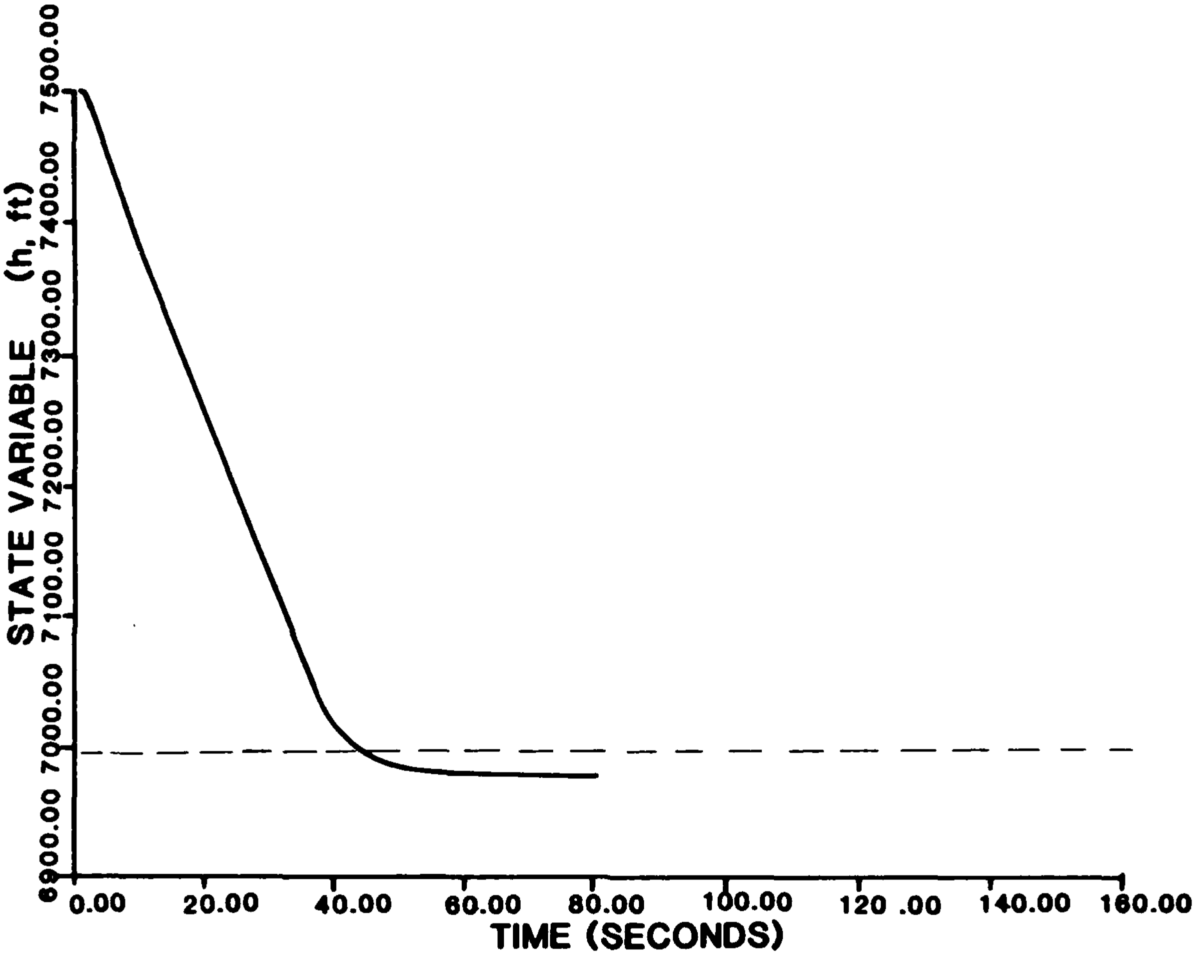

FLIGHT HISTORY

Figure 18. Multi-command Simulation - h

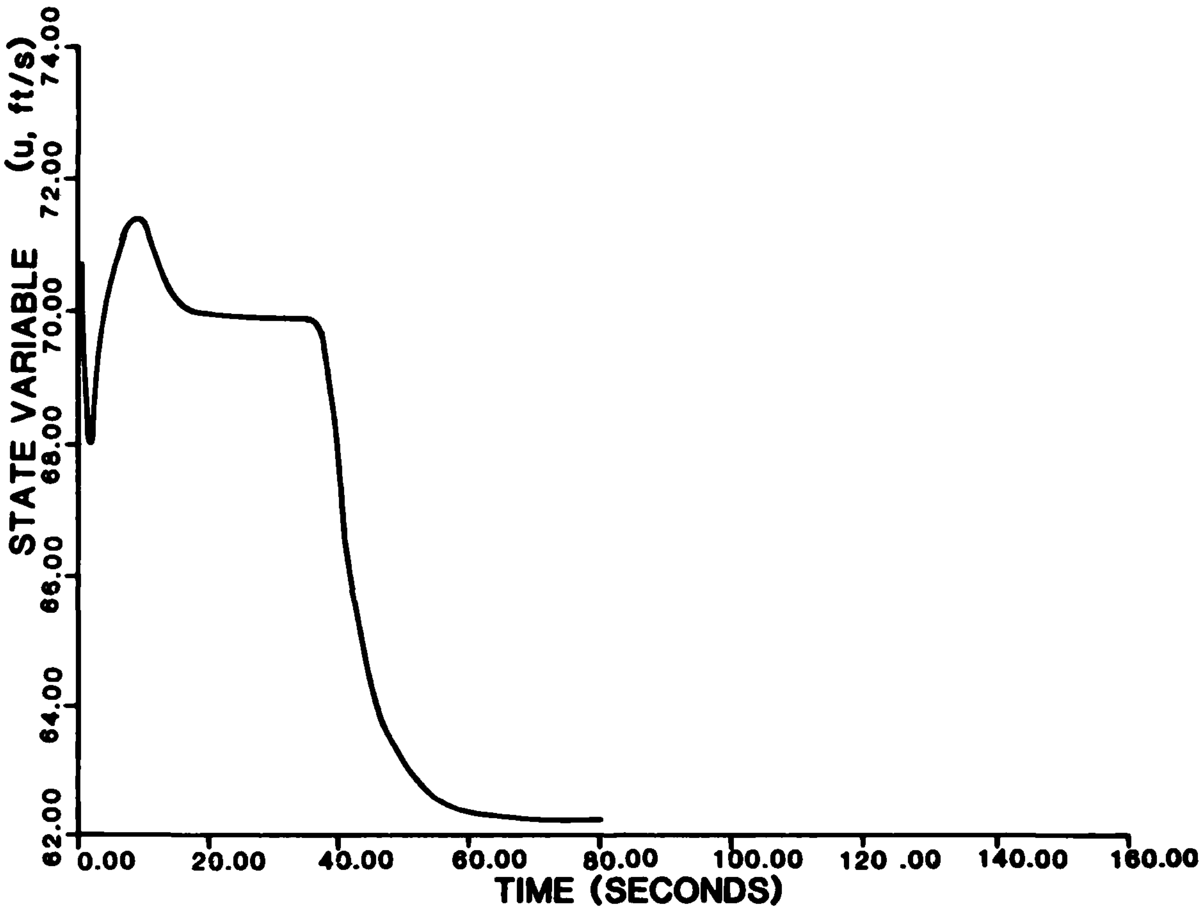

FLIGHT HISTORY

Figure 19. Multi-command Simulation - u

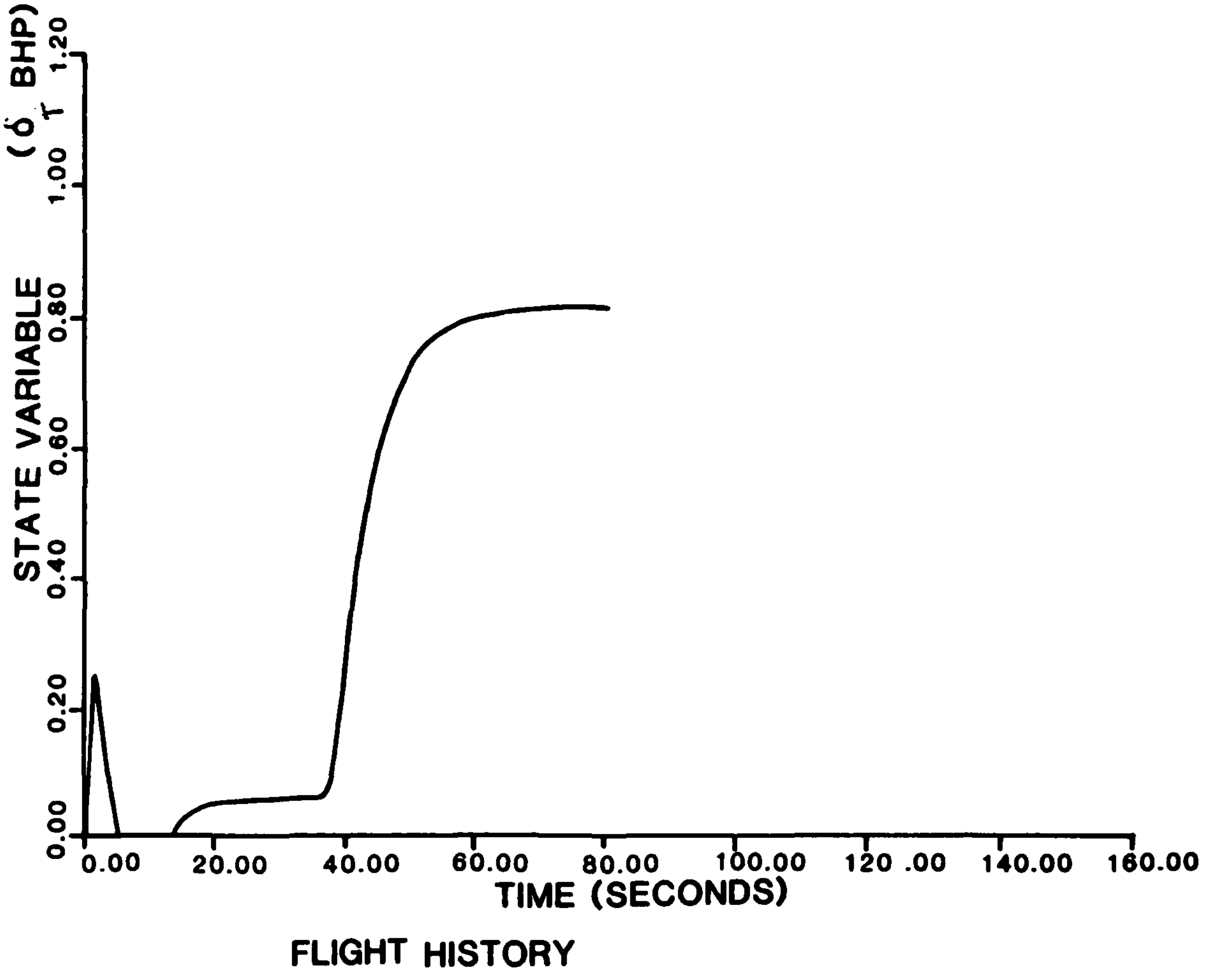

Figure 20. Multi-command Simulation - δ_T

VI. Recommendations

Based on the previous analysis, the following recommendations are made for the Big Stick flight control system:

1. That the control structure of Figure 5 be used.
2. That the following control gains be used:

   K_h = .2 (ft/s)/ft

   $K_{\dot{h}}$ = -.2 deg/(ft/s)

   K_V = .1 BHP/(ft/s)

   K_ψ = .1 (rad/s)/rad

   K_r = 1 deg/(rad/s)

   K_{ny} = 30 deg/g

   K_{YD} = -20 deg/(rad/s)
3. That $\dot{h}_c$ be limited to ±11.5 ft/s and r_c be limited to ± 12 rad/s.
4. That a washout filter be included in the yaw damper feedback loop to pass the dutch roll frequency (4 rad/s) and attenuate the steady-state commanded yaw rate.
5. That the trim control settings be determined from flight test at the steady-state flight condition of straight and level at 73.33 ft/s and 7500 feet.

In implementing the flight control system, the same sign conventions must, of course, be used as are used in the aircraft equations of motion. These are (from Appendices C and D and Reference 1):

δe positive for trailing edge down

δr positive for trailing edge left

δa positive for right up and left down, $\delta_a = (\delta_{a_L} + \delta_{a_R})/2$

r positive to right

ψ positive to right

n_y positive to right

References

1. Roskam, Jan, Airplane Flight Dynamics and Automatic Flight Controls, Roskam Aviation and Engineering Corporation, 1979.

2. Myers, Charles T. "Analysis of Stability and Control Coefficients for the 'Big Stick'," unpublished Aero 499 report for Department of Aeronautics, United States Air Force Academy, May 1983.

3. O'Berg, Thomas A. "Moment of Inertia Determination for the 'Big Stick' Aircraft," unpublished Aero 499 report for Department of Aeronautics, United States Air Force Academy, Dec. 1984.

4. Ogata, Katsuhiko, Modern Control Engineering, Prentice-Hall, Inc., Englewood Cliffs, N.J., 1970.

5. Roskam, Jan, Methods for Estimating Stability and Control Derivatives of Conventional Subsonic Airplanes, Roskam Aviation and Engineering Corporation, 1971.

APPENDICES

APPENDIX A . 122 SCALE WIND TUNNEL MODEL DRAWINGS

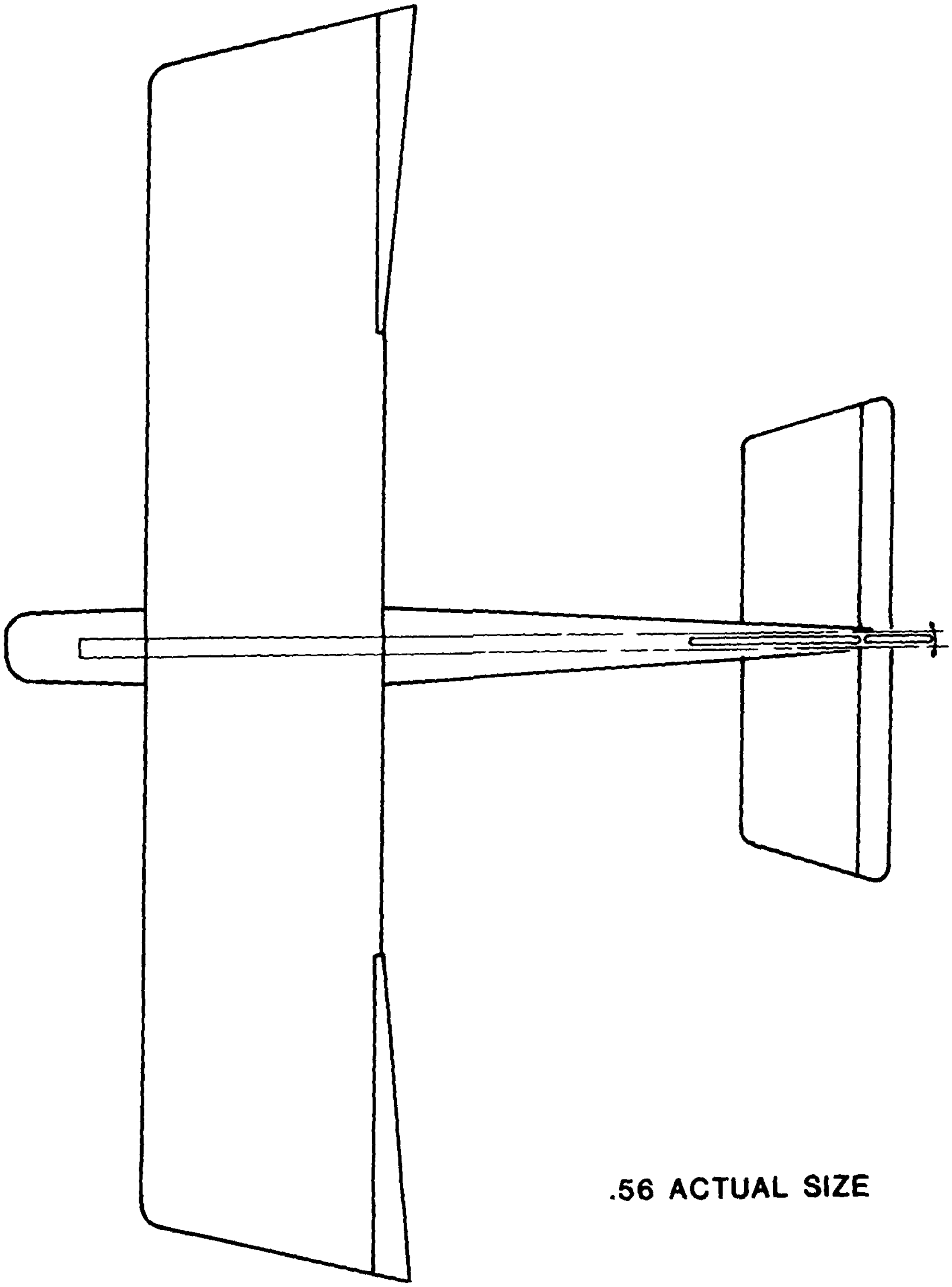

.56 ACTUAL SIZE

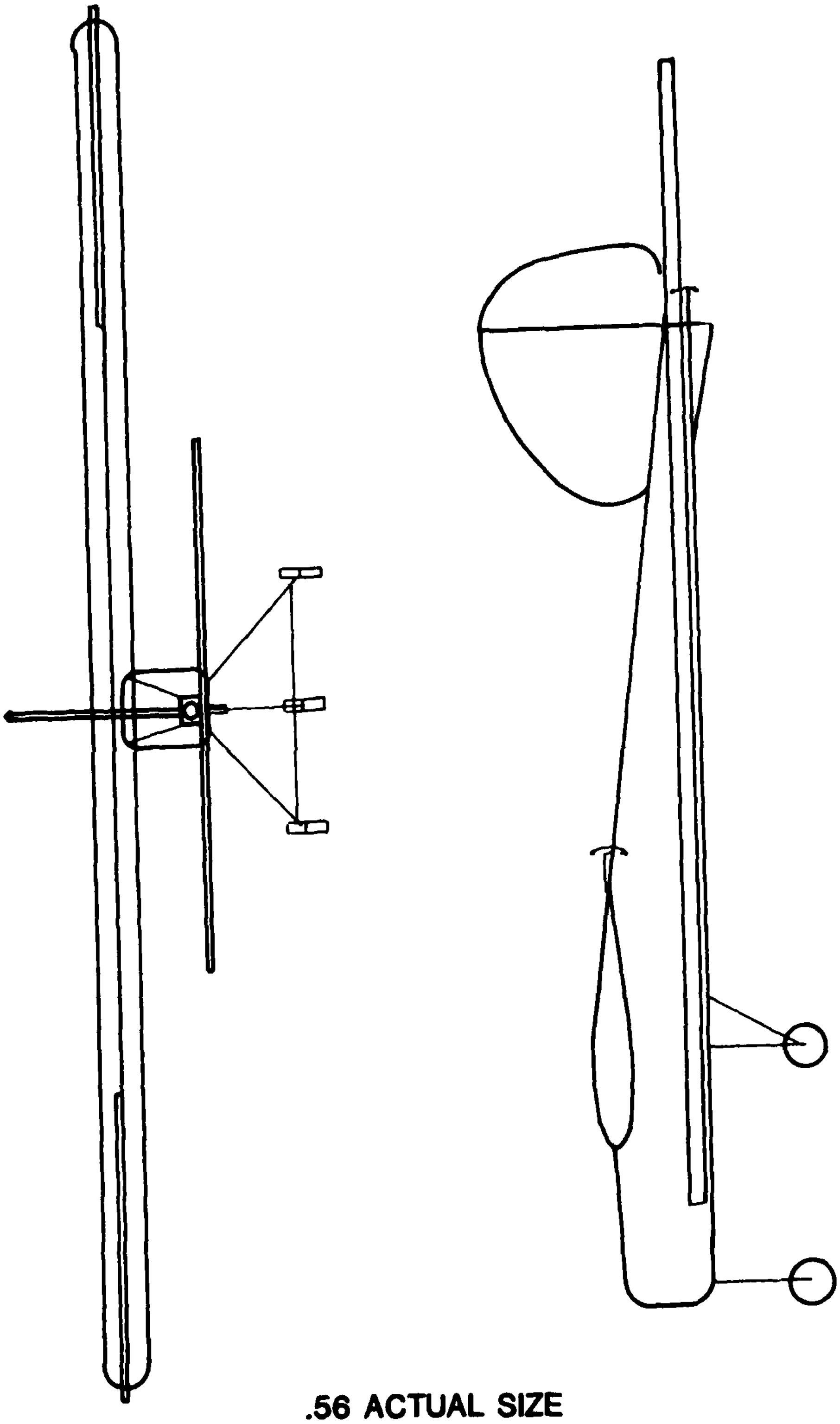

.56 ACTUAL SIZE

APPENDIX B- Big Stick Aerodynamic Coefficients, Stability Derivatives, and Mass Data

1. Miscellaneous Aircraft Data:

Weight	30 lb_F
Reference area (wing, S)	15.6 ft^2
Chord ($\bar{c}$)	1.784 ft
Span (b)	8.73 ft
Propeller efficiency (η)	.7

2. Wind Tunnel Data (Reference 2):

C_{D_o} = .061

K = .086

C_{L_o} = -.13

C_{L_α} = 4.0/rad

$C_{L_{\delta_e}}$ = +.005/deg

C_{m_o} = .0093

C_{m_α} = -.29/rad

$C_{m_{\delta_e}}$ = -.01/deg

$C_{D_{\delta_e}}$ = .0003/deg

$C_{y_{\delta_a}}$ = 0

$C_{y_{\delta_r}}$ = .00235/deg

C_{y_β} = -.46/rad

$C_{\ell_{\delta_a}}$ = .025/deg

$C_{\ell_{\delta_r}}$ = .00105/deg

C_{n_β} = .17/rad

$C_{n_{\delta_a}}$ = -.002/deg

$C_{n_{\delta_r}}$ = -.00144/deg

3. Estimated Aerodynamic Data (Reference 1 and 5):

$$C_{m_u} = C_{L_u} = C_{D_u} = C_{m_{T_u}} = C_{m_{T_\alpha}} = 0$$

$C_{m_{\dot{\alpha}}} = -4.0$

$C_{m_q} = -11.0$

$C_{L_{\dot{\alpha}}} = 1.66$

$C_{L_q} = 4.16$

$C_{T_{x_u}} = -.22$

$C_{y_p} = -.004$

$C_{y_r} = .18$

$C_{n_{T_\beta}} = 0$

$C_{n_r} = -.046$

$C_{n_p} = -.03$

$C_{\ell_\beta} = -.078/\text{rad}$*

$C_{\ell_p} = -.36$

$C_{\ell_r} = .096$

$C_{T_{x_{\delta_T}}} = .066/\text{BHP}$

*wind tunnel data not used because model had no wing dihedral

4. Mass Data (Reference 4):

rolling moment of inertia (I_{xx}) = 1.7 slg-ft^2

pitching moment of inertia (I_{yy}) = 6.8 slg-ft^2

yawing moment of inertia (I_{zz}) = 9.3 slg-ft^2

product of inertia (I_{xz}) = 0

note: these inertia terms are relative to body axes

APPENDIX C– Aircraft Linearized Equations of Motion

The methods of Reference 1 were used to linearize the aircraft equations of motion about a steady-state condition of coordinated, straight and level flight at 7500 feet and 73.33 ft/s (50 mph). The angle of attack required for this condition was 7.2 degrees relative to body axes. Since the linearized model uses stability axes (longitudinal axis parallel to the steady-state relative wind), the inertia terms I_{xx}, I_{zz}, and I_{xz}, of Appendix B had to be transformed from body axes to stability axes.

The remaining necessary coefficients and derivatives, listed below, were obtained by linearizing the drag polar around the steady-state condition and by assuming that the propeller thrust acts through the aircraft center of gravity.

$C_{D_1} = .073$ $\quad C_{m_1} = 0$ $\quad C_{T_{x_1}} = .073$

$C_{D_\alpha} = .259/\text{rad}$ $\quad C_{m_{T_1}} = 0$

$C_{L_1} = .376$ $\quad C_{m_{T_\alpha}} = 0$

From Reference 1, the linearized longitudinal equations of motion are (using the definitions from Table C-1):

$$\dot{u} = -g\theta + X_u u + X_{T_u} u + X_\alpha \alpha + X_{\delta_e} \delta_e + X_{T_{\delta_T}} \delta_T$$

$$U_1 \dot{\alpha} - U_1 q = Z_u u + Z_\alpha \alpha + Z_{\dot{\alpha}} \dot{\alpha} + Z_q q + Z_{\delta_e} \delta e$$

$$\dot{q} = M_u u + M_{T_u} u + M_\alpha \alpha + M_{T_\alpha} \alpha + M_{\dot{\alpha}} \dot{\alpha} + M_q q + M_{\delta_e} \delta e$$

In addition, the following approximations were added:

$$\dot{\theta} = q$$

$$\dot{h} = U_1 \theta - U_1 \alpha$$

The values were substituted in and the equations were manipulated algebraically to obtain first order matrix form.

$$\begin{bmatrix} \dot{q} \\ \dot{\theta} \\ \dot{u} \\ \dot{\alpha} \\ \dot{h} \end{bmatrix} = \begin{bmatrix} -3.733 & 0 & .01189 & -1.341 & 0 \\ 1 & 0 & 0 & 0 & 0 \\ 0 & -32.2 & -.2566 & 10.01 & 0 \\ .9193 & 0 & -.01169 & -4.642 & 0 \\ 0 & 73.33 & 0 & -73.33 & 0 \end{bmatrix} \begin{bmatrix} q \\ \theta \\ u \\ \alpha \\ h \end{bmatrix} + \begin{bmatrix} -.2033 & 0 \\ 0 & 0 \\ -.0257 & 5.63 \\ -.0057 & 0 \\ 0 & 0 \end{bmatrix} \begin{bmatrix} \delta_e \\ \delta_T \end{bmatrix}$$

Table C-1

$$X_u = \frac{-\bar{q}_1 S(C_{D_u} + 2C_{D_1})}{mU_1} (\text{sec}^{-1})$$

$$X_{T_u} = \frac{\bar{q}_1 S(C_{T_{x_u}} + 2C_{T_{x_1}})}{mU_1} (\text{sec}^{-1})$$

$$X_\alpha = \frac{-\bar{q}_1 S(C_{D_\alpha} - C_{L_1})}{m} (\text{ft sec}^{-2})$$

$$X_{\delta_e} = \frac{-\bar{q}_1 S C_{D_{\delta_e}}}{m} (\text{ft sec}^{-2}\text{deg}^{-1})$$

$$Z_u = -\frac{\bar{q}_1 S(C_{L_u} + 2C_{L_1})}{mU_1} (\text{sec}^{-1})$$

$$Z_\alpha = -\frac{\bar{q}_1 S(C_{L_\alpha} + C_{D_1})}{m} (\text{ft sec}^{-2})$$

$$Z_{\dot{\alpha}} = -\frac{\bar{q}_1 S C_{L_{\dot{\alpha}}} \bar{c}}{2mU_1} (\text{ft sec}^{-1})$$

$$Z_q = -\frac{\bar{q}_1 S C_{L_q} \bar{c}}{2mU_1} (\text{ft sec}^{-1})$$

$$Z_{\delta_e} = -\frac{\bar{q}_1 S C_{L_{\delta_e}}}{m} (\text{ft sec}^{-2}\text{deg}^{-1})$$

$$M_u = \frac{\bar{q}_1 S\bar{c}(C_{m_u} + 2C_{m_1})}{I_{yy}U_1} (\text{ft}^{-1}\text{sec}^{-1})$$

$$M_{T_u} = \frac{\bar{q}_1 S\bar{c}(C_{m_{T_u}} + 2C_{m_{T_1}})}{I_{yy}I_1} (\text{ft}^{-1}\text{sec}^{-1})$$

$$M_\alpha = \frac{\bar{q}_1 S\bar{c}C_{m_\alpha}}{I_{yy}} (\text{sec}^{-2})$$

$$M_{T_\alpha} = \frac{\bar{q}_1 S\bar{c}C_{m_{T_\alpha}}}{I_{yy}} (\text{sec}^{-2})$$

$$M_{\dot{\alpha}} = \frac{\bar{q}_1 S\bar{c}^2 C_{m_\alpha}}{2I_{yy}U_1} (\text{sec}^{-1})$$

$$M_q = \frac{\bar{q}_1 S\bar{c}^2 C_{m_q}}{2I_{yy}U_1} (\text{sec}^{-1})$$

$$M_{\delta_e} = \frac{\bar{q}_1 S\bar{c}C_{m_{\delta_e}}}{I_{yy}} (\text{sec}^{-2}\text{deg}^{-1})$$

$$X_{T_{\delta_T}} = \frac{\bar{q}_1 S C_{T_{x_{\delta_T}}}}{m} (\text{ft sec}^{-2}\text{BHP}^{-1})$$

From Reference 1, the linearized lateral-directional equations of motion are (using the definitions from Table C-2):

$$U_1\dot{\beta} + U_1 r = g\phi + Y_\beta \beta + Y_p p + Y_r r + Y_{\delta_a}\delta_a + Y_{\delta_r}\delta_r$$

$$\dot{p} - A_1\dot{r} = L_\beta \beta + L_p p + L_r r + L_{\delta_a}\delta_a + L_{\delta_r}\delta_r$$

$$\dot{r} - B_1\dot{p} = N_\beta \beta + N_{T_\beta}\beta + N_p p + N_r r + N_{\delta_a}\delta_a + N_{\delta_r}\delta_r$$

$$A_1 = \frac{I_{xz}}{I_{xx}} \quad , \quad B_1 = \frac{I_{xz}}{I_{zz}}$$

In addition, the following approximations were added:

$$\dot{\phi} = p$$
$$\dot{\psi} = r$$

The values were substituted in and the equations were manipulated algebraically to obtain first order matrix form.

$$\begin{bmatrix} \dot{\beta} \\ \dot{p} \\ \dot{r} \\ \dot{\phi} \\ \dot{\psi} \end{bmatrix} = \begin{bmatrix} -.5366 & -.000278 & -.9875 & .439 & 0 \\ -38.18 & -8.55 & 2.41 & 0 & 0 \\ 16.7 & .72 & -.448 & 0 & 0 \\ 0 & 1 & 0 & 0 & 0 \\ 0 & 0 & 1 & 0 & 0 \end{bmatrix} \begin{bmatrix} \beta \\ p \\ r \\ \phi \\ \psi \end{bmatrix} + \begin{bmatrix} 0 & .00274 \\ 10.14 & .48 \\ -1.17 & -.157 \\ & \\ 0 & 0 \end{bmatrix} \begin{bmatrix} \delta_a \\ \delta_r \end{bmatrix}$$

$$Y_{\beta} = \frac{\bar{q}_1 S C_{y_{\beta}}}{m} \text{ (ft sec}^{-2}\text{)}$$

$$Y_{p} = \frac{\bar{q}_1 S b C_{y_{p}}}{2 m U_1} \text{ (ft sec}^{-1}\text{)}$$

$$Y_{r} = \frac{\bar{q}_1 S b C_{y_{r}}}{2 m U_1} \text{ (ft sec}^{-1}\text{)}$$

$$Y_{\delta_a} = \frac{\bar{q}_1 S C_{y_{\delta_a}}}{m} \text{ (ft sec}^{-2}\text{deg}^{-1}\text{)}$$

$$Y_{\delta_r} = \frac{\bar{q}_1 S C_{y_{\delta_r}}}{m} \text{ (ft sec}^{-2}\text{deg}^{-1}\text{)}$$

$$L_{\beta} = \frac{\bar{q}_1 S b C_{\ell_{\beta}}}{I_{xx}} \text{ (sec}^{-2}\text{)}$$

$$L_{p} = \frac{\bar{q}_1 S b^2 C_{\ell_{p}}}{2 I_{xx} U_1} \text{ (sec}^{-1}\text{)}$$

$$L_{r} = \frac{\bar{q}_1 S b^2 C_{\ell_{r}}}{2 I_{xx} U_1} \text{ (sec}^{-1}\text{)}$$

$$L_{\delta_a} = \frac{\bar{q}_1 S b C_{\ell_{\delta_a}}}{I_{xx}} \text{ (sec}^{-2}\text{deg}^{-1}\text{)}$$

$$L_{\delta_r} = \frac{\bar{q}_1 S b C_{\ell_{\delta_r}}}{I_{xx}} \text{ (sec}^{-2}\text{deg}^{-1}\text{)}$$

$$N_{\beta} = \frac{\bar{q}_1 S b C_{n_{\beta}}}{I_{zz}} \text{ (sec}^{-2}\text{)}$$

$$N_{T_{\beta}} = \frac{\bar{q}_1 S b C_{n_{T_{\beta}}}}{I_{zz}} \text{ (sec}^{-2}\text{)}$$

$$N_{p} = \frac{\bar{q}_1 S b^2 C_{n_{p}}}{2 I_{zz} U_1} \text{ (sec}^{-1}\text{)}$$

$$N_{r} = \frac{\bar{q}_1 S b^2 C_{n_{r}}}{2 I_{zz} U_1} \text{ (sec}^{-1}\text{)}$$

$$N_{\delta_a} = \frac{\bar{q}_1 S b C_{n_{\delta_a}}}{I_{zz}} \text{ (sec}^{-2}\text{deg}^{-1}\text{)}$$

$$N_{\delta_r} = \frac{\bar{q}_1 S b C_{n_{\delta_r}}}{I_{zz}} \text{ (sec}^{-2}\text{deg}^{-1}\text{)}$$

APPENDIX D- Simulation Program

This nonlinear simulation program was written in FORTRAN 77 for the Burroughs 6900 computer at the Air Force Academy by Cadet First Class Daniel A. Draeger. The program numerically integrates the six aircraft equations of motion for u, v, and w (velocity components in body axes) and for p, q, and r (rotational rates in body axes). Six kinematic equations are also integrated to get the Euler angles ψ, θ, and ϕ; and displacements in the earth axes: altitude (h), north distance (N), and east distance (E). The results of simulation runs are delivered in graphical form using plotting routines not included in the listing. The aircraft data are read in from separate data files, a feature which allows the program to be used to simulate other aircraft. The twelve equations solved by the program are listed below in general form (Reference 1).

$$m(\dot{u}-vr+wq) = \text{forces in x direction}$$
$$m(\dot{v}+ur-wp) = \text{forces in y direction}$$
$$m(\dot{w}-uq+vp) = \text{forces in z direction}$$

$$I_{xx}\dot{p} - I_{xz}\dot{r} - I_{xz}rq + (I_{zz}-I_{yy})rq = \text{moment about x axis}$$
$$I_{yy}\dot{q} + (I_{xx}-I_{zz})pr + I_{xz}(p^2-r^2) = \text{moment about y axis}$$
$$I_{zz}\dot{r} - I_{xz}\dot{p} + (I_{yy}-I_{xx})pq + I_{xz}qr = \text{moment about z axis}$$

$$\dot{\psi} = (q\sin\phi + r\cos\phi)\sec\theta$$
$$\dot{\theta} = q\cos\phi - r\sin\phi$$
$$\dot{\phi} = p + q\sin\phi\tan\theta + r\cos\phi\tan\theta$$

$$\dot{N} = (\cos\psi\cos\theta)U + (\cos\psi\sin\theta\sin\phi - \sin\psi\cos\phi)V + (\cos\psi\sin\theta\cos\phi + \sin\psi\sin\phi)W$$
$$\dot{E} = (\sin\psi\cos\theta)U + (\sin\psi\sin\theta\sin\phi + \cos\psi\cos\phi)V + (\sin\psi\sin\theta\cos\phi - \cos\psi\sin\phi)W$$
$$\dot{h} = (\sin\theta)U + (-\cos\theta\sin\phi)V + (-\cos\theta\cos\phi)W$$

```
$RESET FREE
FILE  4(TITLE="CNSTNT.",KIND="DISK",FILETYPE=7)
FILE  5(TITLE="SYSDAT.",KIND="DISK",FILETYPE=7)
FILE  6(KIND="PRINTER")
FILE  7(KIND="REMOTE")
FILE  8(KIND="REMOTE")
$INCLUDE "PLOT/INCLUDE/FORTRAN."
$INCLUDE "(AERO457) DFAN/PLOTTER"
C  ********************************************************************
C  ***FOLLOWING IS A LIST OF VARIABLE NAMES AND USES IN MAIN PROGRAM****
C                  DT = STEP SIZE IN NUMERICAL INTEGRATION
C                   T = TIME THE INTEGRATION IS CURRENTLY AT
C                   X = STATE VAR. ARRAY- U.V.W,P.Q.R,PSI.THE,PHI.N,E,H
C                  DX = DERIVATIVES OF X
C       DE.BHP.DA.DR = AIRCRAFT CONTROLS
C   DETRM,BHPTRM,ETC. = TRIM SETTINGS FOR CONTROLS
C     AKHDOT.AKV,ETC. = AUTO PILOT CONTROL GAINS
C                  IX = VARIABLE OR CONTROL TO BE PLOTTED
C      ALTC.VELC.PSIC = COMMANDS TO FLY (ALT.VEL.HEADING)
C                TMAX = THE TIME LIMIT FOR THE INTEGRATION
C           PLTSPC(5) = SELECTION FOR LP (1), HP (2), BOTH (3)
C                NSPP = NUMBER OF POINTS PLOTTED
C                NPTS = CURRENT POINT NUMBER COUNTER
C                NDIM = 12, THE DIMENSION OF X AND DX
C                ICNT = CURRENT LOOP NUMBER COUNTER
C                  XP = ARRAY STORING THE DESIRED X POINTS
C                  TP = ARRAY STORING THE DESIRED T POINTS
C  ********************************************************************
C  ********************************************************************
      DIMENSION X(12),DX(12),ER(12),XP(1,250),TP(1,250),PLTSPC(5)
      CHARACTER*6XTITLE(4),YTITLE(4),LABEL(4),FLINE(4),SLINE(4).TLINE(4)
      COMMON /BLK12/ CDO,AKD.CLO.CLA.CLAD,CLQ,CLDE.CMO,CMA.CMAD,CMQ,
     1               CMDE.CYB.CYR,CYP,CYDR.CLB.CLP.CLR,CLDA.CLDR,CNB,
     2               CNP,CNR,CNDA,CNDR.S,CB,B,ANP.AIX.AIZ.AIXZ,AM,AIY,
     3               DA.DE.DR,BHP
      DATA LABEL/"      ","FLT HI","STORY ","      "/
      DATA XTITLE/"  TIME"," (SECO","NDS)  ","      "/
      DATA YTITLE/"  STAT","E VARI","ABLE  ","      "/
C  ********************************************************************
C  ********************************************************************
C                          READ IN THE DATA
C  ********************************************************************
      READ (5,*) (X(I),I=1,12)
      READ (5,*) DETRM, BHPTRM, DATRM, DRTRM
      READ (5,*) AKHDOT,AKV, AKH, AKR, AKPSI, AKNY, AKYD
      READ (5,100) DT,TMAX
      READ (5,200) IX, PLTSPC(5)
 100  FORMAT (2(F10.4))
 110  FORMAT (6(F9.3),/,6(F9.3))
 200  FORMAT (2(I5))
 225  FORMAT (" YOUR INPUT DATA WAS: ")
```

```
      WRITE (7,225)
      WRITE (7,110) (X(I),I=1,12)
      WRITE (7,110) DETRM, BHPTRM, DATRM, DRTRM
      WRITE (7,110) AKHDOT,AKV, AKH, AKR, AKPSI, AKNY, AKYD
      WRITE (7,100) DT,TMAX
      WRITE (7,200) IX,PLTSPC(5)
      READ (4,*) CDO,AKD,CLO,CLA,CLAD,CLQ,CLDE,CMO,CMA,CMAD,CMQ,CMDE
      READ (4,*) CYB,CYR,CYP,CYDR,CLB,CLP,CLR,CLDA,CLDR,CNB,CNP,CNR
      READ (4,*) CNDA,CNDR,S,CB,B,ANP,AIX,AIZ,AIXZ,AM,AIY
      WRITE (7,410) CDO,AKD,CLO,CLA,CLAD,CLQ,CLDE,AM
      WRITE (7,420) CMO,CMA,CMAD,CMQ,CMDE,CYB,CYR,CYP,CYDR
      WRITE (7,430) CLB,CLP,CLR,CLDA,CLDR,CNB,CNP,CNR
      WRITE (7,440) CNDA,CNDR,S,CB,B,ANP,AIX,AIZ,AIXZ,AIY
  410 FORMAT(1X,'CDO=',F6.3,' AKD=',F6.3,' CLO=',F6.3,' CLA=',F6.3,/,
     1 ' CLAD=',F6.3,' CLQ=',F6.3,' CLDE=',F6.3,' AM=',F6.3)
  420 FORMAT(1X,'CMO=',F6.3,' CMA=',F6.3,' CMAD=',F7.3,' CMQ=',F7.3,/,
     1 ' CMDE=',F6.3,' CYB=',F6.3,' CYR=',F6.3,' CYP=',F6.3,
     2 ' CYDR=',F6.3)
  430 FORMAT(1X,'CLB=',F6.3,' CLP=',F6.3,' CLR=',F6.3,' CLDA=',F6.3,/,
     1 ' CLDR=',F6.3,' CNB=',F6.3,' CNP=',F6.3,' CNR=',F6.3)
  440 FORMAT(1X,'CNDA=',F6.3,' CNDR=',F6.4,' S=',F6.3,' CB=',F6.3,/,
     1 ' B=',F6.3,' ANP=',F6.3,' AIX=',F6.3,' AIZ=',F6.3,' AIXZ=',F6.3,
     2 /,' AIY=',F6.3)
      WRITE (7,101)
  101 FORMAT(1X,'PLEASE ENTER ALTITUDE, VELOCITY, AND HEADING COMMANDS',
     1 /,' (UNITS ARE FT., FT/SEC, AND RADIANS).')
      READ (8,*) ALTC, VELC, PSIC
C   ****************************************************************
C                  INITIALIZATION BLOCK
C   ****************************************************************
      NSPP = INT((TMAX/DT)/250.) + 1
      PLTSPC(1) = 8
      PLTSPC(2) = 6
      CALL PLOTS(1,0,0)
      IF (IX.GT.12) GO TO 230
      XP(1,1) = X(IX)
      GO TO 240
  230 IF (IX.EQ.13)  XP(1,1) = DE
      IF (IX.EQ.14) XP(1,1) = BHP
      IF (IX.EQ.15)  XP(1,1) = DA
      IF (IX.EQ.16) XP(1,1) = DR
  240 TP(1,1) = 0.
      NPTS = 0
      ICNT = 0
      NDIM = 12
      DO 250 I = 1,12
  250   ER(I) = 0.
      T = 0.
C   ****************************************************************
C           LOOP THROUGH INTEGRATION USING RUNGA-KUTTA METHOD
C   ****************************************************************
C **    CALCULATE CONTROLS FOR EACH INTEGRATION STEP  ****************
  300 VEL = SQRT ( X(1)*X(1) + X(2)*X(2) + X(3)*X(3) )
      ANY = COS( X(8) )*SIN( X(9) ) -  (DX(2) + X(1)*X(6) - X(3)*X(4) )
     1  / 32.17
      HDOTC = AKH * (ALTC-X(12) )
      IF (HDOTC.GT.11.5) HDOTC = 11.5
      IF (HDOTC.LT.-11.5) HDOTC =-11.5
      DE = DETRM + AKHDOT* (HDOTC - DX(12) )
      BHP = BHPTRM + AKV * (VELC - VEL)
```

```
      RC = AKPSI * (PSIC - X(7) )
      IF (RC.GT.0.12) RC = .12
      IF (RC.LT.-0.12) RC =-.12
      DA = AKR * (RC - X(6) )  + DATRM
      DR = -AKNY * ANY - AKYD * X(6) + DRTRM
C **    CHECK CONTROL LIMITS  *************************************
      IF (DE.GT.15.) DE = 15.
      IF (DE.LT.-15.) DE =-15.
      IF (BHP.GT.3.) BHP = 3.
      IF (BHP.LT.0.) BHP = 0.
      IF (DA.GT.15.) DA = 15.
      IF (DA.LT.-15.) DA =-15.
      IF (DR.GT.15.) DR = 15.
      IF (DR.LT.-15.) DR =-15.
      CALL RNGKTA (NDIM, T, DT,  X, DX, ER)
      ICNT = ICNT + 1
      IF (ICNT.NE.NSPP) GO TO 300
      NPTS = NPTS + 1
      ICNT = 0
      IF (IX.GT.12) GO TO 320
      XP(1,NPTS) = X(IX)
      GO TO 340
  320 IF (IX.EQ.13)  XP(1,NPTS) = DE
      IF (IX.EQ.14) XP(1,NPTS) = BHP
      IF (IX.EQ.15) XP(1,NPTS) = DA
      IF (IX.EQ.16) XP(1,NPTS) = DR
  340 TP(1,NPTS) = T
      IF (NPTS.GE.250) GO TO 400
      IF (T.GE.TMAX) GO TO 400
      GO TO 300
C ******************************************************************
C                CPLOT PLOTTING ROUTINE CALL
C ******************************************************************
  400 CALL CPLOT (NPTS,1,TP,XP,PLTSPC,XTITLE,YTITLE,LABEL,FLINE,
     1  SLINE,TLINE)
      STOP
      END
C ******************************************************************
C  SUBROUTINE RNGKTA WRITTEN BY DR D K SCHMIDT, A&AE DEPT, PURDUE UNIV
C ******************************************************************
      SUBROUTINE RNGKTA(NDIM,T,DT,X,DX,ERR)
      REAL X(NDIM),DX(NDIM),ERR(NDIM),A(4),B(4),C(4)
      DATA A,B,C/0.5,0.292893219,1.707106781,0.16666667,2.,1.,1.,
     B  2.,0.5,0.292893219,1.707106781,0.5/
      DT2 = DT/2.
      CALL DXDT (X,DX)
      J = 1
  101 DO 102 I = 1,NDIM
        R1 = DT * DX(I)
        R2 = A(J) * (R1 - B(J) * ERR(I))
        X(I) = X(I) + R2
        R2 = 3. * R2
        ERR(I) = ERR(I) + R2 - C(J) * R1
  102 CONTINUE
      IF (J.EQ.4) RETURN
      J = J+1
      IF (J.NE.3) T = T + DT2
      CALL DXDT(X,DX)
      GO TO 101
      END
```

```
C  ******************************************************************
C              SUBROUTINE DXDT, DETERMINES DX FROM X
C  ******************************************************************
      SUBROUTINE DXDT(X,DX)
      DIMENSION X(12),DX(12)
      COMMON /BLK12/ CDO,AKD,CLO,CLA,CLAD,CLQ,CLDE,CMO,CMA,CMAD,CMQ,
     1               CMDE,CYB,CYR,CYP,CYDR,CLB,CLP,CLR,CLDA,CLDR,CNB,
     2               CNP,CNR,CNDA,CNDR,S,C,B,ANP,AIX,AIZ,AIXZ,AM,AIY,
     3               DA,DE,DR,BHP
C*******FOLLOWING IS A LIST OF VARIABLE NAMES AND USES************
C********                                                ************
C               V = SCALAR VALUE OF VELOCITY VECTOR
C           ALPHA = ANGLE OF ATTACK, RADIANS
C            BETA = SIDESLIP ANGLE, RADIANS
C              V2 = TWO TIMES THE VELOCITY
C            VND1 = ALPHADOT TIMES MEAN CHORD DIVIDED BY V2
C            VND2 = Q TIMES MEAN CHORD DIVIDED BY V2
C            VND3 = R TIMES SPAN DIVIDED BY V2
C            VND4 = P TIMES SPAN DIVIDED BY V2
C              CL = COEFFICIENT OF LIFT
C              CD = COEFFICIENT OF DRAG
C              CY = SIDE FORCE COEFFICIENT
C             CLL = ROLLING MOMENT COEFFICIENT
C              CM = PITCHING MOMENT COEFFICIENT
C              CN = YAWING MOMENT COEFFICIENT
C             RHO = AIR DENSITY, SLG/FT**3
C               Q = DYNAMIC PRESSURE
C           XLIFT = LIFT
C            DRAG = DRAG
C           SIDEF = SIDEFORCE
C          ROLMOM = ROLLING MOMENT
C          PITMOM = PITCHING MOMENT
C          YAWMOM = YAWING MOMENT
C          THRUST = THRUST
C              SA = SIN ALPHA
C              CA = COS ALPHA
C              SB = SIN BETA
C              CB = COS BETA
C            STHE = SIN THETA
C            CTHE = COS THETA
C            SPHI = SIN PHI
C            CPHI = COS PHI
C            TTHE = TAN THETA
C            SPSI = SIN PSI
C            CPSI = COS PSI
C*******************************************************************
      V = SQRT(X(1)*X(1)+X(2)*X(2)+X(3)*X(3))
      ALPHA = ATAN(X(3)/X(1))
      BETA = ASIN(X(2)/V)
      DALPHA = DX(3)/X(1)
      W = AM*32.2
      V2 = 2*V
      VND1 = DALPHA*C/V2
      VND2 = X(5)*C/V2
      VND3 = X(6)*B/V2
      VND4 = X(4)*B/V2
C*******************************************************************
      CL = CLO+CLA*ALPHA+CLAD*VND1+CLQ*VND2+CLDE*DE
      CD = CDO+AKD*(CL*CL)
      CY = CYB*BETA+CYR*VND3+CYP*VND4+CYDR*DR
```

```
17000       CLL = CLB*BETA+CLP*VND4+CLR*VND3+CLDA*DA+CLDR*DR
17100       CM = CMO+CMA*ALPHA+CMAD*VND1+CMQ*VND2+CMDE*DE
17200       CN = CNB*BETA+CNP*VND4+CNR*VND3+CNDA*DA+CNDR*DR
17300 C*****************************************************************
17350       RHO = 0.002377 * (1. - 6.87E-06 * X(12) ) ** 4.2559
17400       Q = .5*RHO*(V*V)
17450       IF (CL.GT.1.55) CL = .1*(1.0/CL)
17500       XLIFT = CL*Q*S
17600       DRAG = CD*Q*S
17700       SIDEF = CY*Q*S
17800       ROLMOM = CLL*Q*S*B
17900       PITMOM = CM*Q*S*C
18000       YAWMOM = CN*Q*S*B
18100       THRUST = ANP*BHP*550/V
18200 C*****************************************************************
18300       SA = SIN(ALPHA)
18400       CA = COS(ALPHA)
18500       SB = SIN(BETA)
18600       CB = COS(BETA)
18700       STHE = SIN(X(8))
18800       CTHE = COS(X(8))
18900       SPHI = SIN(X(9))
19000       CPHI = COS(X(9))
19100       TTHE = STHE/CTHE
19200       SPSI = SIN(X(7))
19300       CPSI = COS(X(7))
19400 C*****************************************************************
19500       DX(1) = (XLIFT*SA-DRAG*CB*CA-SIDEF*SB*CA-W*STHE+THRUST)/AM
19600      1        -X(5)*X(3)+X(6)*X(2)
19700       DX(2) = (-DRAG*SB+SIDEF*CB+W*CTHE*SPHI)/AM -X(6)*X(1)
19800      1        +X(4)*X(3)
19900       DX(3) = (-XLIFT*CA-DRAG*CB*SA-SIDEF*SB*SA+W*CTHE*CPHI)/
20000      1        AM - X(4)*X(2)+X(5)*X(1)
20100       DX(4) = (ROLMOM+(AIY-AIZ)*X(5)*X(6)+AIXZ*(DX(6)+X(4)*X(5)))/AIX
20200       DX(5) = (PITMOM-(AIX-AIZ)*X(4)*X(6)-AIXZ*(X(4)*X(4)-X(6)*X(6)))
20300      1        /AIY
20400       DX(6) = (YAWMOM+(AIX-AIY)*X(4)*X(5)+AIXZ*(DX(4)-X(5)*X(6)))/AIZ
20500       DX(7) = (X(5)*SPHI+X(6)*CPHI)/CTHE
20600       DX(8) = X(5)*CPHI-X(6)*SPHI
20700       DX(9) = X(4)+X(5)*SPHI*TTHE+X(6)*CPHI*TTHE
20800       DX(10) = CPSI*CTHE*X(1)+(-SPSI*CPHI+CPSI*STHE*SPHI)*X(2)+
20900      1         (SPSI*SPHI+CPSI*STHE*CPHI)*X(3)
21000       DX(11) = SPSI*CTHE*X(1)+(CPSI*CPHI+SPSI*STHE*SPHI)*X(2)+
21100      1         (-CPSI*SPHI+SPSI*STHE*CPHI)*X(3)
21200       DX(12) = STHE*X(1)-CTHE*SPHI*X(2)-CTHE*CPHI*X(3)
21300       RETURN
21400       END
```

Data File "CNSTNT"

```
100        .061..088,-.13,4.0,1.66,4.16,.005,.0093,-.29,-4.0,-11.0,-.01
200        -.46,.18,-.004,.00235,-0.078,-.36,.096..025,.00105,.17,-.03,-.046
300         -.002,-.00144,15.65,1.734,8.73,.70 .1.7,9.3,0.0,.9317,6.8
```

Data File "SYSDAT"

```
100        72.70, 0. ,09.5,0,0,0.0,0.000,.130,0.00,0,0,7500.
200         -2.82, 1.11,  0.,  0.
300         -.2 ,   .1,   .2,   1.,   .1,  30., -20.
400            .02      80.0
500          12    2
```

APPENDIX E. System Poles for Root Loci Plots

Longitudinal Poles

```
KHD = 0 DEG / FT/SEC
KH = 0 FT/SEC /FT
KV = 0 BHP / FT/SEC
1 S**5 + 9.63092 S**4 + 20.824544 S**3 + 5.4722025 S**2 + 2.28162392 S + 0

POLES ARE:
-4.19655835     j -1.04669128
-4.19655835     j 1.04669128
-.118901651     j -.32837616
-.118901651     j .32837616
0     j 0
```

```
KHD = -.1 DEG / FT/SEC
KH = .2 FT/SEC /FT
KV = .1 BHP / FT/SEC
1 S**5 + 9.15366437 S**4 + 25.4759382 S**3 + 22.7784477 S**2 + 8.90190019 S + .979279342

POLES ARE:
-.508715358     j -.330638958
-.508715358     j .330638958
-3.35148519     j 0
-4.61266641     j 0
-.17208205     j 0
```

```
KHD = -.15 DEG / FT/SEC
KH = .2 FT/SEC /FT
KV = .1 BHP / FT/SEC
1 S**5 + 9.13277156 S**4 + 25.4378578 S**3 + 26.1930904 S**2 + 12.2120383 S + 1.46793395

POLES ARE:
-2.67610689     j 0
-4.99295612     j 0
-.643864414     j -.457962806
-.643864414     j .457962806
-.175977722     j 0
```

```
KHD = -.2 DEG / FT/SEC
KH = .2 FT/SEC /FT
KV = .1 BHP / FT/SEC
1 S**5 + 9.11187873 S**4 + 25.3997775 S**3 + 29.6077331 S**2 + 15.5221765 S + 1.95593185

POLES ARE:
-2.00669996     j 0
```

```
-5.23439389     j 0
-.846614841     j -.57618756
-.846614841     j .57618756
-.177555202     j 0


KHD = -.25 DEG / FT/SEC
KH = .2 FT/SEC /FT
KV = .1 BHP / FT/SEC
1 S**5 + 9.09098592 S**4 + 25.3616971 S**3 + 33.0223758 S**2 + 18.8323146 S + 2.44327303

POLES ARE:
-5.4207603    j 0
-1.13625785    j -.883970426
-1.13625785    j .883970426
-1.21935259    j 0
-.178357333    j 0


KHD = -.3 DEG / FT/SEC
KH = .2 FT/SEC /FT
KV = .1 BHP / FT/SEC
1 S**5 + 9.0700931 S**4 + 25.3236168 S**3 + 36.4370185 S**2 + 22.1424527 S + 2.92995751

POLES ARE:
-1.15545131    j -1.26088437
-1.15545131    j 1.26088437
-5.57560036    j 0
-1.004782    j 0
-.178808123    j 0



KHD = -.2 DEG / FT/SEC
KH = .1 FT/SEC /FT
KV = .1 BHP / FT/SEC
1 S**5 + 9.11187873 S**4 + 25.4081346 S**3 + 29.6212938 S**2 + 14.1536072 S + .977965923

POLES ARE:
-.0823008552    j 0
-.994005835    j -.525117323
-.994005835    j .525117323
-1.79062917    j 0
-5.25093704    j 0


KHD = -.2 DEG / FT/SEC
KH = .15 FT/SEC /FT
KV = .1 BHP / FT/SEC
1 S**5 + 9.11187873 S**4 + 25.403956 S**3 + 29.6145134 S**2 + 14.8378918 S + 1.46694888

POLES ARE:
```

```
-.128241961     j 0
-.915390605     j -.551649739
-.915390605     j .551649739
-1.91013555     j 0
-5.24272001     j 0


KHD = -.2 DEG / FT/SEC
KH = .2 FT/SEC /FT
KV = .1 BHP / FT/SEC
1 S**5 + 9.11187873 S**4 + 25.3997775 S**3 + 29.6077331 S**2 + 15.5221765 S + 1.95593185

POLES ARE:
-2.00669996     j 0
-5.23439389     j 0
-.846614841     j -.57618756
-.846614841     j .57618756
-.177555202     j 0


KHD = -.2 DEG / FT/SEC
KH = .25 FT/SEC /FT
KV = .1 BHP / FT/SEC
1 S**5 + 9.11187873 S**4 + 25.3955989 S**3 + 29.6009527 S**2 + 16.2064611 S + 2.44491481

POLES ARE:
-2.08932918     j 0
-5.22595506     j 0
-.783362962     j -.600383671
-.783362962     j .600383671
-.229868565     j 0


KHD = -.2 DEG / FT/SEC
KH = .3 FT/SEC /FT
KV = .1 BHP / FT/SEC
1 S**5 + 9.11187873 S**4 + 25.3914204 S**3 + 29.5941724 S**2 + 16.8907457 S + 2.93389777

POLES ARE:
-2.16250743     j 0
-5.21739973     j 0
-.724015404     j -.625789061
-.724015404     j .625789061
-.293940771     j 0



KHD = -.2 DEG / FT/SEC
KH = .2 FT/SEC /FT
KV = .04 BHP / FT/SEC
1 S**5 + 8.77316074 S**4 + 22.5915516 S**3 + 23.3513994 S**2 + 10.8772586 S + 1.02598105
```

```
POLES ARE:
-.123213703     j 0
-.720633944     j -.535506228
-.720633944     j .535506228
-1.97301432     j 0
-5.23566482     j 0


KHD = -.2 DEG / FT/SEC
KH = .2 FT/SEC /FT
KV = .06 BHP / FT/SEC
1 S**5 + 8.88606673 S**4 + 23.5276269 S**3 + 25.436844 S**2 + 12.4255646 S + 1.33596465

POLES ARE:
-.145187511     j 0
-.761329061     j -.553845598
-.761329061     j .553845598
-1.98295914     j 0
-5.23526197     j 0


KHD = -.2 DEG / FT/SEC
KH = .2 FT/SEC /FT
KV = .08 BHP / FT/SEC
1 S**5 + 8.99897273 S**4 + 24.4637022 S**3 + 27.5222885 S**2 + 13.9738705 S + 1.64594825

POLES ARE:
-1.9941163     j 0
-5.23493885     j 0
-.803528034     j -.56736352
-.803528034     j .56736352
-.162961521     j 0


KHD = -.2 DEG / FT/SEC
KH = .2 FT/SEC /FT
KV = .1 BHP / FT/SEC
1 S**5 + 9.11187873 S**4 + 25.3997775 S**3 + 29.6077331 S**2 + 15.5221765 S + 1.95593185

POLES ARE:
-2.00669997     j 0
-5.23439388     j 0
-.846614839     j -.576187561
-.846614839     j .576187561
-.177555202     j 0


KHD = -.2 DEG / FT/SEC
KH = .2 FT/SEC /FT
KV = .12 BHP / FT/SEC
1 S**5 + 9.22478473 S**4 + 26.3358527 S**3 + 31.6931776 S**2 + 17.0704824 S + 2.26591545
```

```
POLES ARE:
-.890089383     j -.580455601
-.890089383     j .580455601
-5.23392534     j 0
-2.02097073     j 0
-.189709889     j 0


KHD = -.2 DEG / FT/SEC
KH = .2 FT/SEC /FT
KV = .14 BHP / FT/SEC
1 S**5 + 9.33769073 S**4 + 27.271928 S**3 + 33.7786222 S**2 + 18.6187883 S + 2.57589904

POLES ARE:
-.933523349     j -.580293241
-.933523349     j .580293241
-5.2334313     j 0
-2.03724597     j 0
-.199966766     j 0


KHD = -.2 DEG / FT/SEC
KH = .2 FT/SEC /FT
KV = .16 BHP / FT/SEC
1 S**5 + 9.45059674 S**4 + 28.2080033 S**3 + 35.8640668 S**2 + 20.1670943 S + 2.88588265

POLES ARE:
-5.23290958     j 0
-.976525323     j -.575809024
-.976525323     j .575809024
-2.05591145     j 0
-.20872506     j 0
```

Lateral-directional Poles

```
KNY = 0 DEG/g
KR = 0 DEG/ RAD/S
KPSI = 0 RAD/S /RAD
KYD = 0 DEG/ RAD/S
1 S**5 + 9.5346 S**4 + 23.4041628 S**3 + 131.745946 S**2 + -10.159496 S + 0

POLES ARE:
.0760546455    j 0
-.500580503    j -3.90704845
-.500580503    j 3.90704845
-8.60949365    j 0
0    j 0


KNY = 0 DEG/g
KR = 1 DEG/ RAD/S
KPSI = .1 RAD/S /RAD
KYD = -20 DEG/ RAD/S
1 S**5 + 11.5046 S**4 + 40.6614048 S**3 + 134.318141 S**2 + 26.6701227 S + 5.47289886

POLES ARE:
-8.54374773    j 0
-1.38137235    j -3.58688741
-1.38137235    j 3.58688741
-.0990537896    j -.183157467
-.0990537896    j .183157467


KNY = 10 DEG/g
KR = 1 DEG/ RAD/S
KPSI = .1 RAD/S /RAD
KYD = -20 DEG/ RAD/S
1 S**5 + 11.8001947 S**4 + 44.659137 S**3 + 150.239301 S**2 + 30.1706699 S + 6.06247998

POLES ARE:
-8.5909749    j 0
-1.50423744    j -3.7655311
-1.50423744    j 3.7655311
-.100372455    j -.181231473
-.100372455    j .181231473


KNY = 20 DEG/g
KR = 1 DEG/ RAD/S
KPSI = .1 RAD/S /RAD
KYD = -20 DEG/ RAD/S
1 S**5 + 12.1379451 S**4 + 49.2270826 S**3 + 168.431667 S**2 + 34.1706543 S + 6.73616742
```

```
POLES ARE:
-8.64578947     j 0
-1.64450809     j -3.95216212
-1.64450809     j 3.95216212
-.101569701     j -.179452201
-.101569701     j .179452201


KNY = 30 DEG/g
KR = 1 DEG/ RAD/S
KPSI = .1 RAD/S /RAD
KYD = -20 DEG/ RAD/S
1 S**5 + 12.5275614 S**4 + 54.4966084 S**3 + 189.418558 S**2 + 38.7851718 S + 7.51334065

POLES ARE:
-8.71023749     j 0
-1.80600033     j -4.14745607
-1.80600033     j 4.14745607
-.10266164     j -.177803379
-.10266164     j .177803379


KNY = 40 DEG/g
KR = 1 DEG/ RAD/S
KPSI = .1 RAD/S /RAD
KYD = -20 DEG/ RAD/S
1 S**5 + 12.9819845 S**4 + 60.6427901 S**3 + 213.897442 S**2 + 44.1676258 S + 8.41982831

POLES ARE:
-8.78719367     j 0
-1.99373372     j -4.35188056
-1.99373372     j 4.35188056
-.10366168     j -.176271039
-.10366168     j .176271039


KNY = 50 DEG/g
KR = 1 DEG/ RAD/S
KPSI = .1 RAD/S /RAD
KYD = -20 DEG/ RAD/S
1 S**5 + 13.5188503 S**4 + 67.9042413 S**3 + 242.818953 S**2 + 50.5271121 S + 9.49083428

POLES ARE:
-8.88083769     j 0
-2.21442524     j -4.56544296
-2.21442524     j 4.56544296
-.104581081     j -.174843122
-.104581081     j .174843122


KNY = 60 DEG/g
KR = 1 DEG/ RAD/S
```

```
KPSI = .1 RAD/S /RAD
KYD = -20 DEG/ RAD/S
1 S**5 + 14.1628327 S**4 + 76.6148123 S**3 + 277.513218 S**2 + 58.1562149 S + 10.775616

POLES ARE:
-8.99750778     j 0
-2.47723309     j -4.78718744
-2.47723309     j 4.78718744
-.105429385     j -.173509154
-.105429385     j .173509154
```

```
KNY = 30 DEG/g
KR = .6 DEG/ RAD/S
KPSI = .1 RAD/S /RAD
KYD = -20 DEG/ RAD/S
1 S**5 + 12.9955614 S**4 + 55.9238229 S**3 + 190.287381 S**2 + 8.80488741 S + 4.50800439

POLES ARE:
-9.14473222     j 0
-1.90550947     j -4.11124422
-1.90550947     j 4.11124422
-.0199051288     j -.153661036
-.0199051288     j .153661036
```

```
KNY = 30 DEG/g
KR = .8 DEG/ RAD/S
KPSI = .1 RAD/S /RAD
KYD = -20 DEG/ RAD/S
1 S**5 + 12.7615614 S**4 + 55.2102156 S**3 + 189.85297 S**2 + 23.7950296 S + 6.01067252

POLES ARE:
-8.92673673     j 0
-1.85720673     j -4.12897346
-1.85720673     j 4.12897346
-.0602056227     j -.170952076
-.0602056227     j .170952076
```

```
KNY = 30 DEG/g
KR = 1 DEG/ RAD/S
KPSI = .1 RAD/S /RAD
KYD = -20 DEG/ RAD/S
1 S**5 + 12.5275614 S**4 + 54.4966084 S**3 + 189.418558 S**2 + 38.7851718 S + 7.51334065

POLES ARE:
-8.71023749     j 0
-1.80600033     j -4.14745607
-1.80600033     j 4.14745607
-.10266164     j -.177803379
```

```
-.10266164     i .177803379


KNY = 30 DEG/g
KR = 1.2 DEG/ RAD/S
KPSI = .1 RAD/S /RAD
KYD = -20 DEG/ RAD/S
1 S**5 + 12.2935614 S**4 + 53.7830012 S**3 + 188.984146 S**2 + 53.775314 S + 9.01600878

POLES ARE:
-8.49525597    j 0
-1.75174853    j -4.16677264
-1.75174853    j 4.16677264
-.1474042     j -.173834725
-.1474042     j .173834725


KNY = 30 DEG/g
KR = 1.4 DEG/ RAD/S
KPSI = .1 RAD/S /RAD
KYD = -20 DEG/ RAD/S
1 S**5 + 12.0595614 S**4 + 53.069394 S**3 + 188.549734 S**2 + 68.7654562 S + 10.5186769

POLES ARE:
-8.28179457    j 0
-1.69432034    j -4.18701812
-1.69432034    j 4.18701812
-.194563085    j -.15620246
-.194563085    j .15620246



KNY = 30 DEG/g
KR = 1 DEG/ RAD/S
KPSI = .06 RAD/S /RAD
KYD = -20 DEG/ RAD/S
1 S**5 + 12.5275614 S**4 + 54.5434084 S**3 + 189.556599 S**2 + 38.85825 S + 4.50800439

POLES ARE:
-8.70522368    j 0
-1.90588843    j -4.14995057
-1.80588843    j 4.14995057
-.105280445    j -.119153661
-.105280445    j .119153661


KNY = 30 DEG/g
KR = 1 DEG/ RAD/S
KPSI = .08 RAD/S /RAD
KYD = -20 DEG/ RAD/S
1 S**5 + 12.5275614 S**4 + 54.5200084 S**3 + 189.487579 S**2 + 38.8217109 S + 6.01067252
```

```
POLES ARE:
-8.7077312     j 0
-1.80594354     j -4.14870324
-1.80594354     j 4.14870324
-.103971572     j -.151346198
-.103971572     j .151346198


KNY = 30 DEG/g
KR = 1 DEG/ RAD/S
KPSI = .1 RAD/S /RAD
KYD = -20 DEG/ RAD/S
1 S**5 + 12.5275614 S**4 + 54.4966084 S**3 + 189.418558 S**2 + 38.7851718 S + 7.51334065

POLES ARE:
-8.71023749     j 0
-1.80600033     j -4.14745607
-1.80600033     j 4.14745607
-.10266164     j -.177803379
-.10266164     j .177803379


KNY = 30 DEG/g
KR = 1 DEG/ RAD/S
KPSI = .12 RAD/S /RAD
KYD = -20 DEG/ RAD/S
1 S**5 + 12.5275614 S**4 + 54.4732084 S**3 + 189.349537 S**2 + 38.7486326 S + 9.01600878

POLES ARE:
-8.71274251     j 0
-1.80605881     j -4.14620905
-1.80605881     j 4.14620905
-.101350644     j -.200805122
-.101350644     j .200805122


KNY = 30 DEG/g
KR = 1 DEG/ RAD/S
KPSI = .14 RAD/S /RAD
KYD = -20 DEG/ RAD/S
1 S**5 + 12.5275614 S**4 + 54.4498084 S**3 + 189.280516 S**2 + 38.7120935 S + 10.5186769

POLES ARE:
-8.71524628     j 0
-1.80611899     j -4.14496219
-1.80611899     j 4.14496219
-.100038582     j -.22143087
-.100038582     j .22143087



KNY = 30 DEG/g
```

```
KR = 1 DEG/ RAD/S
KPSI = .1 RAD/S /RAD
KYD = 0 DEG/ RAD/S
1 S**5 + 8.66437245 S**4 + 29.0232275 S**3 + 184.017261 S**2 + 60.6243416 S + 7.51334065

POLES ARE:
-7.83392609     j 0
-.244986415     j -4.71675079
-.244986415     j 4.71675079
-.170236765     j -.118374156
-.170236765     j .118374156


KNY = 30 DEG/g
KR = 1 DEG/ RAD/S
KPSI = .1 RAD/S /RAD
KYD = -10 DEG/ RAD/S
1 S**5 + 10.5959669 S**4 + 41.7599179 S**3 + 186.71791 S**2 + 49.7047567 S + 7.51334065

POLES ARE:
-8.1515929      j 0
-1.06527568     j -4.50617987
-1.06527568     j 4.50617987
-.136761339     j -.155157179
-.136761339     j .155157179


KNY = 30 DEG/g
KR = 1 DEG/ RAD/S
KPSI = .1 RAD/S /RAD
KYD = -20 DEG/ RAD/S
1 S**5 + 12.5275614 S**4 + 54.4966084 S**3 + 189.418558 S**2 + 38.7851718 S + 7.51334065

POLES ARE:
-8.71023749     j 0
-1.80600033     j -4.14745607
-1.80600033     j 4.14745607
-.10266164      j -.177803379
-.10266164      j .177803379


KNY = 30 DEG/g
KR = 1 DEG/ RAD/S
KPSI = .1 RAD/S /RAD
KYD = -30 DEG/ RAD/S
1 S**5 + 14.4591559 S**4 + 67.2332988 S**3 + 192.119206 S**2 + 27.8655869 S + 7.51334065

POLES ARE:
-9.46568976     j 0
-2.42565618     j -3.65940816
-2.42565618     j 3.65940816
-.0689771065     j -.190797648
-.0689771065     j .190797648
```

```
KNY = 30 DEG/G
KR = 1 DEG/ RAD/S
KPSI = .1 RAD/S /RAD
KYD = -40 DEG/ RAD/S
1 S**5 + 16.3907504 S**4 + 79.9699893 S**3 + 194.819855 S**2 + 16.946002 S + 7.51334065

POLES ARE:
-10.5453974     j 0
-2.88603603     j -3.08809845
-2.88603603     j 3.08809845
-.0366404783     j -.196309277
-.0366404783     j .196309277
```

☆ U.S. GOVERNMENT PRINTING OFFICE:1985— 576-003 / 21074

RETURN ADDRESS REQUESTED

____

____

____

Editor, Aeronautics Digest
HQ USAFA/DFAN
U.S. Air Force Academy
Colorado Springs, CO 80840-5831

------------------------------FOLD---------------------------------------

------------------------------FOLD---------------------------------------

NO ACTION REQUIRED

Dear Reader:

Please let us know if either of the two items below apply. If neither is applicable, please do nothing and you will continue to receive the *Digest*.

1. Please discontinue the *Digest*.
2. Change my address to: (print new address)

____

____

____